UNIVERSITY OF Southampton

University of Southampton Research Repository
ePrints Soton

Copyright © and Moral Rights for this thesis are retained by the author and/or other copyright owners. A copy can be downloaded for personal non-commercial research or study, without prior permission or charge. This thesis cannot be reproduced or quoted extensively from without first obtaining permission in writing from the copyright holder/s. The content must not be changed in any way or sold commercially in any format or medium without the formal permission of the copyright holders.

When referring to this work, full bibliographic details including the author, title, awarding institution and date of the thesis must be given e.g.

AUTHOR (year of submission) "Full thesis title", University of Southampton, name of the University School or Department, PhD Thesis, pagination

http://eprints.soton.ac.uk

UNIVERSITY OF SOUTHAMPTON

FACULTY OF PHYSICAL AND APPLIED SCIENCES
School of Ocean and Earth Sciences

# The response of the Antarctic Subpolar Seas to climatic changes

by

**Craig D. Rye**

Thesis for the degree of Doctor of Philosophy

May 2016

UNIVERSITY OF SOUTHAMPTON

ABSTRACT

FACULTY OF PHYSICAL AND APPLIED SCIENCES
School of Ocean and Earth Sciences

Doctor of Philosophy

THE RESPONSE OF THE ANTARCTIC SUBPOLAR SEAS TO CLIMATIC CHANGES

by Craig D. Rye

The Antarctic Subpolar Seas are a poorly observed and understood region with a disproportionate importance for global ocean-climate processes. The region has been subject, over recent decades, to many dramatic climatic forcing perturbations. In particular, it has seen a substantial increase in surface wind stress, and an increase in freshwater forcing from the Antarctic Ice sheet.

The impact of increased freshwater forcing is investigated here using austral summer satellite altimetry measurements. Between 1992 and 2011, an anomalous circumpolar rise in sea level is observed across the Antarctic Subpolar Seas of 1–5 mm $\mathrm{yr}^{-1}$ above the global mean. Several lines of evidence suggest that the observed Subpolar Sea SSH anomaly is a steric response to a recent decadal increase in glacial runoff. An ocean GCM is used to simulate the response of the Antarctic Subpolar Seas to a realistic increase in glacial run-off. The resulting response agrees well with observations and provides insight into the ocean's adjustment. In particular, the model suggests that approximately half of the steric change in sea level is driven directly by freshening in the upper 800 meters, and that deep ocean warming drives the remainder.

The response of the Subpolar Seas to an increase in surface wind forcing is then investigated using an idealised regional configuration of the MITgcm model, referred to as the gyre model. The gyre model is a simplified, Bousinesq, primitive equation model, designed to explore the dynamics of a southern subpolar gyre's adjustment to wind forcing perturbations. The gyre model has four sub-configurations of ranging complexity. Each configuration is examined for its response to a 20% step-increase in surface wind forcing. The gyre model's response varies between sub-configurations, however some common features are found in all runs. The density surfaces of the southern gyre are shown to dome in all sub-configurations following adjustment. Waves and advective features that move cold anomalies northwards dominate the western boundary adjustment. Two distinct types of boundary propagations occur in the gyre model: comparatively fast numerical short boundary waves (NSBW), which move at around 0.05 to 0.5 m $\mathrm{s}^{-1}$; and slower moving advective features, which propagate at between 0.01 and 0.05 m $\mathrm{s}^{-1}$. Analysis suggests that viscous parameters play an important role in the NSBW balance of terms. Further, the pathlines traced by neutrally buoyant particles seeded into the western boundary flow field suggest that the advective features are by the advection of temperature anomalies. The depth, magnitude and propagation velocity of the boundary features vary considerably following minor adjustments in model parameters, such as viscosity, diffusivity and background GM diffusivity. Further work is required to understand the role of boundary waves and boundary propagations, both in observations and models.

The research presented in this thesis highlights that the recent climatic perturbations in the forcing of the Antarctic subpolar Seas are changing the regions circulation in significant and far reaching ways.

# Contents

# List of Figures

# List of Tables

# Declaration of Authorship

I, Craig D. Rye , declare that the thesis entitled *The response of the Antarctic Subpolar Seas to climatic changes* and the work presented in the thesis are both my own, and have been generated by me as the result of my own original research. I confirm that:

- this work was done wholly or mainly while in candidature for a research degree at this University;
- where any part of this thesis has previously been submitted for a degree or any other qualification at this University or any other institution, this has been clearly stated;
- where I have consulted the published work of others, this is always clearly attributed;
- where I have quoted from the work of others, the source is always given. With the exception of such quotations, this thesis is entirely my own work;
- I have acknowledged all main sources of help;
- where the thesis is based on work done by myself jointly with others, I have made clear exactly what was done by others and what I have contributed myself;
- parts of this work have been published as: Rye et al., (2014)

Signed:........................................................................................................................

Date:...........................................................................................................................

# Acknowledgements

I would like to thank my supervisors, Alberto Naviera Garabato, George Nurser and Mike Meredith, for their support throughout my studentship. I would also like to thank Jeff Blundell, Paul Holland, Chris Hughes, Don Chambers and Andrew Coward for their help and advice at different times. Finally I would like to thank the grad-student community in Southampton and my family for their patience and support.

# Chapter 1

# Introduction

## 1.1 Introduction

The Antarctic Subpolar Seas (Figures 1.1 and 1.6) are a fascinating region that play a disproportionately large role in global climate processes, such as the formation, ventilation and export of dense water (Orsi et al., 1999). Furthermore, the Subpolar Seas have been subject to many interesting and climatically important changes in forcing over recent decades (e.g. Marshall et al., 2004).

As an introduction to this thesis, the following chapter provides a review of the key features of the Southern Ocean. It begins by outlining the main components of the Southern Ocean; it also provides an overview of the changes that have been observed in the area over recent decades. Following this overview, it is suggested that changes to glacial and wind forcing in the Subpolar Sea have been particularly dramatic over recent decades. The following thesis then discusses research on the response of the Antarctic Subpolar Sea to these forcing perturbations.

This chapter is divided into two main areas: section 1.2.1 outlines the physical setting of the Southern Ocean, in particular, the Antarctic Subpolar Sea and the Weddell Gyre. Section 1.3 discusses the climatic changes that have been observed over recent decades, either in the Southern Ocean or in relation to it.

## 1.2 The Southern Ocean Environment

### 1.2.1 Boundary Conditions

The boundary conditions of the Southern Ocean are outlined first before discussing the major components of the Southern Ocean and its climate. These boundary conditions, such the surface wind forcing, are highly influential on the region's dynamics, and character.

#### 1.2.1.1 Topography

A good starting point for an overview of Southern Ocean physics is a review of the region's topographic boundary conditions. The southern extent of the Southern Ocean is defined by the large Antarctic continental shelf which, covers around 15% of the global continental shelf area (Clarke and Johnston, 2003; Smith and Sandwell, 1997). At its northern edge, the continental shelf transitions into a steeply inclined continental slope. The slope merges into the abyssal sea floor at around 3500 m depth.

The topography south-east of South America is particularly interesting. This region is associated with the Weddell gyre (which is described in detail in section 4.4), and dense water export from the Subpolar Seas (e.g. Meredith et al., 2000; Meredith et al., 2001). The Weddell Sea is a semi-enclosed deep basin, lying to the south-east of the South American continent (Figure 1.1). The South Scotia Ridge (SSR) flanks it to the west by the Antarctic Peninsula and to the north. The Scotia Sea then lies to the north of the of Weddell Sea and is a region with many complex topographic features that form an arc of submarine mountains and provide a pathway northward from the Antarctic Peninsula to South America. This complex group of features provides both a pathway and a barrier to deep northward flow (Locarnini et al., 1993).

#### 1.2.1.2 Cryosphere

The Antarctic cryosphere is another important boundary to the Southern Ocean. This thesis emphasises its importance as a source of buoyancy forcing for the Southern Ocean. However, it is a highly important component of the global climate system by itself.

The cryosphere can be thought of as three components: land-based ice (continental ice), floating ice shelves, and sea ice. The continental ice sheet can be further divided into three distinct regions: the East Antarctic (EAIS), West Antarctic (WAIS), and the Antarctic Peninsula (Figure 1.2). The EAIS is relatively stable and may have gained mass over recent decades (Shepherd et al., 2012). Both the WAIS and the Antarctic Peninsula lie below sea level and are considered to be relatively unstable. The combined mass loss of both WAIS and the Peninsula over the last two decades sum to 85 ± 30 Gt yr$^{-1}$ (Shepherd et al., 2012). These trends are discussed further in section (2.2.2.1; Chapter 2)

Floating ice shelves cover about one-third of the continental shelf, and abut the sea ice for most of the year (Figures 1.2 and 1.3). Antarctic Sea ice cover has large seasonal

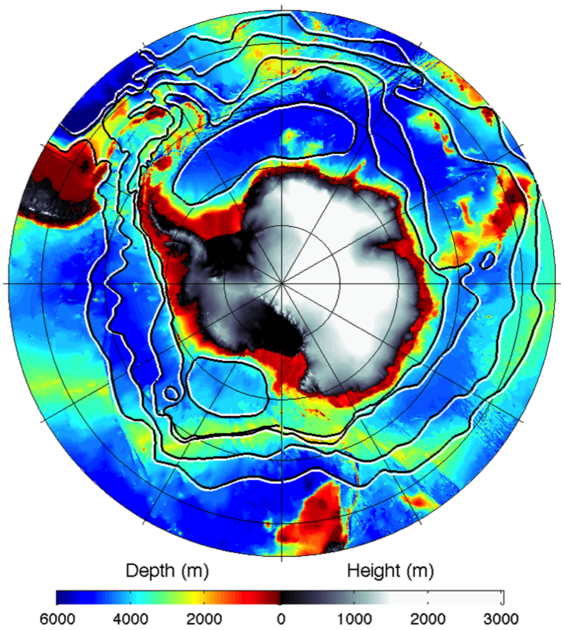

Figure 1.1: Topographic map of the Southern Ocean and the Antarctic continent, black contours show the approximate mean path of the Southern Ocean's main fronts, as well as the Ross and Weddell Gyres, taken from Meredith and Brandon (2015).

variability, at its maximum in the austral spring, it typically covers around 20 × $10^6$ $km^2$, most of which melts during austral summer (Figure 1.3; Bamber et al., 2009).

#### 1.2.1.3 Surface Winds

The Southern Oceans westerly surface winds are amongst the strongest in the world and are one of the most characteristic forcing mechanisms of the Southern Ocean climate. These winds are predominantly zonal. They weaken as they move into high latitudes, and eventually change sign towards the Antarctic continent. They provide a cyclonic curl to the oceans surface that is of great significance to many Southern Ocean processes (Figure 1.4; Deacon, 1937).

Related to the variability of atmospheric forcing over the Southern Ocean is the Antarctic Oscillation Index (AOI; Gong and Wang, 1998,Gong and Wang, 1999). The AOI is a measure of the strength of the atmospheric pressure anomaly between mid and high latitudes and, therefore, is also a measure of the strength of the polar vortex (Gong and Wang, 1999).

Thompson and Wallace (2000) extended this concept, using principal component analysis to define the dominant mode of variability for Southern Ocean winds, referred to as the Southern Annular Mode (SAM). Similar to the AOI, the SAM has a strong link

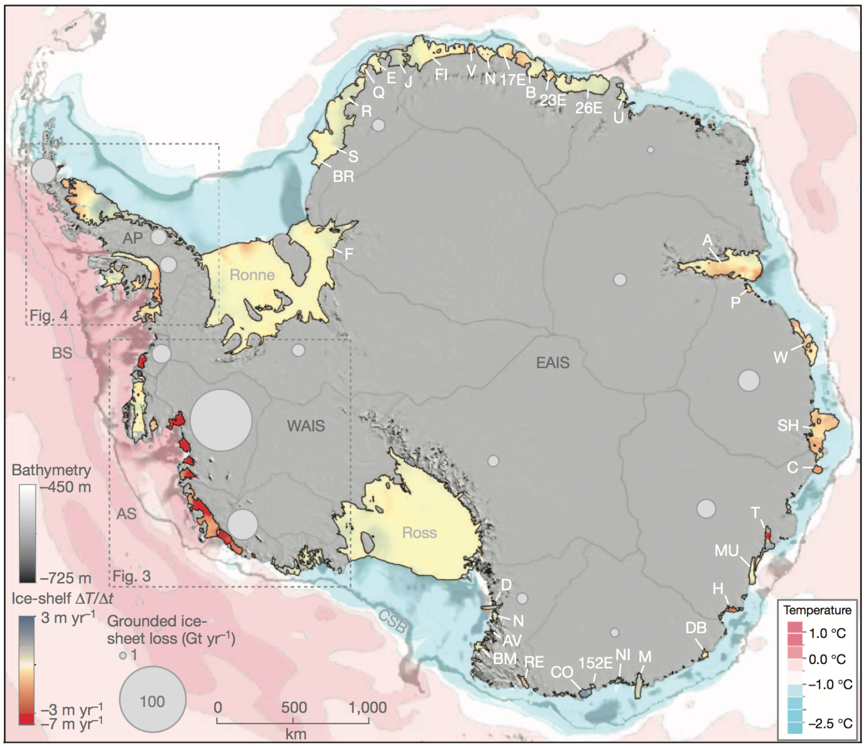

Figure 1.2: Schematic showing the partitioning of the Antarctic Ice Sheet. The East Antarctic Ice Sheet (EAIS), West Antarctic Ice Sheet (WAIS), and the Antarctic Peninsula (AP) are indicated by their acronyms. Topography is shaded in black and white. The average temperature is shaded in pink and blue. The major ice shelves are shaded, red to yellow depending on the rate of thickness loss between 2003 and 2008. The largest ice shelves; the Ross and the Ronne, are labelled. Grey circles indicate the rate of grounded ice sheet loss between 2003 and 2008. Taken from Pritchard et al. (2012).

to surface wind forcing and a relation to the polar vortex (Gong and Wang, 1999). Observations and modelling studies suggest that the SAM describes around one-third of Southern Hemisphere atmosphere climate variability, over a range of time-scales (Baldwin, 2001; Kidston et al., 2009). As shown in Figure 1.5, positive SAM states are associated with an increased pressure gradient between the subtropics and the poles and a stronger polar vortex. The pressure distribution associated with the SAM is almost zonally symmetric, with the notable exception of the region between the Ross Sea and the Antarctic Peninsula, where the Amundsen Sea Low leads to marked meridional components in the wind field. The SAM is commonly used in the following text as a metric for the strength of Southern Ocean winds.

### 1.2.2 The Antarctic Subpolar Seas And The Weddell Gyre

The Antarctica Subpolar Seas are then the main focus of this thesis. They are described here within the context of the Southern Ocean. The Subpolar Seas are a relatively

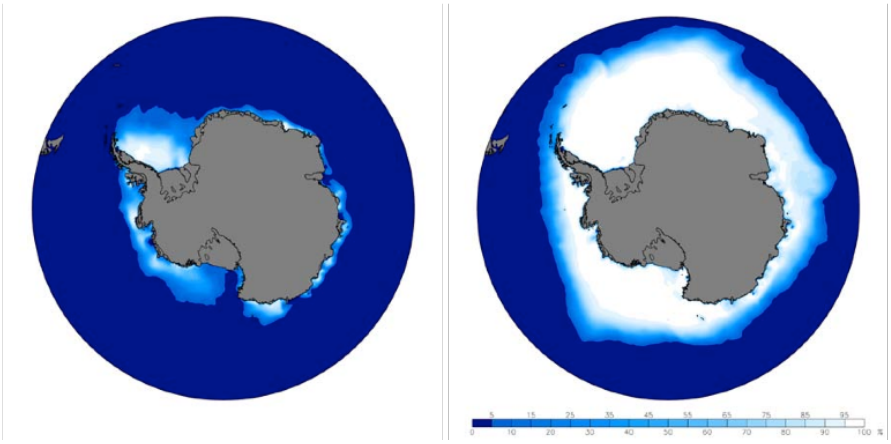

Figure 1.3: Antarctic mean sea ice cover averaged over the period 1979–2007. Left: February, showing the winter extent, right: September, showing the summer extent, taken from NSIDC (see: $http : //nside.org/cgi - bin/bist/bist.pl?config = seaice\_index$).

small region situated between the Antarctic continent and the Antarctic Circumpolar Current (ACC), covering 20 × $10^6$ $\mathrm{km}^2$. However, they host the majority of the air-sea-ice interaction of the Southern Ocean. This interaction is crucial for many climate processes, such as the stability of the Antarctic ice sheet, and the generation of Antarctic Bottom Water (AABW; Orsi et al., 1999, Jacobs, 2004).

The Subpolar Seas are dominated by westward-flowing slope currents, associated with the Antarctic Slope Front (ASF; Figure 2.2) and the Antarctic Coastal Current (AC; Heywood et al., 2004). Superimposed upon these currents are the wind-driven polar gyres. The largest of these are the Weddell and Ross Gyre (Figure 1.6) with transports of around 50 and 40 Sv respectively (Sv; Fahrbach et al., 1994; Klatt et al., 2005 McCartney and Donohue, 2007). These gyres are structured by regional topography (pers. comm.: Ryan Patmore and Paul Holland 2014, British Antarctic Survey, Cambridge, UK), and have domed density surfaces and upwelling in their interior (Orsi et al., 1993). An example of the salinity distribution across the Weddell Gyre, shown in Figure 1.7, highlights the domed structure of density surfaces in the gyre (Carter et al., 2008).

The Weddell Gyre is of particular interest, as previously mentioned, because of its role in deep water export. It is an almost enclosed system, flanked to the west by the Peninsula, to the south by the Antarctic continent, and to the north by the approximately 2500 m deep SSR. At its western boundary, the Antarctic Peninsula acts as a barrier to zonal flow, and facilitates the northward export of Weddell Sea Deep Water (WSDW; Whitworth et al., 1994). To the north, the Weddell Gyre merges into the Scotia Sea, forming the Weddell-Scotia Confluence (WSC), where the juxtaposition of the Weddell Gyre and the ACC combine with the injection of the shelf waters from near the tip of the Antarctic Peninsula to create ventilated waters of unusually low stratification (Whitworth et al. 1944).

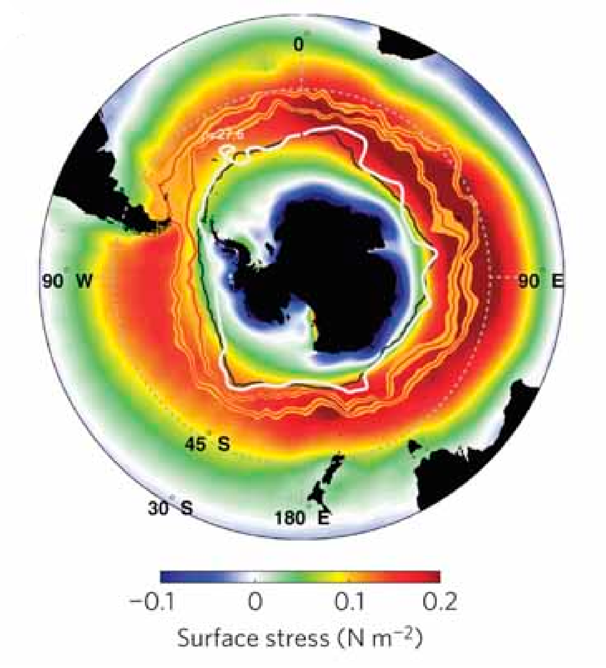

Figure 1.4: Mean Southern Hemisphere zonal wind stress, for the period 1980-2000, derived from the National Centres for Environmental Prediction (NCEP) reanalysis. The Sub-Antarctic and Polar Fronts are marked in orange and the black line marks the winter extent of sea ice. Taken from Marshall and Speer (2012).

The export of WSDW is of critical importance to the global abyssal circulation. WSDW is formed both from the mixing of the denser Weddell Sea Bottom Water (WSBW) with overlying lighter waters in the Weddell Gyre, and from the direct transport of dense waters from the shelf region (Foster and Carmack, 1976; Gill, 1973). Recent work has identified an additional source for WSDW, which enters the Weddell basin as a deep flow from the east (Meredith et al., 2000). This additional source is thought to form as a result of intense ice formation and brine rejection near Cape Darnley (Ohshima et al., 2013). WSBW itself is too dense to leave the Weddell basin. It lies below the topographic barriers to the north and therefore, must mix with lighter waters and become the lighter WSDW before being exported northward (Meredith et al., 2000)

The Scotia Sea (Figure 1.9) is the most direct route for WSDW to flow northward (Locarnini et al., 1993) and is, therefore, important for deep-water export. WSDW can enter the Scotia Sea via deep gaps in the SSR, of which the 3200 m deep Orkney Passage is the deepest (Gordon et al., 2001; Garabato et al., 2002a), or it can enter via gaps in the South Sandwich Island arc (Meredith et al., 2001; Garabato et al., 2002b).

The majority of WSDW exits the Scotia Sea in the vicinity of the Georgia Passage, southeast of South Georgia (Figure 1.9). Upon leaving the Scotia Sea, WSDW spreads northward into the Georgia Basin, where it continues north into the Argentine Basin or

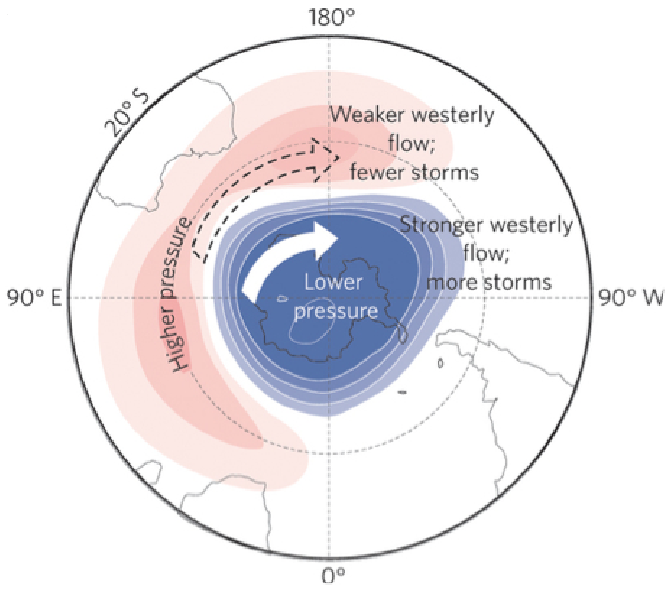

Figure 1.5: Schematic showing the surface atmospheric pressure pattern associated with a positive SAM state, taken from Jones (2012).

recirculates southeastwardly back toward the Weddell Sea (Arhan et al., 1999; Meredith et al., 2001). Bottom waters formed around Antarctica are often referred to collectively as Antarctic Bottom Water (AABW). WSDW and WSBW are the main constituents of global AABW, and north of the Weddell gyre, WSDW and WSBW are commonly described as AABW (Warren, 1981; Orsi et al., 1999).

### 1.2.3 The Antarctic Circumpolar Current

The Antarctic Circumpolar Current (ACC) forms the northern boundary of Subpolar Sea, it is the dominant circulation of the Southern Ocean, and the world's largest, and longest, current, carrying approximately 150 Sv (Cunningham et al., 2003; Rintoul et al., 2001) circumpolar. The ACC acts as a pathway for the exchange of properties, and anomalies between the major ocean basins (see the review of e.g. Rintoul et al., 2001). Therefore understanding the dynamics of ACC is crucial for understanding the Subpolar Sea, and the general response of the Southern Oceans to recent decades changes in ocean forcing.

The absence of zonal boundaries in the Southern Ocean facilitates unique regional dynamics, where gyre-based dynamics, common in other ocean basins, are not applicable (Sverdrup, 1947). It is useful to first describe the complex flow of the ACC qualitatively: the ACC is primarily driven by eastward surface winds, which have an effectively infinite distance (fetch) over which to impart momentum upon the ocean. In addition, these winds impart a cyclonic curl on the Southern Ocean, which drives a divergence in the

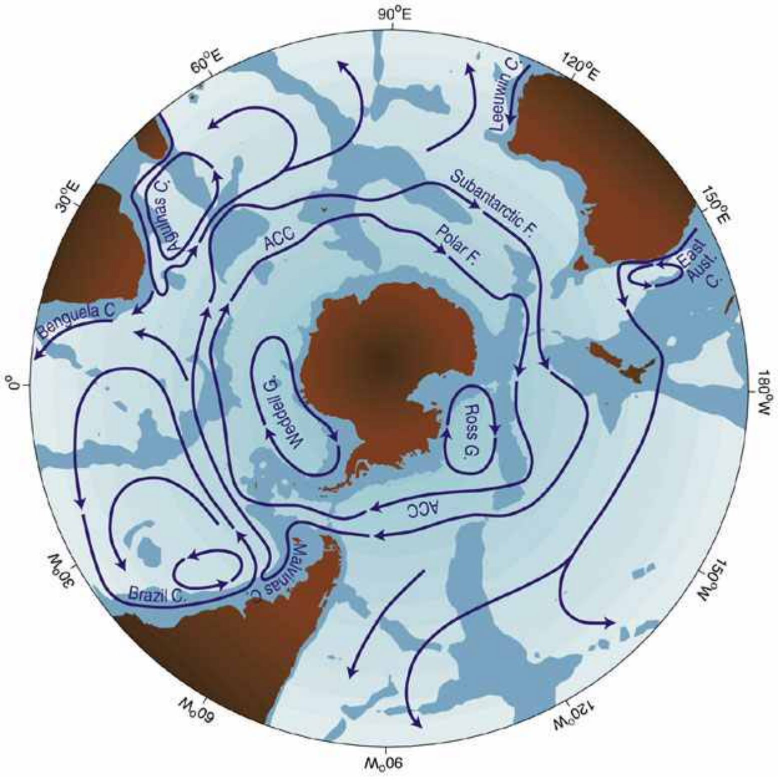

Figure 1.6: Taken from Siedler et al. (2001): Schematic of Southern Ocean circulation, showing the Antarctic Circumpolar Current (ACC) and its major fronts, as well as the Southern Polar gyres. Topography that is less than 3500m deep is shaded.

surface Ekman transport (Figure 1.10). This divergence drives the upwelling of subsurface waters and a resultant tilt of interior isopycnals (density surfaces; Figure 1.10). Isopycnals tilt upwards towards the south, across the ACC, where additional buoyancy forcing supports the tilt. The tilt of isopycnals is related to the strength of zonal flow (the ACC) through geostrophic and is balanced by the slope in sea surface height SSH.

An additional key feature of the ACC is its rich mesoscale eddy field. Multiple authors highlight the importance of eddies in Southern Ocean dynamics, both in models (Hallberg and Gnanadesikan, 2001; Hogg and Blundell, 2006; Hogg et al., 2008) and observations (e.g. Meredith and Hogg, 2006). These eddies act to flatten steeply sloping isopycnals and drive a net-southward bolus transport that carries heat polewards. In this way, northward Ekman transports are balanced by southward eddy fluxes (Rintoul et al. 2001).

It is suggested that the ACC conforms to a relatively eddy-saturated regime where increases in surface wind forcing do not drive large changes in zonal transports. Instead, increases in wind stress impart energy into the mesoscale eddy field, resulting in only small variations in ACC transport (Hallberg and Gnanadesikan, 2001; Meredith et al. 2010; Marshall et al. 2012).

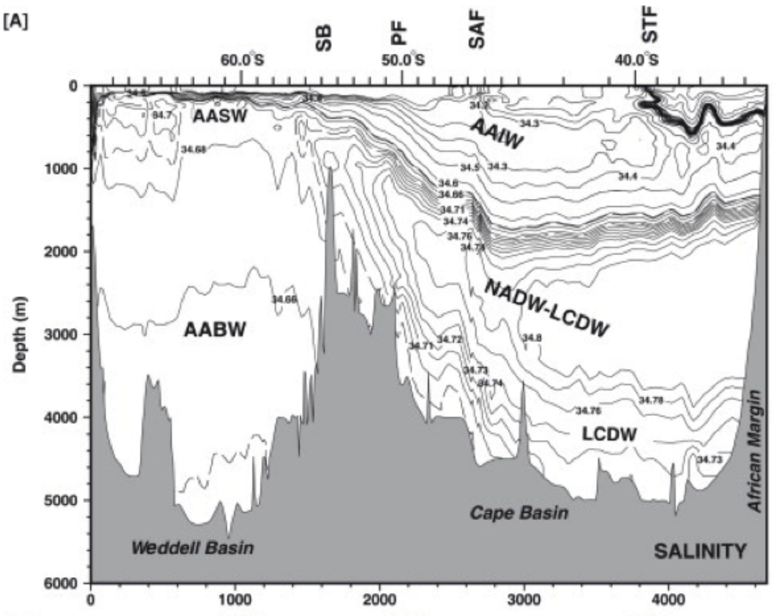

Figure 1.7: A hydrographic cross section through the Weddell Gyre and the Weddell-Scotia confluence. Contours show the salinity distribution. Major water masses are marked by their common acronyms. AABW: Antarctic Bottom Water, AAIW: Antarctic Intermediate Water, NADW: North Atlantic Deep Water, LCDW: Lower Circumpolar Deep Water (taken from Carter et al. (2008), originally derived from WOCE data *http : //woceatlas.tamu.edu/*).

### 1.2.4 The Southern Ocean's Overturning Circulation And Deep Water Formation

The MOC plays a significant role in globally distributing ocean properties and climatically-important tracers (e.g. Lumpkin and Speer, 2007). The Southern Ocean component of the MOC (the SMOC) is of particular importance because of the Southern Ocean's connection with other major oceans basins. Where the SMOC can be considered as the centre of the global MOC (Figure 1.11). The following section describes the main features of the SMOC. Emphasis is given to deep water formation and the lower limb of this circulation as these will be a component of a model discussed in a later chapter.

The SMOC is driven by a combination of zonal wind-stress, and air-sea buoyancy fluxes. The Southern Ocean's winds flow eastward, in an almost meridionaly symetric distribution, with a maximum around 50 $^o$S. An anticyclonic curl in wind stress occurs over the northern region and a cyclonic curl in wind stress occurs towards the continent. This distribution of winds drives surface waters northwards and the tilting (shoaling) of density surfaces upwards towards the Antarctic continent. Upwelling (divergence) occurs close to the Southern Boundary of the ACC (Figure 1.10), and downwelling (convergence) occurs close to the SubAntarctic front. Air-sea buoyancy fluxes generate dense water

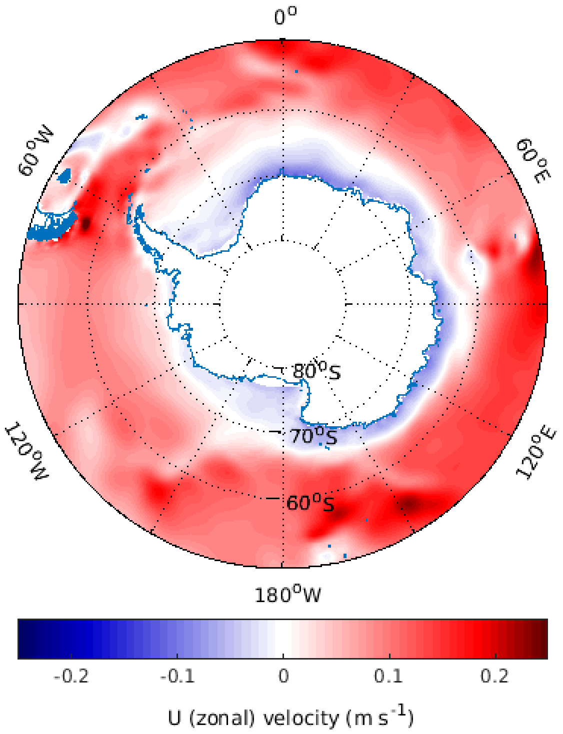

Figure 1.8: A snapshot of Southern Ocean surface zonal velocities, simulated by the $1^o$ NEMO model (Madec, 2008).

near the continent (Fofonoff , 1956; Gill, 1973) and lighten the surface layers within the ACC.

The wind-driven shoaling of density surfaces is balanced by eddies, which are formed from baroclinic instabilities. These eddies act to flatten density surfaces and transport mass, buoyancy and potential vorticity across the ACC (Gill, Green and Simmons, 1975; Marshall et al, 2002; Marshall and Radko, 2003; McWilliams et al, 1973; Marshall, 1981; Johnson and Bryden, 1989; Gnanadesikan, 1999; Hallberg and Gnanadesikan, 2001; Karsten et al, 2002; Marshall and Radko, 2003, 2006; Bryden and Cunningham, 2003; Olbers and Visbeck, 2005). By decomposing the mass transport, density coordinates, to mean and eddy contributions, the 'residual flow' of the SMOC can be identified, where surface wind-driven, and deep geostrophic flows, are largely balanced by the bolus velocity of eddies (Danabasoglu and McWilliams, 1995).

The SMOC consists of Upper and lower circulation cells (Figure 1.12). The upper cell consists of light, Upper CDW (UCDW) which upwells at the surface divergence, and is driven northwards. These waters are then made lighter by warming and precipitation, forming SubAntarctic Mode Water (SAMW) and SubAntarctic Intermediate water (SAIW; Figure 1.10; e.g. Schmitz, 1995; Lumpkin and Speer, 2007; McCartney 1982; Rintoul 1991). SAMW and SAIW downwell around the subtropical front and are transported north (Rintoul et al. 2001).

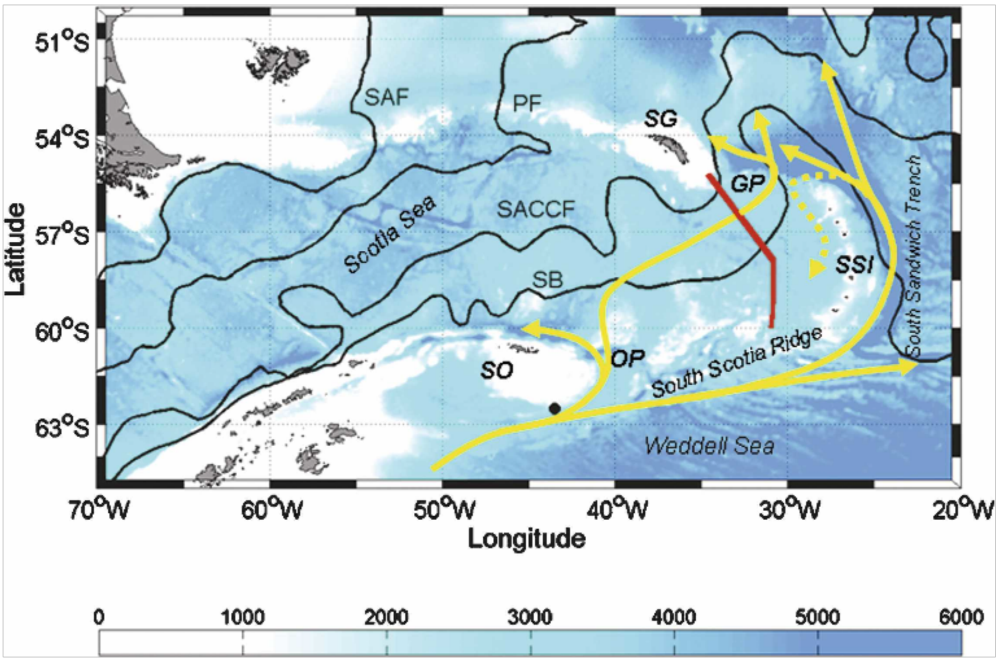

Figure 1.9: Topographic map of the Scotia Sea, with schematic pathways for deep water export drawn on. The ACC mean fronts are shown as black contours. Topographic features such as South Georgia (SG), South Orkney (SO), Orkney Passage (OP), Georgia Passage (GP) and the South Sandwich Islands (SSI), are demarked by their acronyms. The main northward pathway for Antarctic deep water export is shown by the yellow solid lines. An intermittent inflow of the denser Antarctic waters through GP is marked as a yellow dashed line. This Figure is from Meredith et al. (2008), with bathymetry from Smith and Sandwell (1997).

The lower cell consists of denser UCDW and Lower CDW, which upwell on the southern side of the divergence. These waters flow south, entering the Antarctic Subpolar Seas, where they increase in density by loosing heat to the atmosphere and gaining salinity due to brine rejection from sea ice formation (Baines and Condie, 1998; Foldvik et al., 2004; Rintoul et al., 2001). When sufficiently dense, these waters cascade down the continental slope of Antarctica, to form Antarctic Bottom Water (AABW). The densest Subpolar Sea waters form, or are ventilated, in the Weddell Gyre, these are Weddell Sea Deep Water (WSDW) and Weddell Sea Bottom Water (WSBW). After formation, AABW moves northwards northwards, and fills the base of the global abyssal oceans (e.g. Wüst, 1935). This deeper component of the SMOC is shown as a deep cell, highlighted in Figure 1.12.

As suggested by Figure 1.12, the northward transport within the surface and bottom cells is balanced by the southward transport of UCDW, LCDW, and North Atlantic Deep Waters (NADW).

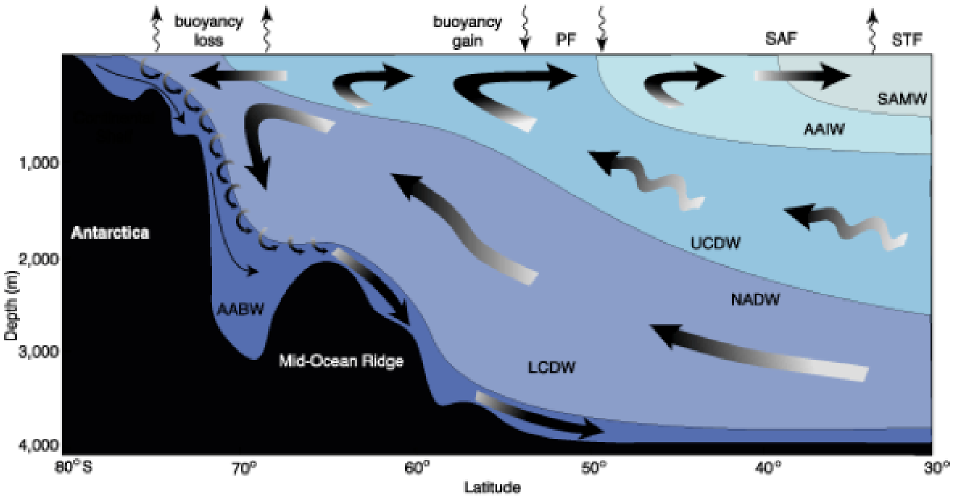

Figure 1.10: Schematic of meridional overturning circulation in the Southern Ocean, taken from Olbers et al. (2004) and Speer et al. (2000). Here shading bands represent density surfaces. Isopycnals tilt upwards towards the Antarctic continent, bringing the Upper and Lower components of Circumpolar Deep Water (UCDW and LCDW) to the surface. These waters then diverge, lighter waters are driven north, and they gain buoyancy and are ultimately subducted to form intermediate water masses. Denser waters are transported south, they lose buoyancy, forming dense water masses; these cascade down the continental shelf and join the abyssal oceans. Additional acronyms, AABW: Antarctic Bottom Water, NADW: North Atlantic Deep Water, AAIW: Antarctic Intermediate Water, SAMW: South Atlantic Mode Water, PF: Polar Front, SAF: Sub-Antarctic Front, STF: Subtropical Front.

## 1.3 The Southern Ocean's Changing Climate

The following sections review recent decadal Southern Ocean climate changes. Of particular interest here are those occurring in the Subpolar Seas, which are a sensitive region for global climate processes. Changes in the surface winds and the cryosphere, are seen to be the most dramatic. The response of the Subpolar Sea to perturbations in buoyancy and wind forcing is explored further in chapters 2-3 and 4-5, respectively.

### 1.3.1 The Changing Winds

As shown in Figure 1.13, over recent decades, the SAM has followed a generally positive trend, which is thought to be driven by a decrease in stratospheric ozone (Thompson and Solomon, 2002), enhanced greenhouse warming (Fyfe et al., 1999; Kushner et al., 2001), and natural variability. This change in SAM has been associated with a number of climate trends such as an increase in the strength of the southern polar vortex, a southward movement and strengthening of the Southern Ocean winds, and a cooling

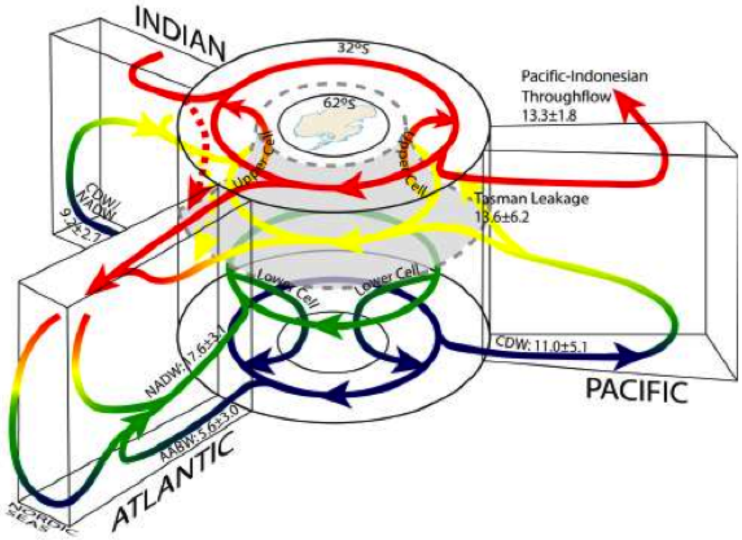

Figure 1.11: Schematic view of the Southern Ocean meridional overturning circulation, with emphasis given to the central role of the Antarctic Circumpolar Current (ACC) and water masses formed in the Southern Ocean in the circulation of the global ocean. Taken from Lumpkin and Speer (2007).

over the majority of the Antarctic continent (Marshall et al., 2004; Thompson and Solomon, 2002). These trends have also been found in modelling studies forced by a positive SAM trend (Fyfe and Saenko, 2005).

Further, the trend in the SAM has been proposed on physical principles to drive an increase in a number of properties: ACC transport, CDW upwelling, eddy kinetic energy and poleward heat transport (Sen Gupta and England, 2006; Hogg et al., 2008; Meredith and Hogg, 2006). Enhanced upwelling of CDW and a southward shift of the ACC are intuitive responses to the trend in SAM, both would act to bring warmer water into contact with the base of floating glacial ice, and facilitate increased glacial melt (Jacobs, 2006). SSH observations imply a southward shift of the ACC, and are discussed in the following section; however, upwelling is difficult to measure, and no observations show an increase in ACC transport (Meredith et al., 2011).

The Weddell Gyre is of particular interest to this thesis because of its role in deep-water ventilation and export. The distribution of the surface wind trend in this region is illustrated in Figures 1.14–1.16. Here a maximum anomaly between 1992 and 2010 occurs around 52 °S, in the northeastern sector of the gyre. The trend in the curl of the zonal wind stress is shown in Figure 1.16. A net positive trend is evident between 60 and 72 °S. This plot also highlights a band of strongly cyclonic curl persisting over the northern edge of the Weddell Gyre.

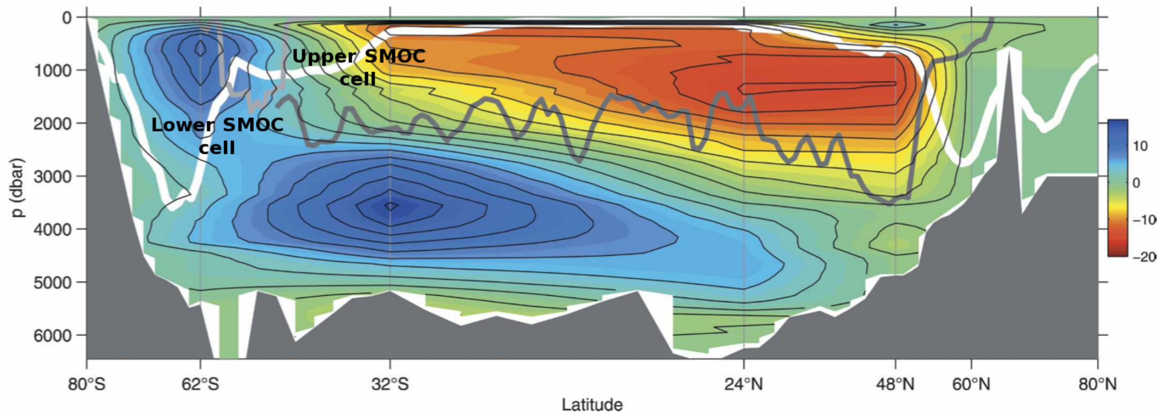

Figure 1.12: Zonally averaged global overturning stream function (Sv) derived from hydrographic sections which are marked as vertical grey lines, between 1992 and 1995. Typical winter mixed layer depths are shown as a white contour, the mean depth of ocean ridge crests is shown as a dark grey line. The depth of the Scotia Arc east of Drake Passage is shown as a light grey line. Taken from Lumpkin and Speer (2007).

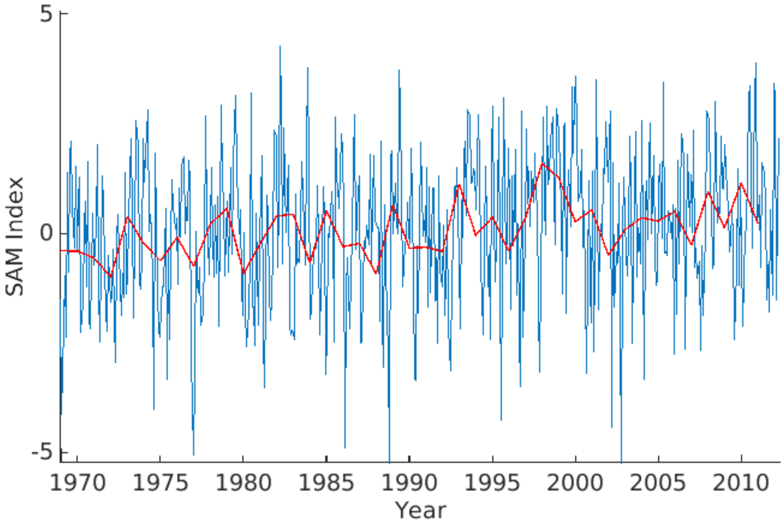

Figure 1.13: Time series of the Southern Annular mode, 1970-2010, provided by Gareth Marshall, British Antarctic Survey, Cambridge, UK (see: http://www.nerc-bas.ac.uk/icd/gjma/sam.html; Marshall, 2003). Blue line: monthly averaged data, red line: yearly averaged data.

### 1.3.2 The Changing SSH

As mentioned in the previous section, the SAM has shown a positive trend over recent decades and intuition suggests that the ACC should have moved southwards, driven by this trend. Sokolov and Rintoul (2002-2009) provide some supporting evidence for the southward movement of the ACC. First, Sokolov and Rintoul (2002; 2007) use a long

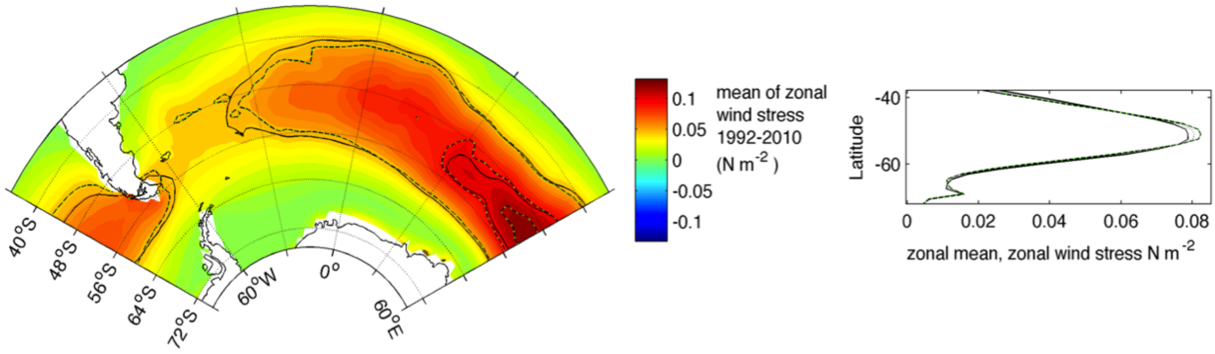

Figure 1.14: Left: Average zonal wind stress over the Weddell Gyre between 1992 and 2010. Black line: contours of wind stress from 1992, red and green dashed line: contours of wind stress from 2010. Right: zonal average wind stress. Derived from ERA-Interim reanalysis data Dee et al. (2011).

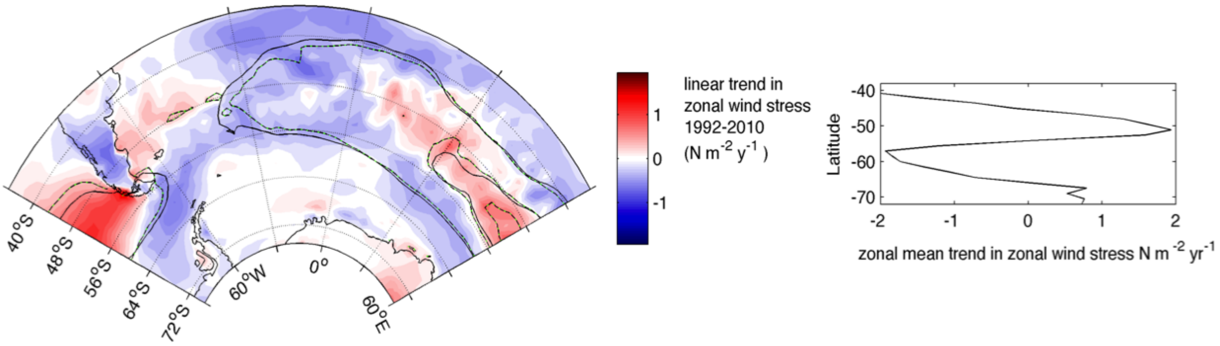

Figure 1.15: Left: Linear trend in zonal wind stress over the Weddell Gyre between 1992 and 2010. Black line: contours of wind stress from 1992, red and green dashed line: contours of wind stress from 2010. Right: zonal average wind stress. Derived from ERA-Interim reanalysis data Dee et al. (2011).

time series of SSH-altimeter maps and historic hydrographic data, along with Argo float data, to show that the distribution of ACC fronts can be linked with constant values of SSH. Sokolov and Rintoul (2007b) then argues, the hydrographic properties associated with the ACC's major fronts coincide with particular values of SSH. Then, Sokolov and Rintoul (2009a) observe a southward shift of SSH contours in satellite altimetry, and therefore, argue a southward shift of the major ACC fronts has occurred. However, the assumptions made by Sokolov and Rintoul (2002-2009) in relating SSH contours to ACC fronts may be incorrect (e.g. Graham et al., 2012).

However, Thompson and Demirov (2006) suggest an alternative definition for the ACC's fronts. They suggest that the fronts can be identified by the skewness and kurtosis of the sea level anomaly (SLA) across ACC jets. In this sense, the fronts are found by

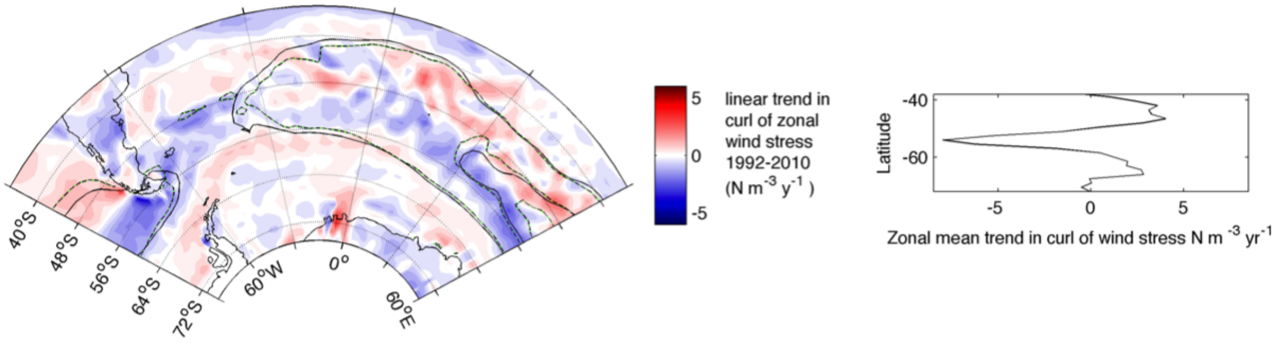

Figure 1.16: Left: Linear trend in the curl of zonal wind stress over the Weddell Gyre between 1992 and 2010. Black line: contours of wind stress from 1992, red and green dashed line: contours of wind stress from 2010. Right: zonal average wind stress. Derived from ERA-Interim reanalysis data Dee et al. (2011).

their horizontal variability in eddy activity. Shao et al. (2015) use the Thompson and Demirov (2006) method to track the ACC's major fronts; the Polar Front (PF) and the Sub-Antarctic Front (SAF), over the last two decades of SLA satellite data. Shao et al. (2015) argue that the PF and the SF have expressed enhanced variability near significant topographic features over recent years, which may occur in relation to an increase in SAM, but neither have a clear meridional shift over the period.

Multiple authors have made observations that support the view of either a southward-moving ACC or a warming Southern Ocean coupled with global sea level rise. The driving force behind these observations is a topic of current research. For example, Gille (2002) showed that the Southern Ocean is warming more rapidly than the rest of the global ocean. Furthermore, Böning et al. (2008) analysed temperature, salinity and density changes along mean streamlines in the Southern Ocean and found that the Southern Ocean was warming and freshening.

### 1.3.3 The Changing Cryosphere

In addition to changes in wind stress, the Subpolar Seas are at present experiencing a significant increase in freshwater discharge from the grounded Antarctic Ice Sheet and its fringing ice shelves (Shepherd et al., 2004, 2010, 2012). The magnitude of freshening and the effect on the Subpolar Sea is the subject of chapters 2-3. Therefore, a brief introductory review of the changes occurring to the Antarctic Cryosphere is given.

The Amundsen Sea sector of West Antarctica is the most rapidly changing region of the Antarctic ice sheet (Jenkins et al., 2010). Its major glaciers have all shown increases in flow speed and thinning over recent decades. It is important to note that these changes in the Amundsen Sea could be driven by a continuing response to historical forcing, or both historical and recent changes in forcing (Jacobs et al., 2011). A number of authors have suggested that the increase in melt in this region is related to the warming of regional shelf waters, which drive an increase in the rate of melting at the base of floating ice shelves, and in turn, facilitates more rapid ice flow upstream (Shepherd et al., 2004; Schmidtko et al., 2014). Moreover, it is suggested that atmospheric or oceanic circulation changes have driven warmer Circumpolar Deep Water (CDW) onto the Amundsen continental shelf in recent decades. This process (and its link to ice melt) is a topic of significant current research.

Ice shelves along the Antarctic Peninsula have also changed rapidly in recent decades, with most western glaciers showing an overall retreat in the last 50 years (Rau et al., 2004). Here, ice loss has been attributed both to surface and sub-surface melting (Scambos et al., 2000). The East Antarctic ice sheet is the most stable component of Antarctic ice, showing modest thickening, but no clear trend for the fringing ice shelves (Pritchard et al., 2012).

### 1.3.4 The Changing Surface Water Properties

As previously discussed, the waters of the ACC have warmed more rapidly than the global average over recent decades, increasing by around 0.24C between 300-1000 m depth, between the 1960s and the 2000s (Figure 1.17). Further this rate is fastest from the 1980s to present (Gille, 2002; Böning et al., 2008). This warming is more intense on the southern side of the ACC than the northern side, supporting the theorised southward shift of the ACC; however, alternative forcing mechanisms have been suggested for the trend (Gille, 2002; Böning et al., 2008). North of the ACC a significant freshening of 0.03 between 1980 and present has been observed (Böning et al., 2008).

Schmidtko et al. (2014) reviews hydrographic data to provide a view of recent decadal changes in the Subpolar Sea, between 1975 and 2012.

Here CDW shows significant warming and shoaling in most regions around the continent. The largest shoaling occurs in the Amundsen and Bellingshausen seas. Further, Winter Water (WW) is found to be freshening along the Southern limb of the Ross Gyre and in the western Indian Ocean, while becoming saltier in the northwestern Weddell Sea.

### 1.3.5 The Changing Deep Water Properties

The changing properties of the Antarctic deep waters are arguably one of the least understood and significant features of recent climate change. Multiple authors have observed a recent widespread warming of Antarctic Bottom Water (AABW; e.g. Jacobs, 2004; Meredith et al., 2000; Fahrbach et al., 2011; Meredith et al., 2008; Coles et al., 1996; Johnson and Doney, 2006; Andrié et al., 2003; Purkey and Johnson, 2010; Purkey and

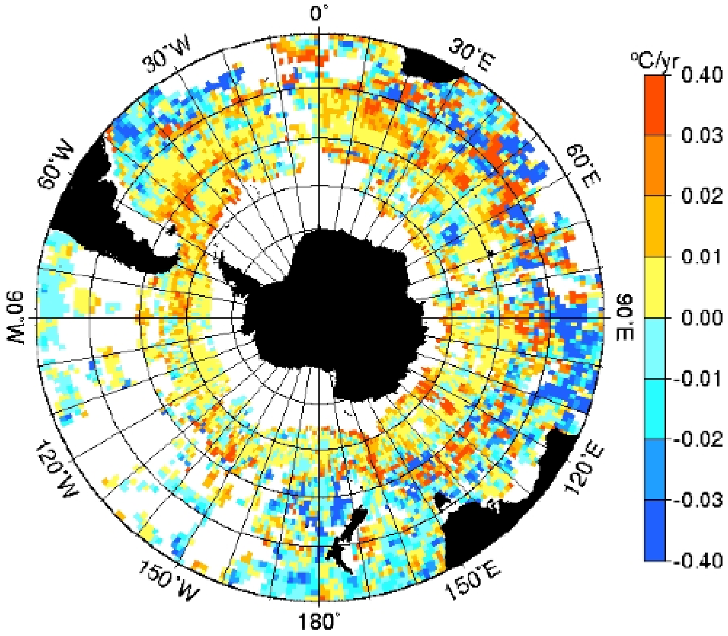

Figure 1.17: Southern Ocean temperature trends at 900 m between 1950 and 2002, taken from Gille (2002).

Johnson, 2012). Separate observations of warming show differences in bottom temperature trends and lateral temperature gradients; however, the net change in temperature at each station and the timing of the changes is clearly suggestive of a decadal warming, which propagates northward from the Southern Ocean. This warming is most prominent in the Southwest Atlantic, close to the source regions of AABW (Johnson and Doney, 2006; Zenk and Morozov, 2007).

As previously mentioned, the global warming of AABW is arguably one of the most prominent and least understood features of recent decadal climate change (e.g. Purkey and Johnson, 2012). It has direct implications for sea level and global heat budget (Purkey and Johnson, 2010). Further, it has been hypothesized that the trend is driven by a reduction in Antarctic abyssal water export (Johnson et al., 2008). If correct, the observed trend may have significant implications for the long-term stability of the southern overturning circulation and deep ocean ventilation.

Here a review is given of warming observations. Discussions are initiated from the source region of AABW and later follow its path northwards. AABW is first derived from the dense waters of the Weddell Gyre. Un-intuitively these source waters, namely WSBW and WSDW, appear decoupled from global AABW variability.

WSBW change is best characterised by a warming before the 1990s, a cooling during the 1990s and a warming thereafter. WSDW warms by around 0.01$^o$C yr$^{-1}$ between 1$^o$C between 1999 and 2005 (Meredith et al., 2008). After 2005, there are no trends in WSDW temperature or salinity (Meredith et al., 2008). The component of dense waters entering the Weddell Gyre from the east show the clearest warming signal (Jacobs, 2004; Meredith et al., 2000; Couldrey et al., 2013). It was argued this warming of eastern Antarctic deep water is due to a greater entrainment of the ACC into eastern deep water formation regions (Jacobs, 2004; Couldrey et al., 2013). This process of increased entrainment of the ACC into these deep water formation sites is expected to also raise the salinity of eastern deep water; however, it is argued that a separate freshening of the AABW to the east of the Weddell Gyre is likely to mask this effect (Couldrey et al., 2013). Salinity trends in the Weddell Gyre are also variable. WSDW salinity increases by around 0.005 between 1995 and 2005 period, reversing after 2005. A decrease in WSBW salinity occurs in the late 1980s, returning to no trend after the early 1990s (Figure 2; Fahrbach et al., 2011).

Further north, Jullion et al. (2013) documents a long-term freshening of AABW in the south-east Drake Passage region, since 1993. This freshening in Drakes Passage implies that WSDW is freshening at its formation site in the western Weddell Sea (Jullion et al., 2013). Freshening is also observed in the shelf waters of the northwestern Weddell Sea (Hellmer et al., 2011). From these observations, it is suggested that this freshening is primarily driven by the collapse of the nearby ice shelves (most dramatically, Larsen B), and the acceleration of the glaciers that were buttressed by the ice shelf prior to its collapse (Jullion et al., 2013).

North of Drake Passage, the dense waters leaving the Weddell Gyre enter the Scotia Sea. Here both a decadal warming trend and a strong interannual cycle (emanating from the Weddell Sea) are observed. Therefore, the Scotia Sea marks the most southerly or initial region where the global AABW warming trend is clearly observed; however, there is still nuance in Scotia Sea property trends over this time. The Scotia Sea WSDW warms by around $0.05^{o}$C between 1995 and 1999 and the overall volume of WSDW decreases between 1995 and 2005. Changes in the properties of Warm Deep Water (WDW) in the Weddell Gyre appear to be transmitted more directly to the Scotia Sea after 1995 (Meredith et al., 2008; Meredith et al., 2013).

After leaving the Scotia Sea, WSDW flows north into the Argentine Basin, where the decadal warming trend becomes clearer. Here the combined time series discussed by Coles et al. (1996) and Johnson and Doney (2006), shows a warming of the coldest abyssal layer from observations between 1980 and 2005. Further warming is then observed in the Vema Channel between the Argentine and Brazil Basins, where the coldest bottom waters warm by 0.0028 (± 0.001) $^{o}$C yr$^{-1}$ from 1991 through to 2006. In the Brazil Basin, the abyssal layers warmed by around 0.0025 (± 0.001) $^{o}$C yr$^{-1}$ between 1989 and 2005 Johnson and Doney (2006). Finally, at the equator, in the Atlantic, bottom temperature values increased by nearly 0.015 (± 0.001)$^{o}$C yr$^{-1}$ between 1993 and 1999 (Andrié et al., 2003).

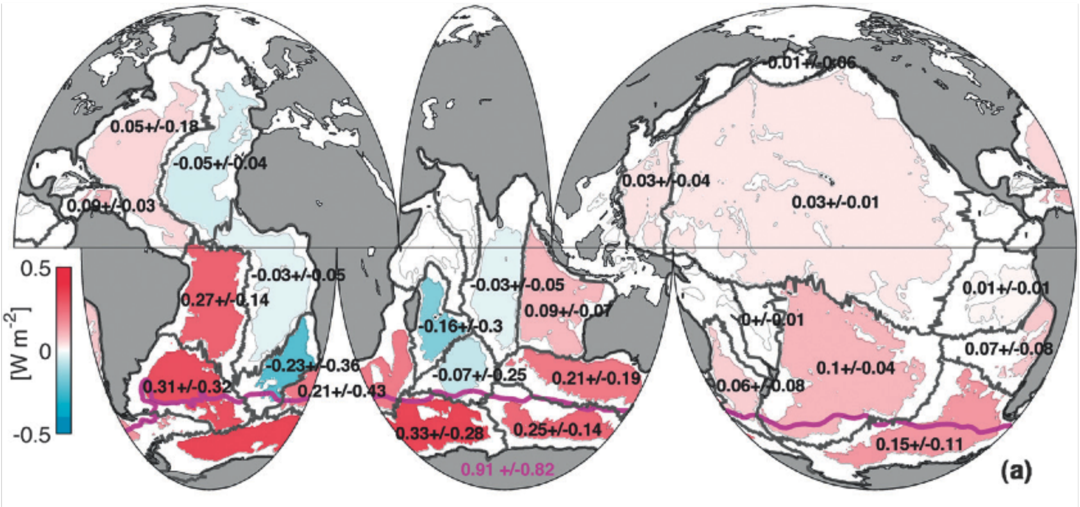

Figure 1.18: Mean heat fluxes to the deep ocean implied by abyssal warming below 4000 m, from the 1990s to the 2000s, with 95% confidence intervals. The contribution to the heat flux through 1000 m south of the SAF (magenta line) implied by deep Southern Ocean warming from 1000 to 4000 m is also given (magenta number) with its 95% confidence interval. Taken from Purkey and Johnson (2010).

Purkey and Johnson (2012) provide a review of warming AABW observations, as shown in Figure 1.18, the warming signal is clearly strongest in the South Atlantic sector of the Southern Ocean, where it extends north, but it is significant at all longitudes (Purkey and Johnson, 2010). Further analysis suggests that the observed warming may be an artefact of a contraction of AABW, relative to a given temperature or density surface. However, the cause of this contraction, i.e. warming versus a reduction in AABW production rate, is poorly understood (e.g. Purkey and Johnson, 2010; Purkey and Johnson, 2012).

## 1.4 Conclusion

It is clear that a number of forcing perturbations to the Southern Ocean, but in particular, the Subpolar Sea, have occurred over recent decades, and are currently underway. Most notable of these changes is the increase in surface winds and the dramatic increase in glacial freshwater. Over the same period, multiple authors have observed a global warming of AABW. The following thesis then attempts to further understanding of the response of the Subpolar Sea to changes in surface forcing, and the driving mechanisms of the global change in AABW properties.

# Chapter 2

# The Antarctic Subpolar Sea SSH Anomaly

## 2.1 Overview

This chapter is an extended review of work recently published in Nature Geosciences (Rye et al., 2014); it is an investigation into the regional sea surface height (SSH) variability of the Antarctic Subpolar Sea, 1992 to 2011. The Antarctic Subpolar Seas are an area of profound academic interest, facilitating strong interactions with the Southern Ocean, the southern polar atmosphere and the Antarctic cryosphere (Shepherd et al., 2012, 2004). Many global climate phenomenan are highly sensitive to these processes, however our understanding of this region and its ocean dynamics is poor compared with many other regions. This is due in part to a lack of observations and thus, a difficulty in collecting data from the Subpolar Seas. The Subpolar Seas are not only one of the most remote and inhospitable environments for oceanographic research; they are also obscured from satellite measurements by sea ice for much of the year.

Despite these difficulties advancing Antarctic ocean science is timely following recent Southern Ocean climate changes. The most prominent of these changes have been the shifting position and increased strength of Southern Ocean winds (Marshall, 2003), as well as the accelerating mass loss from the Antarctic cryosphere, which has provided an increased source of freshwater to the region (Shepherd et al., 2012).

Here satellite measurements of SSH made during ice-free summer months are used to provide insight into the evolution of the region over the last two decades. It is shown that the Antarctic coastal sea level has risen at a rate of approximately 1 mm yr$^{-1}$ above the global mean and at least 2 mm yr$^{-1}$ above the local mean, peaking in the Ross Sea and eastern Indian sector. Clear inter-regional variability in the SSH time-series is observed, with variations around the Antarctic continent and may be a source for further research.

It is noted that sparse *in situ* observations imply a strong surface freshening (of O(0.01) per decade) over recent decades in the Subpolar Sea. This freshening is estimated to drive a steric rise in sea level of between 0.5 and 3.3 mm $yr^{-1}$. It is then argued that satellite SSH observations provide insight into the area affected by this freshening, extending over the majority of south Antarctic Subpolar Sea. It is noted that a freshening of this scale and magnitude is in agreement with the increase in mass loss from the Antarctic ice sheet (Shepherd et al., 2012). In addition, in situ observations Purkey and Johnson (2013) imply a comparable contribution by warming of Antarctic Bottom Water, which is likely related to glacial mass loss.

These findings demonstrate the strength of the sea level response to increasing discharge from the Antarctic ice sheet over the last two decades. Moreover they highlight observations of a major climatic perturbation to the cryospheric forcing of the Southern Ocean over recent decades.

Section 2.2.2 introduces the regional dynamics of the Antarctic Shelf Sea, and 2.2.3 provides further background on the dynamics of sea level variability as well as the global average rate of sea level rise. Section 2.3 describes the primary datasets used, the 19-year record of satellite altimetry data. It then discusses findings from this data set and provides detailed analysis of the uncertainty thereof (section 2.3.0.4). Section 2.4 draws on many auxiliary datasets in its discussion of the driving mechanisms of the observations discussed in previous sections. Section 2.5 then summarises the chapter.

## 2.2 Introduction

### 2.2.1 Antarctic Subpolar Sea Dynamics

The Antarctic Subpolar Seas, are characterised by a SSH distribution (Figure 2.1) that slopes down towards the Antarctic continent, driven primarily by the overlying eastward wind forcing (Carter et al., 2008; Le Traon et al., 1998). Prominent within the SSH distribution are minima that mark the cyclonic circulations of the polar gyres', these are principally wind-driven flows with domed density surfaces and upwelling in their interior (Orsi et al., 1993).

South of the eastward-flowing Antarctic Circumpolar Current and the northern limbs of the Subpolar Gyres, the Subpolar Sea is dominated by the westward-flowing Antarctic Shelf Front (ASF; Figure 2.2) and the Antarctic Coastal Current (AC; Heywood et al., 2004). The ASF is a strong boundary current that separates the cold shelf waters from the warmer subsurface waters found offshore (Gill, 1973; Heywood et al., 2004). The AC then forms an additional narrow, rapid current appearing in broad sections of the continental shelf (Heywood et al., 2004). The dynamics of these combined westward

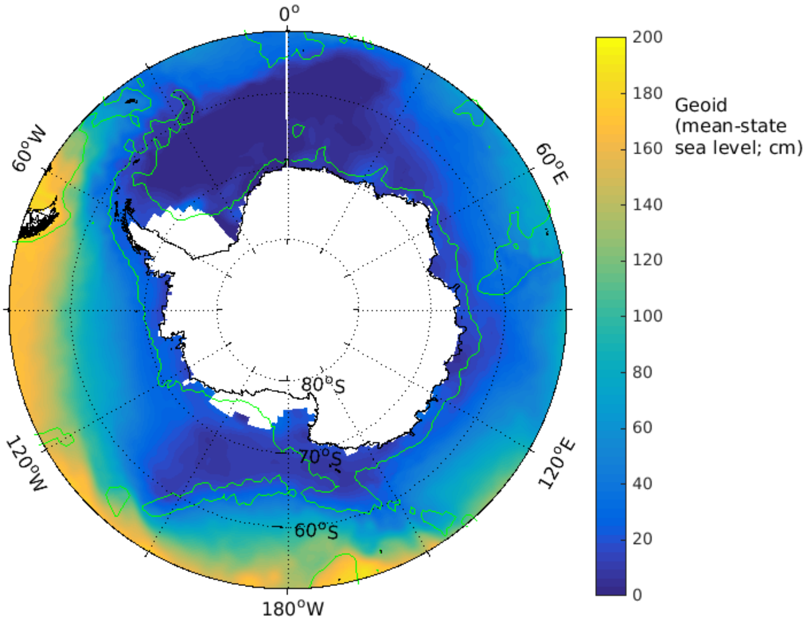

Figure 2.1: Climatology of Southern Ocean SSH. 1992-2011 mean SSH, calculated from AVISO gridded altimetry product MADT (Le Traon et al., 1998).

flows characterise the general circulation of the Subpolar Sea, governing the exchange of heat, salt and freshwater across and along the continental shelf (Smedsrud et al., 2006).

## 2.2.2 Trends In The Antarctic Subpolar Sea Climate

### 2.2.2.1 The Changing Cryosphere

The Subpolar Seas are at present experiencing a significant increase in freshwater discharge from the grounded Antarctic Ice Sheet and its fringing ice shelves (Figures 2.3-2.4; Shepherd et al., 2012, 2004, 2010). However the current state of knowledge concerning the impact on the adjacent ocean of this rapid change in freshwater forcing is extremely limited.

The sign and magnitude of excess freshwater anomaly released in the Antarctic Subpolar Sea over recent decades can be estimated from multiple recent studies. Shepherd et al. (2012) utilise an ensemble of satellite altimetry, inferometry and gravimetry data, along with models of surface mass balance and glacial isostatic adjustment to provide an unparalleled estimate of the grounded ice mass balance over the period (1992 − 2011; Figures 2.3-2.4). From this it is estimated that the grounded ice is, at present, losing mass overall through increased ice discharge (Shepherd et al., 2012; Rignot et al., 2011). The net effect of this mass loss is an excess freshwater discharge, above the grounded ice sheet's pre-1992 rate, of (on average) 75 ± 25 Gt $\text{yr}^{-1}$ (Rignot et al., 2011). Alternatively

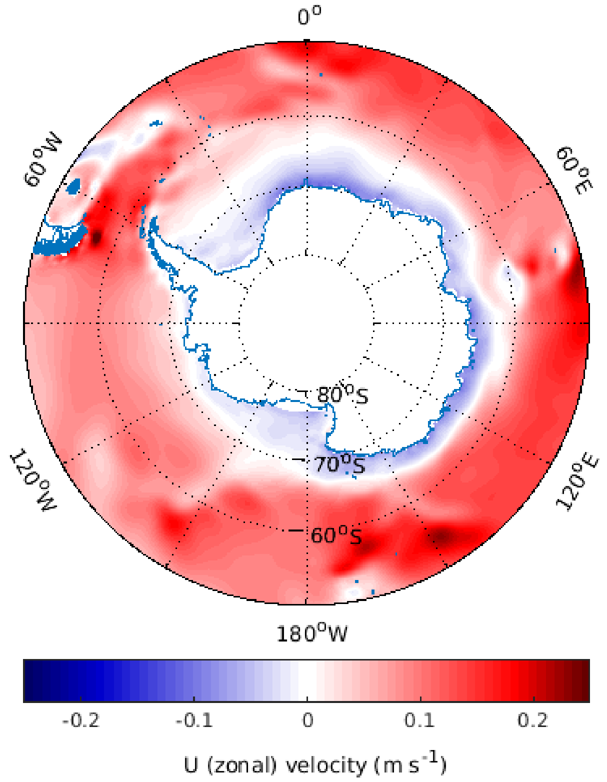

Figure 2.2: A snapshot of Southern Ocean surface zonal velocities, simulated by the NEMO model (Madec, 2008).

it is possible to estimate the net grounded ice mass loss by assuming it is approximately equal to the net losses from West Antarctica and the Antarctic Peninsula, which sum to $85 \pm 30$ Gt $\mathrm{yr}^{-1}$ between 1992 and 2011 (Shepherd et al., 2012).

Within the Antarctic net trend, the grounded ice sheet shows considerable regional variability (Figures 2.3-2.4). The West Antarctic Ice Sheet has lost mass to the oceans at an accelerating rate whilst the East Antarctic Ice Sheet has appeared relatively stable over recent decades (Rignot et al. 2008). A number of authors have suggested the warming of the waters on the Amundsen Sea continental shelf is responsible, driving an increase in the rate of melting at the base of the floating ice shelves, promoting more rapid ice flow upstream (Shepherd et al., 2004; Schmidtko et al., 2014).

In addition to the grounded ice sheet, further excess discharge from the thinning of floating ice shelves around the continent has contributed additional freshwater to the region (Shepherd et al., 2010; Figures 2.3-2.5). Although this mass loss is more uncertain than that of grounded ice, it may be estimated from a combination of satellite measurements and modelled surface accumulation. These methods indicate floating ice is loosing mass at a rate of $280 \pm 50$ Gt $\mathrm{yr}^{-1}$ between 2003 and 2008 (Depoorter et al., 2013; Rignot et al., 2013) and $115 \pm 43$ Gt $\mathrm{yr}^{1}$ for 1994 to 2008 (Shepherd et al., 2010).

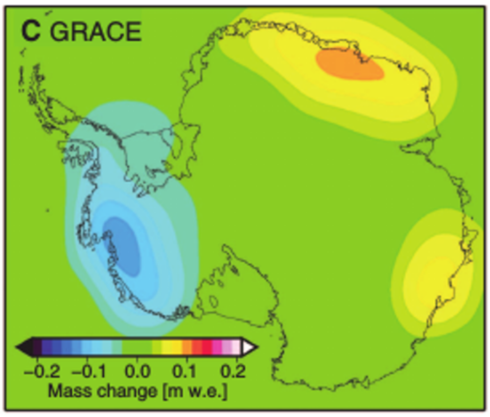

Figure 2.3: Grace derived illustration of grounded Antarctic Ice Sheet mass loss, 2003-2010, (Shepherd et al., 2012).

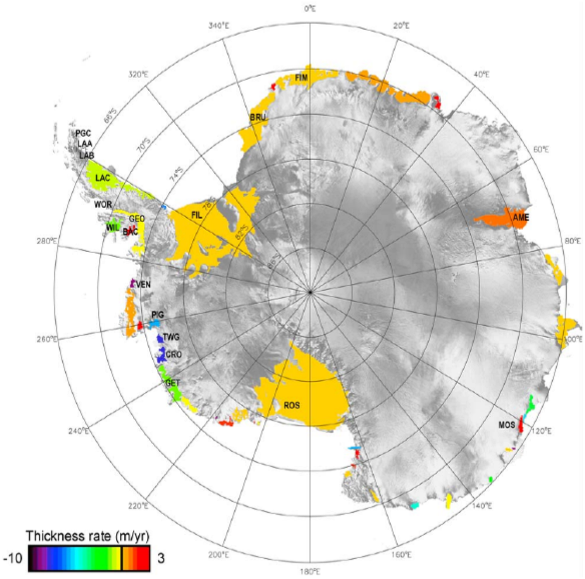

Figure 2.4: Average rate of Antarctic ice shelf thickness change, 1994 to 2008, determined from ERS and ENVISAT radar altimetry and a model of accumulation fluctuations (Helsen et al., 2008; Shepherd et al., 2010) .

Finally, a further source of freshwater discharge to the Shelf Sea results from a series of large ice-shelf retreats that have occurred along the Antarctic Peninsula, and whose contribution is not included in the previous Figures. This additional source of Antarctic freshwater averages 210 ± 27 Gt $\text{yr}^{-1}$ between 1988 and 2008 (Shepherd et al., 2010), however it is unclear how much of this ice has melted into the Antarctic Subpolar Seas, and how much has exited the Subpolar Sea as icebergs. All the above estimates represent changes since the early 1990s, but in situ measurements suggest that the ocean was already freshening before this period (Jacobs et al., 2002), therefore these values must constitute a lower bound for the excess discharge above a steady salinity rate.

The excess freshwater flux to the Antarctic Subpolar Seas in the past two decades is estimated hereafter as the sum of mass losses from the thinning of grounded and floating ice, 350 ± 100 Gt $\text{yr}^{-1}$. The bulk of this discharge is focussed around the Antarctic Peninsula and the Amundsen Sea (Figure 2.3-2.4). This excess freshwater input is anticipated to freshen the Antarctic Subpolar Seas, and to raise regional sea level through both steric (density-induced) and barystatic (mass-induced) effects.

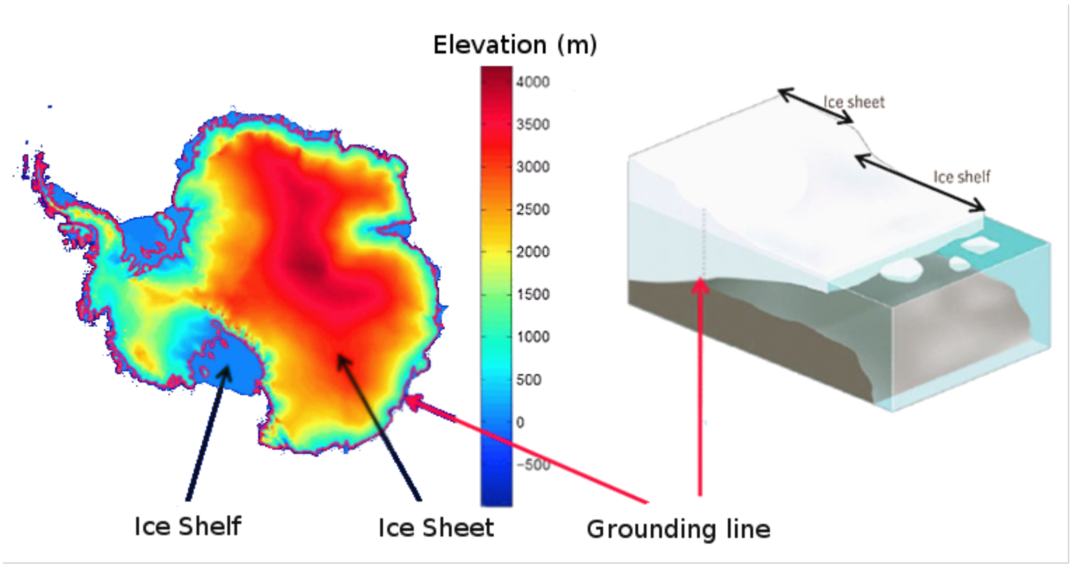

Figure 2.5: Left: A topographic map of the Antarctic continent, highlighting the definitions of an Ice Shelf, Ice Sheet and Grounding line. Right: A schematic of the Antarctic coastal environment.

Consistent with this, the few available time series of in situ hydrographic measurements in the Subpolar Sea, suggest that surface waters have undergone a marked freshening (by an order of 0.01 per decade) in recent decades (Jacobs et al., 2002; Jacobs and Giulivi, 2010; Aoki et al., 2005; Johnson et al., 2008; Ozaki et al., 2009; Hellmer et al., 2011; Figure 2.6). An important limitation of these observations is their sparse distribution, with the majority clustered near the Ross Sea. Isotope measurements from the Ross Sea implicate an increasing fraction of glacial meltwater in inducing local freshening here (Jacobs et al., 2002).

#### 2.2.2.2 The Changing Winds

A pronounced feature of the forcing on the Southern Ocean is the strong westerly winds overlying the eastward-flowing Antarctic Circumpolar Current (ACC), and the cyclonic curl of those winds as they encroach on the Antarctic continent (Figure 2.2; Deacon, 1937). Variability in the curl of the stress of these winds on the surface ocean causes divergence and convergence in the surface layer of the ocean (Ekman, 1902).

The dominant mode of variability within the Southern Ocean winds is ascribable to the Southern Annular Mode (SAM), which is principally a measure of the pressure difference between mid and high southern latitudes (Lefebvre et al., 2004). Observations and models have shown that around a third of Southern Hemisphere climate variability is related to the SAM over a range of time scales, from daily (e.g. Baldwin, 2001) to decadal (e.g. Kidson, 1999). The SAM is currently following a trend towards more positive values resulting in an increase in the strength and a southward shift of the

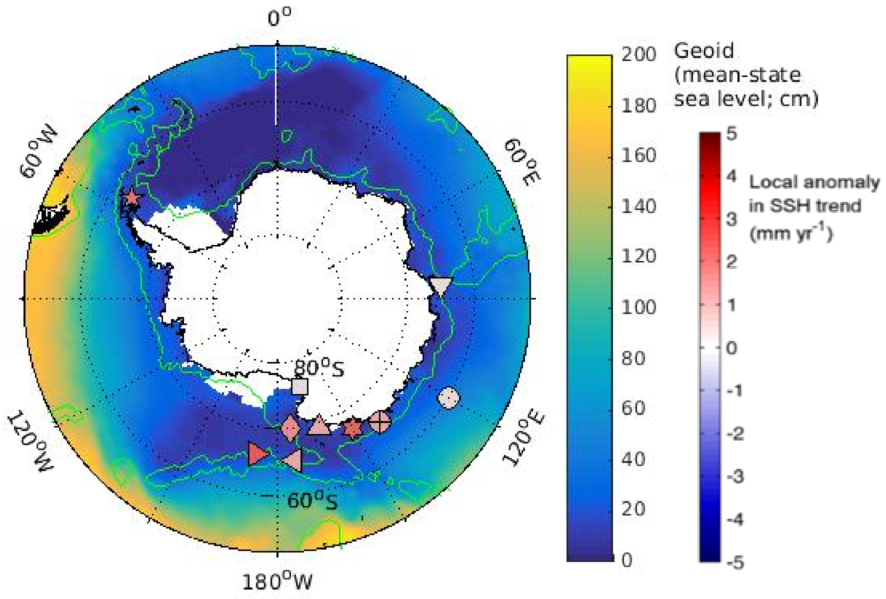

| Source | Time period | Depth range (m) | Trend in salinity (PSU yr$^{-1}$) | Halosteric SLR (mm yr$^{-1}$) | Identifier |
|---|---|---|---|---|---|
| Jacobs & Giulivi 2010 | 1963–2000 | 200–900 | −0.003 | 1.8 | ◆ |
| Jacobs et al. 2002 | 1979–2001 | 1,900–3,000 | −0.002 | 1.4 | ▲ |
| Aoki et al. 2005 | 1994–2002 | 2,500–3,500 | −0.004 | 2.8 | ✶ |
| Johnson et al. 2008 | 1995–2007 | 3,000–3,500 | −0.0008 | 0.4 | ▽ |
| Johnson et al. 2008 | 1995–2007 | 3,000–4,500 | −0.0004 | 0.5 | ● |
| Ozaki et al. 2009 | 1974–2004 | 2,500–3,300 | −0.003 | 1.6 | ◀ |
| Ozaki et al. 2009 | 1969–2004 | 2,600–3,600 | −0.004 | 3.3 | ▶ |
| Jacobs & Giulivi 2010 | 1958–2005 | 200–800 | −0.003 | 1.4 | ■ |
| Hellmer et al. 2011 | 1989–2006 | 0–500 | −0.005 | 2.0 | ★ |

Figure 2.6: Above: Distribution and magnitude of halosteric trends derived from the available insitu hydrographic data in the Antarctic Subpolar Seas. Below: Tabulated information for the datasets illustrated above.

Southern Ocean surface wind stress, a pattern it has been following since around 1980 (Marshall, 2003; Figure 2.7).

Sokolov and Rintoul (2009a) found that for the circumpolar average, each of the ACC fronts has shifted to the south by around 60 km over recent decades. The view of the ACC moving southward is supported by a number of other authors, e.g. Gille (2002, 2008) showed that the Southern Ocean is warming more rapidly than the rest of the global ocean and suggested the warming likely reflected a southward shift of the ACC, as well as subduction of warmed surface waters. Böning et al. (2008) analysed temperature, salinity and density changes along mean streamlines in the Southern Ocean and found that the Southern Ocean was warming and freshening, consistent with a southward migration of isopycnals. However it has recently been shown that the satellite data used

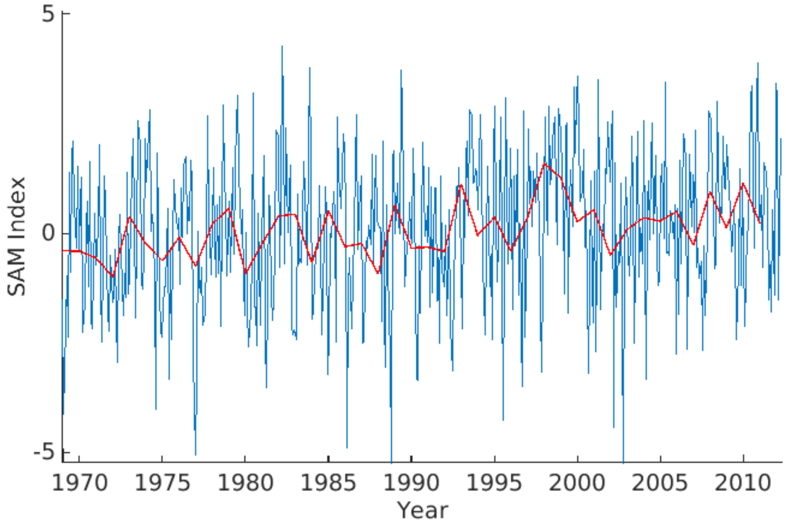

Figure 2.7: Time series of the Southern Annular mode, 1970-2010, taken from the NOAA website (Lefebvre et al., 2004).

to infer the southward motion of the fronts can be interpreted as an alternating response and the evidence for a circumpolar shift is not conclusive (Gille, 2008)

Of particular interest here is the front defining the Southern Boundary (SB) of the ACC and therefore the extent of Upper Circumpolar Deep Water (UCDW; $1.8^{o}$C). Following Sokolov and Rintoul (2009a), one may speculate that the SB should be following the southward trend of the ACC, bringing with it warmer waters. It is likely from the zonal variability in the distance between the SB and the Antarctic coast that coastal warming resulting from movement of front will be more prominent in some regions then others. Evidence from satellite radar data (Rignot, 1998; Shepherd et al., 2001) of rapid ice melt occurring to the Pine Island Glacier has led several researches to suggest that the ocean in the region could be warming (Payne et al., 2007).

#### 2.2.2.3 The Changing Hydrography

Schmidtko et al. (2014) furthers the work discussed in the previous section by utilizing historical hydrographic data between 1975 and 2012 to estimate temperature and salinity trends for the Shelf Sea region, providing significant insight into the dynamics of Shelf Sea hydrographic variability. Here Schmidtko et al. (2014) describes the Shelf Sea water column as three dominant water masses: Winter water (WW) a surface layer which represents the remnant of the winter mixed layer, Circumpolar Deep Water (CDW) a warm intrusive water mass originating from the Antarctic Circumpolar Current, and the dense Antarctic Shelf Bottom Water (ASBW) which constitutes the temperature minimum layer and is derived from a mixture of WW, CDW, Antarctic freshwater discharge and complex interactions with the Atmosphere and Antarctic ice.

Schmidtko et al. (2014) finds regional trends in the characteristics of WW, CDW and ASBW. Here ASBW shows significant warming and salinification in the Bellinghausen and Amundsen Sea regions of the shelf, with the Ross Sea freshening and the western Weddell Sea cooling and freshening. Here the cross shelf gradient in freshwater anomaly suggests Antarctic runoff as an important driving mechanism; no cross shelf gradient in temperature anomaly is apparent. CDW shows significant warming and shoaling in most regions around the continent, with the largest shoaling occurring in the Amundsen and Bellinghausen seas. Further WW is freshening along the Southern limb of the Ross Gyre and in the western Indian Ocean, while becoming saltier in the northwestern Weddell Sea.

Schmidtko et al. (2014) then proposes a link between the linear trends in ASBW properties over recent decades, and the distribution and variability of CDW. Stating that the shape of the CDW's density structure close to the Antarctic Shelf can be described as ether sloping upwards towards the shelf or downwards towards the shelf. It is found, in regions of weaker westward or even eastward flow, such as the Amundsen and Bellinghausen seas, that CDW's isopycnals slope upwards towards the shelf break, promoting intrusions of CDW onto the shelf. Moreover these regions of increased CDW intrusion are associated with enhanced warming and shoaling trends. Schmidtko et al. (2014) argues that this effect exposes regions such as the Amundsen and Bellinghausen seas to variability in CDW, while shielding regions such as the Ross Filchner and Ronne ice shelves from CDW variability.

### 2.2.3 An Introduction To Sea level

#### 2.2.3.1 Types Of Sea Level Change

Before discussing observations and their importance within the context of current literature, it is useful to establish an understanding of what causes SSH variations. SSH variability is driven by two distinct sources, changed in mass (barystatic) and changes in density (steric). This distinction is important because the ocean responds on different time-scales to barystatic and steric anomalies. Therefore, the cause of a regional SSH anomaly may be determined by its distribution, and location. The following section reviews analysis techniques for understanding the partition between barystatic and steric responses to sea level anomalies.

Mass anomalies, (barystatic anomalies) are rapidly communicated away from their source by fast barotropic waves. Modelling work shows that barystatic signals in the Antarctic Subpolar Sea are communicated to the global ocean within 2 weeks (Lorbacher et al., 2012).

Density anomalies (baroclinic anomalies) are driven by ether temperature (thermosteric), or salinity (halo-steric) variability (Munk, 2003). They are communicated away by slow baroclinic processes, such as advection and baroclinic waves. Further, these anomalies are more susceptible to becoming dynamically trapped, and forming regionally confined anomalies.

The majority of SSH forcing mechanisms will have both barystatic and steric effects. For example a glacial melt imbalance in the Antarctic Subpolar sea will both add mass to the ocean and reduce the density of the surrounding seawater by freshening (barystatic and steric effects respectively). Second-order effects also occur, for example, the primary response may influence the Subpolar Sea circulation and thus drive secondary changes in sea level.

The steric response of the ocean for an observed density anomaly can be approximated from the linear equation of state:

$$\rho = \rho_0(1 - \alpha\theta + \beta S) \tag{2.1}$$

Where $\rho$ and $\rho_0$ are the density and reference density respectively, $\alpha$ is the thermal expansion coefficient ($k^{-1}$; typical value: $1.70 \times 10^{-4}$) and $\beta$ is the haline contraction coefficient ($g\, kg^{-1}$; typical value: $7.60 \times 10^{-4}$).

The themo- and halo- steric components can then be separated, respectively:

$$h_t = -\alpha\delta\theta h_0 \tag{2.2}$$

$$h_s = \beta\delta S h_0 \tag{2.3}$$

Where $h_t$ and $h_s$ are the expected changes in sea level due to thermo- and halo- steric responses, $\delta\theta$ and $\delta S$ are the respective changes in temperature and salinity, and $h_0$ is the depth of the water column over which the change is observed (Wunsch et al., 2007).

Conversely, the (lower bound) mass anomaly required to explain an observed, change in steric sea level, can be estimated from similar working (Munk 2003). Here, consider the response of the Antarctic Subpolar Sea to a change in freshwater forcing. The region will have both a barystatic and steric response. However, it is argued that the barystatic response is rapidly distributed around the global ocean by fast barotropic waves, and it therefore has a negligible impact on local sea level Lorbacher et al. (2012). Further it is argued that the steric signal is expected to be relatively contained within the Subpolar Sea, with only a small loss of freshwater to the ACC. Following these assumptions, the amount of freshwater required to produce an observed steric anomaly in the Subpolar Sea can be derived principally from the ratio of the steric and barystatic responses to a given freshwater anomaly.

This ratio is most intuitively found from the definition of steric height anomaly ($h_s$) in pressure coordinates. This is the integral between atmospheric pressure (ap) and bottom pressure (bp), of the specific volume anomaly, $v_f - v_s$:

$$\Delta h_s = \int_{ap}^{bp} \frac{v_f - v_s}{g} dp, \tag{2.4}$$

where $v_s = \frac{1}{\rho_s}$ is the specific volume of seawater, $v_f$ is the specific volume of fresh water and $g$ is gravity.

The mass anomaly associated with a freshwater release in the Antarctic Subpolar Sea is assumed to be locally negligible, therefore there is negligible change in bottom pressure following a freshwater release. Equation (2.4) then simplifies to an integral over the freshwater layer (from $ap$, to the base of the freshwater layer, $lp$).

The change in pressure over this freshwater layer can be defined as

$$\int_{ap}^{lp} dp = lp - ap = \rho_t \, g \, \delta h, \tag{2.5}$$

where $\delta h$ is the depth of the freshwater layer. Therefore, as $\frac{v_f - v_s}{g}$ is constant, (2.4) becomes

$$\Delta h_s = \rho_f \, g \, \delta h \, \frac{v_f - v_s}{g} \tag{2.6}$$

After re-arrangement, we find

$$\Delta h_s = \frac{\delta h(\rho_s - \rho_f)}{\rho_s} \tag{2.7}$$

and

$$\Delta h_s = (1 - \frac{\rho_f}{\rho_s})\delta h \tag{2.8}$$

Following equations (2.8) and (2.3), the change in steric height of the water column is then

$$\Delta h_s \approx \delta h \beta S_s \tag{2.9}$$

Where $S_s$ is the salinity of seawater. Therefore, the amount of freshwater required to produce a given change in steric height in the Antarctic shelf seas is

$$\delta h \approx \Delta h_s \frac{1}{\beta} S_s = \Delta h_s \cdot 37.6 \tag{2.10}$$

Here we observe for a given freshwater discharge, the resultant steric change in SSH is approximately 37.6 times smaller than the height of freshwater added. This is a useful property of oceanic freshwater anomalies that allows an estimate of the mass of freshwater required to produce an observed steric height anomaly.

#### 2.2.3.2 The Global Average Rate Of Sea Level Rise

In addition to any observed regional variability in SSH there is also a global average rate of sea level rise. For 1993 to 2009 the estimated global average rate of rise made from corrected satellite altimeter data (TOPEX/Poseidon, Jason-1, ERS1-2, ENVI-SAT and OSTM/Jason-2) is 3.1 ± 0.4 mm year$^{-1}$ (Church and White, 2011). Perhaps the greatest caveat to using satellite data is that the record is relatively short (around 20 years) and it is therefore not easy to ether rule out or identify observed variability as decadal oscillations or longer scale phenomenon.

The global average rate of sea level rise can then be decomposed into steric and barystatic components. Accounting for estimates of excess glacial, and river discharge, as well as changes in the hydrological cycles, it is unlikely that the global-mean rate of barystatic sea level rise accounts for more then half of the trend in total sea level (Gregory et al., 2013; Leuliette and Miller, 2009). Therefore the sea level budget requires a global-average steric contribution of 1.5 mm yr$^{-1}$ to balance. In the tropics the majority of this steric signal is readily accounted for by upper-ocean warming. The thermal expansion coefficient for seawater decreases in colder waters and therefore salinity dominates steric sea level in polar regions.

## 2.3 Sea Surface Height Observations

#### 2.3.0.3 Data

Despite the importance of the Antarctic Subpolar Sea and the availability of sea level altimeter measurements, there have been relatively few investigations of Subpolar Sea sea level. The following section attempts to gain insight in the regions recent variability utilising satellite altimeter measurements. The central tool for this work is a 19-year record of Antarctic Subpolar SSH. This dataset is derived from multiple satellite altimeters, it is interpolated and concatenated into a gridded product generated by AVISO (Archiving, Validation, and Interpretation of Satellite Oceanographic Data; Le Traon et al., 1998), at 1/3 degree horizontal and weekly time resolution.

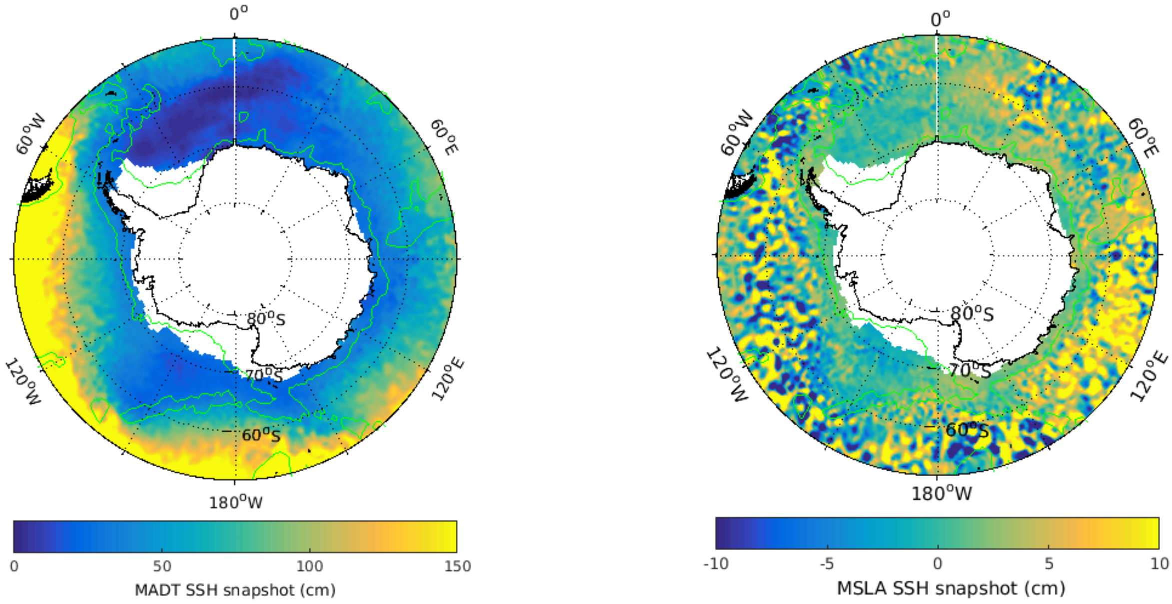

Figure 2.8: Snapshots of AVISO gridded datasets, Left: MADT. Right: MSLA (Le Traon et al., 1998).

There are multiple variants of the AVISO altimetry data, here the two main types are used, mean Sea Level Anomaly data (MSLA) and mean Absolute Dynamic Topography (MADT). These datasets differ by an estimate of the global time-average sea level distribution, which is present in MADT but subtracted from MSLA to highlight the regional anomaly.

The MSLA or MADT datasets are available in two further variants: 'ref' which uses a consistent measurement platform, utilising only two satellites at any one time, and 'upd' which uses all available altimeter satellites, therefore the number of satellites and the orbit patterns change with time. Here the 'ref' variant of the MSLA dataset is used between 1992 and 2012, however to ensure validity, all analyses (discussed below) are further conducted with both 'ref' and 'upd' versions of both MSLA and MADT, finding negligible differences. In addition, a number of single satellite data and an external variant of MSLA with alternative processing are used to verify the gridded AVISO products.

Despite correcting for a number of measurement errors, the AVISO sea level products do not intrinsically correct for changes in the geoid, of which the dominant component is glacial isostatic adjustment (GIA). This correction was estimated using output from a GIA model (Tamisiea, 2011; Figure 2.12) and subtracted from, the altimetry fields before analysis. In addition, an estimate of the more recent changes in the geoid resulting from e.g. mass loss from the Antarctic Peninsula (e.g. Figure 2.11) is made. The recent geoid trend is estimated by subtracting the GIA correction from the total GRACE geoid correction (Chambers et al., 2010; Figure 2.12). This provides an estimate of

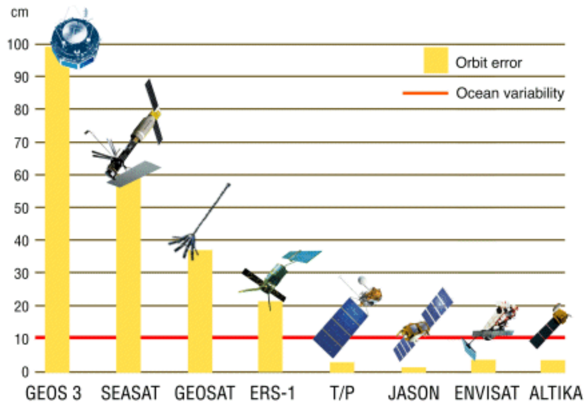

Figure 2.9: Cartoon of historical satellite altimeters and their orbit error ref AVISO-web.

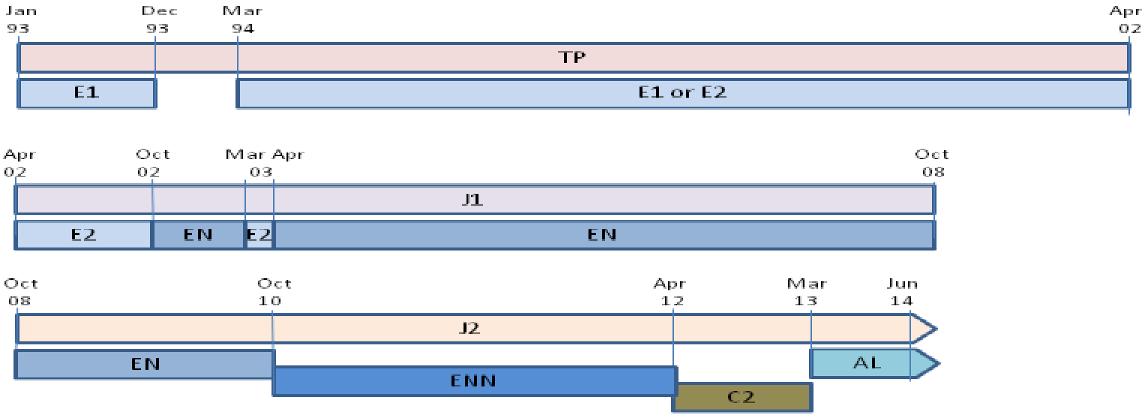

Figure 2.10: Schematic time-line of the satellites from which the primary dataset used here, MSLA-ref, is derived ref AVISO-web.

recent changes to the geoid over the GRACE period (2003-2011). As the altimetry record is initiated in 1992, the recent geoid correction cannot be easily compared and thus cannot be directly subtracted from the altimetry data. The recent geoid correction shows a strong negative anomaly with a maximum of -2 mm $yr^{-1}$ in the Amundsen-Bellingshausen region, and a weaker positive anomaly of approximately 0.5 mm $yr^{-1}$ between the Weddell Sea and the Amery region. An Antarctic Subpolar Sea mean of this correction yields -0.2 mm $yr^{-1}$, which is subtracted from the circumpolar-average shelf sea level anomaly and accounted for in its error budget. If subtracted, the SSH trend anomaly would increase in the Amundsen-Bellingshausen region, and decrease in East Antarctica.

#### 2.3.0.4 Altimeter Analysis And Results

Measurements of sea level close to the Antarctic continent cannot be readily obtained in the presence of sea ice. Our analysis focuses on the largely ice-free summer months

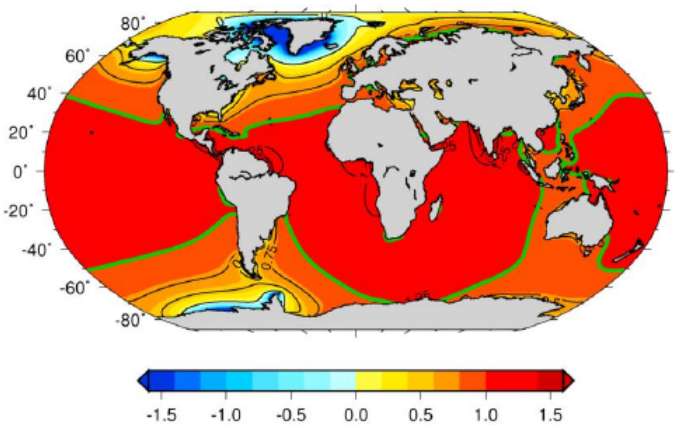

Figure 2.11: Barystatic relative sea level rise resulting from glacial melt between 2003 and 2009. Derived from GRACE gravimetry (Riva et al., 2010).

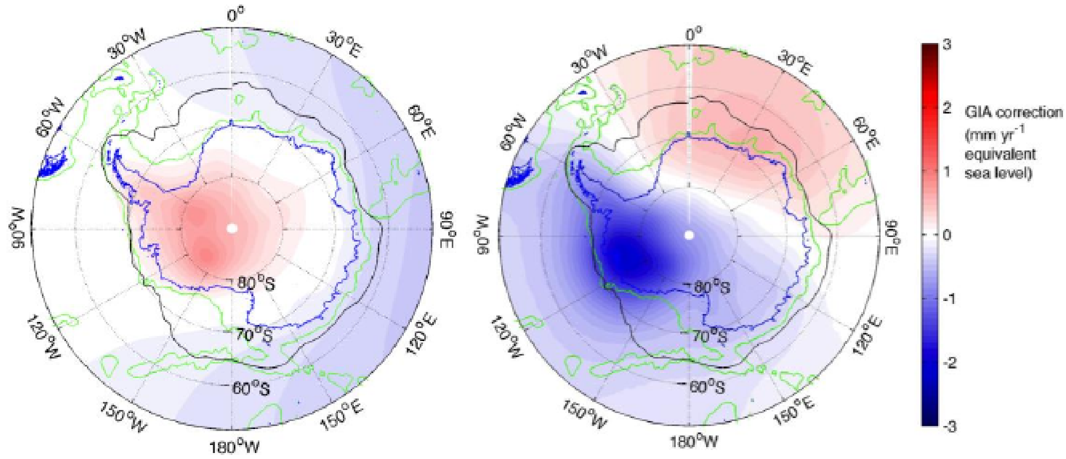

Figure 2.12: GIA corrections for the AVISO-MSLA altimetry data. Left: the correction made to altimetry data associated with the Tamisiea (2011) GIA model. Right: the (highly uncertain) correction for recent ice mass loss, predominantly from the Antarctic Peninsula, computed from Tamisiea (2011) GIA correction and Chambers (2010) GRACE-derived geoid data.

(January to April). Using data from these months, a linear trend in SSH for each data point with at least 20% (ice-free) coverage is calculated over the altimeter period. To estimate the regional anomaly from global average rate of sea level rise, the global-mean rate of sea level rise for the southern hemisphere, 3.1 mm $\mathrm{yr}^{-1}$ (between 1992 and 2012), is subtracted from trend data.

South of $62^{o}S$, this analysis reveals a remarkable, circumpolar-coherent signal of anomalously rapid sea level rise that has not been previously documented and becomes a basis for the following text (Figure 2.14). The signal extends across the Antarctic Subpolar Seas, closely following the pattern of the underlying topography. It displays characteristic values of 1 to 5 mm $\mathrm{yr}^{-1}$, with local peaks in the Ross Sea and Prydz Bay. A northern boundary of the region affected by this rapid sea level rise is defined as the line

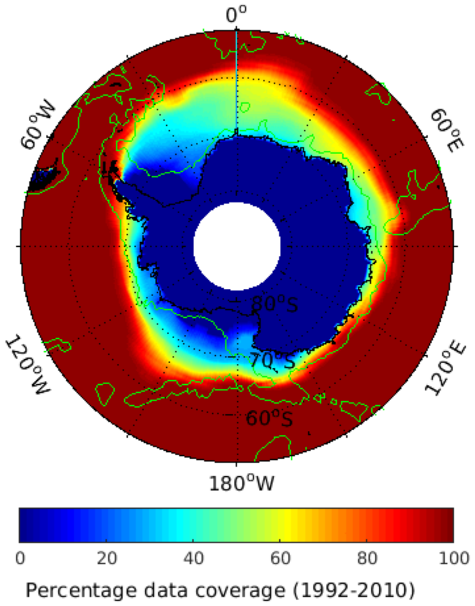

Figure 2.13: Percentage MSLA-ref data coverage, 1992-2010, (Le Traon et al., 1998).Low coverage indicates high incidence of sea ice obscuring measurements.

where the SSH trend anomaly first decays to zero or reaches a minimum with increasing distance from Antarctica (Figure 2.14). The mean sea level rise south of this boundary is 1.1 ± 0.6 mm $\text{yr}^{-1}$ above the global-mean value and at least 2 mm $\text{yr}^{-1}$ above the Southern Ocean-mean value, yielding net SSH increases of approximately 2 cm above the global and 4 cm above the regional average during the instrumental period.

Closer examination of the temporal progression and regional distribution of SSH change across the Antarctic Subpolar Seas (Figure 2.15) reveals several important properties of the signal. First, SSH displays a pronounced and ubiquitous seasonal cycle of amplitude $3 - 7$ cm that is most likely forced by seasonal fluctuations in upper-ocean temperature and salinity (Meredith et al., 2004). This hypothesis is supported by a time series of hyrdographic data collected at the British Antarctic Survey base, Rothera (Meredith, pers. comm.; Figure 2.16).

Furthermore, there are clear regional variations in the SSH time series around the continent. There is weak evidence to suggest that these regional variations in SSH relate to modes of atmospheric variability (such as the SAM and ENSO), as is suggested for the Southern Ocean SSH variability and has been shown to occur in the lower-latitude Southern Ocean. For example, a certain degree of interannual correlation between SSH in the Weddell and Ross seas is plainly visible, associated with an atmospheric standing wave pattern onto which the ENSO oscillation projects (Yuan and Martinson, 2001). Here however, we focus on the causes of the long-term sea level rise signal.

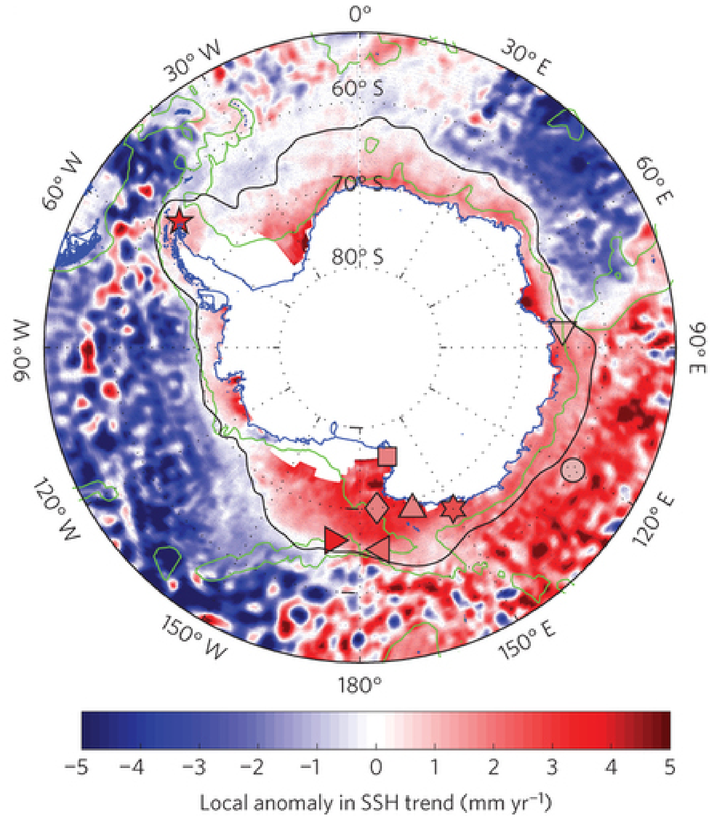

Figure 2.14: Regional anomaly in summer (JanuaryApril) sea-level trend, 1992 to 2011. The anomaly is calculated relative to the full (barystatic and steric) global-mean rate of sea-level rise for summer months. Black line: Northern boundary of the sea-level anomaly. Green line: 3000 meter isobath. Markers: In situ estimates of interdecadal freshening shaded by the magnitude of the corresponding halosteric sea-level rise. The information for each marker is given by Figure (2.6).

#### 2.3.0.5 Measurement Uncertainty In Altimetry Observations

A significant challenge in working with the gridded altimetry datasets is estimating the error or uncertainty associated with the data. Despite the generally strong significance of the SSH trends, both for each data point and the Antarctic Subpolar Sea mean (relative to the Southern Ocean), the uncertainties given for the SSH trends should be viewed as lower bounds. The multiple sources of measurement error for satellite SSH altimeters are well understood, formally reviewed by e.g. (Ablain et al., 2009), however detailed information on the specific corrections made to the MSLA data is not publically available. It is not possible to state that a rigorous test of the regional trends relative to measurement errors has been conducted. Here ’worst case scenarios’ are considered, the largest sources of error in altimeter datasets, their amplitude and probable distribution, these possible spurious signals are then compared to observations.

The largest single source of uncertainty in the altimetry data is that arising from the frame of reference used to correct for the satellites orbit error (Ablain et al., 2009;

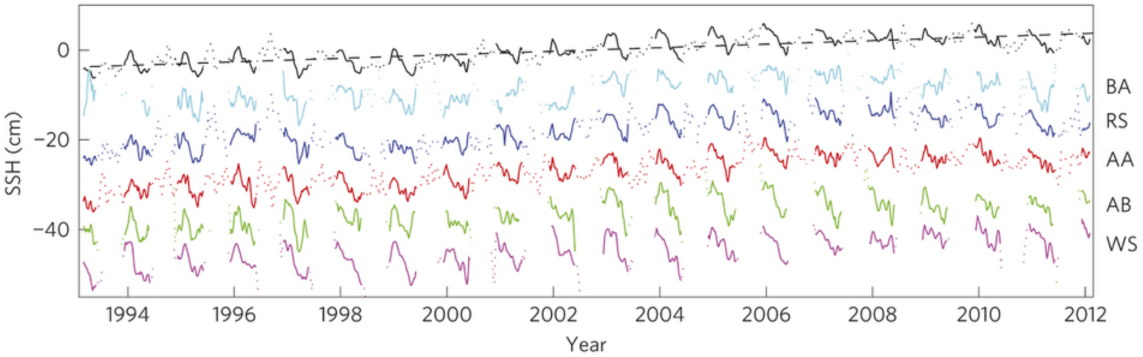

Figure 2.15: Time series of sea-level anomaly in the Antarctic Subpolar Seas, 19922011. Dotted lines show the full time series, and solid lines the ice-free summer month record. Black: circumpolar average south of the signals boundary (trend = 1.2 mm $\text{yr}^{-1}$); light blue: Bellingshausen and Amundsen seas (BA; 135–60 W; trend = 0.2 mm $\text{yr}^{-1}$ ); dark blue: Ross Sea (RS; 130$^o$ E- 135$^o$ W; trend = 1.3 mm $\text{yr}^{-1}$); red: Australian-Antarctic basin (AA; 50-130$^o$ E; trend = 1.9 mm $\text{yr}^{-1}$ ); green: Amery Basin (AB; 10-50$^o$ E; trend = 1.0 mm $\text{yr}^{-1}$ ); pink: Weddell Sea (WS; 60$^o$ W– 10$^o$ E; trend = 0.5 mm $\text{yr}^{-1}$ ). The dashed black line indicates the linear trend fitted to the circumpolar average sea level.

Beckley et al., 2007; Prandi et al., 2012). Preceding estimates of this orbit error for the TOPEX / Jason satellites are as high as 1.5 mm $\text{yr}^{-1}$ in the z-direction (Beckley et al., 2007), although this error is thought to be smaller for more recent data processing. Here an upper limit of 1 mm $\text{yr}^{-1}$ is assumed. The orbit correction is known to be symmetric along the z-axis. For a z-translation the error is proportional to the sine of the latitude; therefore, an error of magnitude 1 mm $\text{yr}^{-1}$ gives a value of 0.9 mm $\text{yr}^{-1}$ at 65 $^o$S, and a difference of 0.09 mm $\text{yr}^{-1}$ between 65$^o$S and 75$^o$S. From this small difference, it is clearly not possible to produce the narrow band of increased sea level observed (Figure 2.14). The lower orbit heights of ERS and Envisat result in larger orbit errors, particularly in the y-direction, but the dominant role of TOPEX / Jason observations in the AVISO gridded data essentially eliminates this error, which has also greatly reduced in recent solutions. Additionally, the altimetry data north of 62$^o$S have been re-processed with an improved frame of reference that reduces orbit errors (Beckley et al., 2010). The sea level anomaly data in the Antarctic shelf seas north of 62$^o$S are well correlated (p > 99%) with this improved data set, and our sea level rise estimates in that region are unchanged.

Following orbit error, the main sources of uncertainty in SSH trend are the wet troposphere correction, and the biases applied to link together SSH records from different altimeters (Ablain et al., 2009). The wet troposphere error is a function of atmospheric water content and therefore latitude; it can be as high as 2 mm $\text{yr}^{-1}$ in the tropics but is negligible at high latitudes (Ablain et al., 2009). Further biases are applied to link together SSH records from different altimeters (Ablain et al., 2009) which contribute an uncertainty for the reference TOPEX / Jason missions of about 0.15 mm $\text{yr}^{-1}$. Other

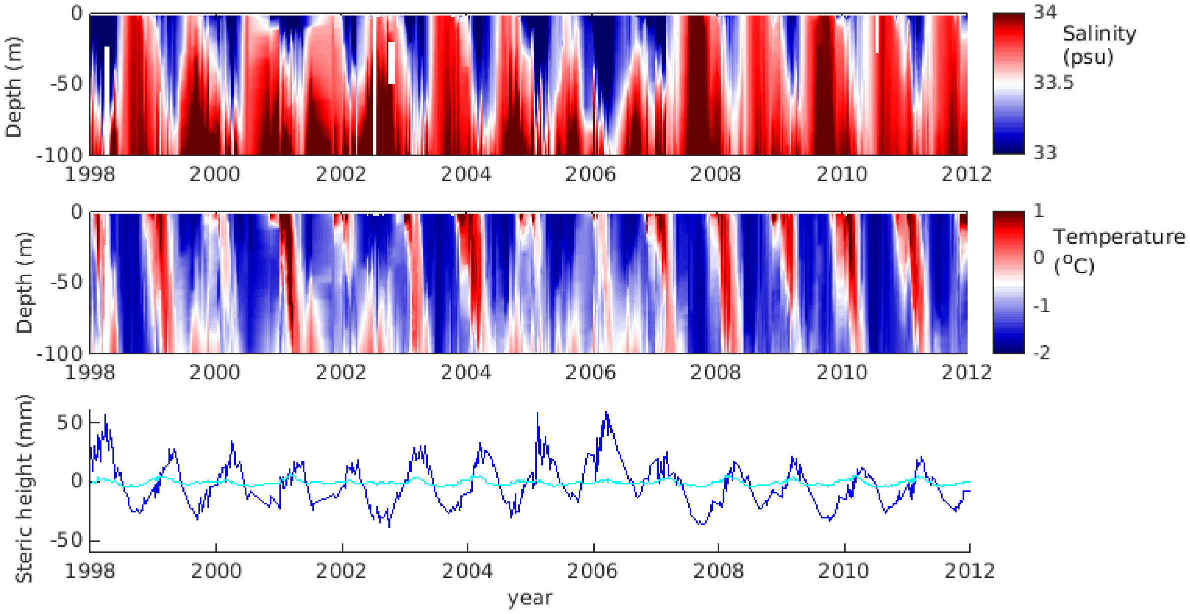

Figure 2.16: Time series of RATS hydrographic data. Above: Salinity variability between 1998 and 2012. Middle: Temperature variability between 1998 and 2012. Below: Time series of estimated steric height variability from temperature and salinity anomalies, calculated from the upper 200 meters using a linear equation of state. Light blue line: Thermosteric anomaly. Dark blue line: Halosteric anomaly.

sources of uncertainty, such as instrumental, meteorological, and tide-related factors contribute less than 0.1 mm yr$^{-1}$ (Ablain et al., 2009).

Further examination of cross calibration errors was conducted. Figure 2.18 shows the sea level trend for a region of rapid sea level change in the Ross Sea using multiple single satellites. Unlike the dataset shown in Figure 2.15, these data were not interpolated onto a grid but are derived from single-satellite track datasets for ERS1, ERS2 and ENVISAT, produced by the Centre National d'Etudes Spatiales (CNES; Le Traon et al., 1998). A small region of high SSH anomaly was selected in the Ross Sea (shown in inset of Figure 2.18), every 10 days the SSH data recorded in this area is averaged thus eliminating gridding errors. The datasets shown in Figure 2.18 are not cross calibrated; each individual dataset shows a rise in sea level of between 1.4 and 7.2 mm yr$^{-1}$ above the global average rate of sea level rise, which is consistent with our previous findings.

#### 2.3.0.6 Error In Temporal Aliasing Of SSH Measurements

A further issue arises not from measurement errors but from the requirement for correct interpretation of the data. Our calculation of the linear trend in summertime SSH over the 1992-2011 period incorporates all data points between January and April not covered by sea ice. Summertime sea ice cover across the Antarctic Subpolar Seas is highly

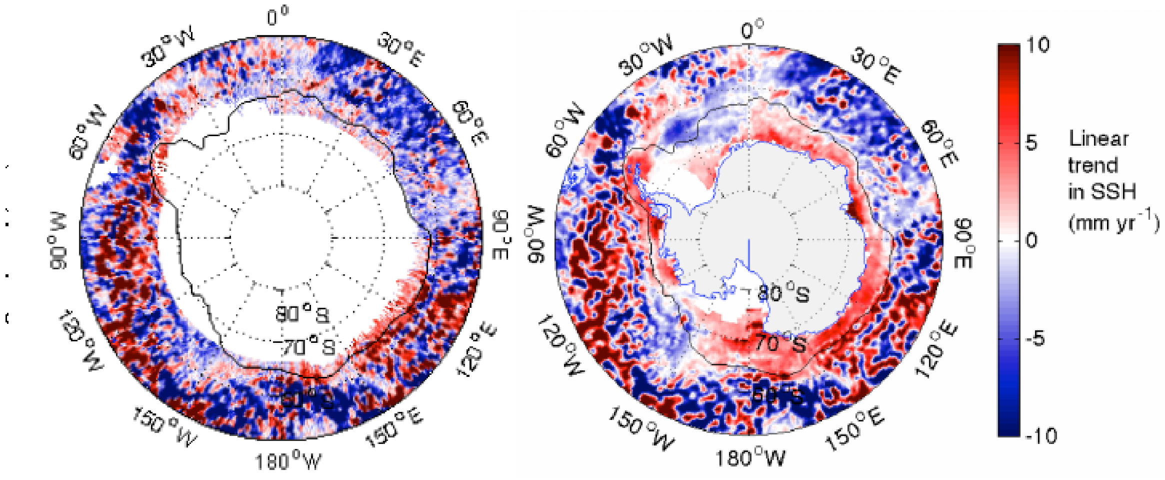

Figure 2.17: Comparison between the linear trend in AVISO MSLA-ref (right) and MSLA (Both datasets are derived from Le Traon et al. (1998)).

variable in both space (i.e. the regularity of sea ice cover varies with location across the Antarctic shelf seas) and time (i.e. at any given location, there may be substantial interseasonal and interannual variability in sea ice cover), so that any estimate of interdecadal SSH change in the region may be affected by aliasing. Indeed, there are significant regional trends in Antarctic summertime sea ice extent during this period (Jacobs et al., 2002).

In order to show that our results are robust to this aliasing issue, the time series of circumpolar-mean SSH anomaly south of the oceanic boundary of the Antarctic coastal sea level rise signal (Figure 2.19) is compared to a time series of SSH anomaly averaged over the 5% of that region that is ice-free over the entire altimetry record (Figure 2.13). The two time series are in good agreement, with a high correlation coefficient of r=0.8. The agreement of the two time series suggest that both the mean and spatial distribution of the trend in the Antarctic Subpolar Seas are unaffected by aliasing. Moreover, the year-round time series highlights that while the seasonal cycle is larger than the interdecadal sea level rise anomaly, it is distinct from the latter, as evident from the observation that the linear trend in SSH anomaly affects all stages of the seasonal cycle.

#### 2.3.0.7 Concluding Remarks On The Uncertainty Of Altimetry Measurements

Despite numerous issues with measurement errors, the magnitude and consistency of the observed trend, is evident. The relative significance (assuming negligible systematic error) of the linear trend in SSH for each data point in the gridded AVISO data set was

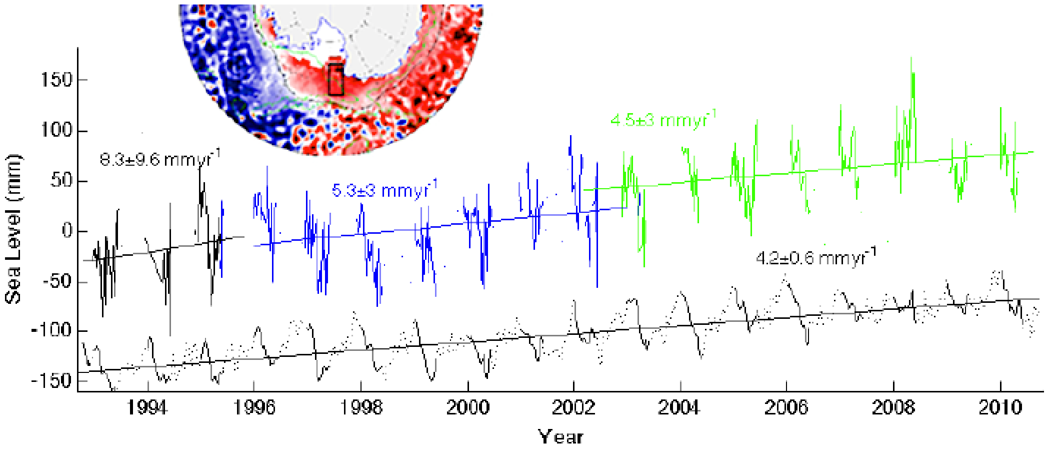

Figure 2.18: Linear trend in SSH anomaly in the western Ross Sea for individual satellite missions. The global-mean rate of sea level rise is not removed for simplicity, and the bin-averaging box is indicated in the inset. ERS-1 (black), ERS-2 (dark blue) and Envisat (green) records are shown alongside the Antarctic Subpolar Sea mean SSH anomaly, including the rate of global-mean sea level rise (light blue). The average linear trend in the western Ross Sea box for the gridded AVISO data set is 6 mm yr$^{-1}$. The uncertainties for the single-mission trends are estimated using a bootstrap method accounting for the standard deviation of SSH within the box for each time step.

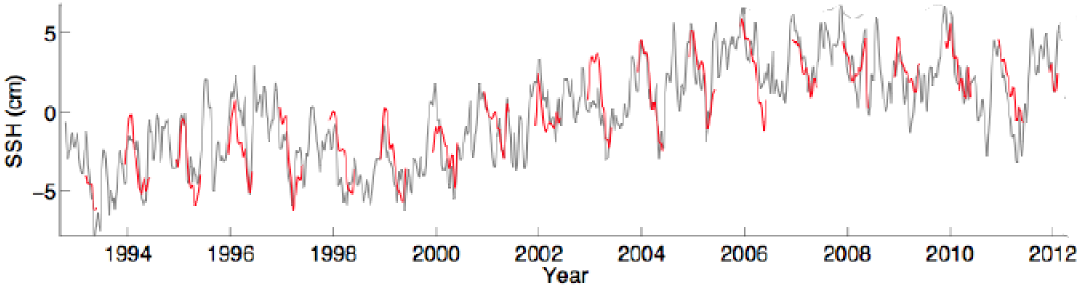

Figure 2.19: Time series of Antarctic Subpolar Sea SSH anomaly, showing both summer and winter months. The circumpolar average Subpolar Sea SSH anomaly (Figure 2.14) is shown in red. The average Subpolar Sea SSH anomaly that is permanently sea ice-free is indicated in grey. Both data sets have had the global-mean rate of sea level rise subtracted. The grey line also indicates periods of extensive sea ice cover.

estimated with a Patterson t-test accounting for auto-covariance in the sea level record (Figure 2.20). This indicates that, in general, the Antarctic coastal sea level rise signal is significantly different from zero with 95% confidence, with some exceptions in areas of weak anomalous sea level rise in the Amundsen Sea, eastern Ross Sea and Weddell gyre (Figure 2.20).

Finally, it is noted that the Antarctic coastal sea level rise signal identified in this

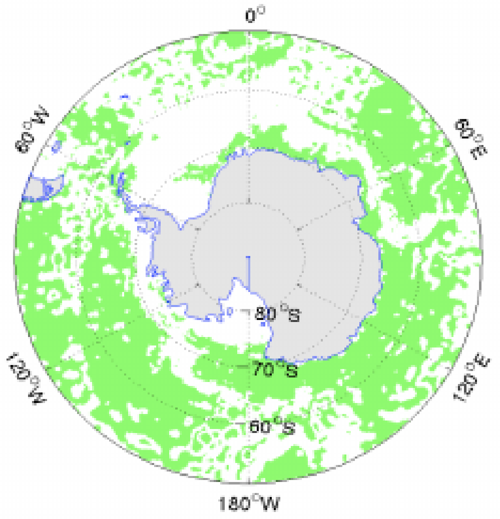

Figure 2.20: Significance of Antarctic Subpolar Sea linear trend in SSH anomaly. Green shading indicates the area in which the anomalous linear trend in SSH (Figure 1) is significantly different from zero with 95% confidence, determined using the Patterson t-test accounting for auto-covariance under the assumption of negligible systematic error.

study has a spatial footprint that is both distinct from those of any known sources of uncertainty in altimetry measurements and consistent with expectations from numerical simulations of the present deglaciation of Antarctica (Stammer, 2008; Lorbacher et al., 2012). The distribution of the Antarctic Subpolar Sea SSH trend shown in (Figure 2.14) clearly follows topographic contours implying that its shape is a result of oceanographic processes. This provides further endorsement for the inference that the signal is of physical origin. Following these arguments, the combination of dominant error terms suggests an overall regional average error of $1 - 1.5$ mm yr$^{-1}$, and an error of $0.2 - 0.6$ mm yr$^{-1}$ for the difference between $65^oS$ and $75^oS$. Here the upper bounds of these values are used.

## 2.4 Plausible drivers of the Subpolar Sea SSH Anomaly

The following section is a discussion of the driving mechanisms of the observed change in sea level. Emphasis is given to wind and buoyancy forcing, as these are the most likely mechanisms.

### 2.4.1 Surface Wind

The winds of the Southern Ocean and their variability are a dominant component of Southern hemisphere climate. As previously discussed, recent decades have seen marked

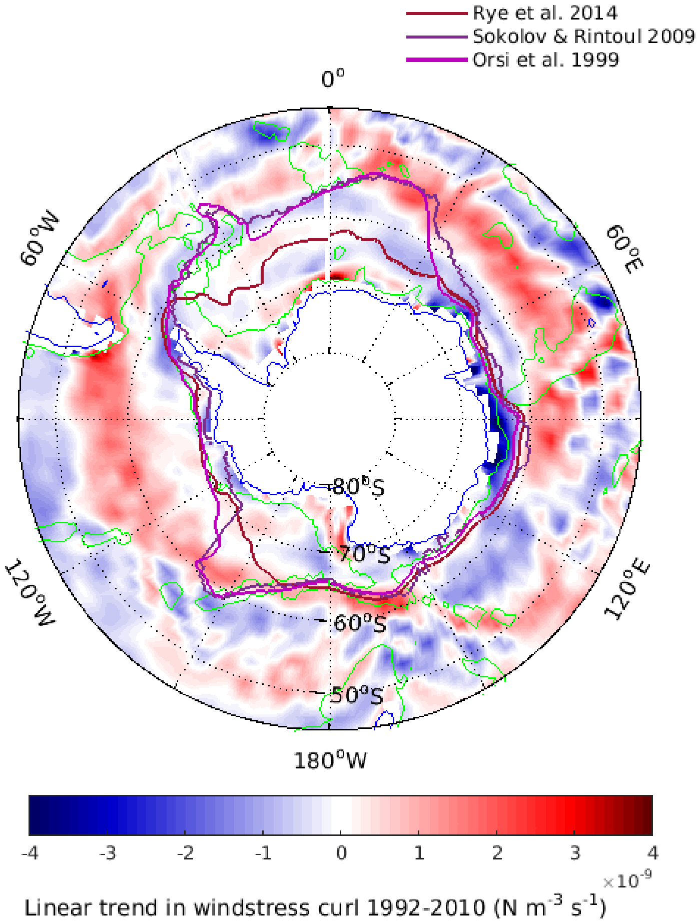

Figure 2.21: Linear trend in wind stress curl derived from ERA-Interim reanalysis surface wind fields (at 10m height). Green contours: 3000m isobath. Red and purple contours: differing definitions of the northern boundary of the Subpolar Sea relevant for Ekman transport into and out of the region.

changes in the SAM and the Southern Ocean winds, leading to a strengthening of surface wind stress and a southward shift of the ACC. Surface wind variability is therefore a good candidate for driving the observed SSH anomaly.

Here the European Centre for Medium-Range Weather Forecasts (ECMWF) Era-Interim reanalysis output (Dee et al., 2011) is used, averaged into 10-day bins, to assess the role of the winds in the observed SSH trend. The Era-Interim dataset was selected following inter-comparison with other reanalysis products (Dee et al., 2011), as well as verification from sea-ice drift measurements (Holland and Kwok, 2012) and in situ observations (Bracegirdle and Marshall, 2012).

The surface wind data is used to generate a time series of Ekman transport into, and out of, the Subpolar Sea, across the boundary contour that defines the northern extent of the observed SSH anomaly (Figures 2.14, 2.21). This time series is then compared to the monthly mean SSH over the same region during ice-free months (Figure 10).

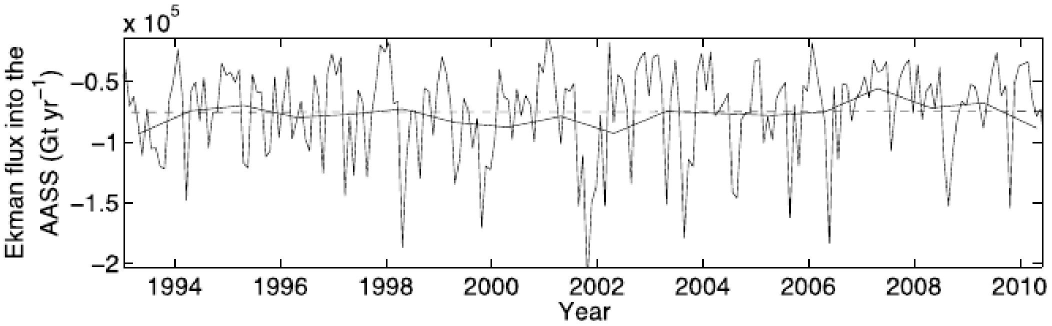

Figure 2.22: Time series of Ekman transport into the Antarctic Subpolar Seas. Full lines show the monthly and yearly averaged Ekman transport into the Antarctic Subpolar Seas, with the dashed line indicating the linear fit to the yearly averaged data.

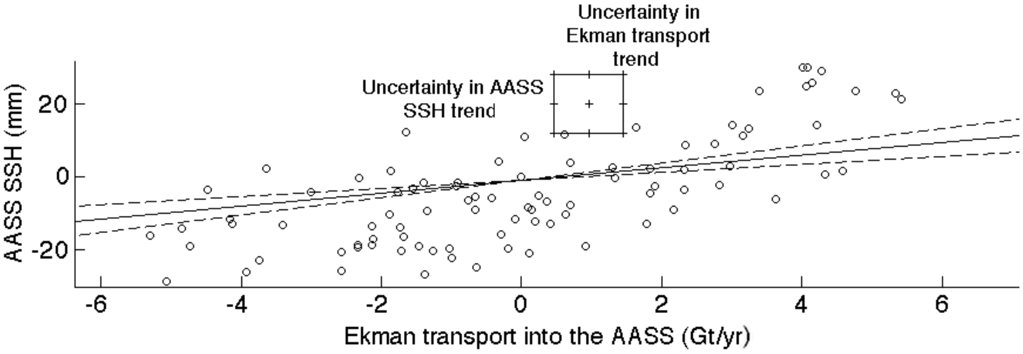

Figure 2.23: Relationship between the Ekman transport into the Antarctic Subpolar Seas and regional SSH anomaly. The circles indicate monthly averaged values of the two variables (AASS: Antarctic Subpolar Seas). The solid line shows the linear fit to the circles, with the $2\sigma$ uncertainty denoted by the dashed lines. The rectangle has sides of length defined by uncertainties in the trends in both variables, and indicates the area of Ekman transport - sea level space that the solid line would have to pass through in order for the observed trend in regional SSH anomaly to be explained by wind forcing.

A significant anti-correlation between Ekman transport out of the region and Subpolar Sea SSH was found ($r^2 = 0.5$; Figure 2.23), with a linear relationship of $-(3.9 \pm 0.6) \times 10^{-4}$ mm (Gt yr$^{-1}$)$^{-1}$. This relation then implies that the change in surface wind forcing during our research period has driven a change in SSH in the Subpolar Seas of approximately 0.2 mm yr$^{-1}$. The frequency-dependence of this relationship can be assessed by temporally averaging both time series with a moving window of variable width (Figure 2.24). This exercise demonstrates that the transfer function between the Ekman transport away from the Antarctic Subpolar Seas and the regional SSH anomaly is essentially constant at $3.8 \times 10^{-4}$ mm Gt$^{-1}$ yr, for periods of 1 month to longer than a decade.

This method of assessment of the relationship between Antarctic Subpolar Sea level and the cross-boundary Ekman transport suffers from both a lack of resolution of sub-annual time scales and the previously discussed temporal aliasing issues. To assess the robustness of our basic result on the frequency-insensitivity of the relationship, the analysis is repeated with the mean SSH anomaly in the 5% of the Antarctic shelf region that is permanently ice-free (Figures 2.13, 2.24). The resulting transfer function is, again, relatively stable, ranging from $1 \times 10^{-4}$ to $3 \times 10^{-4}$ mm $\mathrm{Gt}^{-1}$ yr, for periods of 2 months to longer than a decade, where the different value of the transfer function simply reflects its relevance to a distinct area.

The analysis was also repeated following a number of alternate boundaries of the Subpolar Sea, including the Sokolov and Rintoul (2009a) definition of the Southern Boundary, the Orsi et al. (1999) definition, a single latitude band along $60^oS$ and the 3000 m isobar. However each provided similar results showing negligible impact on the Shelf Sea sea level.

Moreover, it is important to note that this method of assessment, of the relationship between Antarctic Subpolar Sea level and Ekman transport, is purely empirical, and statistical. It does not attempt to use an analytical model. However it provides a best estimate given all available evidence. Thus, it is argued that the estimate of the transfer function is robust and representative of the sensitivity of the mean SSH anomaly in the Antarctic Subpolar Seas to changes in wind forcing.

### 2.4.2 Surface Temperature

A second possible forcing of anomalous sea level rise is surface (or interior) temperature variability. Subpolar Sea surface temperature data is highly variable and only available during ice-free austral summer months. Limited in situ temperature measurements are available for the Ross Sea, a region of anomalously rapid sea level rise (Figure 6). These show a negligible thermosteric sea level rise between 1958 and 2008 for upper-ocean waters (200-800 m; Jacobs and Giulivi, 2010).

In addition a number of Sea Surface Temperature (SST) products are available, from which it is possible to estimate linear trends in surface temperature forcing, shown in Figure 2.25. However these products give varying answers suggesting their inaccuracy for long term trends. Moreover assessment of the linear trends in these datasets reveals no significant trends in SST which have the magnitude or distribution sufficient to drive the observed SSH anomalies (Figure 2.25; Reynolds and Marsico, 1993). It is therefore likely that surface warming is not significant.

In contrast, in situ measurements suggest that the Southern Ocean deep and bottom waters have warmed significantly in during recent decades, inducing a thermosteric increase in SSH of 1 mm $\mathrm{yr}^{-1}$ (Purkey and Johnson, 2013). This rate of sea level rise is comparable in magnitude to the signal discussed here, and is thus likely to contribute non-trivially

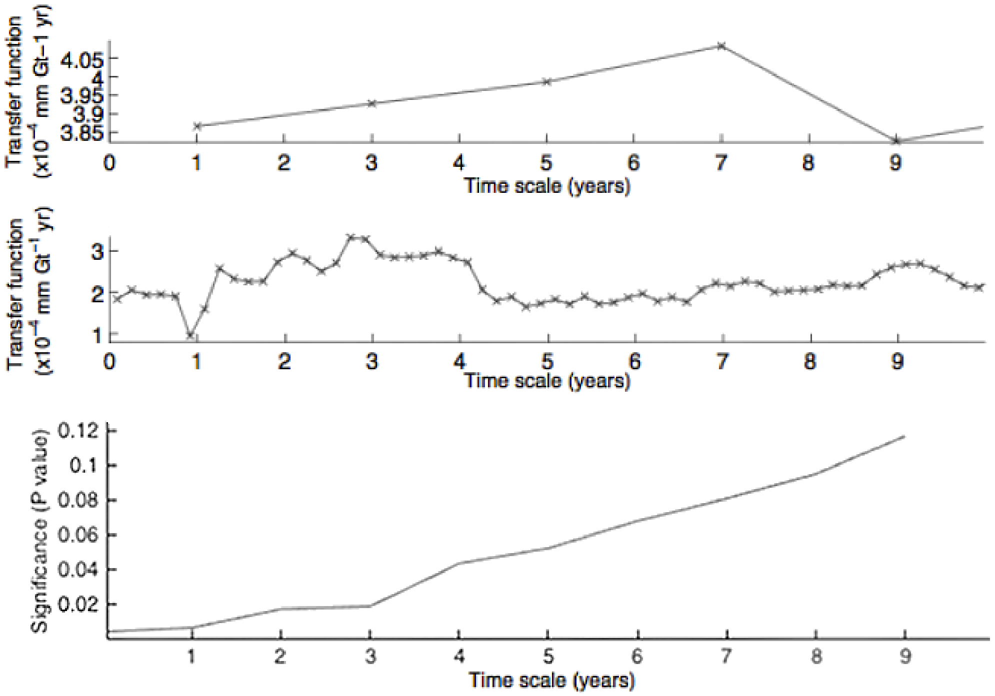

Figure 2.24: Time scale dependence of the transfer function between changes in the Ekman transport across the northern boundary of the Antarctic Subpolar Seas (Figure 2.14) and the regional SSH anomaly. The upper panel illustrates results using SSH anomaly measurements in the entire Antarctic Subpolar Seas, the middle panel shows results derived from the SSH anomaly record in the subset of the Antarctic Subpolar Seas that is permanently sea ice-free. The bottom pannel shows the significance (p value) of the transfer function shown in the middle panel, i.e. for the subset of the Antarctic Subpolar Seas data that is permanently sea ice-free. The transfer function was estimated by averaging the time series of Ekman transport and SSH anomaly in temporal bins of variable length (indicated by the horizontal axis in both panels) and calculating the linear gradient of the resulting Ekman transport versus Antarctic Subpolar Seas SSH anomaly distribution.

to the signals occurrence. However, the spatial footprint of the deep thermosteric change extends well beyond the Antarctic Subpolar Seas and across the entire Southern Ocean (Purkey and Johnson, 2013), in poor agreement with our observed signal. The lack of spatial correspondence between thermosteric effects and regional sea level trends may relate to other factors, such as the changes in wind forcing or self-gravitation. Thus, the existence of a significant contribution of deep-ocean thermosteric adjustment to the observed sea level rise is not inconsistent with the available observations.

### 2.4.3 Precipitation

Precipitation variability has significant potential to influence steric as well as barystatic sea level, with both primary and tertiary effects. A widespread increase in Antarctic

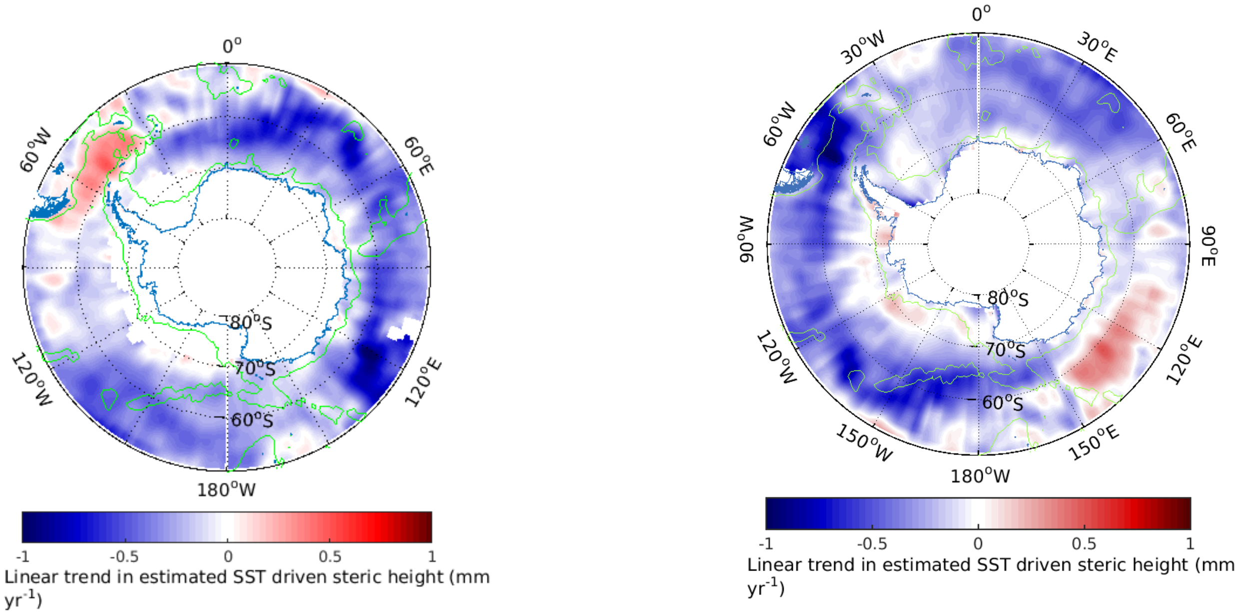

Figure 2.25: Linear trend thermosteric anomalies derived from satellite observed Sea Surface Temperature (SST) products, 1992 to 2010. Left: Hadley centre gridded SST data (Rayner et al., 2003; Kennedy et al., 2011). Right NOAA gridded SST data (Reynolds et al., 2002).

precipitation is a common feature in climate models simulating the atmospheric response to changes in global climatic forcing over the late 20th and the 21st centuries (Masson-Delmotte et al., 2006; Genthon et al., 2009). While the uncertainties in atmospheric reanalyses data have thus far proven too large to confirm that this predicted precipitation increase is presently underway (Masson-Delmotte et al., 2006; Bromwich et al., 2011), there is evidence from reanalysis products that the contribution of precipitation anomalies to the observed change in sea level is negligible (Bromwich et al., 2011).

Analysis of the most commonly used reanalysis datasets conducted by (Bromwich et al., 2011) found negligible variability in evaporation and precipitation in subpolar waters. The authors found spurious trends in mean Antarctic precipitation in NCEP-2, JRA-25, and MERRA, driven by errors, which vary between, reanalyses products. For example, a proportion of the precipitation trends in MERRA can be related to assimilation of new datasets, namely data from the Advanced Microwave Sounding Unit. ERA-Interim and CFSR appear to be the most realistic datasets and do not exhibit any significant trends. However, the authors suggest concern over ERA-Interim's assimilation of rain-affected radiances and inhomogeneities in the CFSR pressure fields. The authors conclude that ERA-Interim is arguably the most realistic depiction of precipitation changes in high southern latitudes between 1989 and 2009. Over this period ERA-INTERIM and CFSR show no significant trends in Antarctic mass balance (Precipitation - Evaporation). It is assumed therefore that there has been no significant change in precipitation over the Antarctic Subpolar Sea.

### 2.4.4 Sea Ice

Unfortunately due to the lack of accurate sea ice thickness data it is not possible to make quantitative conclusions on the effect of sea ice trends on Antarctic Subpolar Sea steric height (e.g. Zwally et al., 2002). However, evidence derived both from model simulations and satellite observations implies that a decrease in Antarctic Sea ice over recent decades is highly unlikely. i.e. Both models and observations support a small or negligible increase in sea ice volume over our study period, which would result in a net salinification and thus decrease in sea level(Massonnet et al., 2013; Parkinson and Cavalieri, 2012; Vaughan et al., 2003).

Similarly, a significant reduction in sea ice volume may have contributed to halosteric sea level rise. While this possibility cannot be excluded due to the scarcity of sea ice thickness measurements, it seems highly unlikely given satellite observations and model reconstructions suggest that Antarctic sea ice volume has increased slightly over our study period (Massonnet et al. 2013; Parkinson and Cavalieri 2012).

### 2.4.5 Glacial Melt

Finally the excess fresh water discharge from the Antarctic cryosphere is considered as a driver. Glacial melt variability has both steric and barystatic effects on Antarctic Subpolar Sea level. As previously noted, recent decades have seen a significant increase in freshwater discharge to the Subpolar Sea, and here this is estimated as the sum of grounded and floating ice contributions; $350 \pm 100$ Gt $\text{yr}^{-1}$, with the bulk of this discharge focussed around the Antarctic Peninsula and the Amundsen Sea.

Several lines of evidence suggest a prevalence of the halosteric contribution in underpinning the measured signal. Foremost is a comparison between our altimetry-based estimate of the local anomaly in sea level rise and values implied by in situ measurements of inter-decadal ocean freshening in several locations around Antarctica (Jacobs, Giulivi and Mele 2002; Jacobs 2004; Jacobs and Giulivi 2010; Aoki et al. 2005; Rintoul 2007; Purkey and Johnson 2012). This indicates that the Antarctic Subpolar Sea freshening anomaly (relative to global-mean freshening) may account for the bulk of the observed SSH increase.

Moreover the likely importance of a cryospheric source for this freshening is suggested by the coastal enhancement and topographically constrained character of the sea level rise signal. The role of an accelerated freshwater discharge from the Antarctic ice sheet in the freshening of shelf waters in the Amundsen and Ross seas has been indicated previously by isotopic tracer analyses (Jacobs et al. 2002).

The contribution of Antarctic glacial ice mass loss to regional sea level may be assessed directly by comparing measured changes in SSH with the expected steric response to the amount of excess freshwater released into the region. It is possible to estimate the amount of freshwater required to explain the observed sea level signal as a solely halosteric change. This is estimated by multiplying the linear trend in ocean volume inside the signals boundary (9.3 $\mathrm{km}^3\ \mathrm{yr}^{-1}$) by the Munk multiplier (36.7; Munk (2003); section 2.2.3.1), yielding a requirement for $860 \pm 200$ Gt $\mathrm{yr}^{-1}$ of ice melting in excess of a nominal steady salinity discharge. One then concludes that halosteric changes resulting from Antarctic ice discharge can directly account for around half of our SSH signal within formal error bounds given the mass loss estimate of $350 \pm 100$ Gt $\mathrm{yr}^{-1}$ (Shepherd et al. 2012). Further, it is also taken into account that the error bounds for these estimates overlap.

### 2.4.6 Tertiary Forcing Mechanisms

Finally, it is note that the mass loss associated with glacial melt has an effect on the local gravity field. As mass is lost from the Antarctic ice sheet the decrease in gravitational attraction between the ocean and ice will cause a reduction in SSH around Antarctica (Riva et al. 2010). Satellite measurements of mass loss from the Antarctic ice sheet suggest a drop in relative sea level centred on the Amundsen Sea of approximately 1 mm $\mathrm{yr}^{-1}$ over 1993 – 2009 (Riva et al., 2010). This self-gravitation effect may help to explain the attenuation of the sea level rise signal in the Amundsen Bellingshausen sector, and it can be identified qualitatively in the GRACE data in (Figure 2.12), and is accounted for in the estimate of uncertainty for the Subpolar Sea anomaly.

## 2.5 Summary

Austral summer satellite altimetry measurements show a pronounced circumpolar rise in sea level over the Antarctic Subpolar Seas that significantly exceeds the global-mean rise. The trend increases towards Antarctica, with a mean value of $1.1 \pm 0.5$ mm $\mathrm{yr}^{-1}$ above the global mean and at least 2 mm $\mathrm{yr}^{-1}$ above the local mean, peaking in the Ross Sea and eastern Indian sector. The anomaly shows regional variability, which varies with longitude around the Antarctic continent and is suggested to be a focus for further research.

There is no good evidence of changes in precipitation or sea surface temperature contributing significantly to the trend. A linear relationship between Antarctic coastal sea level and Ekman transport was found derived from atmospheric reanalysis data. However this relation shows a weak effect, with winds accounting for only a minor fraction (1/5th at most) of the observed SSH signal.

Sparse observations show a surface freshening (of O(0.01) per decade) over recent decades in the Subpolar Sea, with an associated steric rise in sea level of between 0.5 and 3.3 mm $yr^{-1}$, consistent with satellite altimetry measurements. It is noted, that the amount of freshwater required to produce a halo-steric anomaly of similar magnitude to that observed is in approximate agreement with the increase in mass loss from the Antarctic ice sheet, where direct halosteric rise from the observed freshening of the Antarctic Subpolar Seas can account for at least half of the observed signal. Thermosteric rise from the observed warming of the deep Southern Ocean, which has itself been linked to the freshening of the shelf waters ventilating AABW (Purkey and Johnson, 2010, 2013), is also suggested to contribute to the trend.

It is concluded that the local anomaly in sea level rise is likely to be predominantly steric in origin and ultimately originates from the increased discharge of freshwater from Antarctica. Our findings reveal that the accelerating discharge from the Antarctic ice sheet has had a pronounced and widespread impact on the Antarctic Subpolar Seas over the last two decades, constituting a major climatic perturbation to the cryospheric forcing of the Southern Ocean circulation.

# Chapter 3

# A Modelling Investigation Of The Antarctic Subpolar Sea SSH Anomaly

## 3.1 Overview

The previous chapter discusses an observed circumpolar trend in Antarctic Shelf Sea SSH and provides an investigation into the forcing mechanisms driving the trend. A number of datasets: Satellite altimetry, hydrographic observations, glacial melt observations, satellite SST data, and atmospheric reanalysis are discussed. Available evidence suggests the main driver of the observed trend is the steric response of the Shelf Sea to anomalous Antarctic freshwater discharge. Furthermore, the magnitude of the halosteric response required to replicate the observed Shelf Sea SSH trend is consistent with the amount of discharge produced by the recent acceleration in Antarctic ice melt. Surface wind forcing is shown to contribute a small, or negligible increase in Antarctic Shelf Sea SSH.

It is evident from these findings that a significant perturbation of the Antarctic climate system is currently underway, however observations are limited. Here the discussion is furthered by modelling realistic freshwater perturbations to the region.

The Simulated steric response to shows a realistic anomaly distribution, with a magnitude that is similar to SSH observations. In addition the model output provides detailed information on the distribution of the hydrographic response, e.g. the response of temperature, salinity, sea ice. Here we find that approximately half of the steric change in sea level is driven directly by freshening, with the remainder is driven by warming. The warming response is assumed to result from changes in circulation or isopycnal heave (shoaling). The majority of the warming signal in the model is concentrated in the deep

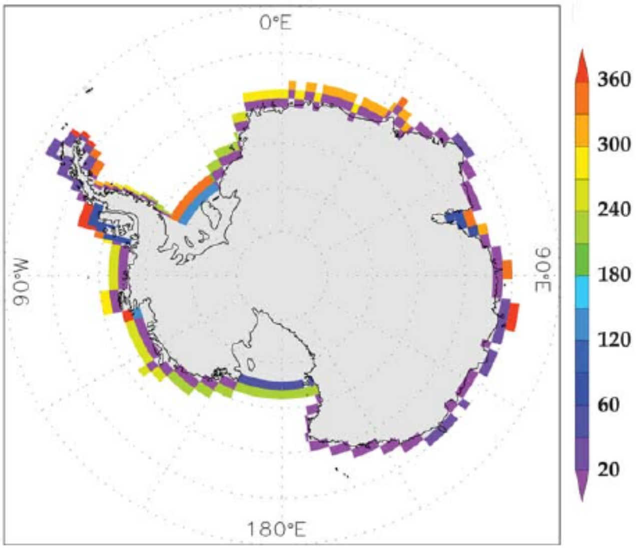

Figure 3.1: Equivalent surface freshwater flux anomaly resulting from loss of salinity (per grid box; $m^3s^{-1}$), used by Stammer (2008).

ocean below 800 meters, whereas the majority of the freshening signal is concentrated in the surface 800 meters.

The following chapter first provides a review of relevant ocean modelling literature in section 3.2. An extension of this work is then directed towards simulating the dominant forcing mechanisms of the Shelf Sea SSH trend. Section 3.3.2 then provides introductory information on the model, some model validation, the experiment design and results. A discussion of model results is given in section 3.4, and section 3.5 then summarises the results from both chapters (2 and 3).

## 3.2 Review Of Previous Modelling Studies

Interpretation of the observed Antarctic SSH trend may first be guided by published modelling research: Stammer (2008), utilises a $1^o$ resolution, global configuration of the MIT general circulation model to simulate the halo-steric effect of an anomalous Antarctic freshwater flux. Here the freshwater anomaly is simulated as a decrease in salinity, with no addition of volume, therefore it can only simulate the steric-SSH response to freshwater anomalies, the barystatic response must be neglected. Further, unfortunately the total value of the excess discharge added to the model is not stated in the text and it is difficult to estimate from Figure 3.1. Lorbacher et al. (2012), estimates the excess discharge used by Stammer (2008) as around 800 Gt $yr^{-1}$. It is noted that this value is unrealistically large compared to glaciological observations (e.g. Shepherd et al., 2012).

Two model runs are used by Stammer (2008); a control run, where no anomaly is applied, and a perturbation run where a step increase in freshwater discharge is applied to the

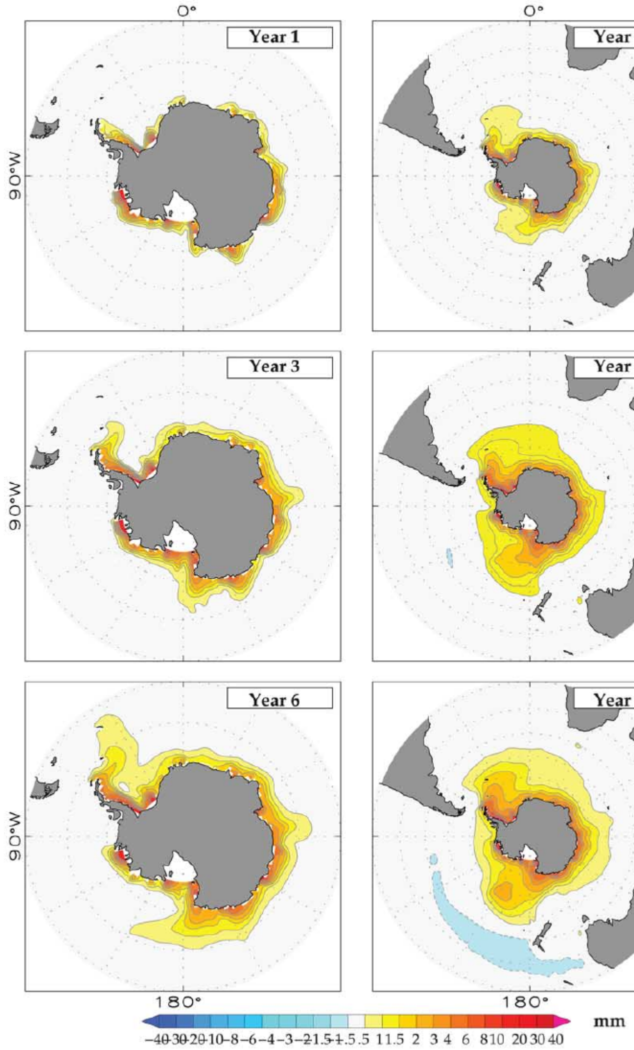

Figure 3.2: Modelled December-mean steric SSH anomaly, for 1, 3, 6, 10, 30 and 50 years after a step increase in Antarctic freshwater forcing (Stammer, 2008).

Antarctic Shelf Sea. The difference between perturbation and control runs provides the simulated steric SSH response, shown in Figure 3.2. A positive circumpolar SSH anomaly is found to dominate south of the ACC, spreading slowly over larger areas in the southern hemisphere over a period of 50 years. This response is in broad agreement with the distribution of the SSH trend found in satellite observations Stammer (2008).

Lorbacher et al. (2012), improves the solution using the AusCOM coupled ocean-ice model, with a resolution ranging between 1 and 0.25$^o$. Here, increased horizontal resolution is used around the equator and towards the southern pole (around 78$^o$S). Unlike Stammer, the Lorbacher et al. (2012) model is able to simulate an increase in model volume. Therefore, it is able to simulate both the barystatic and steric response to excess discharge. The amount of anomalous freshwater forcing applied is 0.1 Sv, or 3150 Gt yr$^{-1}$, which is highly unrealistic and even larger then used by Stammer (2008).

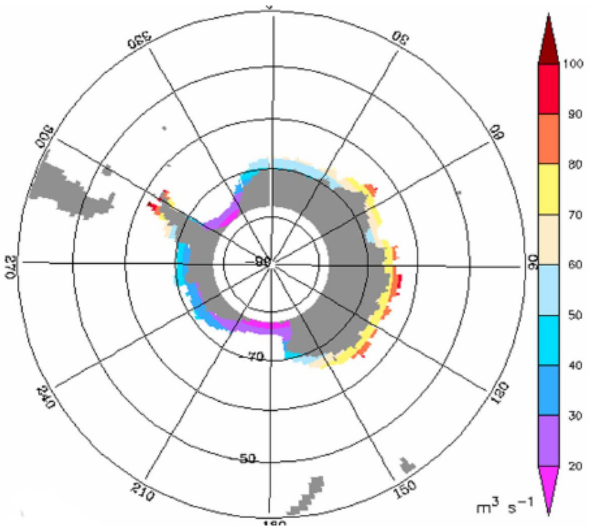

Figure 3.3: Surface freshwater flux anomaly (per grid box; m$^3$ s$^{-1}$) used by Lorbacher et al. (2012).

Again both control and perturbation runs are used and a similar, step change, freshwater anomaly is applied to the shelf seas. The resultant SSH anomaly is shown in Figure 3.3.

Lorbacher et al. (2012), first notes a fast barotropic response, which is communicated to the majority of the global ocean within 7-8 days (Figure 3.4). Here the initial adjustment acts to increase sea level over a region within and south of the Antarctic Circumpolar Current (ACC), this then excites a boundary Kelvin wave which propagates northward along the east coast of South America, it then crosses the Atlantic at the equator, propagating globally thereafter. Following this initial adjustment the most pronounced barystatic sea level response appears qualitatively similar to the steric response identified by Stammer (2008), i.e. a strong signal south of the ACC. A steric response then occurs in agreement with Stammer (2008). Lorbacher et al. (2012), further notes an amplification of the response close to the source of the freshwater anomaly. This is attributed to the halosteric effect of the freshwater anomaly, which is found to be relatively restricted to the Shelf Sea region. Lorbacher et al. (2012) also report an almost linear relationship between the barystatic SSH response and the magnitude of discharge anomaly applied, following adjustment (Figure 3.5). Unfortunately Lorbacher et al. (2012) also use unrealistic, large freshwater anomalies, and therefore it is not possible to use this work alone to further our discussion.

In summation both the barystatic and steric responses to freshwater anomalies on the Antarctic shelf appear to produce qualitatively similar responses in the distribution local sea level anomaly. However the steric response is much larger in magnitude then the barystatic response. As stated by Lorbacher et al. (2012) 'To some degree the pattern of a global barotopic sea level adjustment is reflective of the mostly steric adjustment discussed by Stammer (2008), as well as Hsieh and Bryan (1996) and Bryan (1996)'. In

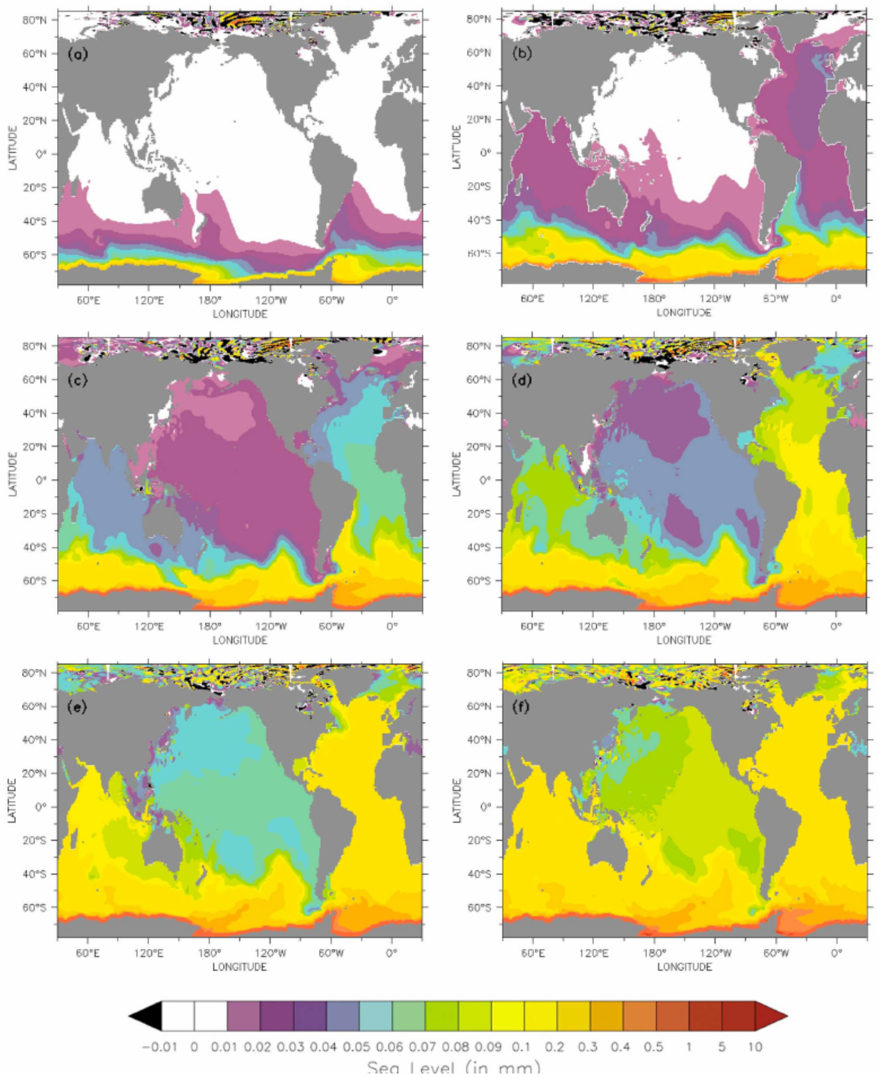

Figure 3.4: The modelled distribution of barotropic sea level anomaly (mm) following a step change in Antarctic freshwater forcing (Lorbacher et al., 2012). Subplots a, b, c, d, e and f show the distribution following 12, 36, 60, 84, 108 and 132 hours respectively.

conclusion, both Stammer (2008), and Lorbacher et al. (2012), are very useful, however, for direct comparison to SSH observations, a case specific modelling investigation is required to further our discussion.

## 3.3 Modelling: Methods And Results

### 3.3.1 Introduction

The following text reviews a case specific modelling effort designed to describe the response of the Antarctic Shelf Sea to anomalous freshwater forcing. Here, enthuses is

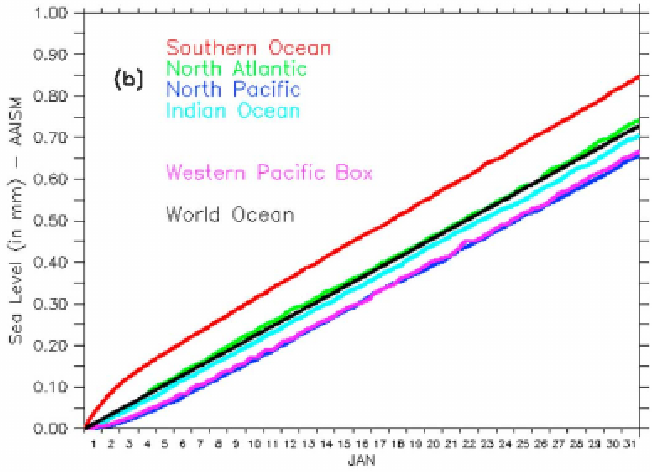

Figure 3.5: Time series of hourly sea level response (mm) to freshwater perturbation of 0.1 Sv, taken from Lorbacher et al. (2012).

given to the steric response. This follows the work of Stammer (2006), and Lorbacher et al. (2012), which show that the barystatic response is negligibly small. Analysis of results and discussion is given in the discussion section (section 3.4).

### 3.3.2 The NEMO Model

#### 3.3.2.1 Introduction

The steric response of the ocean to realistic freshwater forcing is explored using the NEMO (Nucleus for European Modelling of the Ocean; Madec 2008) model. NEMO is an ocean-modelling framework consisting of multiple components. The configuration used here is a coupled ocean-ice model, it utilises OPA ocean dynamics, and LIM2 sea-ice. The model has a $1^o$ resolution, 75 z-level, tri-polar grid (ORCA1). It is Boussinesq, and uses a linear free surface where precipitation and evaporation affect the model via volume input through the ocean surface. Therefore precipitation has both barystatic and steric impacts on the sea surface. The model is forced by NCAR Common Ocean Reference Experiments (CORE2) atmospheric reanalysis data, and utilises the Gent-McWilliams eddy parameterisation (Madec, 2008).

The model is spun-up over 4 cycles of the CORE2 forcing dataset, equivalent to 225 years. Perturbation experiments are then conducted over the CORE2 forcing years 1997-2007. In addition to the anomalous freshwater release, a constant runoff from Antarctica is assumed of 0.073 Sv, or 2200 Gt yr$^{-1}$ (Large and Yeager, 2009).

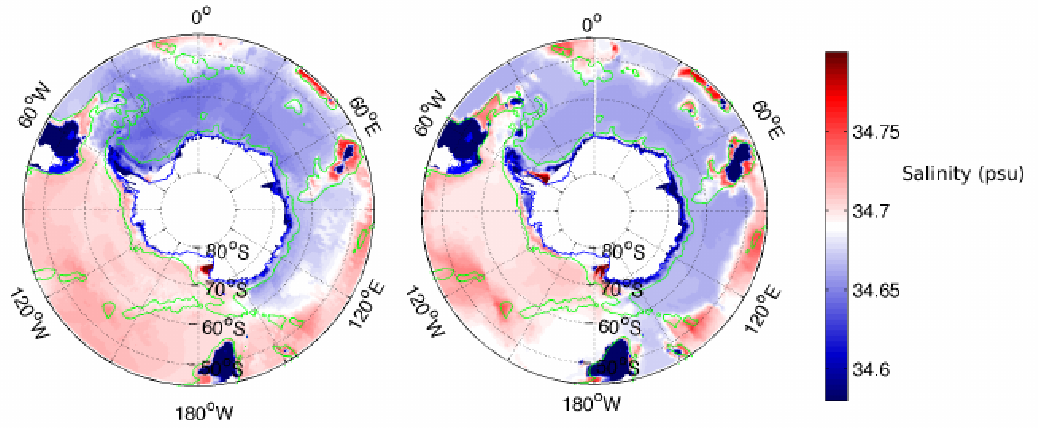

**a. CARS bottom salinity** **b. NEMO bottom salinity**

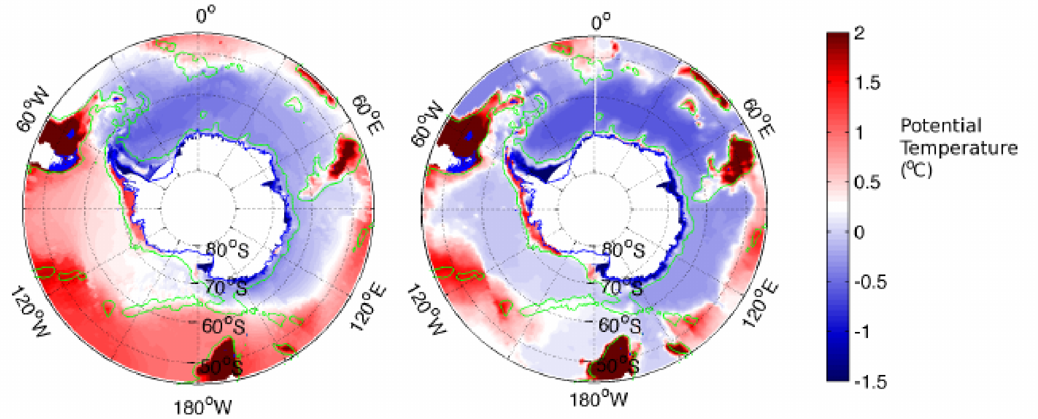

**c. CARS bottom temperature** **d. NEMO bottom temperature**

Figure 3.6: Comparison of bottom temperature and salinity in the NEMO model and the CARS Southern Ocean climatology. a. and c. show bottom salinity and temperature distributions from the CARS Southern Ocean climatology. b. and d. indicate bottom salinity and temperature distributions for the NEMO model.

#### 3.3.2.2 Model Validation

The model is qualitatively validated by comparison to the CSIRO Atlas of Regional Seas (CARS; Danabasoglu et al. (2014); Figures 3.6-3.8), Southern Ocean climatology (reanalysis), which is based on ARGO float data and other in situ measurements. Here we compare the NEMO annual-mean fields for 1992 with the CARS mean fields, which are derived from the last 50 years of measurements. The data and model agree surprisingly well, most notably in the zonal-mean diagnostics (Figures 3.7,3.8). Figure 3.6 compares the bottom distributions of temperature and salinity between the NEMO model and the CARS climatology, illustrating the models satisfactory degree of realism, particularly as regards the salinity and density fields, though bottom temperatures are shown to be too cold in the Pacific sector. Further information on and extensive validation of the model are provided in Ridgway et al. (2002) and Downes et al. (2015).

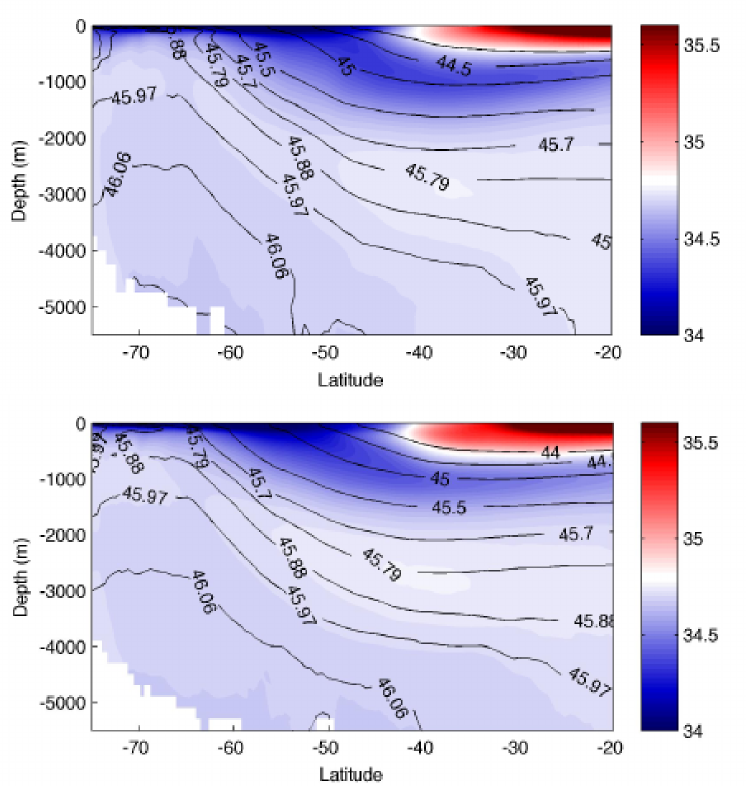

Figure 3.7: Comparison between zonal-mean sections of salinity in the CARS climatology and the NEMO model. The zonal-mean salinity distributions for CARS (upper) and NEMO (lower), with $\sigma$-4 density contours.

However, there are a number of caveats associated with using the $1^o$ NEMO model for this study. Foremost the resolution of the model is too low to accurately represent the thin boundary current surrounding the Antarctic continent. In the Bellingshausen Sea for example this current becomes weak allowing a proportion of our freshening signal to be injected into the Antarctic Circumpolar Current (ACC). Moreover the simulated thermosteric trends are likely to result from changes in circulation and deep water formation, but the NEMO models simulation of deep-water formation in the Antarctic is not thought to be realistic. It is important to consider these caveats when interpreting the model output.

### 3.3.2.3 Method

Two types of model run are used, a standard control run (see Danabasoglu, 2013), with no anomalous freshwater perturbation, and a perturbation run, with a freshwater anomaly. Both runs are forced by CORE2 forcing, over the period, 1992 to 2007. The perturbation run is identical to the control run, except for a surface freshwater flux anomaly applied to a $2^o$ by $2^o$ area centred on the Bellingshausen Sea shelf (Figure 3.9).

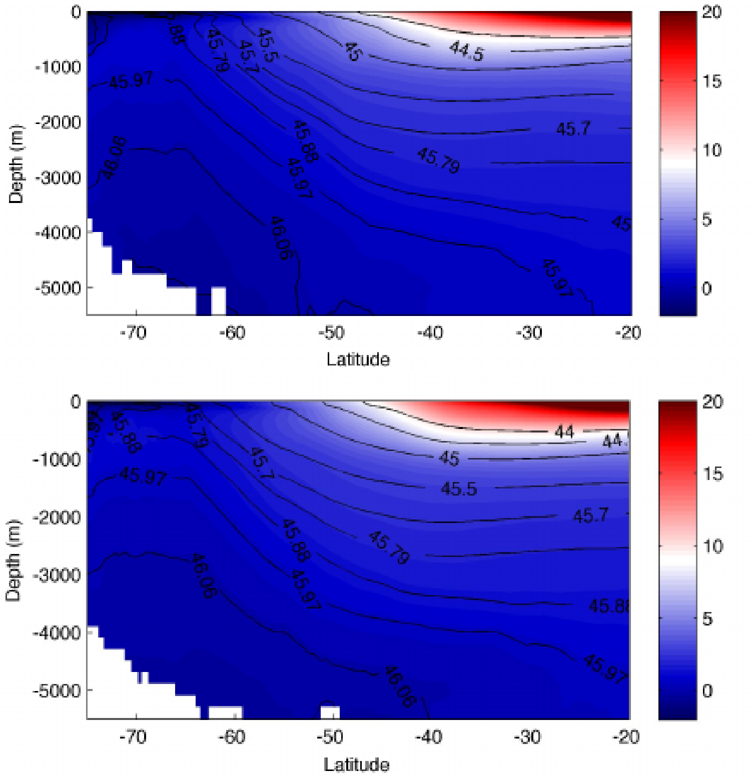

Figure 3.8: Comparison between zonal-mean sections of temperature in the CARS climatology and the NEMO model. The zonal-mean temperature distributions for CARS (upper) and NEMO (lower), with $\sigma$-4 density contours.

Three magnitudes of anomaly are used, 150 Gt yr$^{-1}$, 300 Gt yr$^{-1}$ (the measured approximate excess Antarctic freshwater discharge averaged over the last 20 years; Shepherd et al., 2012) and 600 Gt yr$^{-1}$. The SSH anomaly resulting from the anomalous freshwater forcing in the perturbation run is evaluated by subtracting the SSH in the control run from the perturbation run. The linear trends in the halosteric and thermosteric components of sea level change were calculated for each depth level, in conjunction with the linear trend in SSH.

#### 3.3.2.4 Results

The main results for the 300 Gt yr$^{-1}$ perturbation run are shown in Figures 3.10, 3.11. The simulated linear trend in steric SSH anomaly agrees well with satellite SSH observations, both in magnitude and in spatial distribution. The simulated trend is circumpolar, positive and ranges between (approximately) -1 and 4 mm yr$^{-1}$. Notable extreme positive values exist in the Bellingshausen Sea, on the Pacific Antarctic Ridge, and in the Australian Antarctic Basin. Negative extremes are present on the Southeast Indian Ridge and in the ACC east of the Peninsula. It is found that halosteric and thermosteric contributions each account for approximately half of the SSH trend (i.e.

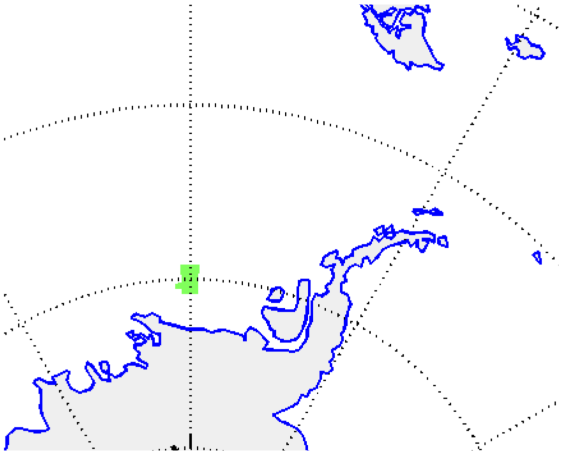

Figure 3.9: Schematic showing the region over which the NEMO freshwater anomaly is applied.

the barystatic response is negligible; Figure 3.11). Further, it should be noted that a barystatic response is nether exported nor observed in the NEMO model runs.

A vertical decomposition of the steric constituents reveals that the halosteric change occurs mainly in the upper ocean where approximately half of the vertically integrated halosteric change is accounted for in the top 800 m. Within this region the halosteric response close to the shelf is mainly circumpolar and positive, the strongest response occurs between the Bellingshausen and Ross Seas, and the weakest response south of the Amery. In addition, there are notable negative and positive trends in the halosteric response north of the 3000m isobath. The thermosteric response in the upper 800m is smaller then the halosteric, but contains interesting inter-regional variability. Notably the largest positive trend occurs on the western shelf of the Peninsula, with cooling to the west of this region in the Amundsen sea.

The bulk of the thermosteric signal then occurs in the deep ocean, between 800m and the sea floor (Figure 3.11). There is a positive, almost circumpolar, trend in thermosteric sea level close to the continent. A notable maximum exists in the Australian Antarctic Basin and over the South Indian Ridge. The deep halosteric response is small except for a pronounced positive response associated with the Southeast Indian and the Pacific Antarctic Ridges. These model results are broadly consistent with the analyses of in situ observations described in the previous chapter, section 2.2.2.

The link between increased freshwater forcing, and deep warming is unclear. It is possible to speculate that the upper decrease in salinity is associated with an increase in surface stratification. Further, this increase in stratification facilitates a reduction in the decent of newly formed dense waters, down the continental shelf, to form new bottom waters. However, as previously noted, the representation of deep water formation is known to

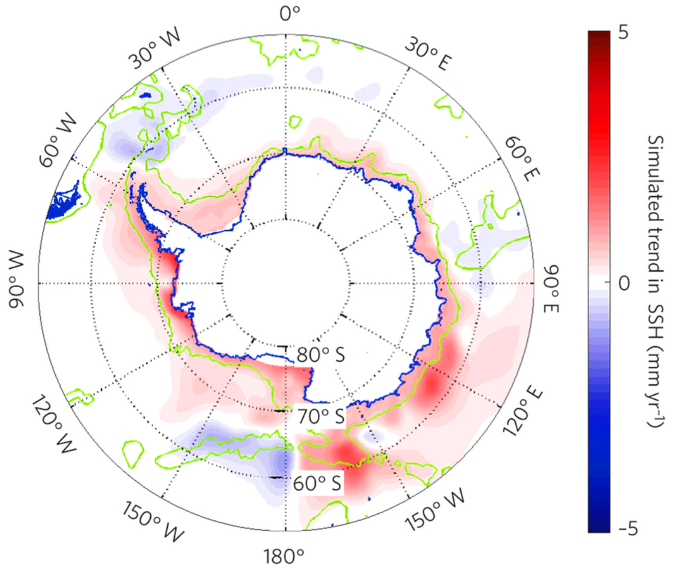

Figure 3.10: NEMO simulation of the regional anomaly in sea-level trend, 1997-2007, associated with a freshwater anomaly of 300 Gt yr$^{-1}$. the 3000m isobath is indicated in green.

be poor in the NEMO model. Further work is required to better understand the crucial link between surface freshening and deep water warming.

Furthermore, the simulated deep water warming agrees well with observations of deep water warming (e.g. Purky and Johnson, 2010) discussed in chapter 1, and in later chapters. This warming is similar in magnitude, and distribution around the Antarctic continent, however the simulated warming does not extend into the Atlantic and the Pacific Oceans, as it does in observations. It may be possible to associate this observed abyssal warming with Subpolar Sea freshening, however this is not the subject of this text, it is left for further research.

In addition to the sea level response, a small but notable trend is observed in the models sea ice fields. The sea ice response is largest in Austral summer (Figure 3.12). Both the control and perturbation runs express an increasing trend in Antarctic sea ice, shown in Figure 3.12, that is believed to be driven by changes in surface wind forcing. The wind driven Antarctic sea ice trend is modelled and discussed in detail by Holland et al. (2014); Holland and Kwok (2012). However the freshwater perturbation experiments also show an additional positive sea ice trend that is approximately 10-15% the magnitude of the wind driven component in the Ross Sea (Figure 3.12). Thus suggesting the Shelf Sea discharge anomaly may also amplify the response of the sea ice to recent changes in wind forcing.

The results for the 300 Gt yr$^{-1}$ distribution experiment were found to be consistent with the experiments for higher and lower freshwater forcings. The magnitude of the

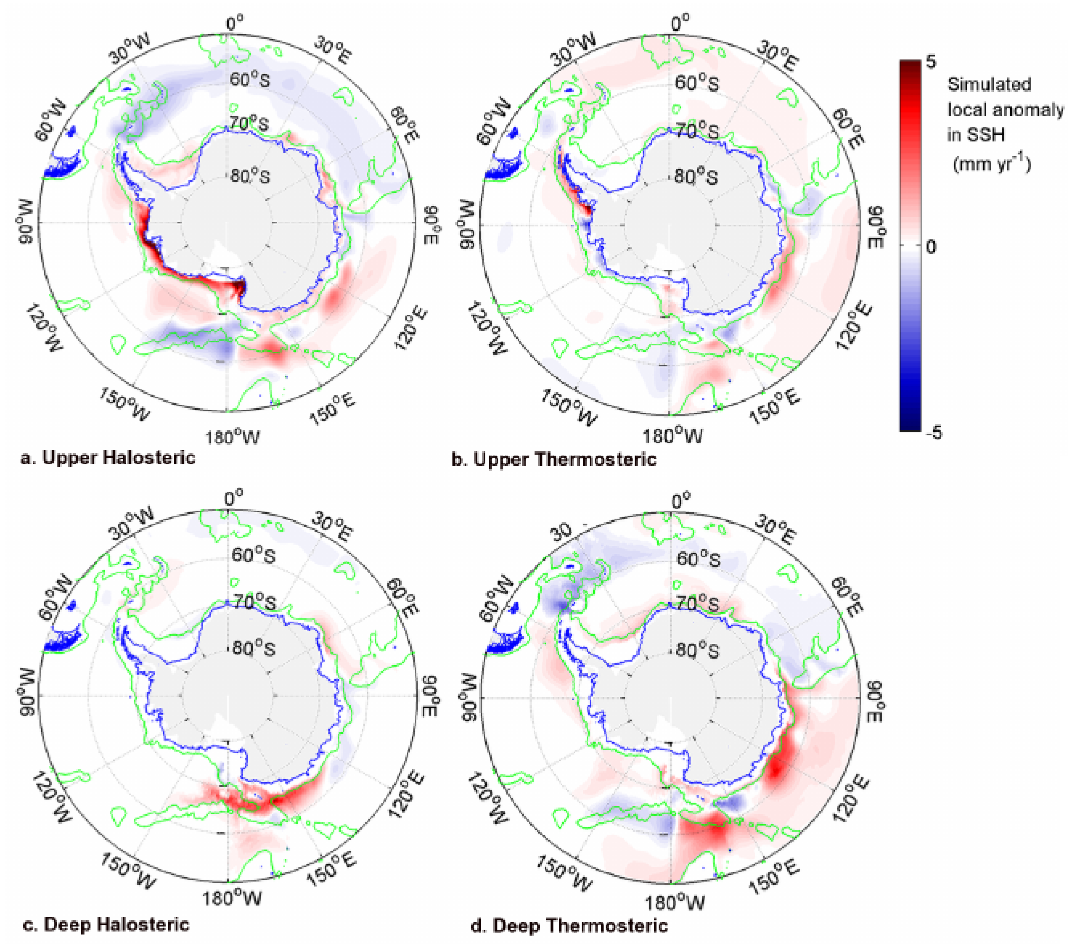

**a. Upper Halosteric** **b. Upper Thermosteric**

**c. Deep Halosteric** **d. Deep Thermosteric**

Figure 3.11: A decomposition of the NEMO-simulated linear trend in Antarctic subpolar sea steric height anomaly. a. Upper-ocean (0-800 m) trend in halosteric height. b. Deep (greater then 800 m) trend in halosteric height. c. Upper-ocean (0-800 m) trend in thermosteric height. d. Deep (greater then 800 m) trend in thermosteric height. The green contours show the 3000m isobath.

SSH response scales approximately linearly with the amplitude of the freshwater forcing anomaly, echoing the findings of Lorbacher et al. (2012).

## 3.4 Discussion

Before discussing model results, one examines the accuracy of the model, and the reader is encouraged to consider results within the context of the research question and the chosen methods caveats. The NEMO model has a number of known issues (see section 3.3.2), for example, the model is not expected to accurately produce Antarctic Bottom Waters, an important process when considering steric effects in the Shelf Sea. Furthermore, it is understood that the mechanism used to simulate the discharge anomaly in

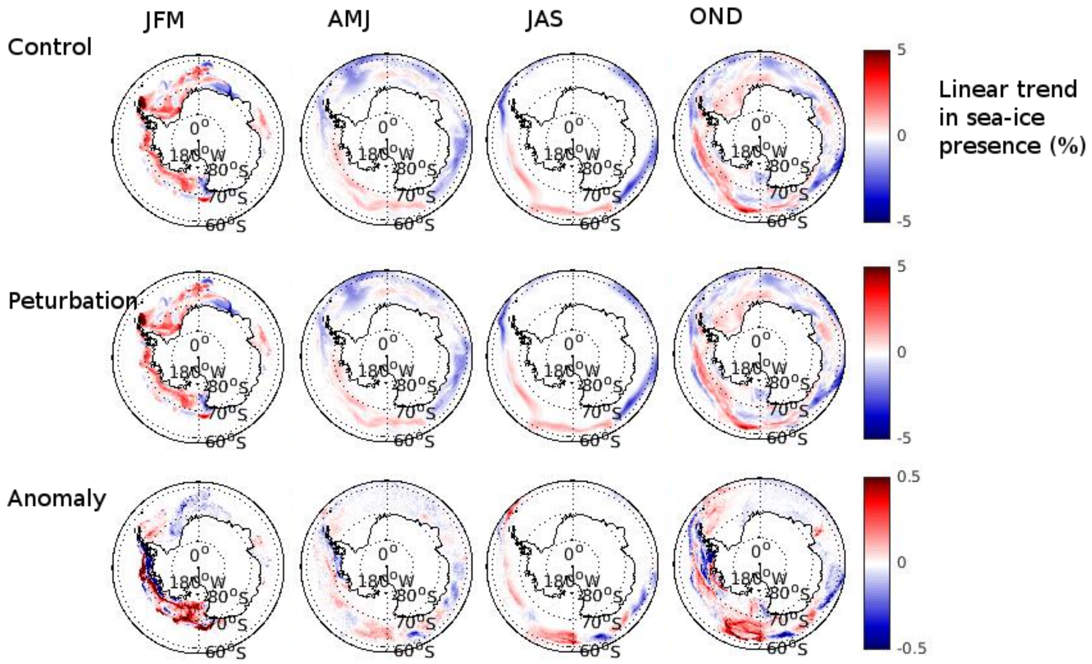

Figure 3.12: NEMO sea ice concentration trends (by season), in response to 300 Gt $yr^{-1}$ excess discharge over 16 years, 1992 - 2007. Top: Control run, middle: Perturbation run, and bottom: Anomaly, (or the difference between the control and the perturbation), where JFM, AMJ, JAS, OND demark linear trends in months, January-Febuary-March, April-May-June, July-August-September, October-November-December.

these models, i.e. excess precipitation, applied to single region, is an inaccurate representation of Antarctic Ice freshwater discharge. This mechanism was chosen as a small simplification in consideration of the models deficiencies. Therefore, the model results should be considered qualitative and within the context of observations discussed in the previous chapter. In other words, the model output cannot be discussed in precise terms, but the results of the steric modelling clearly provide significant insight into observations.

In the case of the steric simulations, a clear circumpolar positive trend in sea level is found in response to realistic freshwater forcing, providing strong support for the assertions of the previous chapter. The simulated steric trend is in agreement with both the magnitude and distribution of the satellite observed trend in Shelf Sea SSH, providing support both for the validity of the model and the hypothesis that the observed trend is driven by freshening. Following this, the model provides insight into the approximate response of the temperature field to freshening. A decrease in the salinity of the shelf waters, predominantly in the upper ocean, is shown to drive an increase in temperatures at depth. This temperature trend is assumed to be driven by isopycnal heave (shoaling); however this is a source for further research.

The magnitude of the simulated steric SSH trend (for a freshwater flux of 300 Gt $\text{yr}^{-1}$) is slightly smaller then observed, equal to approximately two-thirds of the observed trend. The model was forced with a slightly smaller value of freshwater anomaly then observations suggest (300 instead of 350). In addition, errors associated with the altimetry measurements and estimates of Antarctic discharge anomaly are large (order 0.8 mm $\text{yr}^{-1}$ and 100 Gt $\text{yr}^{-1}$ respectively). Therefore, it is argued that agreement between model and observations is sufficient within present error bounds. Additional tertiary forcing, such as the barystatic response to changes in wind forcing and the barystatic response to a realistic acceleration in discharge, are thought to further increase sea level close to the content by a small amount. These additional contributions sum to a maximum of 0.35 mm $\text{yr}^{-1}$, so are unlikely to be significant.

As previously discussed it is possible to estimate the amount of freshwater required to drive an observed increase in regional steric sea level, using the linear equation of state approximation (Munk, 2003). The unexpected thermosteric response to glacial melt suggests that the estimate of this value in the previous chapter is too large. Dividing this value by two, as implied by the steric model results, gives a new estimate of 300 ± 230 Gt $\text{yr}^{-1}$. This estimate is then in better agreement with the observed trend in Antarctic discharge of 350 ± 100 Gt $\text{yr}^{-1}$ (Shepherd et al., 2012).

Additional research is required to understand the regional variability both in the modelled and observed Shelf Sea SSH trend. For example, both show pronounced maxima in SSH associated with the Australian Antarctic Basin (Figures 3.10 and chap1fig1), and the Pacific Antarctic Ridge, as well as minima over the Southeast Indian Ridge. Furthermore, there are interesting differences between the sea level distribution identified for the barystatic and steric models.

## 3.5 Summary

In summary, austral summer satellite altimetry measurements show a pronounced circumpolar rise in sea level across the Antarctic subpolar sea between 1992 and 2011 that significantly exceeds the global mean. In situ measurements of freshening on the Antarctic Shelf suggest an important halosteric role in the observed SSH trend. Multiple datasets were analysed to investigate the dominant forcing mechanism in driving the observed trend. Precipitation, surface temperature, and wind forcing were found to provide small or negligible anomalies to the region over recent decades. However observations of Antarctic discharge strongly implicate a glacial melt driven halosteric response as the primary driver of the trend. An idealised modelling study was conducted to simulate the response of the Antarctic Shelf Sea to realistic freshwater anomalies. The barystatic response to freshwater forcing was found to be small, but the steric response is shown to produce a distribution and magnitude in close agreement with satellite SSH observations. The simulated steric response is shown to consist of equal halosteric and thermosteric components. Findings therefore reveal that the accelerating discharge from the Antarctic Ice has had a pronounced and widespread impact on the adjacent subpolar seas over the past two decades. Given the key dependence of the Southern Ocean on freshwater forcing, this perturbation has major implications for the regions stratification, and circulation as well as important biogeochemical and ecological processes in the region.

# Chapter 4

# An Investigation Into The Wind-Adjustment Of A Southern Subpolar Gyre: Model Development

## 4.1 Overview

Over recent decades, the Southern Ocean winds have been observed to increase in intensity in association with a positive trend in the SAM (Marshall et al., 2004; Thompson and Solomon, 2002). The impact of this change on the dynamics of the Antarctic Subpolar Sea, especially the Subpolar Gyres, is poorly understood. The following chapters document a modelling study that seeks to increase our understanding of the wind adjustment of a southern subpolar gyre.

The response of a southern Subpolar Gyre to an increase in wind forcing is simulated with a regional configuration of the MITgcm model, referred to as the 'gyre model'. The gyre model is $1^o$ resolution, it is forced at its surface by constant wind and buoyancy forcing. The model has 4 subconfigurations of ranging complexity, which are designed to assist in analysis of complex model behaviour.

The first chapter provides an introductory literature review and documents the development of the model. The second chapter then discusses the results of the model.

In this chapter, section (4.2.1) provides a literature review, discussing the motivation for the development of the gyre model and the theoretical background to the gyre adjustment problem. Section (4.3.1) reviews the main tool for this modelling study, the MITgcm. Section (4.4-4.5) describes the development of the gyre model. Section (4.6) provides some validation of the gyre model, using analytical theory. Section (4.7) outlines the subconfigurations of the model, which are used in model analysis. Finally the chapter is summarised by section (4.8).

## 4.2 Introduction To The Study

### 4.2.1 Review of Modelling motivation

As previously discussed, the SAM has generally increased over recent decades, associated with a southward movement and strengthening of the Southern Ocean winds (Marshall et al., 2004; Thompson and Solomon, 2002). The change in surface wind forcing can be characterised by an approximate 20% increase in magnitude over the instrumental period. The trend is discussed in chapter 1 and illustrated in Figures 1.14–1.16. The response of the Weddell Gyre to the increase in wind forcing is of particular scientific interest because of the Southern Ocean's role in deep-water ventilation and export. However, relatively little is known about this response.

In addition to the change in winds, a prominent feature of recent oceanic climate change has been a general warming of abyssal waters throughout the Southern and Atlantic Oceans. The timing and distribution of warming is suggestive of a decadal trend propagating northward from the Southern Ocean. However, the properties of the deep waters in the source regions for these warming abyssal waters (WSDW and WSBW), appear to be decoupled from global trends (e.g. Fahrbach et al., 2011, Zenk and Morozov, 2007).

It is plausible that a link exists between the increase in winds over the Weddell Gyre and the global warming of Southern Ocean derived abyssal waters. Meredith et al. (2008) suggests that an increase in the surface wind stress has driven a change in the hydrography of the Weddell Gyre and that this change in hydrography has driven a reduction in the northward export of the densest waters. Here, the authors suggest an increase (decrease) in cyclonic surface wind stress is associated with a spin-up (spin-down) of the gyre circulation and therefore an increase (decrease) in isopycnal doming. This change in doming constitutes steeper (less inclined) isopycnals at the northern boundary of the Weddell gyre, which facilitates increased light (dense) water export over the South Scotia ridge and therefore abyssal warming (cooling; Fig. 4.1). The Meredith et al. (2008) hypothesis is summarized by Figure 4.1.

Additionally (Meredith et al., 2011) provides an alternative hypothesis. Here, it is argued that wind-driven variability in the barotropic flow along the South Scotia Ridge, has a rapid impact on both AABW temperature and flow speed through the Orkney passage. This in-turn modulates the properties of deep water export from the Subpolar Sea. This theory suggests that mixing plays an important role in the link between surface wind forcing and bottom water properties. However, this theory assumes that

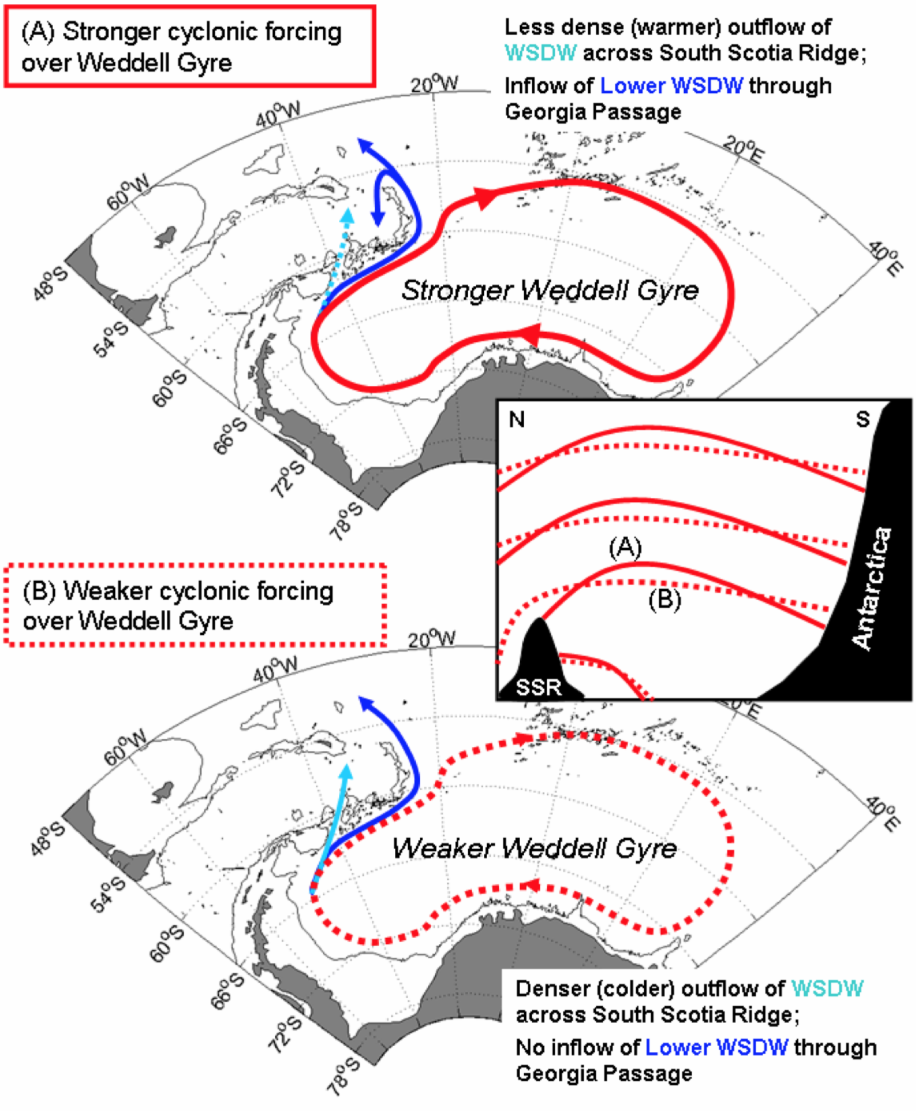

Figure 4.1: A summary of the (Meredith et al., 2008) wind control hypothesis taken from the same paper. The doming of isopycnal surfaces in the Weddell Sea is shown in response to gyre spin-up (A) or a spin-down (B). Case (A; upper panel): Here the density of the deepest WSDW exported across the SSR to the Scotia Sea decreases resulting from a spin-up of the gyre. Case (B; lower panel): Here the density of the deepest WSDW exported across the SSR to the Scotia Sea increases resulting from a spin-down of the gyre. Taken from (Meredith et al., 2008).

mixing is relatively large in the Scotia Sea. Transient tracer data provide estimates of Scotia Sea diapycnal mixing that are small, i.e. $1\times10^{4}$ m$^{2}$ s$^{1}$. Estimates of mixing based upon water mass budgets are much larger, e.g. $39\times10^{4}$ m$^{2}$ s$^{1}$ (Heywood et al., 2002). Therefore it is likely that mixing in this region is highly inhomogeneous.

Jullion et al. (2010) provides useful insight following analysis of reanalysis and observation data, finding a high correlation, with a 5-month lag, between surface wind data and observations of AABW export. This suggests that local winds are an important driver of AABW export variability (Fig. 4.2). In addition, modelling studies further find a seasonal (and extended) correlation between surface wind forcing and Weddell Sea export variability (Wang et al., 2012, Kida, 2011).

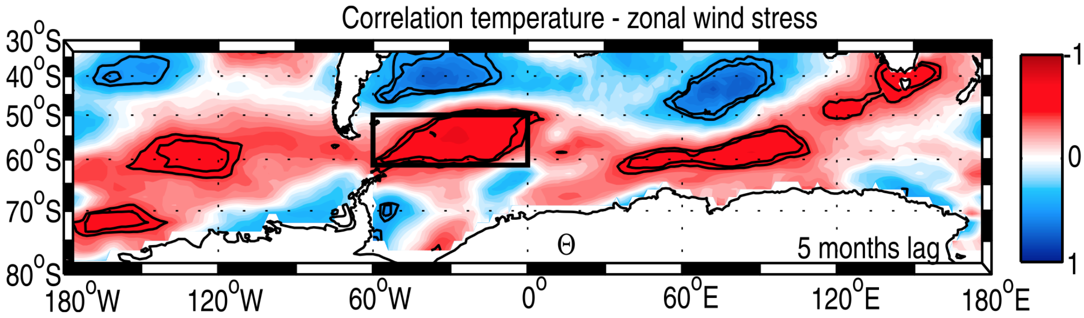

Figure 4.2: Taken from Jullion et al. (2010): The distribution of correlation between zonal wind anomalies and AABW temperature (a time lag of 5 months is applied). The black lines show the 90% and 95% confidence interval levels. The black box is not used in this text.

Meredith et al. (2011) shows further insight using data from two mooring stations within the boundary current, upstream and downstream of Orkney Passage. Mooring data are also compared to local (Era-Interim) reanalysis surface wind data. Time series of temperature anomalies from the mooring stations correlate well. A time lag for anomalies to propagate from the south to the north of the passage is observed. The most common lag is 120 days between stations. During 2001 the rate of the flow increased where a lag of 60 days best suits this period. This period of rapid flow is also coincident with an increased number of warm anomalies, suggesting that a wind-induced reduction in the export of the colder classes of AABW from the Weddell Gyre could also be associated with an increase in the export of the warmer classes of dense water. Regardless, the general timescale of a few months shows consistency with Jullion et al. (2010).

In general, it is evident from these observations that the Southern Ocean and particularly the Weddell Gyre, is subject to interesting climate trends. The following chapters seek to provide useful new insight into these changes using a simplified numerical model. Following Meredith et al. (2008), attention is given to the response of an idealised southern Subpolar Gyre to an increase in wind forcing and the potential for a link between a trend in surface winds and abyssal temperature trends.

### 4.2.2 A Review Of Gyre dynamics

Before discussing the development of the gyre model, a review of background literature on the wind-driven adjustment of a gyre is required. Three influential papers arguably dominate the literature on gyre dynamics. These are Sverdrup (1947) on the wind driven circulation, Anderson and Gill (1975) on the wind driven adjustment and Stommel and Arons (1960) on the abyssal circulation.

Sverdrup (1947) is discussed in section 4.6, in analysing early model output. Anderson and Gill (1975) is used in section 4.2.2.1 to initiate a discussion of the wind-adjustment of a gyre. Stommel and Arons (1960) is used in section 4.2.2.2, to initiate a discussion on the abyssal circulation of a gyre. Finally, Section 4.2.2.3 discusses boundary waves, which are shown to be crucial features in gyre adjustment.

#### 4.2.2.1 The Wind Driven Adjustment Of A Gyre

Anderson and Gill (1975; henceforth referred to as AG) provide the foundation for modelling research on the wind-adjustment of a gyre. They develop a linearised model that describes the adjustment of a wind-driven gyre to an increase in wind stress. The governing equations of the AG model are first projected onto the dynamical modes of an ocean system in polar co-ordinates. AG then assume the wind driven circulation varies periodically with latitude and therefore it can be simulated as a single section across a gyre. Further, AG assumes that the ocean domain is flat-walled, with a fixed depth and the horizontal velocity is zero at the boundaries ($u = 0$ at $x = -L$ and $x = L$). AG examine the response of this model to an increase in wind forcing both analytically and numerically; both on an f and $\beta$-plane.

Following non-dimensionalisation, a key non-dimensional parameter emerges:

$$\Lambda = \mu^2 2L^2, \tag{4.1}$$

where $\mu$ is given by:

$$\mu^2 = \left(\frac{f}{c}\right)^2 + l^2 \tag{4.2}$$

and $L$ is the zonal length scale of the basin (m), $l$ is the wave number (m$^{-1}$), $f$ is the Coriolis parameter (s$^{-1}$) and $c$ is the barotropic gravity wave speed (m s$^{-1}$).

The AG model is explored analytically in terms of planetary waves and then solved numerically. The analytical solution is constructed from the sum of a time-independent, or space-independent solution and a wave solution for the homogenous equation. The time independent solution is shown to be a form of Sverdrup-balance and the homogenous equation is shown to be a form of the planetary, or Rossby wave equation. In this way, AG shows that, following a change in wind forcing, the gyre system adjusts towards a steady-state described by Sverdrup balance and the mechanisms for this adjustment are types of Rossby waves. The adjustment of the gyre is then characterised by the transit speed of the different wave components. AG show that the westward propagating long-wavelength Rossby waves have a non-dimensionalised group speed described by:

$$c_{gl} = -1/(\Lambda), \tag{4.3}$$

whereas the short-wavelength Rossby waves are shown to have eastwards (non-dimensionalised) group velocity;

$$c_{gs} = 1/(8\Lambda). \tag{4.4}$$

AG go on to describe the spin-up, as implied by equations (4.3 - 4.4) and observed in numerical experiments. The initial zonal velocity in the ocean interior is shown to increase linearly. Then, model properties set by boundary conditions at the eastern and western boundaries propagate towards the interior. Long Rossby waves, travel quickly westward from the eastern boundary at $c_{gl}$ and short Rossby waves travel eastward from the western boundary at $c_{gs}$. A steady-state Sverdrup's-balance is set following the passage of the long Rossby wave from the east. The long Rossby wave propagates eight times faster than the short wave and therefore travels much further. At the western boundary, a boundary layer is formed by the eastward moving slow Rossby wave, which travels at a rate of $c_{gs}$ (Figure 4.3).

The work of Killworth (1985) then supports the work of AG. Killworth (1985) uses a simplified 2-layer model, with a domain that is 4000 m deep and 4000 km by 4000 km, in the horizontal (equivalent to 66 $^o$ Longitude at 75 $^o$S). Again, the entire basin responds linearly to a sudden increase in wind stress, until the passage of long Rossby waves. These waves propagate information from the eastern to the western boundary. Regions to the east of the long Rossby wave are left in a steady-state Sverdrup-like balance. Killworth (1985) suggests a time-scale of around 5 years for the baroclinic component of this adjustment, therefore implying the model has a long Rossby wave speed of around 0.02 m s$^{-1}$.

The models of AG and Killworth (1985) both make assumptions that may not hold generally. For example, they both assume inertial-scale motions are unimportant and therefore neglect Poincare waves and inertial oscillations. These near-inertial motions have proven prominent in ocean models (Blaker et al., 2012) and may play a role in model adjustment. Both the AG and Killworth (1985) models are based upon the propagation

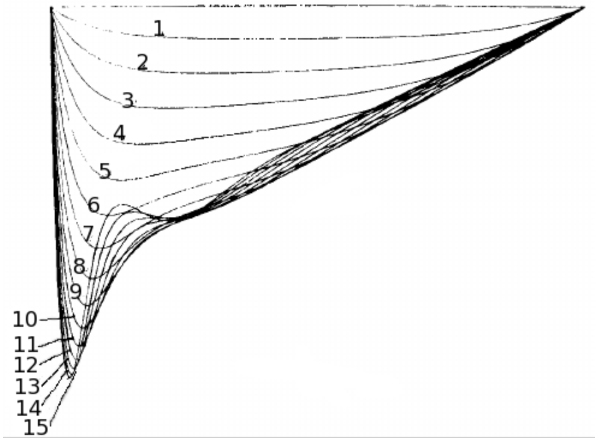

Figure 4.3: Taken from (Anderson and Gill, 1975): the numerically determined solution of the AG model of gyre adjustment ($\lambda = 20$), showing the zonally distribution of the zonally velocity anomaly. Each contour shows a zonally cross section of $u$ anomaly at a given time, from 1 to 15. The anomaly is shown to rapidly propagate westwards from the eastern boundary and slowly eastwards from the western boundary.

of Rossby waves, but our current theory of Rossby waves may be incomplete. LaCasce (2000), highlights that the speed of satellite-observed Rossby waves is greater, then theorised, especially at high latitudes (Chelton et al., 2007). This disparity has been discussed widely by e.g. Killworth et al. (1997), Dewar (1998) and LaCasce (2000). However, LaCasce and Pedlosky (2004) suggest that the observed waves are faster, because the waves are subject to baroclinic instabilities while in transit. It is suggested that instabilities cause the waves to break-up and form barotropic waves that transit the gyre at two to four times the long Rossby wave speed. LaCasce (2000) provides a way to estimate the timescale for a Rossby wave to remain stable in a given velocity field and also a new estimate of the timescale for the transit of anomalies from the eastern to the western boundary of an ocean basin. This new, shorter, timescale suggests that the adjustment process described by AG may occur quicker then previously theorised.

#### 4.2.2.2 The Buoyancy Driven Circulation

Following discussion of the ocean's adjustment to a change in wind forcing, consideration is given to the adjustment associated with a change in buoyancy forcing. Stommel and Arons (1960), henceforth referred to as SA, provide a seminal discussion of buoyancy driven abyssal dynamics. The SA model describes the circulation of an abyssal water layer with a point source of dense water and a uniform upwelling (or vertical diffusivity) that is distributed evenly over the layer. The SA model produces a cyclonic circulation, that is intensified along the western boundary and which has a strong (vorticity-based) similarity to the dynamics of the wind driven circulation described by Sverdrup (1947). The simulated circulation is shown in Figure (4.4).

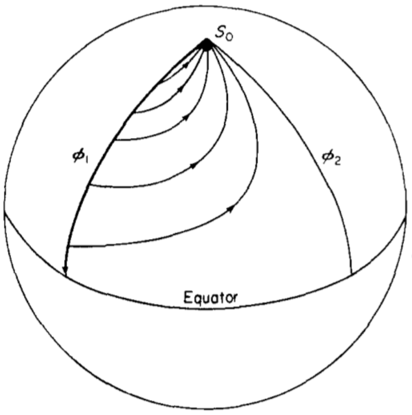

Figure 4.4: Taken from (Stommel and Arons, 1960): The density driven, abyssal circulation pattern estimated by the (Stommel and Arons, 1960) model for a similar domain to the gyre model. i.e. the domain is meridionally bound, with a concentrated source at the North Pole and a uniformly distributed vertical diffusivity.

Alternatively, Stommel (1961) uses a box model to simulate the density driven overturning circulation. The model consists of a well stirred box with temperature and salinity properties that are determined by mixing, adjacent to two forcing boxes with fixed temperature and salinity, shown in Figure 4.5. This model considers a meridional circulation in a zonally integrated sense, with an overturning strength proportional to the density difference between latitudes. It expresses multiple steady states and provides insight into the dynamics of overturning circulations.

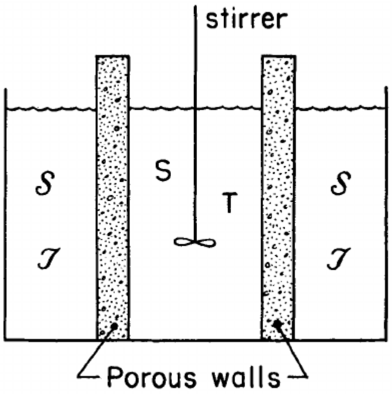

Figure 4.5: An idealised schematic of the Stommel (1961) model (taken from Stommel, 1961): consisting of a well stirred box, with temperature T and salinity S and two adjacent boxes connected by porous walls, who's salinity $S$ and temperature $T$ are fixed at constant values.

Straub (1996) suggests that there is an interesting inconsistency between the models of SA and Stommel (1961). Straub (1996) uses a two layer version of the SA model, to show that the rate of exchange between different regions in the SA model is clearly related to the (zonally averaged) difference in density between these regions. This finding is in disagreement with the Stommel (1961) model. Further, it is argued that western boundary currents in the SA model have a very small influence on the zonally averaged density field, despite constituting a dominant component of the zonally averaged meridional transport. Straub (1996) suggests that the east-west pressure gradient, which is required to geostrophically balance overturning from the north-south buoyancy forcing, plays an important role in setting the abyssal meridional transport.

Greatbatch and Lu (2003) then examine these different models of abyssal circulation using the Kawase (1987) model and suggest that two states of abyssal circulation exist. First, a 'weak-damping' or SA state, where the diapycnal diffusivity is low and boundary waves are able to propagate with low attenuation. In this state thickness anomalies are rapidly communicated as Kelvin boundary waves and the east-west pressure gradient is first-order in setting the overturning strength. Second, a strong damping, or Stommel (1961) state, where boundary waves are rapidly attenuated and the overturning circulation at a given latitude is directly proportional to the local zonally-averaged meridional density gradient. Greatbatch and Lu (2003) therefore argue, that the level of 'damping' in a model, could affect the abyssal dynamics of the model and alter the way it adjusts to changes in forcing. Furthermore, it is suggested that low-resolution GCMs are likely to follow a 'high damping', Stommel (1961) regime (Wright et al. 1998), when a SA regime may be more realistic.

#### 4.2.2.3 Boundary Waves

A number of authors have highlighted the role of boundary waves in the adjustment of ocean models (e.g. Doscher et al., 1996; Capotondi, 2000; Goodman, 2001; Getzlaff et al., 2005; Chiang et al., 2008; Zhang et al., 2011; Hodson and Sutton, 2012). It is probable that boundary waves will play an important role in the adjustment of the gyre model, particularly in the adjustment of the abyssal circulation, as suggested by the previous section. The following section therefore provides a review of literature on boundary waves, particularly in low-resolution models.

Ivchenko et al. (2004) and Lorbacher et al. (2012), highlight the role of fast barotropic Kelvin waves in the initial response to density anomalies in the Southern Ocean. Ivchenko et al. (2004) and Lorbacher et al. (2012) show that such signals propagate globally on a timescale of weeks. This timescale is consistent with wave theory, which estimates the barotropic Kelvin wave speed to be around 100 m $s^{-1}$. However, these papers do not discuss the baroclinic wave response.

Many authors have found the baroclinic boundary wave response in low-resolution ocean models to be complex and variable (e.g. Doscher et al., 1996; Capotondi, 2000; Goodman, 2001; Getzlaff et al., 2005; Chiang et al., 2008; Zhang et al., 2011; Hodson and Sutton, 2012). Theoretical 1st mode baroclinic Kelvin wave speed estimates are around

1 m $s^{-1}$. Multiple authors have observed boundary waves in 'low resolution' ocean models to move more slowly than predicted by theory, but faster then advective pathways (e.g., Doscher et al., 1996; Capotondi, 2000; Goodman, 2001; Getzlaff et al., 2005; Chiang et al., 2008; Zhang et al., 2011; Hodson and Sutton, 2012). Where, 'low resolution' is considered as $1^o$, or less.

The issue of slow boundary waves in low resolution ocean models is first discussed by Hsieh et al. (1983), who find baroclinic Kelvin wave speeds to vary depending on model grid, boundary conditions and viscosity parameterisations. Hsieh et al. (1983) typifies the issue by highlighting that a model with a grid spacing of between 20 and 500 km, is unable to explicitly resolve the baroclinic Kelvin wavelength scale of around 20 km. Hsieh et al. (1983) points out that it is not possible to accurately model the baroclinic Kelvin wave with such low-resolution models and therefore baroclinic boundary waves observed in low resolution models cannot be Kelvin waves. Hsieh et al. (1983) suggests optimal parameterisations for simulating boundary waves at low resolutions, namely a C-grid configuration, free-slip boundary conditions and low viscosity. However, Hsieh et al. (1983) do not discuss the mechanisms by which anomalies propagate along boundaries if the traditional Kelvin wave theory is inappropriate.

Killworth (1985) and Winton (1996) both provide analytical theories for baroclinic boundary propagation in low-resolution models. Both highlight the importance of viscous or frictional terms. Marshall and Johnson (2013) provide a review of the problem and advance the theory. Marshall and Johnson (2013) and Killworth (1985) find a similar balance of terms for the boundary waves, suggesting their theoretical arguments are robust.

In an appendix entitled 'The Numerical Boundary Instability', Killworth (1985) outlines the numerical propagation of anomalies along the western boundary of a highly simplified, almost geostrophic, two-layer model. He finds that the zonal velocity divergence due to the no normal flow condition at the model boundary dominates the divergence of the horizontal velocity field.

$$\nabla u_{ib+1,j} \approx \frac{u_{ib+1,j} - u_{ib,j}}{\Delta x} = \frac{u_{ib+1,j} - 0}{\Delta x}, \tag{4.5}$$

where $\nabla \cdot \mathbf{u}$ is the horizontal divergence of the zonally velocity field, subscripts denote nodes and $\Delta x$ is the zonal grid spacing. Stated informally, equation (4.5) indicates that if $u = 0$ at the boundary, then $\nabla \cdot u$ must be large. As a consequence, a wave equation arises from the buoyancy equation considered over one grid box. This is approximately

$$\frac{\partial \theta_b}{\partial t} \approx \frac{1}{f\Delta x}\frac{g(H_1 + H_2)\Delta\rho}{4\rho_0}\frac{\partial \theta}{\partial y}, \tag{4.6}$$

where $H_1 + H_2$ is the total water depth, $\rho$, $\rho_0$, $\Delta\rho$ are the density, the reference density and the difference in density between levels respectively (kg $m^{-3}$) and $\theta$ is the potential temperature ($^o$ C). It is shown that this wave propagates at the speed

$$\frac{c^2}{f\Delta x} \tag{4.7}$$

where $c^2 = \frac{g(H_1+H_2)\Delta\rho}{4\rho_0}$ is the theoretical speed of the first baroclinic mode (m $s^{-1}$). Equation (4.7) can be rearranged in terms of the baroclinc Rossby radius $L_d = \frac{c}{f}$ here c is the baroclinic Rossby wave speed. Equation (4.7) then becomes

$$c\frac{L_R}{\Delta x}. \tag{4.8}$$

The numerical boundary wave described by equations (4.6–4.8) must be resolved in time to ensure model stability. Therefore it must exist for the model to be stable. Killworth (1985) states that the numerical boundary wave 'immediately generalizes to multilevel models', therefore suggesting analogous processes should arise in similar models. However, Killworth (1985) also suggests that it is possible to eliminate this wave by reformulating the zonal velocity at the boundary.

Marshall and Johnson (2013) further the analytical discussion of low-resolution model boundary waves by considering a linear, semi-geostrophic, reduced-gravity model of boundary wave propagation. The Marshall and Johnson (2013) model is similar to the commonly used Kelvin wave model. However, the Marshall and Johnson (2013) system includes a linear friction (or viscous) term in the meridional direction. This model is illustrated by equations (4.9–4.13), showing the $u$ and $v$ components of momentum, the continuity equation and the associated vorticity equation, respectively:

$$-\beta y v' + g'\frac{\partial h'}{\partial x} = 0 \tag{4.9}$$

$$\frac{\partial v'}{\partial t} - \beta y u' + g'\frac{\partial h'}{\partial y} = \nu\frac{\partial v'}{\partial x^2} = 0 \tag{4.10}$$

$$\frac{\partial h'}{\partial t} + h_0(\frac{\partial u'}{\partial x} + \frac{\partial v'}{\partial y}) = 0 \tag{4.11}$$

$$\frac{\partial}{\partial t}(\frac{\partial^2 h'}{\partial x^2} - \frac{h'}{L_d^2}) + \beta\frac{\partial h'}{\partial x} - \nu\frac{\partial^4 h'}{\partial x^4}) = 0 \tag{4.12}$$

where,

$$g' = g\frac{(\Delta\rho)}{\rho_0}, \tag{4.13}$$

is the reduced gravity and $\Delta\rho$ (Kg m$^{-3}$) is the local vertical density gradient. Here, $u$ and $v$ are the horizontal components of velocity (m s$^{-1}$), prime quantities denote anomalies, $h'$ and $h_o$ indicate the depth of a given mode and the total water depth respectively (m). $L_d$ is the Rossby radius (m), $\beta$ is the change of $f$ with meridional distance (s$^{-1}$ m$^{-1}$) and $\nu$ is a viscosity parameter (m$^2$ s$^{-1}$). In order to examine the wave response at the model boundaries, the boundary conditions are applied to the zonal momentum equation, namely $u = 0$ and $\frac{\partial h'}{\partial x} = 0$ (no slip), at $x = 0$. Applying these to equation 4.13 yields the modified vorticity equation:

$$\beta y \frac{\partial h'}{\partial y} - \nu \frac{\partial^3 h'}{\partial x^3} = 0 \tag{4.14}$$

Then a trial solution is sought, of the form.

$$h' = A(y) \left( \frac{e^{ik_a(y)x} + \gamma e^{ik_b(y)x}}{1+\gamma} \right) e^{-i\omega t} \tag{4.15}$$

Here, division by the coefficient $(1 + \gamma)$ is required to ensure that A(y) is equal to the wave amplitude at the boundary. Substituting a trial solution of this form into the vorticity equation 4.13 gives the quartic dispersion relation:

$$-\nu k_c^4 + i\omega k_c^2 + i\beta k_c + \frac{i\omega}{L_d^2} = 0 \quad (c = a, b) \tag{4.16}$$

There are 4 roots to the dispersion relation; two are solutions for the western boundary and two for the eastern boundary. $k_a$ and $k_b$, are solved for by the authors using singular perturbation theory. These wave numbers are then used when substituting the trial solution into the boundary condition, providing information about the wave amplitude and velocity.

The problem is then considered in terms of three regimes. The waves produced in all regimes propagate around the boundaries of the domain cyclonically, i.e. northwards along the western boundary in the southern hemisphere. First, it is assumed that the friction or viscosity is negligible along the boundary and the scale of the wave is $L_d$, giving the Kelvin wave formulation, where the speed of boundary wave propagation is the familiar $c_g = \sqrt{gH}$, but unlikely (these waves are unlikely to exist, please clarify this).

Secondly, a Rossby wave formulation is assumed, where viscosity (or friction) is important in the boundary layer balance, facilitating the existence of short Rossby waves. These waves propagate along the boundary at the first baroclinic mode speed, scaled by the ratio of the Rossby Radius to the Stokes viscous boundary layer:

$$c_{sg} = c_g \frac{L_d}{\sqrt{\nu/2\omega}}, \tag{4.17}$$

One then notes the similarity between equations (5.7,4.17) where the numerical baroclinic boundary wave arises as a short Rossby wave and where the wave speed is scaled by the ratio between the Rossby radius and a pertinent length scale. In the arguments of Marshall and Johnson (2013), this length-scale is representative of a boundary layer width. It is common for low-resolution models to set viscosity or friction parameters so that the boundary layer is a similar scale to the model resolution. This is chosen for limiting the magnitude of parameters within numerical stability, however it results in a similar scaling factor for the waves discussed by Killworth (1985) and Marshall and Johnson (2013). The agreement between these different theoretical arguments then highlights the importance and validity of these waves, which are referred to as numerical short boundary wave (NSBW) in the remainder of this chapter.

Throughout this discussion it has been assumed, for simplicity, that the boundary of the domain is vertical (flat). It is understood that in a more realistic domain with sloping sidewalls, anomalies are able to propagate using the change in depth cross-slope as a vorticity restoring mechanism. These waves fall into a class of topographic Rossby waves (Huthnance 1978; Elipot et al., 2013) and can travel significantly faster than first baroclinic mode Kelvin waves (O'Rourke 2009). Here these are not considered as they are highly complex and are only relevant for our 4th model sub-configuration, where the sidewalls are sloped.

Following this discussion, the importance of planetary waves, especially boundary waves, is apparent. From the study of these waves, a number of key time and length scales are identified. These are presented in Table 4.1, along with other important time scales and constants. These will be useful when analysing model output.

## 4.3 Introduction To The Model

The introductory information in the previous section (4.2) provides both a guide for model design and interpretation of results. Before specifying the model design, the following sections introduce fundamental information on the chosen model framework.

### 4.3.1 The MITgcm

The primary tool used for studying the response of a southern subpolar gyre to changes in wind forcing is the Massachusetts Institute of Technology general circulation model

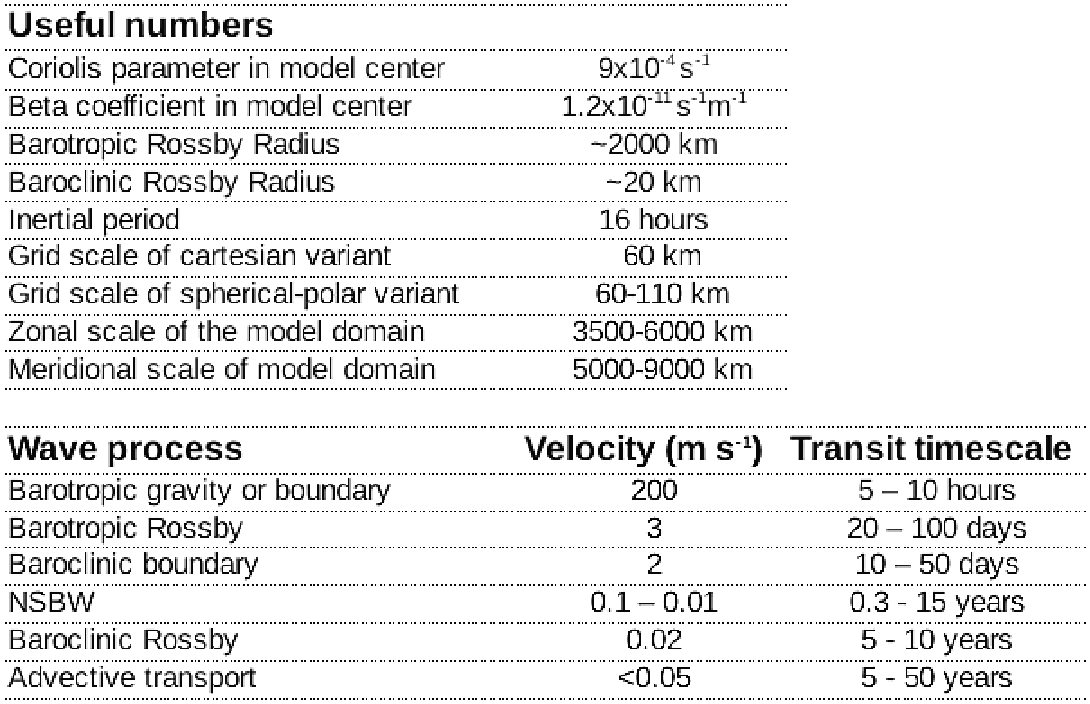

| **Useful numbers** | |
|---|---|
| Coriolis parameter in model center | $9\text{x}10^{-4}\,s^{-1}$ |
| Beta coefficient in model center | $1.2\text{x}10^{-11}\,s^{-1}m^{-1}$ |
| Barotropic Rossby Radius | ~2000 km |
| Baroclinic Rossby Radius | ~20 km |
| Inertial period | 16 hours |
| Grid scale of cartesian variant | 60 km |
| Grid scale of spherical-polar variant | 60-110 km |
| Zonal scale of the model domain | 3500-6000 km |
| Meridional scale of model domain | 5000-9000 km |

| **Wave process** | **Velocity (m $s^{-1}$)** | **Transit timescale** |
|---|---|---|
| Barotropic gravity or boundary | 200 | 5 – 10 hours |
| Barotropic Rossby | 3 | 20 – 100 days |
| Baroclinic boundary | 2 | 10 – 50 days |
| NSBW | 0.1 – 0.01 | 0.3 - 15 years |
| Baroclinic Rossby | 0.02 | 5 - 10 years |
| Advective transport | <0.05 | 5 - 50 years |

Table 4.1: A table of useful constants, wave speeds, lengths and time scales associated with the gyre model or mechanisms of ocean adjustment. Here NSBW refers to Numerical Short Boundary Waves, in reference to Marshall (2003)

(MITgcm; Marshall et al., 1997b, Marshall et al., 1997a, Adcroft et al., 1997, Adcroft et al., 1999). The MITgcm is a widely portable, primitive equation, general circulation model. It is used for the study of the Atmosphere, Ocean or coupled systems. This chapter describes the development of a specific configuration of MITgcm as the tool for modelling a Southern Subpolar gyre system, referred to herein as, 'the gyre model'. This section then provides review of MITgcm's fundamental physics and some general model information. It is not meant to be comprehensive; the reader is referred to the MITgcm manual for greater detail (see: http://mitgcm.org/).

### 4.3.2 Fundamental Equations

Here the fundamental model equations are derived following consideration of the real ocean in a general form: a fluid continuum, subject to a range of forcing and perturbations. The adjustment of the ocean to anomalies occurs on a wide spectrum of time and length scales (Figure 5.2). The speed of sound for example is many orders of magnitude faster then the typical velocity associated with large-scale circulation. It is not useful or efficient to represent all of these scales of variability, therefore when describing the system numerically a number of simplifying assumptions can be made. These assumptions simplify the problem greatly, allowing efficient simulation of the system, they also characterise the model and may restrict model behaviour.

Before making assumptions, a general description of the three-dimensional flow from a Eulerion view is outlined informally. The material derivative of the velocity field yields the acceleration of the flow:

$$\frac{D\mathbf{u}}{Dt} = \frac{\partial \mathbf{u}}{\partial t} + (\mathbf{u}.\nabla)\mathbf{u} \tag{4.18}$$

Where $\mathbf{u}$ (m $s^{-1}$) is the velocity vector field ($\mathbf{u} = u\mathbf{i} + v\mathbf{j} + w\mathbf{k}$) and $\nabla$ is the gradient operator:

Following Newton's second law, multiplying (4.18) by the density of the fluid $\rho$, provides the fundamental momentum equation:

$$\frac{\partial \mathbf{u}}{\partial t} = -(\mathbf{u}.\nabla)\mathbf{u} + \frac{\mathbf{F}}{\rho} \tag{4.19}$$

Where $\mathbf{F}$ contains forcing and parameterisation terms, e.g. surface wind stress, the Coriolis 'force' and viscous dissipation. A conservation equation can similarly be derived from basic principles, here it is stated:

$$\frac{D\rho}{Dt} + \nabla \cdot (\rho \mathbf{u}) = 0, \tag{4.20}$$

Combining equations 4.19 and 4.20, with an equation of state, such as 4.21, then provides a set of governing equations, which form a fundamental basis for theoretical discussion.

$$\rho = \rho(T, S, P) \tag{4.21}$$

Where for seawater $\rho$ is a function of temperature ($^o$C), salinity and pressure (kg $m^{-1}$ $s^{-2}$).

Equations 4.19, 4.20 and 4.21 must then be adapted for the Earth's Ocean. To a first approximation ocean circulation is driven by a pressure field and dissipated by eddy viscosity and diffusivity terms. The $\mathbf{F}$ term in equation 4.19 can then be expanded such that:

$$\frac{\partial \mathbf{u}}{\partial t} + (\mathbf{u}.\nabla)\mathbf{u} = -\frac{1}{\rho}\nabla p + \frac{1}{\rho}( \mathbf{D}_v + \mathbf{D}_T + \mathbf{F} ) \tag{4.22}$$

Where $\mathbf{D}_v$, $\mathbf{D}_T$ are viscous and diffusive terms respectively, $p$ is pressure and

$$\nabla^2 = \frac{\partial^2}{\partial x^2} + \frac{\partial^2}{\partial y^2}. \tag{4.23}$$

Moreover the effect of rotation is accounted for by a Coriolis term:

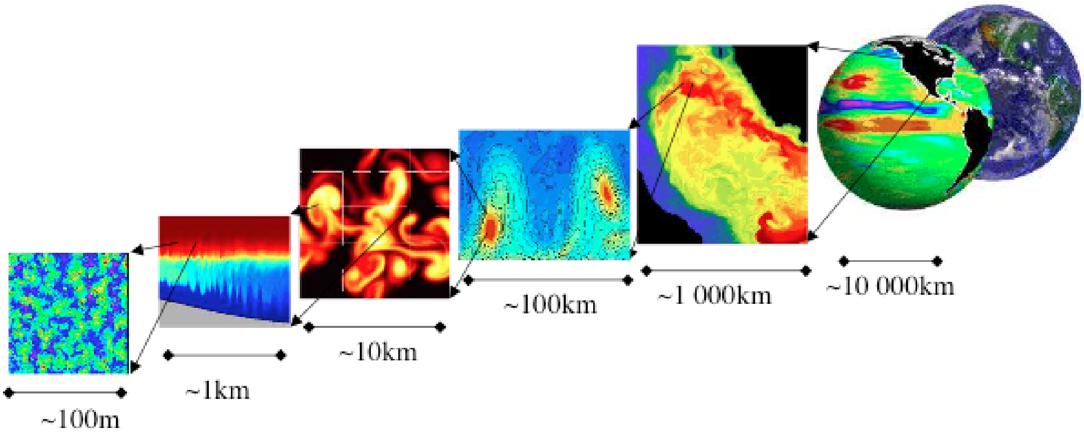

Figure 4.6: Taken from the MITgcm manual: A schematic illustration of the various scales of motion present in fluid flow and which are modelled using gcm models. The left side of the Figure displays sub mesoscale processes such as deep convection. The right side of the Figure displays large, climate scale processes, such as El-Nino (see MITgcm.org).

$$\frac{\partial \mathbf{u}}{\partial t} + (\mathbf{u}.\nabla)\mathbf{u} - 2\Omega \times \mathbf{u} = -\frac{1}{\rho}\nabla p + \frac{1}{\rho}(\ \mathbf{D}\ _v + \ \mathbf{D}\ _T + \ \mathbf{F}\ ) + g\hat{\mathbf{k}} \tag{4.24}$$

The centrifugal term is small (0.03 m $s^{-2}$) and absorbed into the gravitational acceleration g (m $s^{-2}$). $\Omega$ is the angular velocity of the Earth (rad $s^{-1}$), aligned northward along Earth's axis of rotation.

### 4.3.3 Fundamental Assumptions And Parameterisations

As previously noted, not all ocean variability is of interest to large-scale ocean models. The speed of sound for example, $c_s$, is of the order 1500 m $s^{-1}$, while typical zonal flow speeds, $\mathbf{u}$, are of order 1 m $s^{-1}$. Resolving all scales that lie between these two characteristic speeds would not only be impractical but also unnecessary. The researcher therefore must make simplifying approximations to e.g. equation 4.24.

First, it is noted that the aspect ratio of ocean currents is generally small, i.e. the magnitude of horizontal flow is much greater then vertical flow, therefore the vertical acceleration of the fluid is assumed small relative to gravitational acceleration and it can be neglected. This is mathematically represented as:

$$\mid \frac{\partial w}{\partial t} \mid + \mid (\mathbf{u}.\nabla)w \mid \ll - \mid \frac{1}{\rho}\frac{\partial p}{\partial z} \mid + \mid g\hat{\mathbf{k}} \mid, \tag{4.25}$$

so that:

$$\frac{\partial p}{\partial z} \simeq -\rho g, \tag{4.26}$$

This approximation is known as the hydrostatic approximation.

Second, the traditional approximation is used. Here it is assumed that Coriolis terms involved in vertical velocity and smaller metric terms are negligible. Further, as previously noted, the centrifugal forces are absorbed into the gravitational term g. Following these simplifications, the momentum equation may be split into horizontal and vertical components:

$$\frac{\partial \mathbf{v}}{\partial t} + (\mathbf{v}.\nabla)\mathbf{v} - 2\Omega sin(\theta)\mathbf{k} \times \mathbf{v} = -\frac{1}{\rho}\nabla_h p + \frac{1}{\rho}(\ \mathbf{D}\ _v +\ \mathbf{D}\ _T +\ \mathbf{F}\ ), \tag{4.27}$$

$$\frac{\partial p}{\partial z} = -\rho g, \tag{4.28}$$

Where $\mathbf{v} = (u, v)$ is the horizontal velocity. Furthermore since density variations in the ocean are small relative to the mean density, the density term $\rho$ is decomposed such that:

$$\rho = \rho_0 + \delta\rho(x, y, z, t), \tag{4.29}$$

where, $|\delta\rho| \ll \rho_0$ Therefore it is assumed $\delta\rho$ is negligible everywhere except where it is multiplied by g, this is known as the Bousinesq approximation. Applying this to the horizontal momentum equation results:

$$\frac{\partial \mathbf{v}}{\partial t} + (\mathbf{v}.\nabla)\mathbf{v} - 2\Omega sin(\theta)\mathbf{k} \times \mathbf{v} = -\frac{1}{{}_0}\nabla_h p + \frac{1}{\rho}(\ \mathbf{D}\ _v +\ \mathbf{D}\ _T +\ \mathbf{F}\ ), \tag{4.30}$$

and for the vertical equation:

$$\frac{\partial \delta\rho}{\partial z}\rho_0 = -g\frac{\delta\rho}{\rho_0} = b, \tag{4.31}$$

This new set then implies vertical accelerations must be small in comparison to $b$, not -$\rho$g as in equation (4.28). Furthermore, using the Bousinesq approximation, the continuity equation (4.20) becomes:

$$\nabla \cdot \mathbf{u} = 0, \tag{4.32}$$

As a result sound waves, which depend on the compressibility of the fluid, are eliminated from the fundamental equations.

The following work focuses on the impact of wind anomalies on a southern polar gyre circulation, for simplicity we ignore salinity and assume a sufficiently realistic circulation can be simulated by an equation of state dependent wholly on temperature. The equation of state (4.21) is altered accordingly $\theta$ ($^o$ C):

$$\rho = \rho_c(1 - \alpha\theta), \tag{4.33}$$

Equations 4.30–4.33 then form a set of governing equations known as the Bousinesq, hydrostatic, primitive equations. These are the set used by the MITgcm model in the following research (Marshall et al., 1997a).

The viscosity and diffusion then can be further decomposed and discussed. For example a common form of the viscous dissipation $\mathbf{D}_v$ is:

$$\mathbf{D}_V = A_h \nabla_h^2 \mathbf{v} + A_v \frac{\partial^2 \mathbf{v}}{\partial z^2} + A_4 \nabla_h^4 \mathbf{v} \tag{4.34}$$

where $A_h \nabla_h^2 \mathbf{v}$ is the harmonic horizontal viscosity, $A_v \frac{\partial^2 v}{\partial z^2}$ is the harmonic vertical viscosity and $A_4 \nabla_h^4 \mathbf{v}$ is a horizontal biharmonic viscosity. Many increasingly complex viscosity parameterisations are available for MITgcm. For simplicity the gyre model uses harmonic terms for horizontal and vertical components. Spherical polar co-ordinates are used by some model configurations, the horizontal harmonic viscosity is then chosen to scale with the area of model grid boxes but the vertical value is kept constant. When discussed, an average value of the horizontal harmonic viscosity is given.

Diffusive terms $\mathbf{D}_T$ are parameterised here by MITgcm's GM-Redi package, also known as the Gent McWilliams (Gent and Mcwilliams, 1990) and Redi (Redi, 1982) parameterisation. This scheme was developed to simulate the mixing effects of subgrid scale processes; in particular the effects of geostrophic eddies, whose scale $\backsim$ 10 km is considerably below the smallest grid scale of 60 km. The package is composed of two components, the Redi Scheme (Redi, 1982) that acts to mix tracers along isopycnals and the GM scheme, which utilises a bolus velocity to advect thickness anomalies and act to flatten isopycnals. As previously mentioned, the gyre model's equation of state depends only on temperature and therefore the Redi scheme has no effect on the dynamics. The GM parameterisation (Gent and Mcwilliams, 1990) then aims to represent the advective effect of geostrophic eddies by imposing a bolus velocity, which is a function of the local slope in isopycnals. It can be considered as an advective flux term, included in the tracer equation as:

$$(\mathbf{u} \cdot \nabla) T + \nabla \cdot (\mathbf{u}^* T) = 0 \tag{4.35}$$

where $\mathbf{u}^*$ is ultimately given by:

$$\mathbf{u}^* = \begin{bmatrix} u^* \\ v^* \\ w^* \end{bmatrix} = \begin{bmatrix} -\frac{\partial}{\partial z}(K_{GM} S_x) \\ -\frac{\partial}{\partial z}(K_{GM} S_y) \\ \frac{\partial}{\partial x}(K_{GM} S_x) + \frac{\partial}{\partial y}(K_{GM} S_y) \end{bmatrix} \tag{4.36}$$

$K_{GM}$ is the GM background diffusivity, set here to 1000 $\mathrm{m}^2\ \mathrm{s}^{-1}$ and $S_x$ , $S_y$ are the isopycnal slopes in the $x$ and $y$ directions respectively.

Additional complexities arise from the multiple advection schemes available for use with MITgcm, here the 3rd order DST Flux limiter scheme (namelist no. 33) was chosen. This is for its common use, good performance, low numerical diffusion and relatively small, 5 point numerical 'foot-print'.

### 4.3.4 Model Discretisation

A finite volume method is used to spatially discretise the model. This method is similar to a grid-point based discretisation but it allows topography at the boundaries to intersect the regular grid and therefore provides a more accurate representation of these areas (Adcroft et al., 1997). The model domain is first split into tiles, within which there is a regular grid that facilitates simple parallelisation. Variables are staggered in the horizontal and vertical plane using an Arakawa C-grid (Arakawa and Lamb, 1977). Velocity components ($u$, $v$, $w$) are located at the centre of cell faces. Tracers, such as potential temperature ($\theta$) are averaged over the tracer cell volume and are located in the centre of model cells (see Figures 4.7 and 4.5).

## 4.4 Gyre Model Design

As discussed at the begining of this chapter, the Southern Ocean and particularly the southern subpolar gyres, are currently subject to interesting climate trends. In particular the subpolar gyres are subject to an increasing trend in zonal wind stress. The response of the gyres to this increase in wind stress is likely to be complex and it may highlight a dynamical link between surface wind anomalies, and anomalies in abyssal properities (Meredith et al. 2008).

A highly simplified regional model that simulates the response of an idealised southern subpolar gyre to changes in wind forcing would be an ideal tool in furthering our understanding of the adjustment of the southern subpolar gyres. Following sections 4.2-4.3, a number of fundamental requirements for such a model design can be identified.

- The model must be simplified and adaptable.
- It must be computationally agile.
- It must accurately simulate an upper wind driven gyre circulation (Sverdrup, 1947)
- It must accurately simulate a density driven abyssal flow (Stommel and Arons, 1960).
- The model must have a realistic overturning circulation.

Following these core requirements, the 'baroclinic gyre' MITgcm tutorial is chosen as the starting-point for model development. The tutorial uses a regional model, with spherical polar coordinates. It has 4 depth levels and is centred in the tropical Atlantic. The tutorial's configuration is similar to the problems described analytically by Stommel (1948) and numerically by Holland and Lin (1975).

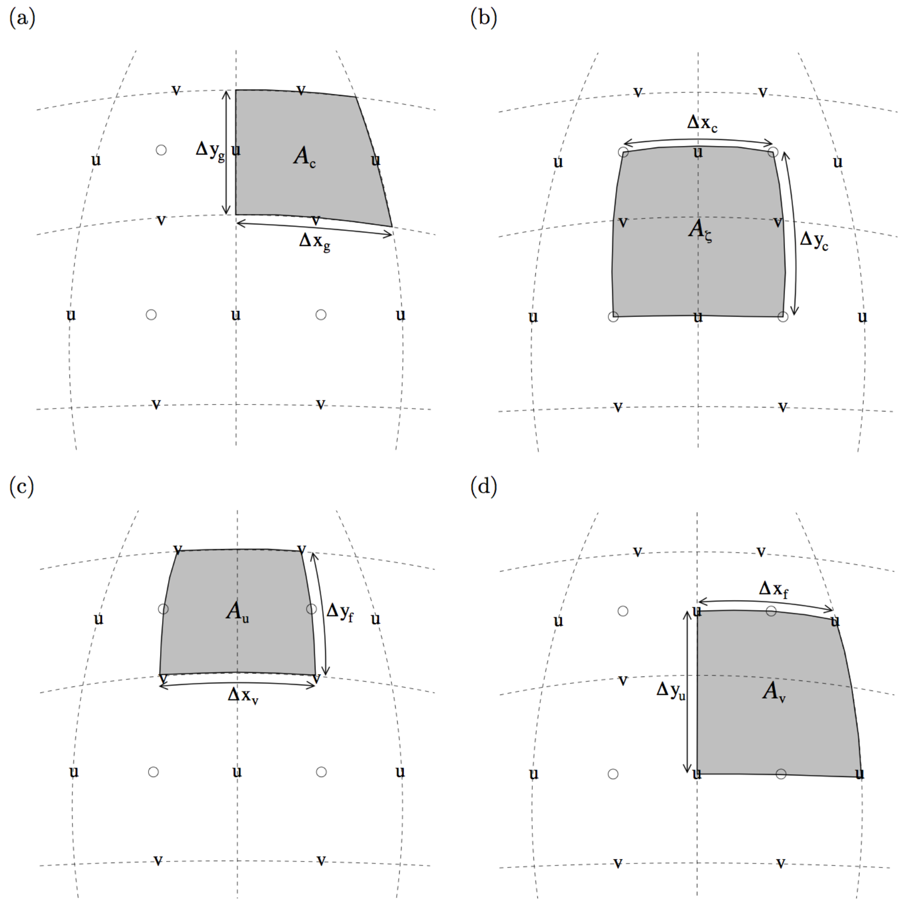

Figure 4.7: Taken from the MITgcm manual (see MITgcm.org): Schematic showing the MITgcm horizontal grid, with the dashed lines indicating the tracer cell boundaries. (a) The area of a tracer cell, $A$, is bordered by the southern edge, $\Delta x$ and the western edge, $\Delta y$, with the subscript $g$ indicating that the lengths are along the defining grid boundaries and the subscript $c$ is accosted with the tracer cell centre; (b) the area of the vorticity cell, $A_\zeta$, is bordered by the southern edge, $\Delta x_c$ and the western edge, $\Delta y_c$, where the subscript $c$ indicates that the lengths are measured between the tracer cell centres and the subscript $\zeta$ indicates the vorticity point; (c) The area of the zonal velocity or $u$ cell, $A_u$ is defined by the southern edge $\Delta x_v$ and the eastern edge $\Delta y_f$ with the subscript $v$ indicating that the length is measured between the $v$-points, the subscript $f$ indicates that the length is measured between the tracer cell faces. The subscript $y$ denotes association with $u$–points; (d) the area of a meridional velocity or $v$ cell, $A_v$, is bordered by the northern edge $\Delta_f$ and the western edge $\Delta y_u$ with the subscript $u$ denoting the length that is measured between the $u$–points, the subscript $f$ indicating that the length is measured between the tracer cell faces and the subscript $v$ associates with the $v$ points. For further details, see Adcroft et al. (1997).

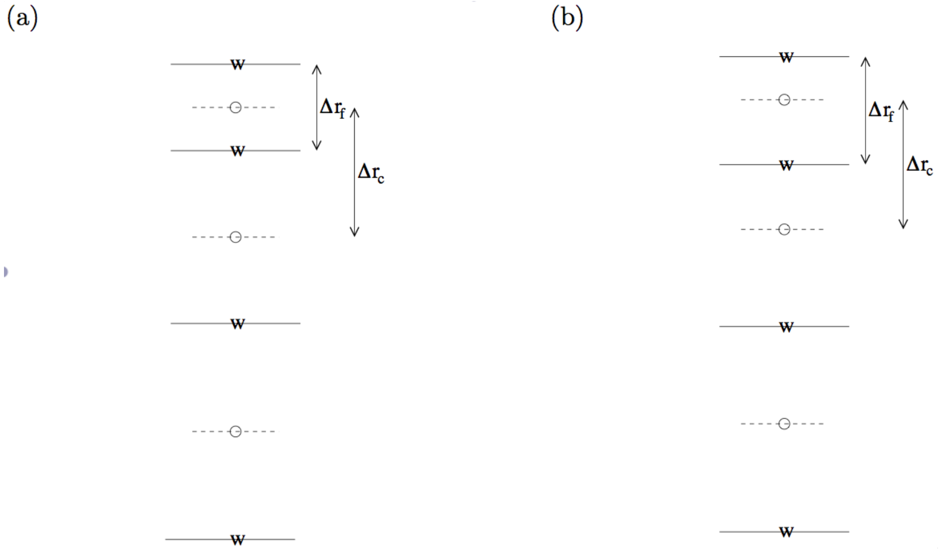

Figure 4.8: Taken from the MITgcm manual (see MITgcm.org): Schematic showing the MITgcm vertical grid. subscripts $c$ and $f$ denote cell faces and centres, $\Delta r_f$ is the difference in $z$ between the tracer cell faces, while $\Delta r_c$ is the difference in $z$ between tracer cell centres. (a) shows the cell centred approach (b) shows the interface centred approach.

First, the tutorial's domain is shifted towards southern polar latitudes and is re-shaped into the approximate dimensions of the Weddell gyre and the South Atlantic (75 to 35 $^o$S and 0 to 60 $^o$E). The number of depth levels is increased from 4 to 75, mimicking the depth spacing of the 1$^o$ NEMO model. This spacing provides relatively inexpensive, good resolution for surface and abyssal processes, while being easily comparable to the most common GCM climate models. The maximum depth of the domain is chosen as the average depth of the abyssal Weddell Sea, 4 km deep. The side walls of the domain are set to ether be flat, or sloping depending on the model run.

The horizontal resolution of the model is set to 1$^o$ (around $70-120$ km). This resolution is chosen because it is sufficient to resolve the large-scale circulation of the region, without facilitating eddies. Eddy permitting resolutions are avoided in order to maintain simplicity and low computational cost. However, as discussed by Marshall (2003) and Killworth (1985), low-resolution models produce unrealistic boundary waves. This issue can be considered as a 'trade-off'.

The model is forced by a zonal wind stress that varies sinusoidally with latitude and that is constant in time (Figure 4.9). The maximum amplitude of this wind stress is guided by analysis of ERA-Interim reanalysis data discussed in section 1.3.1 and chosen to range between 0.1 and 0.3 (N m$^{-2}$) depending on model configuration.

The hydrostatic primitive equations described in the previous section (as well as Marshall et al., 1997a), are employed here, with an implicit free surface. The horizontal Laplacian operator provides viscous dissipation and a diffusive sub-grid scale closure for

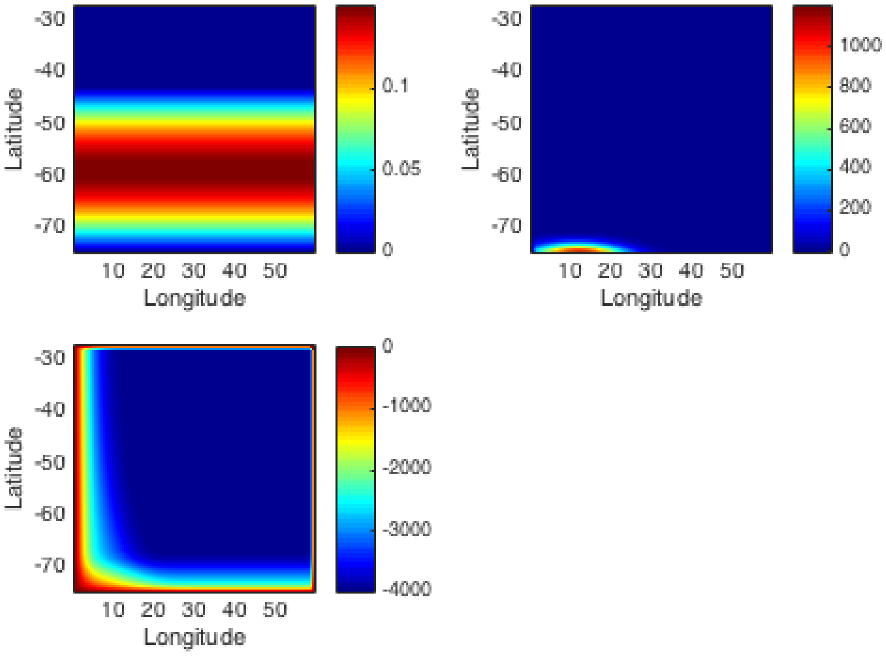

Figure 4.9: Constant forcing fields of the polar gyre model. a: Surface buoyancy forcing, heat flux (W $m^{-2}$). b: Topography (m). c: Surface wind stress forcing (N $m^{-2}$).

the temperature equation. Following Munk (1950), a value of harmonic viscosity ranging from $1\times10^{-5}$ to $5\times10^{-4}$ is carefully chosen to ensure that the Munk boundary length, which refers to the thickness of the western boundary current, is resolved. This ensures a realistic western boundary layer and a stable model.

A confined region of enhanced (10 times stronger) vertical mixing is applied to the north of the domain, shown in Figure 4.10. This region of increased mixing is designed to represent the integrated vertical mixing of the global ocean, allowing dense waters that have formed at the southern edge of the gyre to return to the surface. The region occupied by this layer is shown in Figure (4.10).

Preliminary experiments utilise a re-entrant channel to simulate an eastward flowing ACC at the northern edge of the gyre. However, this addition is found make the model's behaviour complicated and difficult to analyse. In order to maintain simplicity, the re-entrant channel is removed. The gyre model then constitutes a double gyre model. A cyclonic gyre is formed in the south, simulating an Antarctic Subpolar gyre. An additional anticyclonic gyre is formed in the north. The northern gyre is primarily used to ensure realistic conditions for the southern gyre.

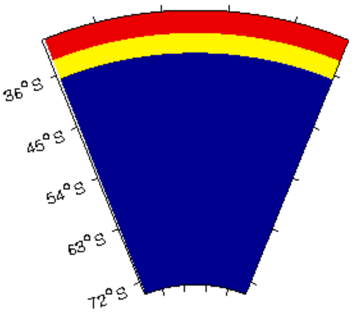

Figure 4.10: Schematic of the gyre model, showing regions of enhanced vertical diffusivity (yellow) and temperature and velocity restoring (red).

## 4.5 Model Spin-Up

Before conducting experiments, the model is spun-up to a steady-state. All model runs are initially run for at least 2000 years, with a staggered time step, i.e. a momentum time-step of 1200 s and a tracer time-step of 12000 s. Where using different time-steps reduces numerical expense whilst allowing the model to maintain stability (Higdon, 2002). As shown in Figure (4.17), during this spin-up period, the velocity field reaches an equilibrium within 500 years, whereas the density or temperature field reaches an equilibrium within 1500 years.

Following the initial spin-up, runs are re-initialised with equal time-steps of 1200 s for both momentum and tracer equations, then integrated forward for another 100 years. In addition, before conducting experiments, a damping or restoring (sponge) layer is applied to the northern boundary of the domain, to prevent boundary waves (that emanate from the gyres) from propagating cyclonically around the basin and creating unrealistic dynamics. This layer restores temperature and velocity profiles to time-average values, every 30 minutes or less (Figure 4.10). Adjustment experiments are then run.

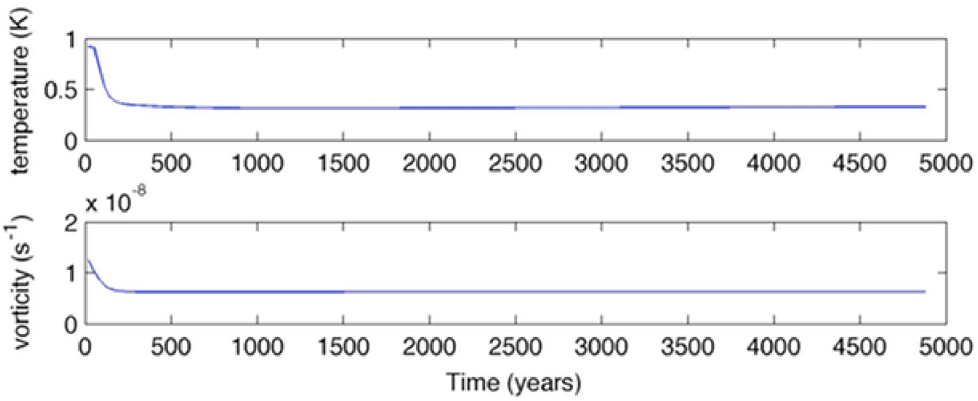

Figure 4.11: Plots showing the spin up of the gyre model to a steady state. From top to bottom: model-mean sea surface height, model-mean temperature and model-mean vorticity.

## 4.6 Model Validity: Comparison To Analytical Theory

Following model spin-up, the simulated wind driven circulation can be verified by comparison to analytical models. For this purpose equations (4.30–4.33) are simplified and solved for the specific case of a steady-state wind driven gyre. Following (Sverdrup, 1947), we assume that the ocean is of uniform density, that the circulation is barotropic and that the domain has a uniform depth with flat sidewalls. The dissipation of the flow is assumed to occur through linear friction rather then viscosity and the Coriolis term f can be approximated as a $\beta$-plane:

$$f = f_0 + \frac{\partial f}{\partial y} y = f_0 + \beta y, \tag{4.37}$$

Following these assumptions, equations 15-18 become:

$$\frac{\partial u}{\partial t} + (\mathbf{u}.\nabla)u - fv + \frac{1}{\rho_0}\frac{\partial p}{\partial x} = \frac{\tau_x}{\rho_0 H} - ru \tag{4.38}$$

$$\frac{\partial v}{\partial t} + (\mathbf{u}.\nabla)v - fu + \frac{1}{\rho_0}\frac{\partial p}{\partial y} = \frac{\tau_y}{\rho_0 H} - rv \tag{4.39}$$

$$\frac{\partial u}{\partial x} + \frac{\partial v}{\partial y} = 0 \tag{4.40}$$

Here the flow is forced from the surface by the wind-stress term $\tau$ and $r$ is a linear drag coefficient. Note that there is no vertical momentum equation as the fluid is homogenous. The pressure term is removed by cross differentiating the lateral components of the momentum equation. In addition by assuming that the ocean floor is flat and that the ocean surface is also flat, then the system becomes non-divergent and it is possible to combine the u and v variables into a stream function:

$$u = -\frac{\partial \psi}{\partial y} \tag{4.41}$$

$$v = \frac{\partial \psi}{\partial x} \tag{4.42}$$

It is possible then to formulate the vorticity equation in terms of $\psi$:

$$\frac{\partial}{\partial t}\nabla^2\psi + \left(\frac{\partial \psi}{\partial x}\frac{\partial}{\partial y}\nabla^2\psi - \frac{\partial \psi}{\partial y}\frac{\partial}{\partial x}\nabla^2\psi\right) + \beta\frac{\partial \psi}{\partial x} = \frac{1}{\rho_0 H}\left(\frac{\partial \tau_y}{\partial x} - \frac{\partial \tau_x}{\partial y}\right) - r\nabla^2\psi \tag{4.43}$$

Where $r$ is now a viscosity or drag term. As outlined by Sverdrup (1947), the inertial terms in this system compared to the Coriolis term are small (low Rossby number) and therefore can be neglected. Further by seeking a solution for the 'steady-state' of the system the $\frac{\partial}{\partial t}$ is neglected. The bottom friction is also neglected when solutions for the interior alone are considered. It is assumed that $|r| \ll |\beta v|$ and therefore the vorticity equation becomes a balance between the meridional mass transport and surface wind forcing:

$$\beta\frac{\partial\varphi}{\partial x} = \frac{1}{\rho_0 H}\left(\frac{\partial\tau_y}{\partial x} - \frac{\partial\tau_x}{\partial y}\right) \tag{4.44}$$

This relation is known as Sverdrup balance, it is the most fundamental model of gyre circulation and will be used herein to diagnose the more complex circulations simulated by the MITgcm model. Sverdrup balance is integrated from the east to the west of an idealised domain providing the stream function equation:

$$\varphi = \frac{1}{\beta\rho_0 H}\frac{\partial\tau_x}{\partial y}(x_e - x). \tag{4.45}$$

This is applied to a comparable domain and surface wind forcing, to provide an estimate of the surface circulation expected for a given wind forcing (Figure 4.18). Here xe denotes the distance from the eastern boundary.

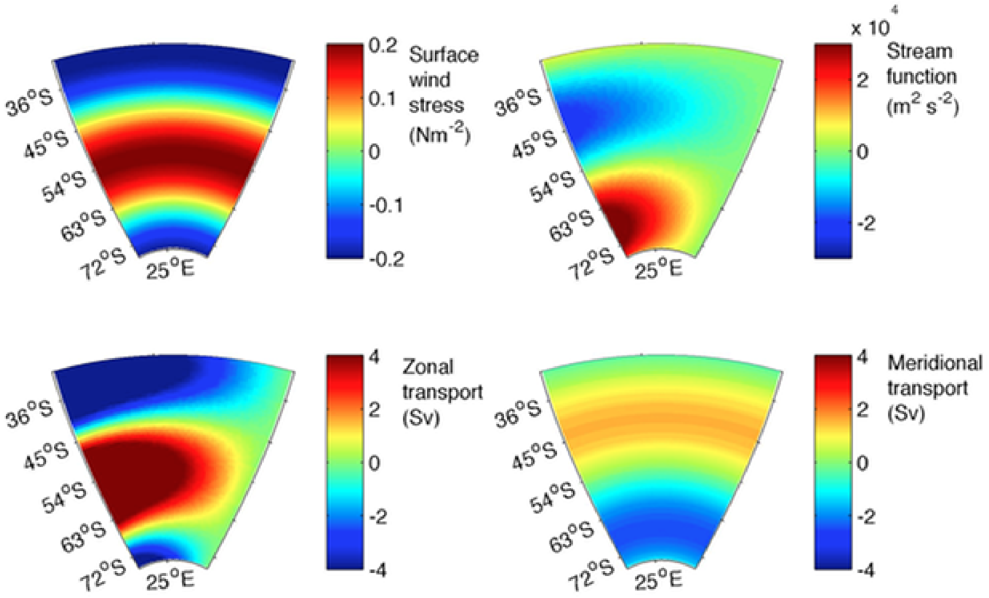

Figure 4.12: Wind driven flow field estimated by the Sverdrup (1947) model. Top left: surface wind forcing, top right: steady-state horizontal stream function, bottom left: zonal transport, bottom right: meridional transport .

The Sverdrup model is then compared to MITgcm runs where buoyancy forcing is removed and the model is forced only by the zonal wind forcing, shown in Figure 4.19. It is clear that the two different models of wind driven circulation agree well in magnitude and in circulation. Both have cyclonic gyres to the south and anticyclonic gyres in the north. As the Sverdrup model does not contain any drag terms, the magnitude of the circulation is larger. In addition, as it is only representative of the ocean interior, it does not simulate a western boundary current. Further, there is longitudinal asymmetry in the MITgcm flow field, with stronger circulation on the western boundary that appears to span a greater latitudinal distance. This asymmetry is a result of the western boundary current and of the sloping sidewalls in the west, which are included in the MITgcm model but absent from Sverdrup's-balance.

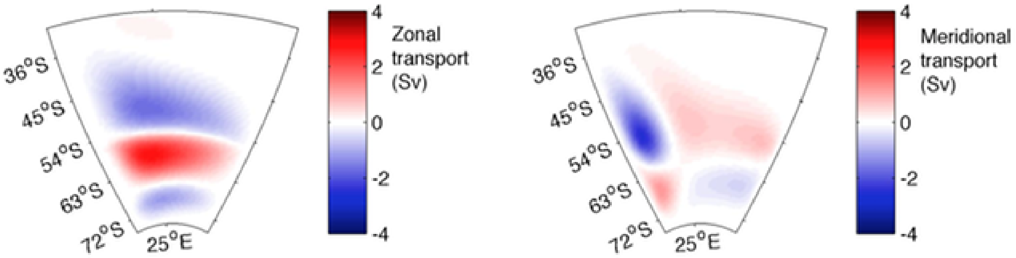

Figure 4.13: The wind driven circulation simulated by the gyre model. Left: zonal transport, right: meridional transport.

## 4.7 Subconfigurations

To assist in analysis of the complex behaviour of the model, the gyre model is split into four sub configurations, each with increasing complexity. Model parameters in each sub configuration are tuned to first ensure that a given run expresses a clearly defined wind-driven circulation and deep abyssal circulation. Specific flows within the system are then checked against observations. For example, the southern gyre has a typical circulation of 20 Sv, both in model runs and observations. Further, model density profiles are tuned to give a realistic stratification compared to observations, shown in Figure 4.14.

Preliminary work used more complex configurations then those discussed here. These configurations included features such as a re-entrant channel and more realistic topography. However, the adjustment response of the configurations described here (CPD to SSBSB) is found to be sufficiently complicated, that the analysis of these simple cases provides sufficient results.

### 4.7.1 CPD

The simplest configuration employed, is referred to as the CPD version (Cartesian coordinate, prescribed density; Figure 4.15). It is a Cartesian co-ordinate configuration with flat sidewalls and the Coriolis term is simplified using the beta-plane assumption, namely:

$$f = f_0 + \frac{\partial f}{\partial y} = f_0 + \beta y. \tag{4.46}$$

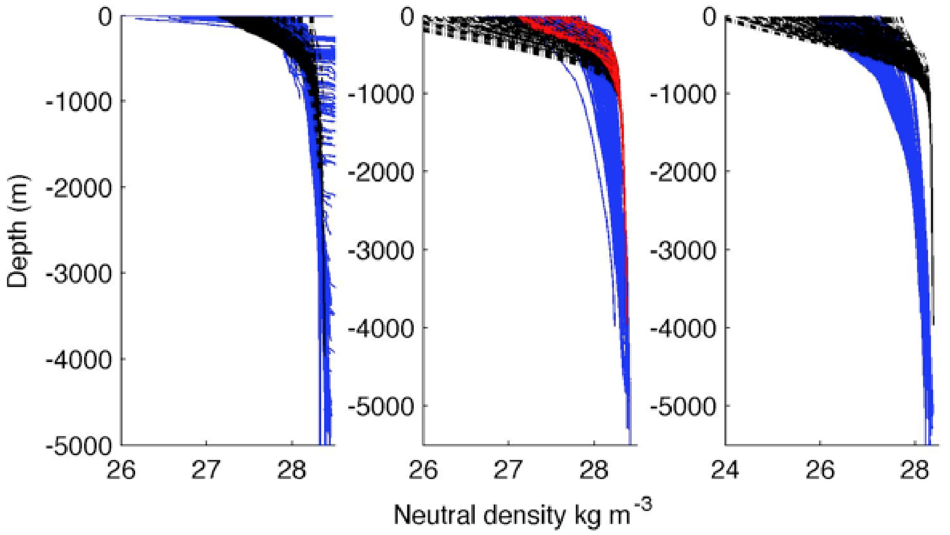

Figure 4.14: Density profiles from the CSB version of the gyre model (black), compared to Weddell Gyre in-situ data (blue). In-situ data are recorded in the austral summer, taken from the Southern Ocean Data Atlas (SODA; Schlitzer, 2000). Subplots show profiles for specific regions in the gyre model, all are compared to the same in situ profiles. Left: the southern cyclonic gyre, centre: the confluence region between gyres, right: the northern gyre. The red profiles in the centre plot highlight data from the southern side of the confluence region

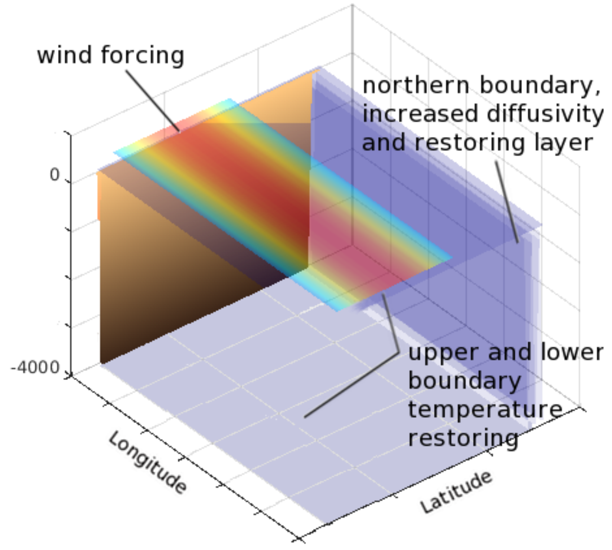

Figure 4.15: Schematic showing the main characteristics of the CPD configuration of the gyre model. The brown western boundary wall represents the flat sidewalls. The surface wind forcing is shown as a Gaussian band parallel to the zonal direction. Surface and bottom temperature restoring levels are shaded in blue. The northern restoring layer that dampens boundary waves is also shaded in blue.

The CPD configuration has no surface buoyancy forcing and therefore no deep water formation. The model is forced to restore to a constant temperature at the surface and the bottom, this induces a fixed stratification without having a region of dense water formation.

By avoiding surface buoyancy forcing, the CPD configuration is very stable, therefore low values of viscosity parameter can be used. Low viscosity parameter values facilitate faster and more realistic boundary waves (Marshall and Johnson, 2013). The CPD subconfiguration is therefore useful for the analysis of boundary waves.

The shapes of the wind driven gyres in the CPD configuration are the simplest of any configuration (Figure 4.16). It therefore provides the simplest representation of the adjustment of the wind driven circulation.

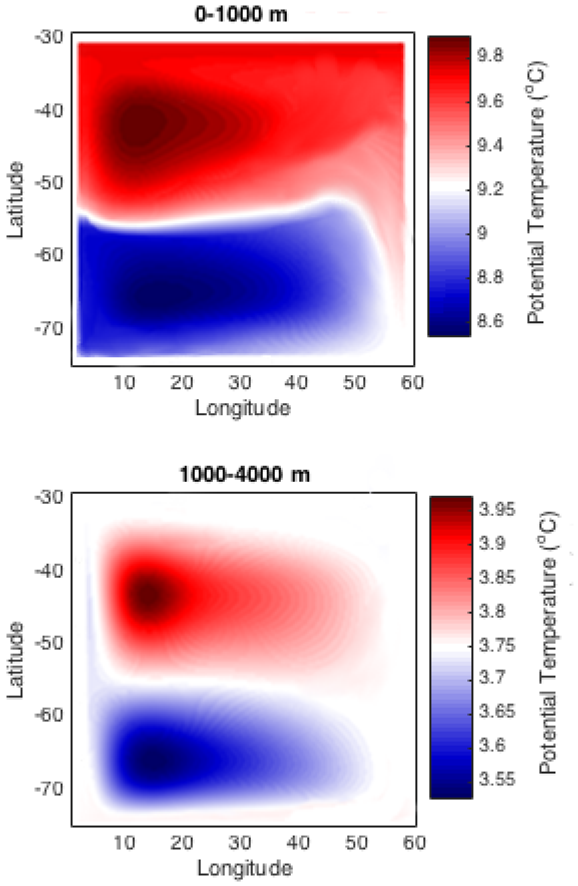

Figure 4.16: Potential Temperature ($^o$C), in the CPD version of the gyre model. Highlighting the structure of the gyre. The upper panel shows the depth-integrated value for the upper 1000 m, the lower panel shows the same value for 1000–4000 m.

### 4.7.2 CSB

The second configuration is referred to as the CSB configuration (Cartesian co-ordinate, surface buoyancy forced model; Figure 4.11). It is also a Cartesian, beta-plane model, however, unlike CPD, it has surface buoyancy forcing.

The surface buoyancy forcing is designed to drive a realistic meridional overturning circulation, shown in e.g. Figure (5.2). Here, a strong, gaussian, surface cooling is applied in the south-western corner of the southern subpolar gyre. Then a crude represenation of the Antarctic Peninsula is created by applying no buoyancy forcing to the southern boundary of the model. The remainder of the surface of the model is slightly heated, to balance the cooling. The total integrated surface buoyancy forcing is set to zero to ensure the model's mean temperature is constant.

Observations suggests realistic values of buoyancy loss over the southern ocean range between $-50$ and $-150$ W m$^{-2}$ e.g. Marshall and Speer (2012). The integrated value of the gaussian bouyancy forcing is initaly chosen to be around 300 W m$^{-2}$. This elevated magnitude is chosen to account for the small size of the region of bouyancy loss. This value is then adjusted over multiple experiments as the model is optimised for a horizontal flow field with realistic magnitude and distribution.

The additional feature of the buoyancy forcing distorts the shape of the southern gyre, adding additional cyclonic forcing in the south-west corner (Figure 4.18).

The CSB model is therefore important because it is the simplest model with buoyancy forcing. It has the simplest flow distribution, for a configuration with a buoyancy driven abyssal circulation.

### 4.7.3 SSB

The third model is referred to as the SSB configuration (The spherical-polar co-ordinate, surface buoyancy forced model; Figure 4.19), it utilises a full Coriolis force and has a spherical polar co-ordinate system. It also has flat sidewalls and the same surface buoyancy forcing as described for the CSB configuration. As discussed in the following chapter, this subconfiguration displays further distorted gyres (Figure 4.20).

The adjustment response of the SSB configuration is more complex then the previous configurations because of the introduction of spherical polar coordinates, and a full Coriolis term. The sidewalls of this model are kept flat so that new model behaviour can be viewed as a result of the new coordinate system alone, and not a response to a change in topography.

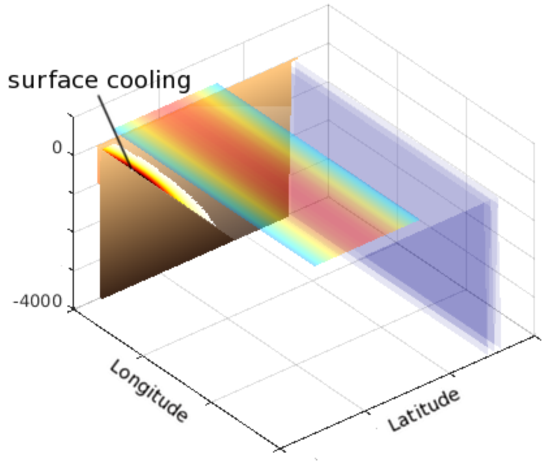

Figure 4.17: Schematic showing the main characteristics of the CSB configuration of the gyre model. The brown western boundary wall represents the flat sidewalls. The surface wind forcing is shown as a red and blue Gaussian band parallel to the zonal direction. Surface buoyancy forcing is shown as a yellow and red Gaussian area on the southern boundary. The northern restoring layer that dampens boundary waves is shaded in blue.

### 4.7.4 SSBS

The final model, referred to as the SSBS (spherical-polar co-ordinate, surface buoyancy forced, with sloping boundaries; Figure 4.21) configuration, is the most complex. It is the same as the SSB configuration, except its southern and western sidewalls are sloped, simulating the topography of the Weddell gyre and South America. This topography then further distorts the structure of flow on the western boundary so as to conserve $f/h$ contours (Figure 4.22).

The inclusion of sidewalls allows for increased dissipation on the western boundary through the interaction of the baroclinicity of the flow with the sloping bottom (Jackson et al., 2006). It may also facilitate a different class of boundary wave, known as Topographic Rossby Waves, which utilise the change in vorticity across the sloping sidewalls in their restoring force.

## 4.8 Summary

This chapter then describes the development of a configuration of the MITgcm ocean model, referred to here as the gyre model. The gyre model is a simplified regional model, designed to explore the dynamics of a southern subpolar gyre. It is a $1^o$ resolution, Boussinesq, primitive equation model, forced from the surface by constant wind and buoyancy forcing. It has a temperature and velocity, restoring layer at its northern edge

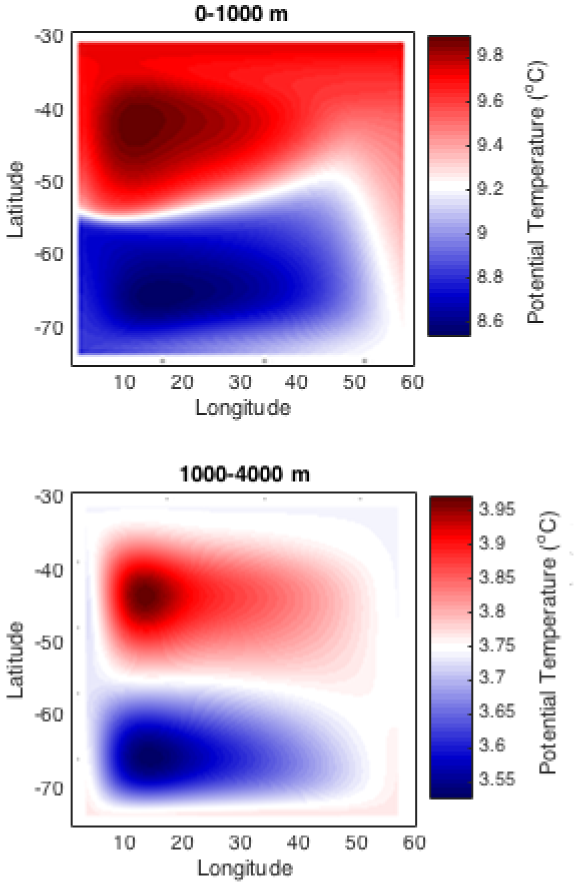

Figure 4.18: Potential Temperature ($^{o}$C), in the CSB version of the gyre model. Highlighting the structure of the gyre. The upper panel shows the depth-integrated value for the upper 1000 m, the lower panel shows the same value for 1000–4000 m.

that dampens boundary waves and it has enhanced vertical diffusivity at its northern edge to support a strong overturning circulation.

The gyre model has four sub-configurations of ranging complexity. The CPD configuration is the most simplified, it is a Cartesian $\beta$–plane model, characterised by its lack of surface buoyancy forcing and its prescribed stratification. The stratification of the CPD is prescribed by restoring the top and bottom levels to a constant temperature. The CSB configuration is the same as the CPD, except it has surface buoyancy forcing instead of a prescribed stratification. The SSB configuration uses a full Coriolis term and spherical polar co-ordinates. It is otherwise the same as the CPD model; it has flat sidewalls and surface buoyancy forcing. Finally the SSBS configuration is the same as the SSB configuration, except that its sidewalls are sloped, representing the sloping topography of the Weddell gyre and South America. All model subconfigurations are allowed to ‘spin–up’ to a steady-state over, around 2000 years.

In the following chapter, the response of these subconfigurations to a 20% step–increase

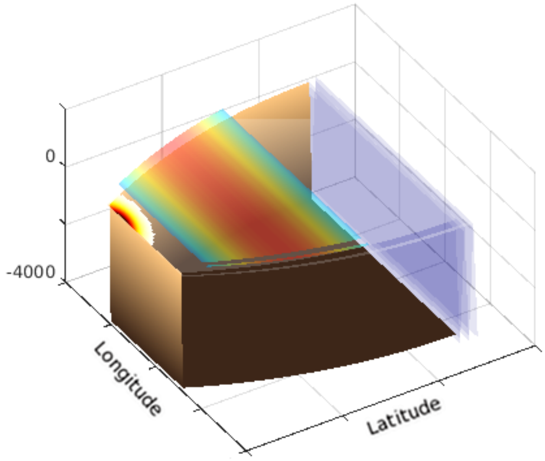

Figure 4.19: Schematic showing the main characteristics of the SSB configuration of the gyre model. The brown southern and western boundary walls represent flat sidewalls. The surface wind forcing is shown as a red and blue Gaussian band parallel to the zonal direction. Surface buoyancy forcing is shown as a yellow and red Gaussian area on the southern boundary. The northern restoring layer that dampens boundary waves is shaded in blue

in surface wind forcing will be analysed. The results from this experiment are then used to further the discussion on the response of the Subpolar Seas to recent decades increase in wind forcing. They are also used in relation to the Meredith 2008 hypothesis.

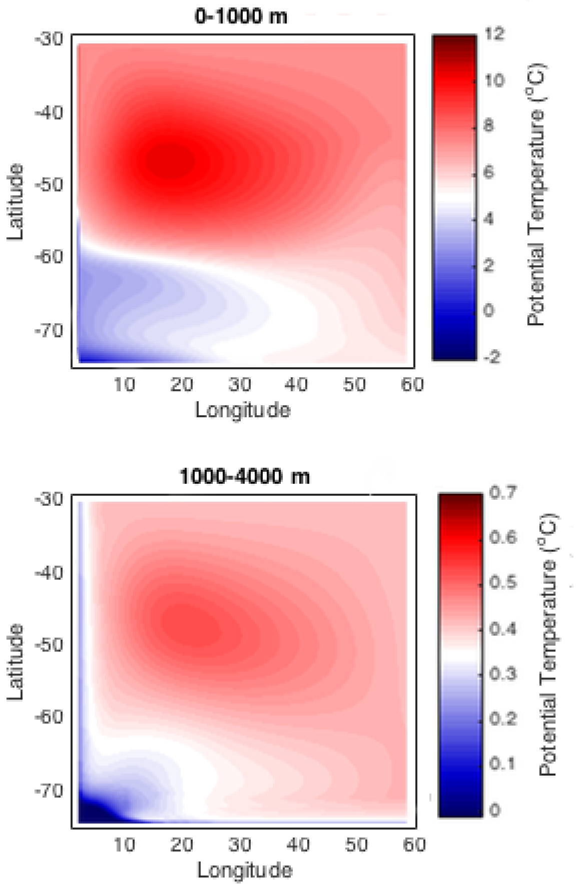

Figure 4.20: Potential Temperature ($^o$C), in the SSB version of the gyre model. Highlighting the structure of the gyre. The upper panel shows the depth-integrated value for the upper 1000 m, the lower panel shows the same value for 1000–4000 m.

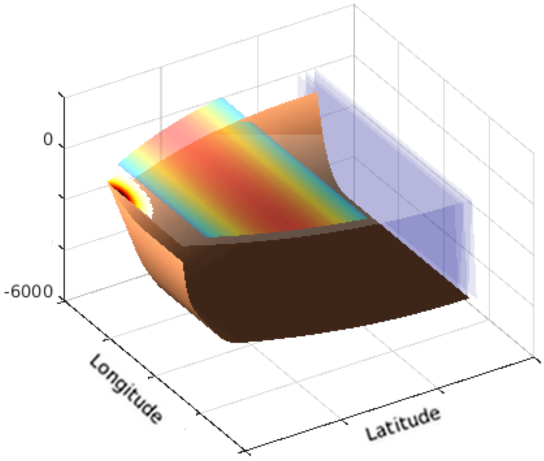

Figure 4.21: Schematic showing the main characteristics of the SSBSB configuration of the gyre model. Here the brown sidewalls are clearly shown to slope upwards towards the model boundaries on the southern and western edges. The surface wind forcing is shown as a red and blue Gaussian band parallel to the zonal direction. Surface buoyancy forcing is shown as a yellow and red Gaussian area on the southern boundary. The northern restoring layer that dampens boundary waves is shaded in blue

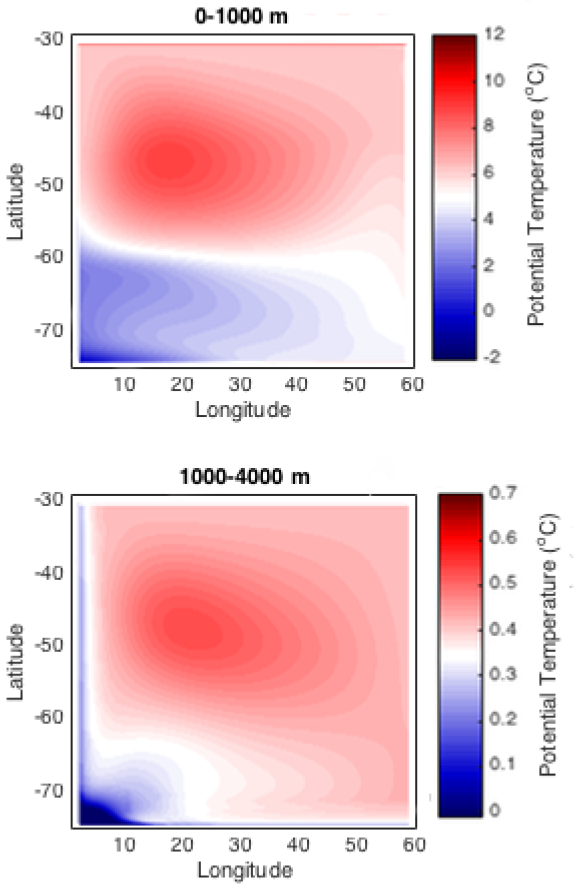

Figure 4.22: Potential Temperature ($^o$C), in the SSBS version of the gyre model. Highlighting the structure of the gyre. The upper panel shows the depth-integrated value for the upper 1000 m, the lower panel shows the same value for 1000–4000 m.

# Chapter 5

# An Investigation Into The Wind-Adjustment Of A Southern Subpolar Gyre: Model Results

## 5.1 Overview

This chapter describes the main results from the gyre model and follows from the previous chapter, which describes the gyre model's set-up and preliminary results. Here, the model is tested for its response to a step-increase in surface wind stress.

The model's adjustment (much like the ocean's adjustment) occurs on a range of time-scales. These time-scales are set by the mechanisms available for a given anomaly to be communicated, as well as the shape and size of the model domain. These pathways can be characterised by the dynamical modes of the system, i.e. the vertical distributions of properties that constitute the most variance. These modes propagate horizontally as various forms of waves, communicating and distributing anomalies across the domain.

All of the gyre model subconfigurations express a group of similar adjustment processes. These are grouped here into fast barotropic processes, and slower baroclinic processes. Interesting differences between subconfigurations, and analytical theory, occur because of the different assumptions, parametersations and domains used in modelling.

Section 5.3 discusses adjustment processes that are common to all gyre model sub-configurations. Section 5.4 discusses the differences between sub-configurations. The chapter is summarised in section 5.5.

## 5.2 Experiment Design

In order to investigate the response of a southern subpolar gyre, to the recent decades trend in Southern Ocean wind forcing, the gyre model is tested for its response to an increase in surface wind stress. The forcing of these wind peturbation experiments is sumerised by Figure 5.1.

As discussed in section 1.3.1 of chapter 1, reanalysis data suggest that the observed trend in wind forcing can be characterised by an (approximate) 20% increase in the latitudinal maximum (Figures 1.14,1.15,5.1). This results in an increase in the curl of the winds both north and south of this maximum, as shown in Figure 5.1.

For simplicity, the gyre model is examined for its response to a 20% step-increase, in the maximum strength of the eastward winds. Here, each model configuration is run twice, once with no change in forcing as a control, and once again with an increase in the zonal wind stress. The resulting anomaly is estimated by subtracting the control from the perturbation run (Figure 5.1 and 5.4).

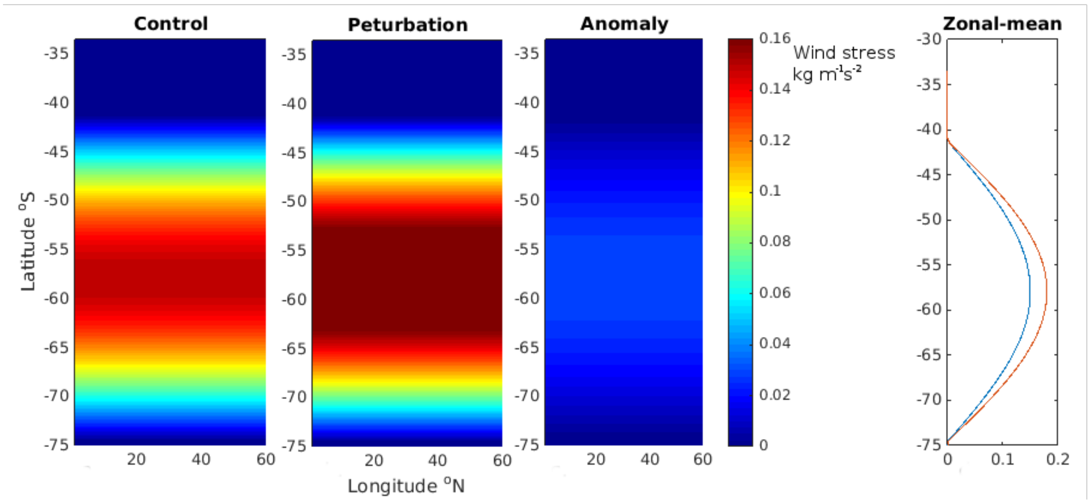

Figure 5.1: An illustration of the wind stress forcing and anomaly applied to the gyre model. From left to right: The control, perturbation and anomalous wind forcing respectively. The far right panel shows the zonal-mean wind pattern for the control (blue line) and the perturbation (red line).

Conventionally, the majority of the model's response is assumed to be driven by the first two dynamical modes, i.e. the barotropic mode and the first baroclinic mode. It is acknowledged that this approach may be reductionist, as suggested by (Maharaj et al., 2007), but it is useful to gain insight into the gyre dynamics. The following sections then use this classification to outline the gyre model's response to anomalous wind forcing; the barotropic processes are discussed in section 5.3.1 and the baroclinic process are discussed in section 5.3.2.

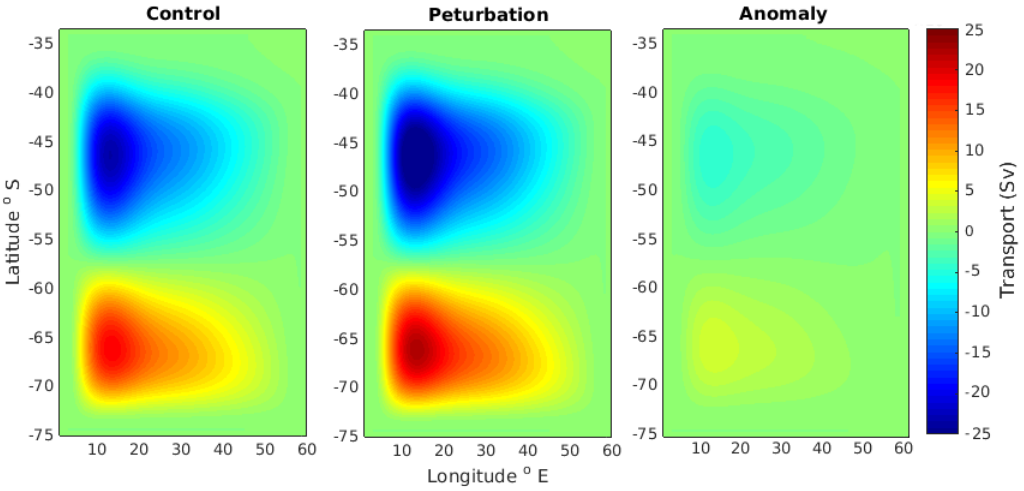

Figure 5.2: An example of the horizontal flow in the gyre model, showing the control, perturbation and anomaly in depth-integrated horizontal stream function, for the CPD configuration.

## 5.3 Common Features Of The Gyre Model's Adjustment

### 5.3.1 The Barotropic Response

Before analysing output, the appropriate rate of model output must be chosen, so as to best capture the barotropic processes. These processes are defined by barotropic waves crossing the domain. Analytical theory states that the fastest speed of a barotropic planetary wave can be approximated as the deep-water wave speed:

$$c_{tg} = \sqrt{gH}, \tag{5.1}$$

and the barotropic Rossby wave speed is defined as:

$$c_{tr} = \beta \frac{l^2 - k^2}{(k^2 + l^2)^2}, \tag{5.2}$$

where $c_{tg}$ and $c_{tr}$ are the speeds of the barotropic gravity and Rossby waves respectively, $g$ is gravity, and $H$ is the depth of the water (4000 m). Values of $\mathrm{c}_{tg} = 200\ ms^{-1}$ and $\mathrm{c}_{tr} = 3\ ms^{-1}$ are typical. These velocities and the scale of the domain, 3000-5000 km, then provide a guide for the time-scales of the initial model response. This initial response is estimated at ~7 hours for the gravity wave transit and ~30 days for the first Rossby wave transit (other important time-scales and parameters are shown in Table 4.1). The model is configured to output data at two rates to ensure capture of these key barotropic processes, as well as to encompass the full barotropic equilibration. The fastest rate is at 30-minute intervals for the first 2 days. The second rate is at 6-hour output for 30 days.

The fastest rate of output shows a series of unintuitive baroclinic patterns which occur in the first 8 hours of adjustment. However, the velocity anomaly at this time is 2 orders of magnitude below that of the later processes. These processes are therefore assumed to be negligible.

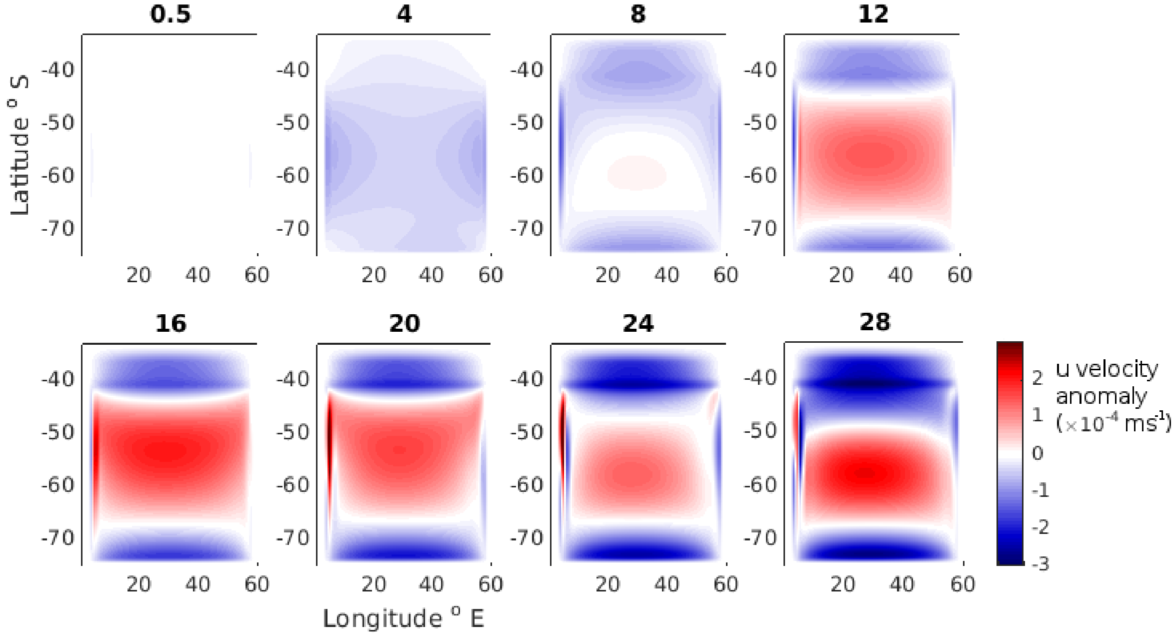

Figure 5.3: Zonal velocity anomaly for the first 28 hours of adjustment, at 500 m depth. Taken from the CPD configuration gyre model.

A Rossby wave adjustment, described by SA, is initiated between 8 and 16 hours (Figures 5.3-5.4). The velocity anomaly pattern that typifies this process is shown in Figures 5.3-5.4. Here an anomalous eastward flow appears around 55 $^o$S, flanked by westward flow to the north and south, and connected by anomalous western and eastern boundary currents.

This zonal velocity anomaly increases linearly over 8 to 10 days, until the passage of the long Rossby wave from the east, after which a Sverdrup-like balance is achieved. This process is depicted by Figure 5.5 (analogous to Figure 4.3, replicated from AG). The time scale of these events occurs in strong agreement with the theoretical work of AG. The establishment of a new Sverdrup balance constitutes an increase in cyclonic flow and interior upwelling in the southern gyre, and the reverse in the northern gyre. The distribution of the temperature and velocity anomaly following the barotropic AG adjustment is shown in Figures 5.6-5.8.

In addition to the Rossby wave adjustment, zonal bands of anomalous velocity occur shortly after 12 hours (Figure 5.9), driven by inertial oscillations. These features are

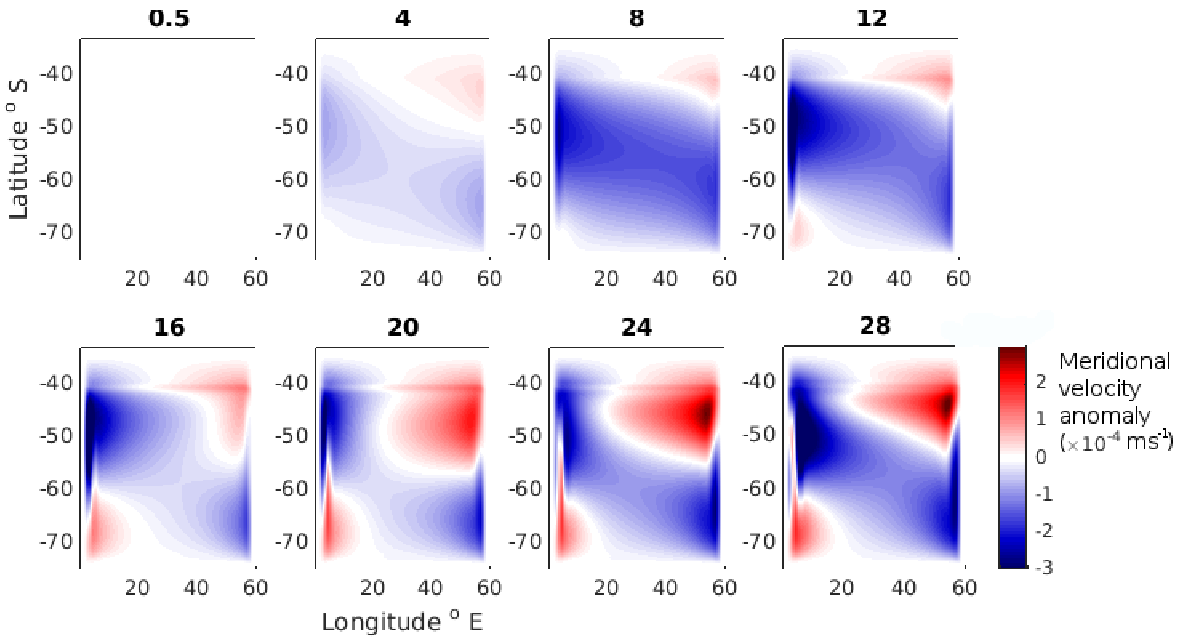

Figure 5.4: Meridional velocity anomaly for the first 28 hours of adjustment, at 500 m depth. Taken from the CPD configuration gyre model.

most clear in the vertical velocity field and falsely appear to propagate northwards. They have wavelengths of approximately 1500 m and periods ranging from around 8 to 20 hours. These meridional oscillations occur in concert with the early component of the AG Rossby wave adjustment.

### 5.3.2 The Baroclinic Response

Following discussion of the barotropic adjustment, the gyre model (described by the previous chapter) is tested for its baroclinic response to a step increase in surface wind forcing. The baroclinic adjustment provides a more complex problem, with greater variability between model sub configurations, and greater dependence on parameterisations. As the baroclinic adjustment varies considerably between sub-model configurations, this section is kept brief with some details left to the next section.

Similar to the previous section, the rate of model output is chosen to highlight key features of interest. The baroclinic adjustment is similarly characterised by baroclinic waves. The baroclinic gravity wave (or Kelvin wave) speed can be estimated as:

$$c_{cg} = \sqrt{g'h'}, \tag{5.3}$$

and the baroclinic Rossby wave speed as:

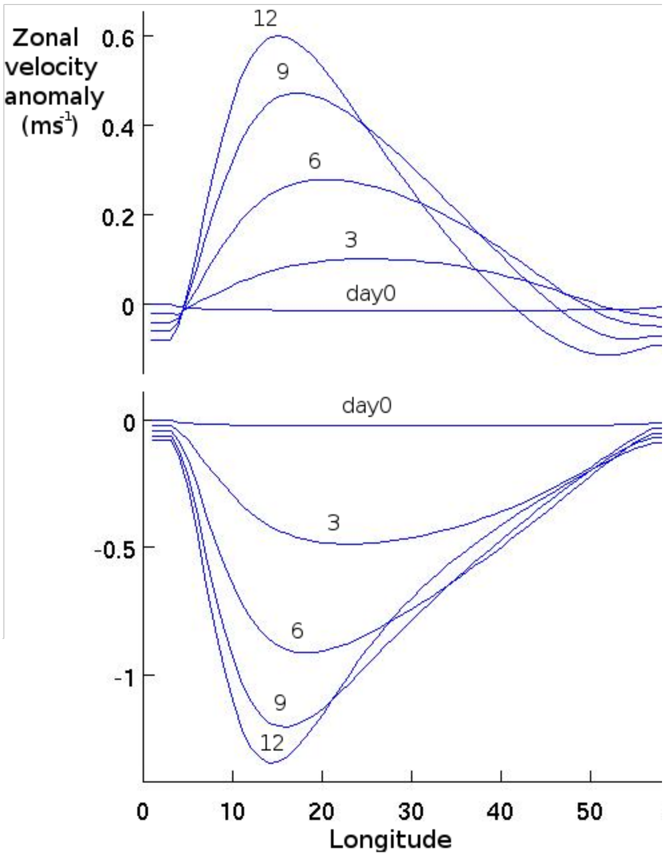

Figure 5.5: Zonal distribution of zonal velocity anomaly for 60 (upper) and 70 (lower) $^o$S. Analogous to Figure 4.3, taken from (Anderson and Gill, 1975). Each contour shows a zonal cross section of zonal velocity anomaly at 3 day intervals for the initial 15 days of model adjustment. The anomaly is shown to rapidly propagate westwards from the eastern boundary and slowly eastwards from the western boundary. Taken from the CPD configuration gyre model.

$$c_{cr} = \beta L_d = \beta \frac{\sqrt{g'h'}}{f}, \tag{5.4}$$

where $c_{cg}$ and $c_{cr}$ are the speed of the respective waves, $g'$ is the reduced gravity, and $h'$ is the specific depth (or thickness) of a given baroclinic mode. The baroclinic wave speeds vary with stratification and latitude, with typical values of c$_{cg}$ $= 2\ ms^{-1}$ and c$_{cr}$ $= 0.02\ ms^{-1}$ for around 70 $^o$ S. However, the theory of e.g. Marshall (2003) (see section 4.2.2), suggests that in low resolution models (such as the gyre model) these waves may be replaced by the slower NSBW waves. The NSBW waves have a first mode baroclinic velocity that is scaled by the ratio $\frac{L_R}{\Delta x}$. Their propagation velocities therefore range between 1 and 10% of the expected value for a baroclinic kelvin wave. All of these wave speeds, and the scale of the domain (Table 4.1), provide a range of estimates for the timescale of baroclinic adjustment.

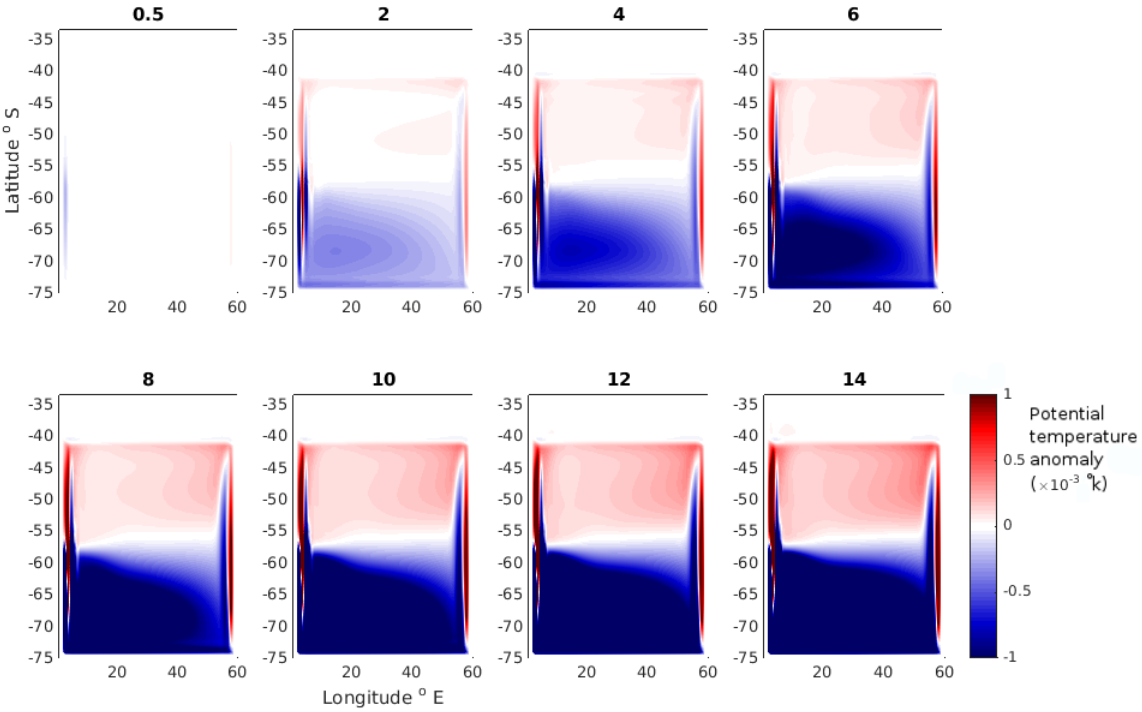

Figure 5.6: Potential temperature anomaly at 500 m for the initial 14 days of model adjustment. Taken from the CPD configuration gyre model.

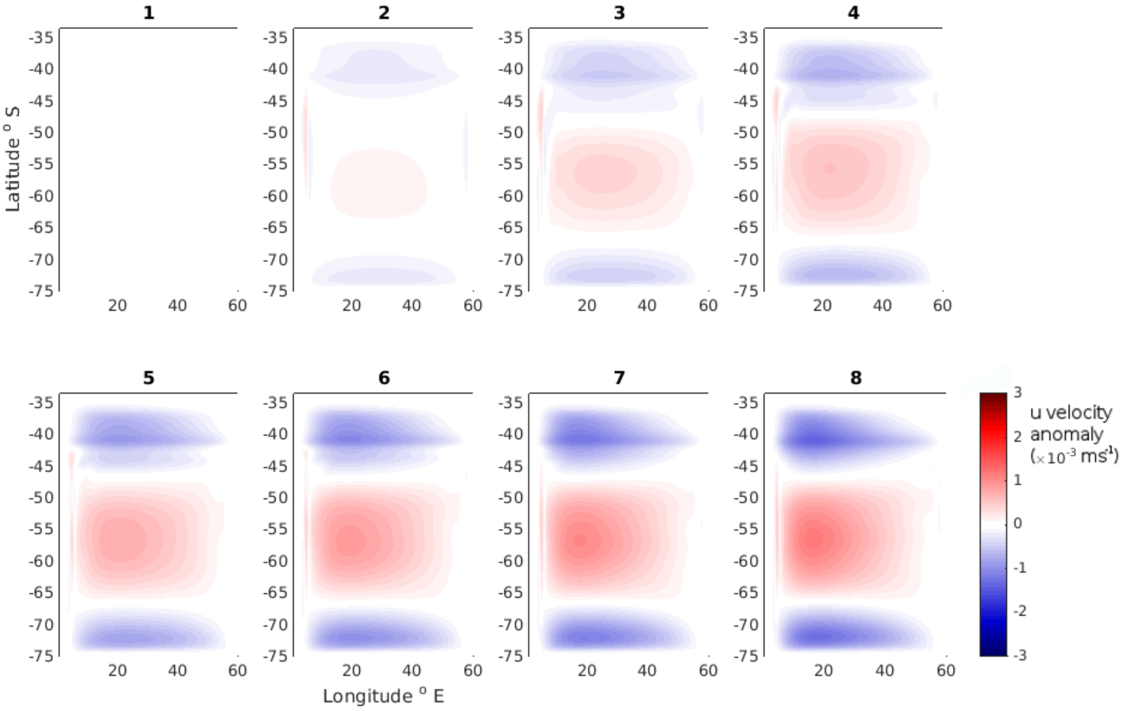

Figure 5.7: Zonal velocity anomaly at 500 m for the initial 8 days of model adjustment. Taken from the CPD configuration gyre model.

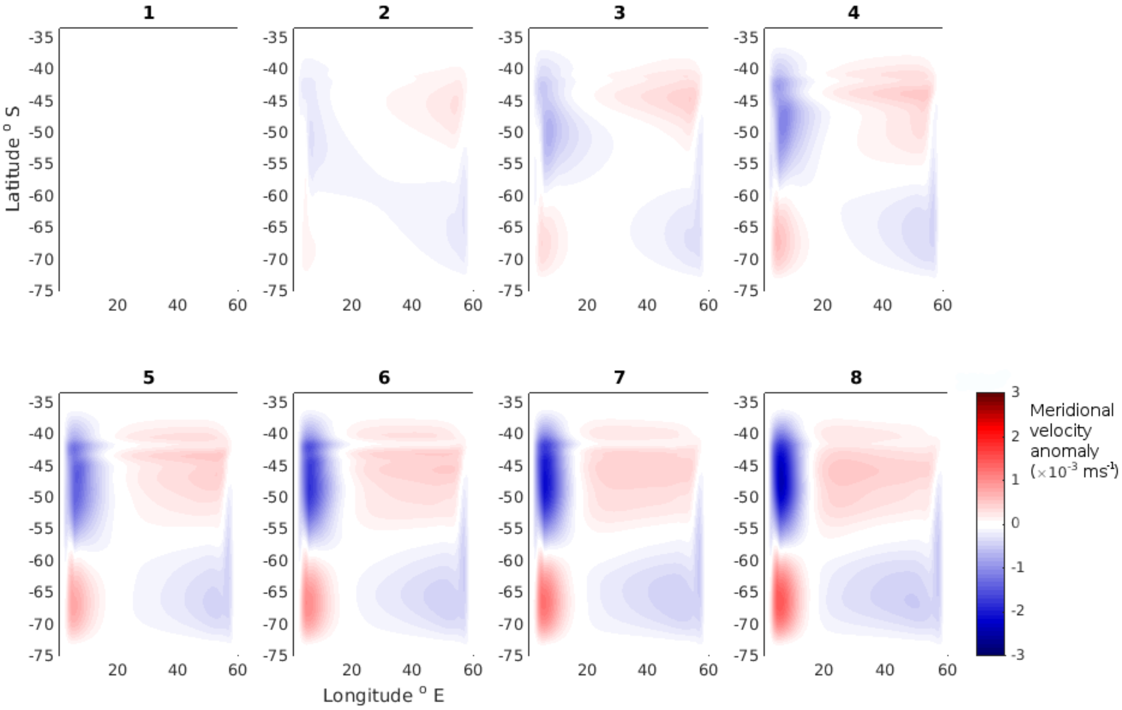

Figure 5.8: Meridional velocity anomaly at 500 m for the initial 8 days of model adjustment. Taken from the CPD configuration gyre model.

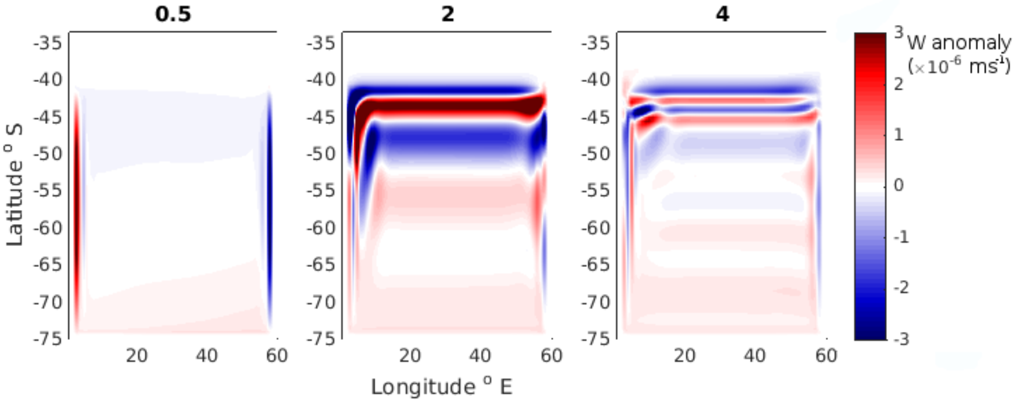

Figure 5.9: Vertical velocity anomaly at 500 m for the initial 4 days of model adjustment. Taken from the CPD configuration gyre model.

The shortest possible time-scales for baroclinic adjustment are estimated to be approximately 30 days and 5 years respectively; these refer to the baroclinic gravity wave and Rossby wave speeds respectively. The slower wave transit time of NSBW waves suggest that longer time-scales of a year, and a decade, are also important. Even longer timescales associated with the initial advective adjustment are also considered: The gyre's typical maximum horizontal velocity is 5 cm $s^{-1}$, and therefore the timescale for anomalies to be advected meridionally across the domain is estimated as ~50 years. The full adjustment of the gyre to advective processes, i.e. the time required for the gyre to adjust by vertical or diapycnal transport, occurs over $\sim$ 2000 years. Here our interest focuses on timescales of around 20 years to conform to the range of expected adjustment timescales.

The model is therefore configured to output data at four rates. First, the model outputs data at 6-hour intervals for 30 days, and is analysed for baroclinic gravity and boundary waves, such as Kelvin waves. Data are then output at 12-hour intervals for 120 days, for the analysis of NSBW waves. Thirdly, 2-month data is output for 30 years for analysis of the slowest boundary waves and advective signals, but also for comparison to the instrumental period. Finally 6-month data is output for 50 years, so as to capture the marginally longer time-scale features of the advective response.

Immediately apparent within the first 30 days, is the absence of anomalies propagating at $c_{cg}$, which should have transited the domain within the first 27 days (assuming a wave speed of around 2 m $s^{-1}$). This finding suggests the importance of the slower forms of baroclinic adjustment. The majority of the response at this timescale appears to be barotropic; the initial stage of the baroclinic Rossby wave response may occur in this time period. The most prominent feature of the following 120 days is the initiation of the AG gyre adjustment, which starts around day 50 and continues into the multi-year output (Figure 5.10).

Between days 10 and 120, an adjustment is visible in the deep circulation. A convergence of the vertical transport, in the southern gyre, between 1000 to 2000 m depth occurs, creating a temperature anomaly in this region (Figure 5.11). The anomaly is most prominent within the southern gyre, in particular its south-western corner. It occurs around the base of the thermocline, where the vertical gradient in temperature is greatest and the abyssal circulation is also large. On the timescale of around 100 days, a relatively quick (NSBW) boundary wave travelling at around 0.1 m $s^{-1}$ (variable between sub-configurations) transmits the thickness anomaly along the western edge of the southern gyre (Figure 5.11). It moves the cold anomaly northwards (cyclonically around the gyre boundary), and follows density contours. This propagation acts to increase the strength of the abyssal circulation.

These NSBW waves show a second or first baroclinic mode distribution in the vertical, however their zonal length-scale (e.g. 300 km) is much larger then the scale of a first

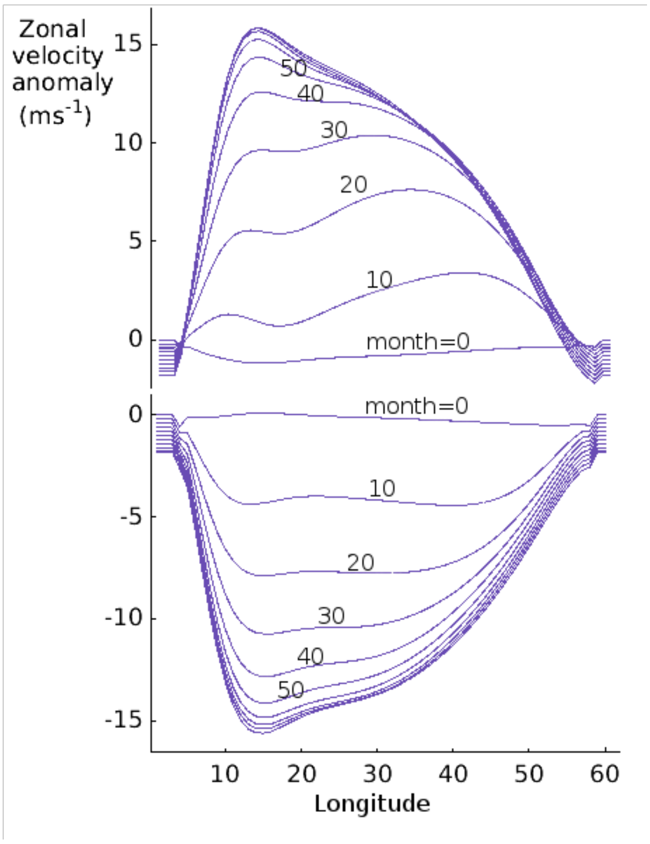

Figure 5.10: Zonal distribution of zonal velocity anomaly at 800 meters depth, for 60 (upper) and 70 (lower) $^o$S. Analogous to Figure 4.3, taken from (Anderson and Gill, 1975). Each contour shows a zonal cross section of zonal velocity anomaly at 10 month intervals for the initial 10 years of model adjustment. The anomaly is shown to rapidly propagate westwards from the eastern boundary and slowly eastwards from the western boundary. Taken from the CPD configuration gyre model.

mode baroclinic Kelvin wave at these latitudes (e.g. 20 km; see Figure 5.11), and their velocity is considerably less then theoretical predictions for a first mode baroclinic wave. The NSBW waves are analysed further by deconstructing the balance of terms at their wave front. The wave fronts are tracked with a 3 by 10 $^o$ box. The data in this box is averaged for each time-step, the terms of the anomaly momentum equation are then estimated. Here, for example, the zonal components of the momentum equation are described as:

$$\frac{\partial u'}{\partial t} + (u'\frac{\partial u}{\partial x} + u\frac{\partial u'}{\partial x}) + \frac{\partial p'_h}{\partial x} - fv' = -\nu(\frac{\partial^2 u'}{\partial x^2} + \frac{\partial^2 u'}{\partial y^2}), \tag{5.5}$$

$$\frac{\partial v'}{\partial t} + (v'\frac{\partial v}{\partial y} + v\frac{\partial v'}{\partial y}) + \frac{\partial p'_h}{\partial y} - fu' = -\nu(\frac{\partial^2 v'}{\partial y^2} + \frac{\partial^2 v'}{\partial x^2}), \tag{5.6}$$

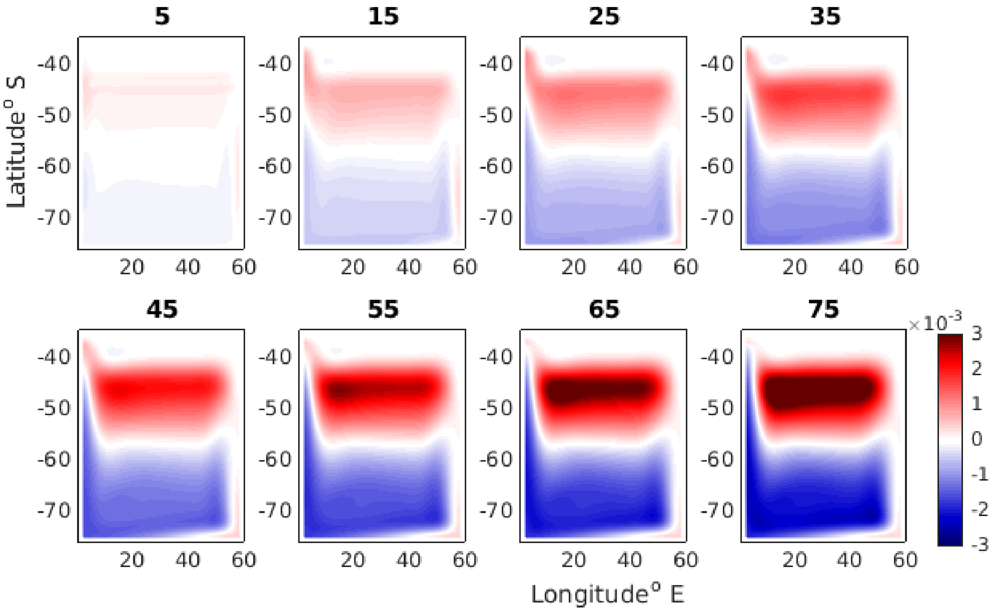

Figure 5.11: Potential temperature anomaly ($^oC$) of the gyre model at 1000 m depth, showing up to 75 days following a 20% increase in surface wind stress. Subplots are marked by days following wind change.

where primes denote anomalies and products of prime terms are assumed to be small, i.e. $u'\frac{\partial u'}{\partial x} \ll 0$. $p'_h$ is the hydrostatic pressure anomaly (N m$^{-2}$). Furthermore, the tracer equation is described as:

$$\frac{\partial \theta'}{\partial t} + (u'\frac{\partial \theta}{\partial x} + u\frac{\partial \theta'}{\partial x}) + (u^{*\prime}\frac{\partial \theta}{\partial x} + u^{*}\frac{\partial \theta'}{\partial x}) + (v'\frac{\partial \theta}{\partial y} + v\frac{\partial \theta'}{\partial y}) + \\ (v^{*\prime}\frac{\partial \theta}{\partial y} + v^{*}\frac{\partial \theta'}{\partial y}) + (w'\frac{\partial \theta}{\partial z} + w\frac{\partial \theta'}{\partial z}) + (w^{*\prime}\frac{\partial \theta}{\partial z} + w^{*}\frac{\partial \theta'}{\partial z}) = -k\frac{\partial^2 \theta'}{\partial z^2} \quad (5.7)$$

where $^*$ terms represent bolus transports of the GM eddy parameterisation (m s$^{-1}$, and the $k$ term represents the vertical diffusive flux of temperature anomaly (m$^2$ s$^{-1}$). The balance for each direction, and the total balance is shown for both equations in Figures 5.12,5.13.

Here geostrophic balance dominates the zonally tracer equation, but the viscosity term plays a significant role in the meridional balance. The vertical terms do not balance, with the dominant term being $\frac{\partial w'}{\partial t}$, however the magnitude of this term is very small. The zonally geostrophic balance represents the largest terms in the overall balance. All other terms shown in equation 5.7-5.27 are then negligible.

The dominant terms in the tracer equation are $u'\frac{\partial \theta}{\partial x}$, $v'\frac{\partial \theta}{\partial y}$, $\frac{\partial \theta'}{\partial t}$ and $w'\frac{\partial \theta}{\partial z}$, with the balance between $w'\frac{\partial \theta}{\partial z}$ and $\frac{\partial \theta'}{\partial t}$ being the most important. The advection effected by zonal and meridional anomalous flow on the mean temperature field cancels out. All other terms

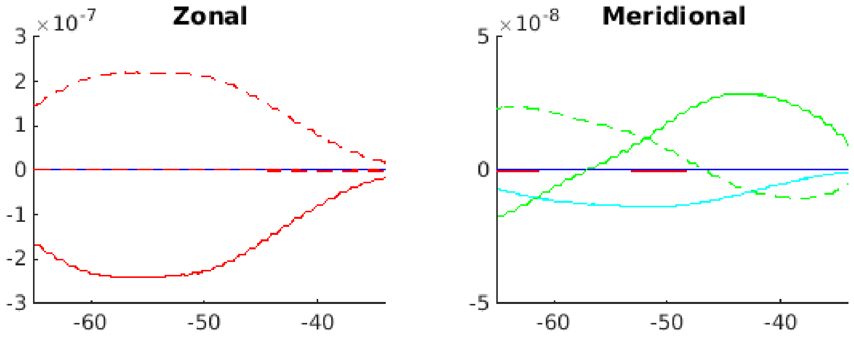

Figure 5.12: Wave-front, momentum balances derived from equation 5.6, the vertical terms are small and are therefore neglected. Here the dominant terms are identified: Red dashed line: $\frac{\partial p'}{\partial x}$ Red line: $fv'$. Green dashed line: $\frac{\partial p'}{\partial y}$. Green line: $fu'$. Cyan line: $\nu(\frac{\partial^2 u'}{\partial x^2} + \frac{\partial^2 u'}{\partial y^2})$ . Black line : $\frac{\partial w'}{\partial t}$. Taken from the CSB configuration gyre model.

shown in equation 5.6 are found to be negligible, notably the GM terms play no role in the balance of terms.

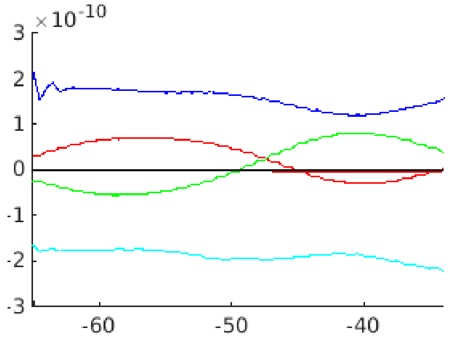

Figure 5.13: Wave-front tracer balances derived from equation 5.7. Here the dominant terms are identified: Red line: $u'\frac{\partial \theta}{\partial x}$ . Green line: $v'\frac{\partial \theta}{\partial y}$. Cyan line: $\frac{\partial \theta'}{\partial t}$ . Blue line : $w'\frac{\partial \theta}{\partial z}$. Taken from the CSB configuration gyre model.

The tracer equation balance thus strongly suggests that the anomaly is wave-like. Further, the importance of the viscosity term in the momentum balance supports the theory outlined by (Marshall and Johnson, 2013), suggesting that these relatively fast boundary propagating feature are similar to NSBW.

Between 1 and 15 years, a secondary propagating feature, is observed, henceforth referred to as an advective feature (Figure 5.14). The secondary anomaly propagates at around 0.05 m s$^{-1}$, which is the maximum velocity of meridional advection, and therefore may be associated with advective pathways. This secondary propagation also transmits a cold anomaly northwards and acts to strengthen the abyssal cyclonic circulation.

Figure 5.15 shows the path lines of neutrally buoyant particles over 14 years, released mainly in the south western corner of the domain at t=0. The strength of the flow in the

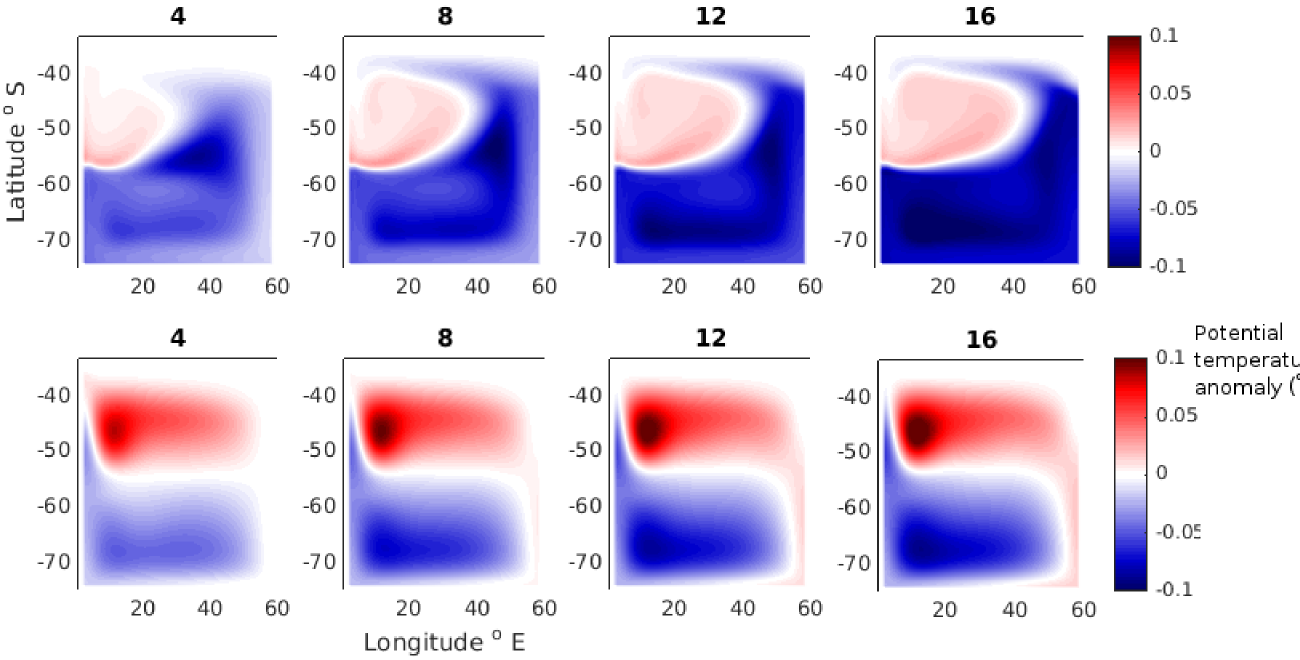

Figure 5.14: Potential temperature anomaly at 50 meters (top), and 1000 meters (bottom), for the initial 16 years of model adjustment, taken from the CPD configuration gyre model.

deep western boundary current is evident, showing agreement between the propagating anomaly and the horizontal flow field. The particles additionally highlight the broad shape of the deep western boundary current, which deflects and flows east along the current's eastern edge in the northern gyre. However, this flow path is only roughly in agreement with the path of the temperature anomaly propagating between 1 and 15 years, which is much more confined to the boundary, implying an additional wave-like component to the propagation.

The baroclinic Rossby wave (AG) response is observed between 50 days and 9 years (Figure 5.10). However, the gyre model is unable to explicitly resolve baroclinic Rossby waves, and therefore this process must be parameterised. Analytical wave theory predicts that the first mode baroclinic Rossby wave should zonally transit the basin between 5 and 10 years. This time scale is in approximate agreement with the gyre model, which shows an adjustment time of around 7 years, Figure 5.10. Killworth (1985) predicts an AG adjustment timescale of 5 years. The time scales of diffusive anomaly transport driven by the '*GM_redi*' eddy parameterisation package can be estimated using a 1D diffusion model which predicts a time scale of approximately 10 years, where the background diffusivity expressed by GM has the typical value k = 1000 $m^2$ $s^{-1}$.

The geostrophy of the gyre following baroclinic adjustment is of particular interest in the study of deep water export from the region. The change in the tilt in the most simple and complex model sub-configurations is shown in Figures 5.16 and 5.17 respectively. Furthermore, a plan view of the geostrophic adjust of the gyre is provided in Figure 5.19.

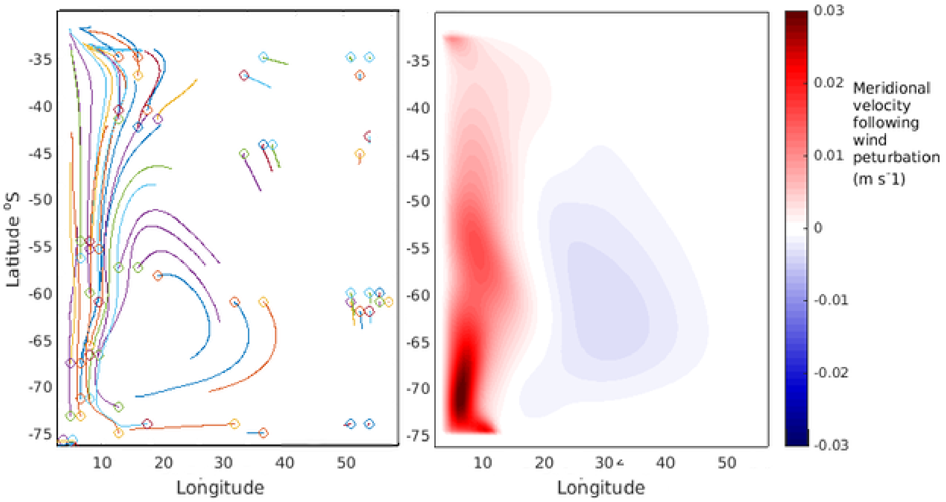

Figure 5.15: Left: The path lines of neutrally buoyant particles, released at 1000 m depth. traced over the initial 14 years of gyre adjustment. Right: snapshot of meridional velocity anomaly after 14 years of adjustment at 1000 m depth. Taken from the CSB configuration gyre model.

The steepening of isopycnals at the confluence zone between the gyres is a consistent in all sub configurations, but the degree of steepening at e.g. 2000 m depth, varies between models depending on their stratification, and other factors. The change in horizontal distribution of temperature contours highlights an unexpected zonal expansion of the gyre.

## 5.4 Differences between the sub-configurations Of The Gyre Model

The previous section outlined the adjustment processes that are common to all model sub-configurations. The following section discusses the differences between model sub-configurations, both in the steady state and in the adjustment processes.

Surface forcing, viscosity parameters and GM parameters are adjusted for each sub-configuration to ensure realistic horizontal circulations, i.e. a wind driven, double-gyre, surface circulation and a single density-driven abyssal circulation. The component of vertical velocity at the model's thermocline driven by wind and buoyancy forcing are estimated as

$$w_{ek} = \frac{1}{\rho_0}\frac{\partial \frac{\Delta\tau}{f}}{\partial y} \tag{5.8}$$

and,

$$w_b = \frac{\left(\frac{g\alpha Q}{C_p H \rho_0}\right)}{N^2} \tag{5.9}$$

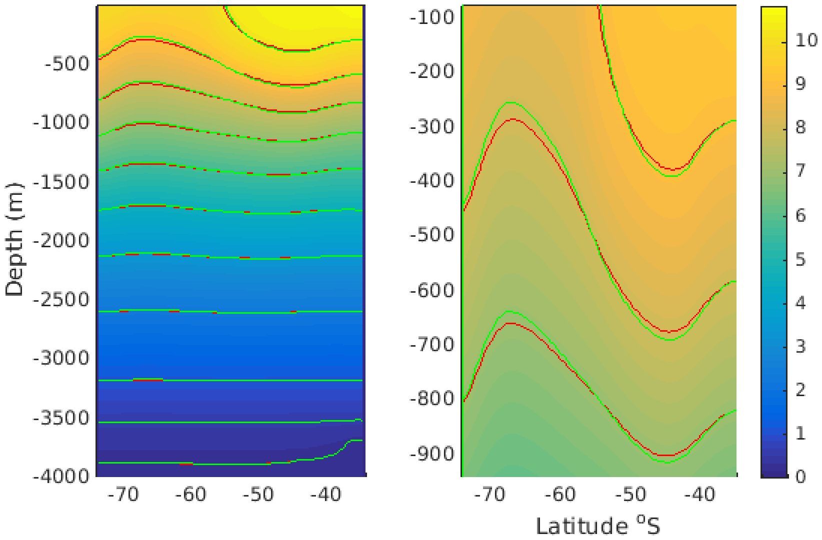

Figure 5.16: The zonal average slope of temperature surfaces in the most simplified sub configuration of the gyre model (CPD). Shading shows the zonal and time averaged temperature distribution. Red contours show temperature surfaces before a step change in wind forcing. Green contours show temperature surfaces following 14 years of adjustment to a step change in wind forcing. The right panel shows a zoom on the upper 1000 m, emphasising the doming of isopycnals.

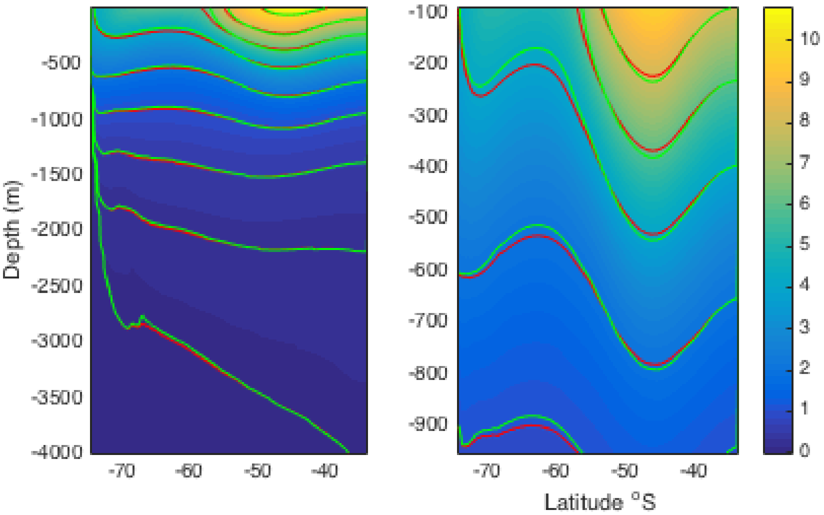

Figure 5.17: The zonal average slope of temperature surfaces in the most complex sub configuration of the gyre model (SSBS). Shading shows the zonal and time averaged temperature distribution. Red contours show temperature surfaces before a step change in wind forcing. Green contours show temperature surfaces following 14 years of adjustment to a step change in wind forcing. The right panel shows a zoom on the upper 1000 m, emphasising the doming of isopycnals.

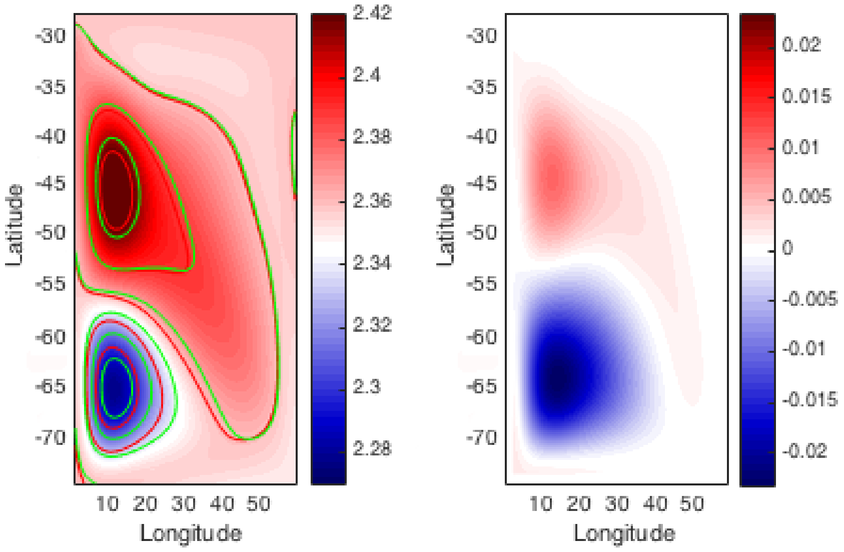

Figure 5.18: Left: The time-mean temperature field at 2000 m depth in the simplest configuration of the gyre model (CPD). Red contours show potential temperature before a step-increase in wind forcing; green contours show potential temperature 14 years after adjustment to increased wind forcing. Right, the corresponding temperature anomaly after 14 years of adjustment.

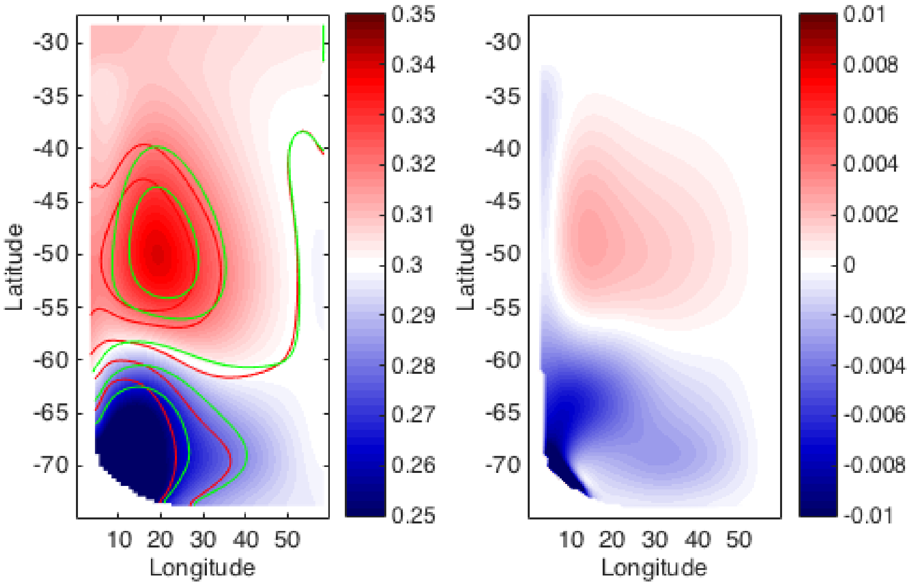

Figure 5.19: Left: The time-mean temperature field at 2000 m depth in the most complex configuration of the gyre model (SSBS). Red contours show potential temperature before a step-increase in wind forcing; green contours show potential temperature 14 years after adjustment to increased wind forcing. Right, the corresponding temperature anomaly after 14 years of adjustment.

respectively. Where $\alpha$ is the thermal expansion coefficient ($\times 10^{-4}$ K$^{-1}$), Q is the surface heat flux (W m$^{-2}$), Cp is the specific heat capacity of sea water (3850 J kg$^{-1}$), H is the water depth (4000 m) and N is the buoyancy frequency (s$^{-1}$). $w_{ek}$ and $w_b$ are used for comparison between sub-configurations.

### 5.4.1 The Cartesian Co-ordinate, Prescribed Density Field Model (CPD; model1)

The CPD is the simplest configuration, and therefore, as discussed in the previous chapter, it exhibits the least complex horizontal velocity distribution. Here the wind-driven gyres have a relatively symmetrical distribution, with close agreement to the Sverdrup-balance equations applied to a square domain (shown in Figures 4.13- 4.12). The CPD is therefore very useful for providing a clear depiction of the surface wind-driven adjustment processes but, it is not able to simulate abyssal processes.

The CPD has a wind-driven thermocline vertical velocity, of $W_{ek}$ =1.7x10$^{-6}$ m s$^{-1}$, and a background horizontal GM diffusivity of 1000 m$^2$ s$^{-1}$. In addition the CPD has a horizontal viscosity of $Ah$ = 3x10$^4$ kg m$^{-1}$ s$^{-1}$. This viscosity is small compared to other sub-configurations and is chosen to be optimal for the propagation of boundary waves. An important parameter that is derived from $A_h$, is the Munk length (Munk 1950; Munk 1951),

$$L_m = \sqrt[3]{\frac{A_h}{\beta}}. \tag{5.10}$$

Which describes the approximate width of the western boundary current for a given value of viscosity. This length must be resolved for the stability of the model. Following equation (4.17), large values of $L_m$ are associated with slower transit speeds for NSBW's. For the CPD, $L_m$ = 130 km, or around two grid cells width. $A_h$ can be set low in CPD because it is a simple, stable sub-configuration. The horizontal viscosity is increased in other configurations to reduce instabilities associated with surface buoyancy forcing and to maintain realistic circulation patterns.

The CPD exhibits a fast-moving boundary wave (NSBW), with a typical velocity 0.1-0.2 m s$^{-1}$, a maximum temperature anomaly of 0.001-0.003 $^o$ K, and a characteristic propagation depth of 700 to 1200 m. The CPD model does not have an abyssal circulation; relaxing the top and bottom levels to a constant temperature sets the vertical stratification (Figure 4.14). The slower propagating, advective feature that is common in other runs, is also absent from this run.

### 5.4.2 The Cartesian Co-ordinate, Surface Buoyancy Forced Model (CSB; model2)

The CSB configuration is the simplest configuration that uses surface buoyancy forcing (Figure 4.17). The balance between wind and buoyancy forcing can be quantified by $W_{ek} = 1.7\text{x}10^{-6}$ and $W_b = 7.06\text{x}10^{-8}$ m s$^{-1}$. CSB has one of the lowest GM background diffusivities of 500 m$^2$ s$^{-1}$. It has a horizontal viscosity of $A_h = 1\text{x}10^5$ kg m$^{-1}$ s$^{-1}$, therefore the Munk length is $L_m = 200$ km, or 3.3 grid cells.

The horizontal velocity distribution for the upper and lower circulation is shown in Figure 4.11, where the distortion of the southern gyre by buoyancy forcing is evident. The vertical velocity distribution implies a maximum in wind driven circulation around 500 m, and maximum in the density driven circulation around 1200 m and 3500 m. The control and anomalous, meridional overturning circulation are shown by Figure 5.22.

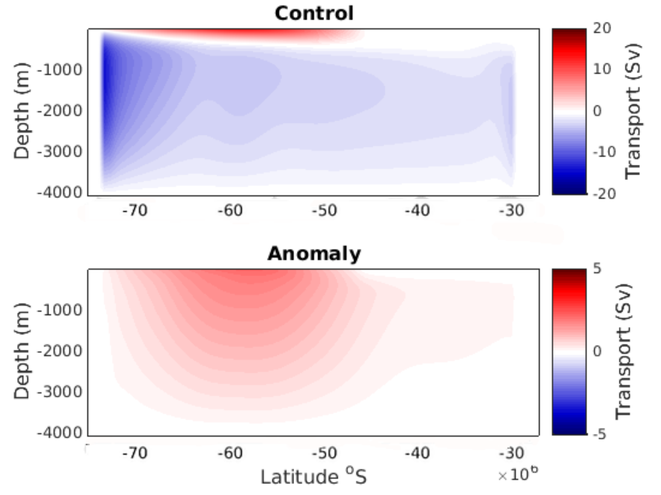

Figure 5.20: Zonally integrated overturning stream function, upper: control run, lower: anomaly (CSB).

The faster moving boundary wave (NSBW) is absent in this configuration, however the slower moving advective feature is present (Figure 5.26), and moves at around 0.01 m s$^{-1}$. The abyssal circulation and the slow boundary propagation extend over a large depth, 1000-4000 m, where the wave response emanates from approximately 1000 meters depth. Most exceptional within this configuration are the pulses of temperature anomaly, which occur as part of the advective feature. These occur with a wavelength of around 20$^o$ (1200 km), a propagation speed of 0.01-0.02 m s$^{-1}$, and a maximum temperature anomaly of 0.003-0.1 $^o$. The advective features transit the domain meridionally, spanning, a zonal thickness of 10$^o$ (600 km) from the western boundary.

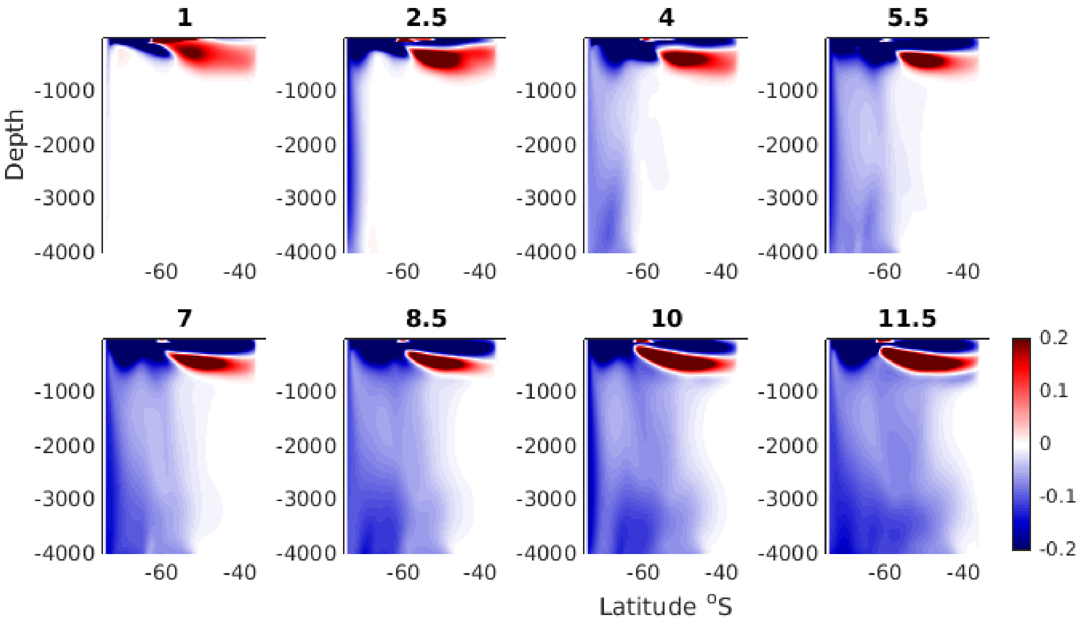

Figure 5.21: Multiple snapshots of temperature anomaly, highlighting the advective feature propagating along the western boundary. Each subplots shows a meridional transect along $5^o$ east. The vertical structure of the propagation is apparent. Subplots are labelled with their time in years after a change in wind forcing (a CSB run).

### 5.4.3 The Spherical-Polar Co-ordinate, Surface Buoyancy Forced Model (SSB; model3)

The SSB is the first configuration to utilise a spherical polar grid and a full Coriolis term. As shown in Figure 5.2, this causes an asymmetry between the northern and southern gyres, as the northern gyre covers a larger area. The abyssal circulation is also distorted.

The wind forcing used in this configuration is somewhat larger at $W_{ek}$ = 6.7x$10^{-6}$ m $s^{-1}$. This is chosen to counter-balance the larger buoyancy forcing of, $W_b$ = 4.5x$10^{-7}$ m $s^{-1}$, which is required to produce a realistic abyssal circulation. The GM background diffusivity is set to its regular value of 1000 $m^2$ $s^{-1}$. The horizontal viscosity is $A_h$ = 1x$10^5$ kg $m^{-1}$ $s^{-1}$, with a resulting the Munk length of $L_m$ = 200 km, or 3.3 grid cells .

The SSB does not exhibit a fast boundary wave (NSBW) for most runs. However, a single SSB run with low viscosity, $A_h$ = 5x$10^{-4}$ kg $m^{-1}$ $s^{-1}$, does exhibit a fast boundary wave which propagates from the south western corner to $50^o$ south, with a typical speed of 0.1 m $s^{-1}$. However, the shape of the gyres and the abyssal circulation in this run are unrealistic.

The slower, advective boundary propagation is evident in all runs, with a maximum temperature anomaly of 0.01-0.02 $^o$ K, and propagation velocity of 0.01 m $s^{-1}$. This

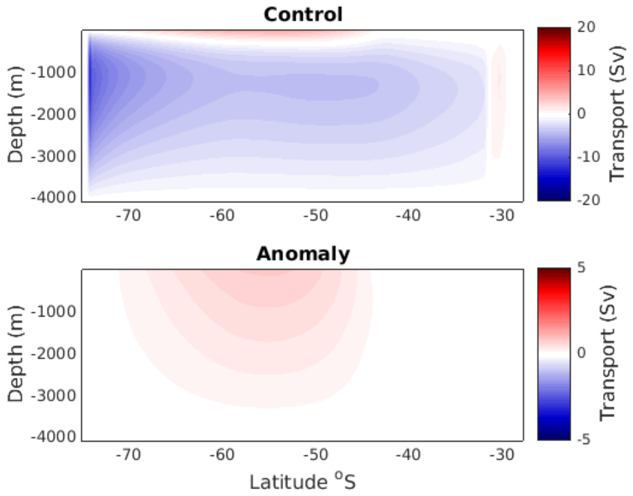

Figure 5.22: Zonally integrated overturning stream function, upper: control run, lower: anomaly (SSB).

advective feature is prominent in the SSB configuration (Figure 5.23). Here the temperature anomaly at the boundary appears to both sink at the southern edge, and propagate north at the surface (Figure 5.23). The intensified surface propagation stops at the boundary between the two gyres, a cold anomaly then propagates into the northern gyre at around 1500 m depth (Figure 5.23). This complex behaviour is suggestive of the importance of advective pathways in this model.

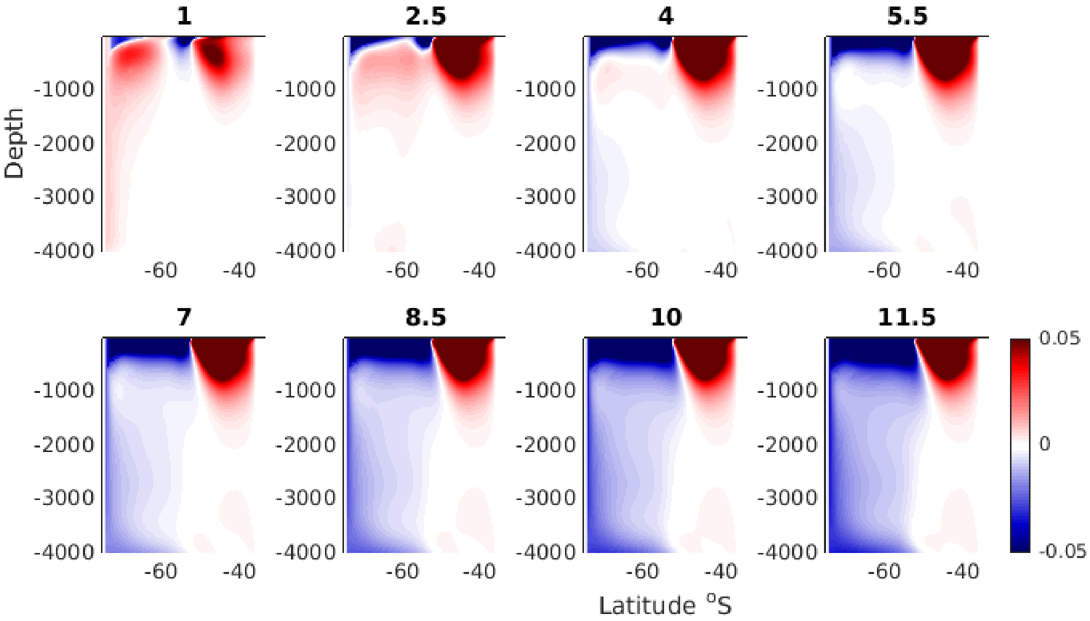

Figure 5.23: Snapshots of the advective feature propagating along the western boundary in the temperature anomaly. Each subplots shows a meridional transect along $5^o$ east. The vertical structure of the propagation is apparent. Subplots are labelled with their time in years after a change in wind forcing (a SSB run).

A further outstanding feature of this configuration is the shape of the deep circulation, which is best described as a ‘peanut’ shape. This distribution is seen in other configurations, but it is most prominent in the SSB. An abyssal anticyclonic circulation is observed at the boundary between the two gyres, on the western edge, extending around $30^0$ into the centre of the gyre. In addition an intensified abyssal cyclonic circulation occurs under the southern gyre.

### 5.4.4 The Spherical-Polar Co-ordinate, Surface Buoyancy Forced Model With Sloping Southern And Western Boundaries (SSBSB; model4)

Finally the SSBSB configuration is the most complex used in this study. It is the same as SSB, except the sidewalls are sloped. The particular configuration used here, which is tuned to display the same approximate velocity distribution as the other configurations, has a wind forcing of $W_{ek}$ = 6.7x$10^{-6}$ m $s^{-1}$, a buoyancy forcing of $W_b$ = 6.9x$10^{-7}$ m $s^{-1}$, a GM background viscosity of 1000 $m^2$ $s^{-1}$ and a horizontal viscosity of $A_h$ = 1x$10^5$ kg $m^{-1}$ $s^{-1}$. Therefore SSBSB has a munk length of $L_m$ = 200 km, or 3.3 grid cells.

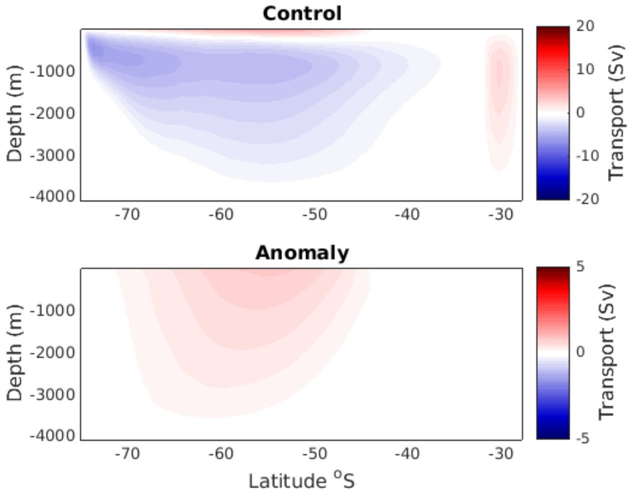

Figure 5.24: Zonally integrated overturning stream function, upper: control run, lower: anomaly (SSBSB).

The SSBS adjustment does not exhibit a fast moving NSBW but includes a slow moving advective feature only (Figure 5.26). Similar to SSB, the temperature anomaly appears to fill the southern western boundary from the south, both at mid depth and as a deep plume, which falls down the sloping topography (Figure 5.26). The anomaly then propagates at a slower rate in the northern gyre along the western boundary at around 1500 m depth. This anomaly is estimated to propagate at around 0.005 m $s^{-1}$, with a maximum temperature anomaly of 0.01 to 0.02 $^o$, and a zonal thickness of 300 km. An additional bottom-trapped boundary propagation occurs around $12^o$ or 600 km off-shelf (Figure 5.26). However this anomaly moves considerably more slowly, and is easily encapsulated by the faster advective feature. The boundary propagation occurs between

1000 and 4000 m, with a zonal thickness of $5^o$ (300 km) at 1000 m, and $7^o$ (420 km) below 3000 m depth. Moreover the lateral distribution of the anomaly varies with depth (Figure 5.26). Between 1000 and 2500 m, the anomaly propagates along the shelf. However at 2500 m and below, a component of the anomaly moves down slope, into the gyre interior. Below 3000 m the majority of the anomaly flows directly down shelf into the southern gyre interior.

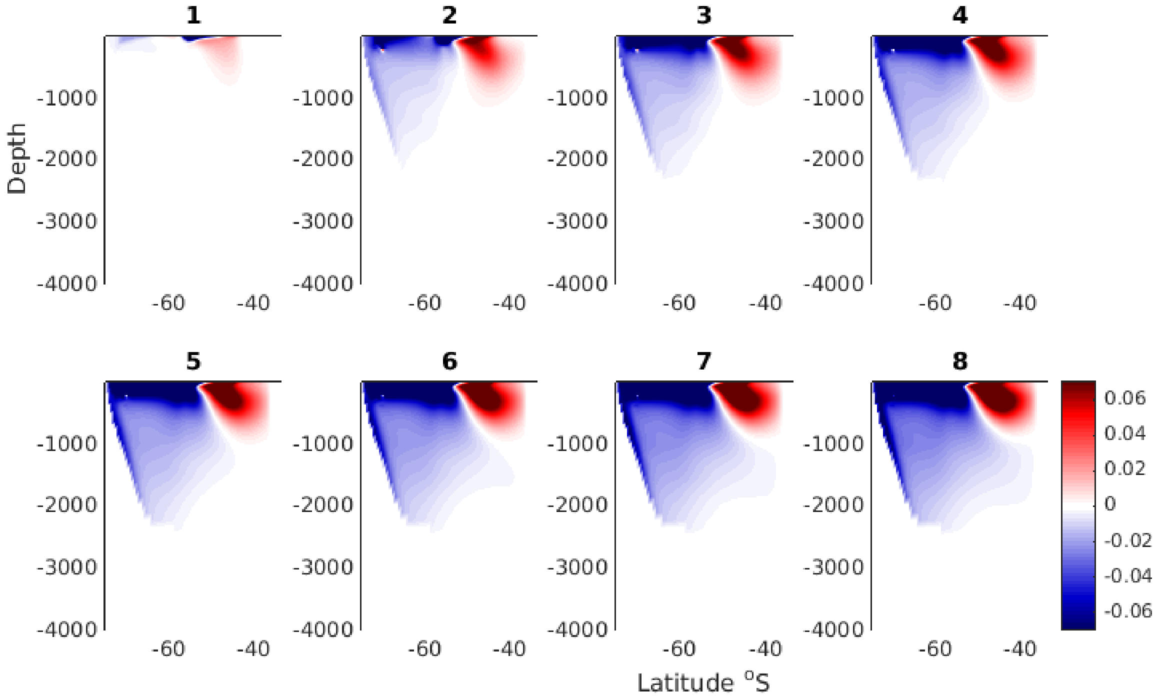

Figure 5.25: Multiple snapshots of the advective feature propagating along the western boundary. Each subplots shows a meridional transect along $5^o$ east. The vertical structure of the propagation is apparent. Subplots are labelled with their time in years after a change in wind forcing (a SSBS run).

## 5.5 Summary

As suggested by Meredith et al. (2008), following a step increase in surface wind forcing, the gyre model 'spins-up', and its isopycnals dome (Figures 5.16 and 5.16). This finding supports the wind-control hypothesis, but the model results also add nuance. Figure 5.19, shows the movement of isopycnals that occurs following model adjustment. For example, the vertical movement of isopycnals is reduced close to sloping topography, therefore, topography may play an important role, particularly if there is a ridge at the north of the gyre.

The boundary propagations are highly consistent features, expressed in all model sub-configurations. Furthermore, similar phenomena are described in previous modelling studies (e.g., Doscher et al., 1996; Capotondi, 2000; Goodman, 2001; Getzlaff et al.,

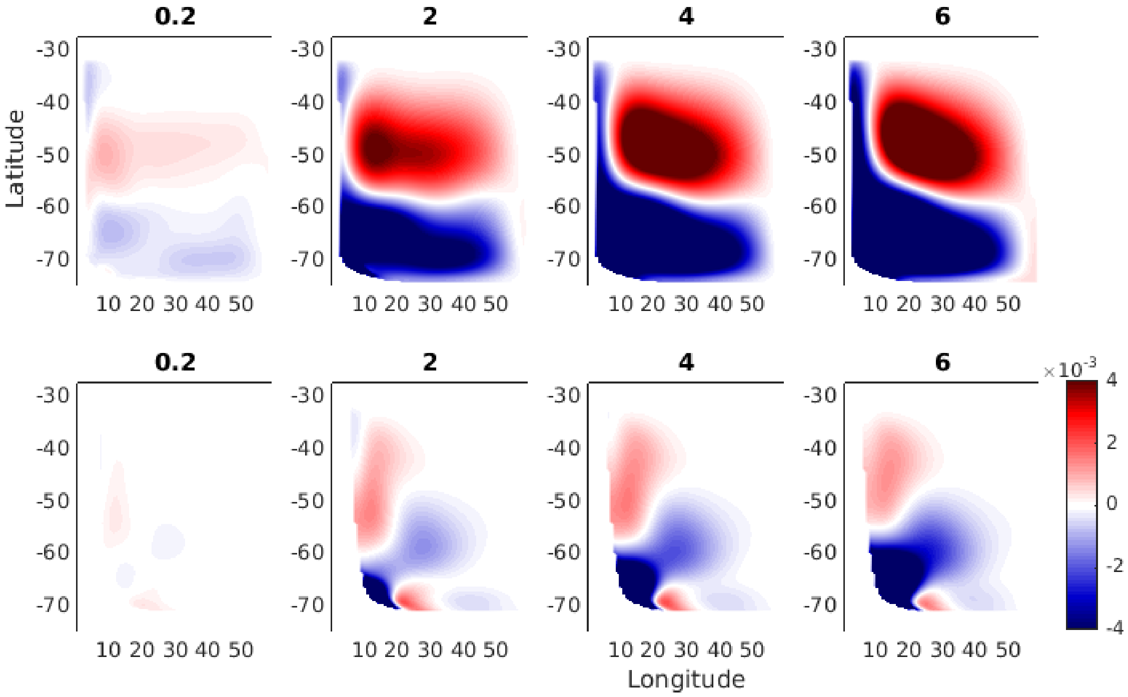

Figure 5.26: Plan view snapshots of temperature anomaly at an 1500 m (upper row) and 3500 m (lower row), highlighting the difference in horizontal pathway taken by the advective feature between depths in the SSBS configuration. Subplots are marked by their time in years after a change in wind forcing (a SSBS run).

2005). However, the expected first baroclinic mode boundary waves propagating at 1 m $s^{-1}$ are consistently not observed. The waves/propagations simulated by the gyre model are difficult to compare directly to real-world observations, because certain features have been shown to be unrealistic, e.g. Marshall and Johnson (2013). However, they express many similar features. It is argued that study of these waves provides insight both into a realistic response to a change in Southern Ocean wind stress, and fascinating issues in numerical model design.

Two distinct types of boundary propagations occur in the gyre mode. The fastest group are labelled in this text as numerical short boundary waves, NSBW, following the work of Marshall and Johnson (2013) and Killworth (1985). These features occur in the CPD, and a modified, low viscosity version of the SSB run. They waves have typical propagation speeds of 0.05 to 0.5 m $s^{-1}$. They have a typical zonal width of around $5^o$ (300 km), which is around 15 times the local Rossby radius. Analysis of these features suggests that viscous terms play an important role in their balance of terms. Further, model runs with stronger viscosity either exhibit slower NSBW waves or no NSBW waves. They are typically excited in relation to a change in vertical transport within the first 20 days, and transit the domain within the first 100 days (following a change in winds). These features tend to typically propagate around 1200 m depth, at the base of the thermocline, or the wind-driven layer.

The slowest group of boundary propagations are labelled as advective features in this text. These features are the least well understood. They are common to all model configurations apart from the prescribed density runs (CPD). The CPD runs have no surface buoyancy forcing, and therefore they have no abyssal circulation. It is therefore argued that ether an abyssal circulation or surface buoyancy forcing facilitates the advective features. The advective features typically propagate between 0.01 and 0.05 m $s^{-1}$, between 1200m and 4000m depth, they are commonly carried by the maximum in meridional abyssal circulation. Particles released in the source region of these propagations follow a similar path, with similar velocity, as shown in Figure 5.15. This suggests that the advective features are likely to be driven by an advection of anomaly fields. Additional support for the argument that the features are advective comes from the sloped walls sub-configuration (SSBS). This configuration shows an anomaly that moves both along the western boundary and down the topographic slope, into the centre of the gyre basin. A wave feature would not exhibit this dual movement, particularly the movement down-slope.

It is noted that all boundary features propagate a cold anomaly along the western boundary. This is interesting because observations show a warming of abyssal waters in the real ocean, and the Meredith et al. (2008) wind-control hypothesis suggests that an increase in wind-stress should be associated with a warm anomaly propagating northwards.

If the Meredith et al. (2008) hypothesis is accurate, then the gyre model's results suggest that gyre model is not accurately simulating a key feature of the Weddell Gyre system. This key feature could be related to model resolution. Where, the general adjustment of the model appears to be sensitive to model parameters, such as viscosity, which depend on model resolution. Alternatively, it could be related to an absent geographical feature, such as the Scotia Sea ridge, or circumpolar current.

The results of the gyre model do suggest that the simplified dynamics it simulates (with its given domain, and resolution) are not sufficient to justify a causal link between an increase in surface wind forcing and deep water warming. The gyre model does however; clearly suggest a boundary propagation link between surface wind forcing and abyssal water properties.

# Chapter 6

# Conclusions

## 6.1 Introduction

As noted in chapter 1 and throughout this thesis, the Southern Ocean is a dynamically interesting region that plays a disproportionately important role in global climate processes. Furthermore, it is a remote and hazardous region, and it is therefore poorly observed. Over recent decades the Southern Ocean, and in particular the Antarctic Subpolar Seas, have been forced by multiple climatic perturbations in wind and buoyancy forcing (e.g. Marshall, 2003; Rye et al., 2014). Therefore, consideration of the Southern Ocean's response to these perturbations is timely.

This thesis discusses two key research areas, both of which consider the response of the Southern Ocean circulation to changes in surface forcing. First, the rapid rise of SSH in the Antarctic Subpolar Seas, and its relation to increasing mass loss from the Antarctic Ice Sheet. Second, the response of the Subpolar Sea's gyres to increased surface wind forcing.

The present chapter reviews the main findings of this thesis; provides additional discussion of the work from previous chapters; suggests areas for future work; and offers some concluding remarks.

## 6.2 Conclusions

Chapters 2 and 3 discuss the Subpolar Sea SSH anomaly (Rye et al., 2014), where austral summer satellite altimetry measurements, between 1992 and 2011, exhibit a pronounced circumpolar rise in sea level across the Antarctic Subpolar Seas. The anomaly has a magnitude of 1-5 mm $\text{yr}^{-1}$ above the global mean that increases towards the continent. The circumpolar average trend is 2 ± 0.8 mm $\text{yr}^{-1}$ above the mean rate of sea level rise south of 50 $^o$S, and 1.2 ± 1.5 mm $yr^{-1}$ above the global-mean rate. Clear inter-regional variability in the SSH time-series is observed, with variations around the Antarctic continent that warrant further research.

Several lines of evidence suggest that the Subpolar Sea SSH anomaly is a steric response to the recent decadal increase in Antarctic glacial runoff. This link is first implied by the coastal enhancement and topographically constrained character of the sea level rise anomaly. In addition, sparse *in-situ* observations indicate a Subpolar Sea surface freshening, of O(0.01) per decade, over recent decades. This observed freshening is associated with a steric rise in sea level of between 0.5 and 3.3 mm $yr^{-1}$ (e.g. Jacobs and Giulivi, 2010, Jacobs et al., 2002, Aoki et al., 2005), which roughly agrees with the satellite-observed Subpolar Sea SSH trend. Moreover, Jacobs et al. (2002) uses isotopic tracer analyses to show an increasing fraction of glacial water in shelf waters of the Amundsen and Ross seas. A warming of Southern Ocean deep waters has also been observed over recent decades, is associated with a comparable steric rise in sea level (Purkey and Johnson, 2010, 2013).

In chapter 3, an ocean GCM is used to simulate the response of the Antarctic Subpolar Seas to a realistic increase in glacial run-off of 300 Gt $yr^{-1}$. The resulting barystatic response to increased freshwater forcing is found to produce a SSH anomaly with a distribution in agreement with SSH observations, but with a magnitude much smaller than observations. The steric response is shown to produce both a distribution and magnitude that are in close agreement with satellite SSH observations. In addition, the model output provides detailed information on the causes of the steric response. Here we find that approximately half of the steric change in sea level is driven directly by freshening, with the remainder driven by warming. The warming response is inferred to result from changes in circulation or isopycnal heave (shoaling). The majority of the warming signal in the model is concentrated in the deep ocean below 800 meters, whereas the majority of the freshening signal is concentrated in the surface 800 meters. This distribution is in broad agreement with observations.

Furthermore, the amount of freshwater required to drive the observed increase in regional steric sea level (if it were solely driven by the addition of freshwater) can be estimated from satellite observations, using the linear equation-of-state approximation and basic physical principles (Munk, 2003; see section 2.2.3.1). To account for the amplifying effect of the thermosteric response, the initial estimate is halved. This gives an estimate of 430 ± 230 Gt $yr^{-1}$. This estimate is then in good agreement with the observed trend in Antarctic discharge of 350 ± 100 Gt yr $^{-1}$ (Shepherd et al., 2012).

Additional (non-glacial) sources of halosteric change must also be considered, although there is little evidence to suggest that they are significant. For example, climate models commonly simulate an increase in Antarctic precipitation over the late 20th and the early 21st centuries, in response to changes in global climatic forcing (Masson-Delmotte et al. 2006, Genthon, Krinner and Castebrunet 2009). Atmospheric reanalyses are currently too uncertain to assess whether this predicted precipitation increase is occurring (Masson-Delmotte et al. 2006). Similarly, a significant reduction in sea ice volume may have contributed to halosteric see level rise. While this possibility cannot be excluded due to the scarcity of sea ice thickness measurements, it seems highly unlikely given satellite observations that show Antarctic sea ice area increasing slightly over recent decades (Bromwich et al. 2011).

Following discussion of steric forcing, variability in Southern Ocean winds is suggested to provide a minor component of the observed trend in SSH. A linear relationship between Antarctic Subpolar Sea SSH and Ekman transport (out of the Subpolar Sea) is observed using atmospheric reanalysis data. The trend in Subpolar Sea SSH derived from this relationship accounts for around 1/5th of the observed SSH signal.

Chapters 4 and 5 document a modeling study, which simulates the adjustment of an idealised southern subpolar gyre to wind forcing pertubations. This study is motivated by observations of two key Southern Ocean climate trends. The increase in eastward wind forcing, associated with the increasing trend in the SAM, and the global warming of AABW.

Chapter 4 describes the development of the model configuration. Which is designed to directly explore the dynamics of a southern subpolar gyre following the recent decadal trend in Southern Ocean eastward wind stress. Particular interest is directed towards analysis of the response of the abyssal circulation, following an increase in wind stress. Chapter 5 presents the results of model experiments.

The model is a simplified regional configuration of the MITgcm ocean model, referred to as the gyre model. It is a $1^o$ resolution, Boussinesq, primitive equation model. It is forced at the surface by constant wind and buoyancy forcing. It has a temperature, and velocity, restoring layer at its northern edge that dampens boundary waves, and it has enhanced vertical diffusivity at its northern edge to support a strong overturning circulation. The gyre model has four sub-configurations of ranging complexity. The model is allowed to 'spin–up' to a steady-state over around 2000 years, and it is then examined for its response to a 20% step–increase in surface wind forcing.

As suggested by Meredith et al. (2008), the gyre model's response to a step increase in surface wind forcing drives a spin-up of the southern gyre and a doming of density surfaces, shown in Figures (5.24-5.25). These findings support the wind-control hypothesis, but the but the model results also reveal the underpinning adjustment dynamics. Figure (5.26) shows that the movement of isopycnals occurs non-uniformly around the edge of the gyre, the most prominent movement occurring on the eastern edge, causing the gyre to elongate zonally. Furthermore, the isopycnal slope is reduced close to sloping topography, therefore, topography may play an important role, particularly if there is a ridge at the north of the gyre.

Waves and advective features dominate the western boundary anomaly in the gyre model. These propagating features appear consistently and are found in all model sub configurations. The features are difficult to compare directly to classical adjustment theory or, real-world observations. They are similar to features described by previous, low–resolution, modelling studies (e.g., Doscher et al., 1996; Capotondi, 2000; Goodman, 2001; Getzlaff et al., 2005), and by the theory of e.g. Marshall and Johnson (2013). The ways in which these boundary features are excited, and propagate, show similarities to real–world observations, and theory (Vallis, 2006,Gill, 1982). It is argued that these features provide insight both into the adjustment of a southern polar gyre to a change in wind stress, and into issues in ocean model design. The first baroclinic mode boundary waves, predicated by classical theory, propagating at 1 m $s^{-1}$, are not found in any configuration of the gyre model.

Two distinct types of boundary propagations occur in the gyre model. The fastest group are labelled in this text as numerical short boundary waves, NSBW, following the work of Marshall and Johnson (2013) and Killworth (1985). These waves have typical propagation speeds of 0.05 to 0.5 m $s^{-1}$, and a typical width of $5^o$ (15 times the local Rossby radius). Analysis of these features suggests that viscous parameters play an important role in their balance of terms. Further, model runs with higher magnitude viscosity parameters either exhibit slower NSBW waves or no NSBW waves. They are typically excited in relation to a change in vertical transport within the first 20 days, and transit the domain within the first 100 days (following a change in winds). These features tend to typically propagate around 1200 m depth, at the base of the thermocline, or the wind-driven layer.

The slowest group of boundary propagating features are labelled as advective features in this text. These features are the least well understood. They are found in all model configurations apart from the prescribed density runs (CPD). The CPD runs have no surface buoyancy forcing, and therefore they have no abyssal circulation. It is argued that ether an abyssal circulation or surface buoyancy forcing is needed to facilitate the advective features. The advective features typically propagate between 0.01 and 0.05 m $s^{-1}$, between 1200m and 4000m depth. They are commonly associated with the maximum in meridional abyssal circulation. The path lines of Lagrangian particles released in the source region of these propagating features follow a similar path, with similar velocity, as shown in Figure (5.23). This suggests that the advective features are likely to driven by the advection of temperature anomalies. Additional support for the argument that the features are advective comes from the sloped walls sub-configuration (SSBS). This configuration shows an anomaly that moves both along the western boundary and down the topographic slope, into the centre of the gyre basin. A wave feature would not exhibit this dual movement, particularly the movement down-slope.

It is noted that all boundary features propagate a cold anomaly along the western boundary. This is interesting because real-world observations show a warming of abyssal waters, and the Meredith et al. (2008) wind-control hypothesis suggests that an increase in wind-stress should be associated with a warm anomaly propagating northwards.

For both the faster and slower types of boundary wave propagations, the depth and magnitude of the boundary features appear to vary considerably following minor adjustments in model parameters, such as viscosity, diffusivity and background GM diffusivity. This is highlighted by differences in model response between sub-configurations.

Aside from the concern of deep water export from the Weddell gyre, the gyre model provides valuable insight into features of a gyres barotropic adjustment that have not been previously documented. These features are probably unimportant for the export of deep water from the region. For example, the basin-wide inertial oscillations discussed in section (5.3.1). These features are also found in other GCM models, discussed by Blaker et al. (2012). Furthermore the seiche also discussed in section (5.3.1), is an interesting feature that agrees well with classical theory.

## 6.3 Outstanding Work

Further work is required to understand the spatial variability of the Subpolar Sea SSH trend, and the link between the surface freshening and deep warming seen in model output. This work may be done through further analysis of current NEMO model output. In particular using a Lagrangian particle tracking routine with current model output would be insightful. For example it may help to determine advective from wave driven processes. In addition, higher-resolution model simulations (ideally 1/4 of a degree or higher), which are able to accurately represent boundary waves, may provide a more detailed and accurate view of the regions response to increased freshwater forcing. The comparison of low to high-resolution simulations should also provide insight into the effect of model resolution on baroclinic adjustment processes, which will be of interest to both the study of the Subpolar Sea freshening, and AABW warming.

Following the results of the gyre model it is clear further work is required to increase understanding of boundary waves in low-resolution models. It would be useful to do additional runs with the gyre model at an increased resolution, where the local Rossby radius is resolved, ideally 1/4 of a degree or higher. This higher resolution configuration could be examined with a range of viscosity, and GM parameterisations, and compared to the lower resolution model. The aim of this would be to produce a realistic simulation of a first-mode baroclinic boundary wave, and then to examine the differences between a model that accurately represents boundary waves and the current low-resolution version. An additional MITgcm configuration with resolution and parameterisations that change with latitude (as is the case with some low-resolution ocean models) could also be used to examine the behaviour of boundary waves in this domain. Furthermore, Killworth (1985), suggests that the formulation of the zonal velocity at the model boundary may be a factor in boundary wave propagation, therefore it may be informative to run low-resolution adjustment experiments (gyre models) with a range of commonly used ocean models e.g. NEMO, MOM. To test if all commonly used, z-level, low-resolution models perform similarly.

In order to further understand deep-water export from a southern subpolar gyre, further analysis of the mechanisms that excite boundary waves in the gyre model is required. In addition, a number of features should be added to the model to better represent the deep outflows from the Antarctic Subpolar Seas. This could be done with the current low-resolution configuration, a higher resolution version, or both. A ridge representing the Scotia Ridge at the northern boundary of the southern gyre should be added. This ridge may act as a barrier to the northward propagation of boundary waves, and therefore alter the adjustment of deep circulation to a change in wind stress. For example, the presence of a ridge could enhance the movement of isopycnals at the northern edge of the southern gyre after an increase in surface wind stress. An ACC-like open-boundary north of the southern gyre should also be added, both with and without the ridge. The presence of an ACC will alter the interaction between the southern and northern gyres, isolating the surface flows in the two gyres. An additional channel in the ridge may also be added to represent Orkney passage. The Orkney passage provides a pathway for the majority of dense water export from the Weddell gyre, therefore it may permit important dynamics.

The processes that occur leading to the passage of AABW water from Antarctic Subpolar Sea to global ocean may depend on seasonal processes and specific topographic features. Following additional idealised modelling, a more realistic, eddy resolving model of the Weddell Sea, Scotia Sea and South Atlantic, would provide an excellent view of the response of the system to recent climate change, and its role in global AABW warming. Before taking this step however, idealised modelling is required to improve understanding of the mechanisms of adjustment, as previously described.

Finally, direct comparison of model output to real-world observations of boundary waves, or Rossby waves in polar environments would significantly enrich analysis of the gyre model and similar models. These observations may be available in historical datasets, such as satellite altimetry and mooring data. If unavailable, model output could be compared to observations of planetary waves in subtropical regions.

## 6.4 Summary

In summary, it is argued that the local anomaly observed in Subpolar Sea SSH is likely to be driven primarily by the steric response to increased discharge of freshwater from Antarctica. Furthermore, the increased strength of the Southern Ocean winds, in relation to the SAM, may play an important role in modulating the export of AABW from the Antarctic Subpolar Seas. However, further work is required to understand the role of boundary waves and boundary propagations, both in observations and models. Both these findings highlight a number of major climatic perturbations to the Southern Ocean circulation that are currently underway.

# References

Ablain, M., Cazenave, A., Valladeau, G., and Guinehut, S. (2009). A new assessment of the error budget of global mean sea level rate estimated by satellite altimetry over 19932008. *Ocean Science*, 5(2):193–201.

Adcroft, A., Hill, C., and Marshall, J. (1997). Representation of topography by shaved cells in a height coordinate ocean model. *Monthly Weather Review*, 125(9):2293–2315.

Adcroft, A., Hill, C., and Marshall, J. (1999). A new treatment of the coriolis terms in c-grid models at both high and low resolutions. *Monthly Weather Review*, 127(8):1928–1936.

Anderson, D. L. and Gill, A. (1975). Spin-up of a stratified ocean, with applications to upwelling. In *Deep Sea Research and Oceanographic Abstracts*, volume 22, pages 583–596. Elsevier.

Andrié, C., Gouriou, Y., Bourles, B., Ternon, J.-F., Braga, E., Morin, P., and Oudot, C. (2003). Variability of aabw properties in the equatorial channel at 35 w. *Geophysical Research Letters*, 30(5).

Aoki, S., Rintoul, S. R., Ushio, S., Watanabe, S., and Bindoff, N. L. (2005). Freshening of the adlie land bottom water near 140e. *Geophysical Research Letters*, 32(23):n/a–n/a.

Arakawa, A. and Lamb, V. R. (1977). Computational design of the basic dynamical processes of the ucla general circulation model. *Methods in computational physics*, 17:173–265.

Arhan, M., Heywood, K. J., and King, B. A. (1999). The deep waters from the southern ocean at the entry to the argentine basin. *Deep Sea Research Part II: Topical Studies in Oceanography*, 46(1):475–499.

Baines, P. G. and Condie, S. (1998). Observations and modelling of antarctic downslope flows: a review. *Ocean, Ice, and atmosphere: Interactions at the Antarctic continental margin*, pages 29–49.

Baldwin, M. P. (2001). Annular modes in global daily surface pressure. *Geophysical Research Letters*, 28(21):4115–4118.

Bamber, J., Gomez-Dans, J., and Griggs, J. (2009). A new 1 km digital elevation model of the antarctic derived from combined satellite radar and laser data–part 1: Data and methods. *The Cryosphere*, 3(1):101–111.

Beckley, B., Zelensky, N. P., Holmes, S. A., Lemoine, F. G., Ray, R., Mitchum, G. T., Desai, S., and Brown, S. (2010). Assessment of the jason-2 extension to the topex/-poseidon, jason-1 sea-surface height time series for global mean sea level monitoring. *Marine Geodesy*, 33:447 – 471.

Beckley, B. D., Lemoine, F. G., Luthcke, S. B., Ray, R. D., and Zelensky, N. P. (2007). A reassessment of global and regional mean sea level trends from topex and jason-1 altimetry based on revised reference frame and orbits. *Geophysical Research Letters*, 34(14):n/a–n/a.

Blaker, A. T., Hirschi, J. J., Sinha, B., De Cuevas, B., Alderson, S., Coward, A., and Madec, G. (2012). Large near-inertial oscillations of the atlantic meridional overturning circulation. *Ocean Modelling*, 42:50–56.

Böning, C. W., Dispert, A., Visbeck, M., Rintoul, S., and Schwarzkopf, F. U. (2008). The response of the antarctic circumpolar current to recent climate change. *Nature Geoscience*, 1(12):864–869.

Bracegirdle, T. J. and Marshall, G. J. (2012). The reliability of antarctic tropospheric pressure and temperature in the latest global reanalyses. *Journal of Climate*, 25(20):7138–7146.

Bromwich, D. H., Nicolas, J. P., and Monaghan, A. J. (2011). An assessment of precipitation changes over antarctica and the southern ocean since 1989 in contemporary global reanalyses*. *Journal of Climate*, 24(16):4189–4209.

Bryan, K. (1996). The steric component of sea level rise associated with enhanced greenhouse warming: a model study. *Climate Dynamics*, 12(8):545–555.

Capotondi, A. (2000). Oceanic wave dynamics and interdecadal variability in a climate system model. *Journal of Geophysical Research: Oceans (1978–2012)*, 105(C1):1017–1036.

Carter, L., McCave, I., and Williams, M. J. (2008). Chapter 4 circulation and water masses of the southern ocean: A review. In Florindo, F. and Siegert, M., editors, *Antarctic Climate Evolution*, volume 8 of *Developments in Earth and Environmental Sciences*, pages 85 – 114. Elsevier.

Chambers, D. P., Wahr, J., Tamisiea, M. E., and Nerem, R. S. (2010). Ocean mass from grace and glacial isostatic adjustment. *Journal of Geophysical Research: Solid Earth*, 115(B11):n/a–n/a.

Chelton, D. B., Schlax, M. G., Samelson, R. M., and de Szoeke, R. A. (2007). Global observations of large oceanic eddies. *Geophysical Research Letters*, 34(15).

Chiang, J. C., Cheng, W., and Bitz, C. M. (2008). Fast teleconnections to the tropical atlantic sector from atlantic thermohaline adjustment. *Geophysical Research Letters*, 35(7).

Church, J. A. and White, N. J. (2011). Sea-level rise from the late 19th to the early 21st century. *Surveys in Geophysics*, 32(4-5):585–602.

Clarke, A. and Johnston, N. M. (2003). Antarctic marine benthic diversity. *Oceanography and marine biology*, 41:47–114.

Coles, V. J., McCartney, M. S., Olson, D. B., and Smethie, W. M. (1996). Changes in antarctic bottom water properties in the western south atlantic in the late 1980s. *JOURNAL OF GEOPHYSICAL RESEARCH-ALL SERIES-*, 101:8957–8970.

Couldrey, M. P., Jullion, L., Naveira Garabato, A. C., Rye, C., Herráiz-Borreguero, L., Brown, P. J., Meredith, M. P., and Speer, K. L. (2013). Remotely induced warming of antarctic bottom water in the eastern weddell gyre. *Geophysical Research Letters*, 40(11):2755–2760.

Cunningham, S., Alderson, S., King, B., and Brandon, M. (2003). Transport and variability of the antarctic circumpolar current in drake passage. *Journal of Geophysical Research: Oceans (1978–2012)*, 108(C5).

Danabasoglu, G., Yeager, S. G., Bailey, D., Behrens, E., Bentsen, M., Bi, D., Biastoch, A., Bning, C., Bozec, A., Canuto, V. M., Cassou, C., Chassignet, E., Coward, A. C., Danilov, S., Diansky, N., Drange, H., Farneti, R., Fernandez, E., Fogli, P. G., Forget, G., Fujii, Y., Griffies, S. M., Gusev, A., Heimbach, P., Howard, A., Jung, T., Kelley, M., Large, W. G., Leboissetier, A., Lu, J., Madec, G., Marsland, S. J., Masina, S., Navarra, A., Nurser, A. G., Pirani, A., y Mlia, D. S., Samuels, B. L., Scheinert, M., Sidorenko, D., Treguier, A.-M., Tsujino, H., Uotila, P., Valcke, S., Voldoire, A., and Wang, Q. (2014). North atlantic simulations in coordinated ocean-ice reference experiments phase {II} (core-ii). part i: Mean states. *Ocean Modelling*, 73(0):76 – 107.

Deacon, G. (1937). The hydrology of the southern ocean, discovery rep. 15. *Inst. of Oceanogr. Sci., Southampton, UK*, pages 3–122.

Dee, D. P., Uppala, S. M., Simmons, A. J., Berrisford, P., Poli, P., Kobayashi, S., Andrae, U., Balmaseda, M. A., Balsamo, G., Bauer, P., Bechtold, P., Beljaars, A. C. M., van de Berg, L., Bidlot, J., Bormann, N., Delsol, C., Dragani, R., Fuentes, M., Geer, A. J., Haimberger, L., Healy, S. B., Hersbach, H., Hlm, E. V., Isaksen, L., Kllberg, P., Khler, M., Matricardi, M., McNally, A. P., Monge-Sanz, B. M., Morcrette, J.-J., Park, B.-K., Peubey, C., de Rosnay, P., Tavolato, C., Thpaut, J.-N., and Vitart, F. (2011). The era-interim reanalysis: configuration and performance of the data assimilation system. *Quarterly Journal of the Royal Meteorological Society*, 137(656):553–597.

Depoorter, M., Bamber, J., Griggs, J., Lenaerts, J., Ligtenberg, S., van den Broeke, M., and Moholdt, G. (2013). Calving fluxes and basal melt rates of antarctic ice shelves. *Nature*.

Dewar, W. (1998). On too fast baroclinic planetary waves in the general circulation. *Journal of physical oceanography*, 28(9):1739–1758.

Doscher, R., Boning, C., and Herrmann, P. (1996). Response of circulation and heat transport in the north atlantic to changes in thermohaline forcing in northern latitudes: a model study. *Oceanographic Literature Review*, 4(43):328.

Downes, S. M., Farneti, R., Uotila, P., Griffies, S. M., Marsland, S. J., Bailey, D., Behrens, E., Bentsen, M., Bi, D., Biastoch, A., et al. (2015). An assessment of southern ocean water masses and sea ice during 1988-2007 in a suite of inter-annual core-ii simulations. *Ocean Modelling*.

Ekman, V. W. (1902). *Om jordrotationens inverkan på vindströmmar i hafvet...*

Elipot, S., Hughes, C., Olhede, S., and Toole, J. (2013). Coherence of western boundary pressure at the rapid wave array: boundary wave adjustments or deep western boundary current advection? *Journal of Physical Oceanography*, 43(4):744–765.

Fahrbach, E., Hoppema, M., Rohardt, G., Boebel, O., Klatt, O., and Wisotzki, A. (2011). Warming of deep and abyssal water masses along the greenwich meridian on decadal time scales: The weddell gyre as a heat buffer. *Deep Sea Research Part II: Topical Studies in Oceanography*, 58(25):2509–2523.

Fahrbach, E., Rohardt, G., Schröder, M., and Strass, V. (1994). Transport and structure of the weddell gyre. In *Annales Geophysicae*, volume 12, pages 840–855. Springer.

Foldvik, A., Gammelsrød, T., Østerhus, S., Fahrbach, E., Rohardt, G., Schröder, M., Nicholls, K. W., Padman, L., and Woodgate, R. (2004). Ice shelf water overflow and bottom water formation in the southern weddell sea. *Journal of Geophysical Research: Oceans (1978–2012)*, 109(C2).

Foster, T. D. and Carmack, E. C. (1976). Frontal zone mixing and antarctic bottom water formation in the southern weddell sea. In *Deep Sea Research and Oceanographic Abstracts*, volume 23, pages 301–317. Elsevier.

Fyfe, J., Boer, G., and Flato, G. (1999). The arctic and antarctic oscillations and their projected changes under global warming. *Geophysical Research Letters*, 26(11):1601–1604.

Fyfe, J. C. and Saenko, O. A. (2005). Human-induced change in the antarctic circumpolar current. *Journal of climate*, 18(15):3068–3073.

Garabato, A. C. N., Heywood, K. J., and Stevens, D. P. (2002a). Modification and pathways of southern ocean deep waters in the scotia sea. *Deep Sea Research Part I: Oceanographic Research Papers*, 49(4):681–705.

Garabato, A. C. N., McDonagh, E. L., Stevens, D. P., Heywood, K. J., and Sanders, R. J. (2002b). On the export of antarctic bottom water from the weddell sea. *Deep Sea Research Part II: Topical Studies in Oceanography*, 49(21):4715–4742.

Gent, P. R. and Mcwilliams, J. C. (1990). Isopycnal mixing in ocean circulation models. *Journal of Physical Oceanography*, 20(1):150–155.

Genthon, C., Krinner, G., and Castebrunet, H. (2009). Antarctic precipitation and climate-change predictions: horizontal resolution and margin vs plateau issues. *Annals of glaciology*, 50(50):55–60.

Getzlaff, J., Böning, C. W., Eden, C., and Biastoch, A. (2005). Signal propagation related to the north atlantic overturning. *Geophysical research letters*, 32(9).

Gill, A. (1973). Circulation and bottom water production in the weddell sea. In *Deep Sea Research and Oceanographic Abstracts*, volume 20, pages 111–140. Elsevier.

Gill, A. E. (1982). *Atmosphere-ocean dynamics*, volume 30. Academic press.

Gille, S. T. (2002). Warming of the southern ocean since the 1950s. *Science*, 295(5558):1275–1277.

Gille, S. T. (2008). Decadal-scale temperature trends in the southern hemisphere ocean. *Journal of Climate*, 21(18):4749–4765.

Gong, D. and Wang, S. (1998). Antarctic oscillation: concept and applications. *Chinese Science Bulletin*, 43(9):734–738.

Gong, D. and Wang, S. (1999). Definition of antarctic oscillation index. *Geophysical Research Letters*, 26(4):459–462.

Goodman, P. J. (2001). Thermohaline adjustment and advection in an ogcm*. *Journal of physical oceanography*, 31(6):1477–1497.

Gordon, A. L., Visbeck, M., and Huber, B. (2001). Export of weddell sea deep and bottom water. *Journal of Geophysical Research: Oceans (1978–2012)*, 106(C5):9005–9017.

Graham, R. M., Boer, A. M., Heywood, K. J., Chapman, M. R., and Stevens, D. P. (2012). Southern ocean fronts: Controlled by wind or topography? *Journal of Geophysical Research: Oceans (1978–2012)*, 117(C8).

Greatbatch, R. J. and Lu, J. (2003). Reconciling the stommel box model with the stommel-arons model: A possible role for southern hemisphere wind forcing? *Journal of Physical Oceanography*, 33(8):1618–1632.

Gregory, J., White, N., Church, J., Bierkens, M., Box, J., Van den Broeke, M., Cogley, J., Fettweis, X., Hanna, E., Huybrechts, P., et al. (2013). Twentieth-century global-mean sea level rise: Is the whole greater than the sum of the parts? *Journal of Climate*, 26(13):4476–4499.

Hallberg, R. and Gnanadesikan, A. (2001). An exploration of the role of transient eddies in determining the transport of a zonally reentrant current. *Journal of Physical Oceanography*, 31(11):3312–3330.

Hellmer, H. H., Huhn, O., Gomis, D., and Timmermann, R. (2011). On the freshening of the northwestern weddell sea continental shelf. *Ocean Science*, 7(3):305–316.

Heywood, K. J., Garabato, A. C. N., and Stevens, D. P. (2002). High mixing rates in the abyssal southern ocean. *Nature*, 415(6875):1011–1014.

Heywood, K. J., Naveira Garabato, A. C., Stevens, D. P., and Muench, R. D. (2004). On the fate of the antarctic slope front and the origin of the weddell front. *Journal of Geophysical Research: Oceans (1978–2012)*, 109(C6).

Hodson, D. L. and Sutton, R. T. (2012). The impact of resolution on the adjustment and decadal variability of the atlantic meridional overturning circulation in a coupled climate model. *Climate dynamics*, 39(12):3057–3073.

Hogg, A. M. C. and Blundell, J. R. (2006). Interdecadal variability of the southern ocean. *Journal of physical oceanography*, 36(8):1626–1645.

Hogg, A. M. C., Meredith, M. P., Blundell, J. R., and Wilson, C. (2008). Eddy heat flux in the southern ocean: Response to variable wind forcing. *Journal of Climate*, 21(4):608–620.

Holland, P. R., Bruneau, N., Enright, C., Losch, M., Kurtz, N. T., and Kwok, R. (2014). Modeled trends in antarctic sea ice thickness. *Journal of Climate*, 27(10):3784–3801.

Holland, P. R. and Kwok, R. (2012). Wind-driven trends in antarctic sea-ice drift. *Nature Geoscience*, 5(12):872–875.

Holland, W. R. and Lin, L. B. (1975). On the generation of mesoscale eddies and their contribution to the oceanicgeneral circulation. i. a preliminary numerical experiment. *Journal of Physical Oceanography*, 5(4):642–657.

Hsieh, W. W. and Bryan, K. (1996). Redistribution of sea level rise associated with enhanced greenhouse warming: a simple model study. *Climate Dynamics*, 12(8):535–544.

Hsieh, W. W., Davey, M. K., and Wajsowicz, R. C. (1983). The free kelvin wave in finite-difference numerical models. *Journal of Physical Oceanography*, 13(8):1383–1397.

Ivchenko, V., Zalesny, V., and Drinkwater, M. (2004). Can the equatorial ocean quickly respond to antarctic sea ice/salinity anomalies? *Geophysical Research Letters*, 31(15).

Jackson, L., Hughes, C. W., and Williams, R. G. (2006). Topographic control of basin and channel flows: The role of bottom pressure torques and friction. *Journal of physical oceanography*, 36(9):1786–1805.

Jacobs, S. (2006). Observations of change in the southern ocean. *Philosophical Transactions of the Royal Society of London A: Mathematical, Physical and Engineering Sciences*, 364(1844):1657–1681.

Jacobs, S. S. (2004). Bottom water production and its links with the thermohaline circulation. *Antarctic Science*, 16(04):427–437.

Jacobs, S. S. and Giulivi, C. F. (2010). Large multidecadal salinity trends near the pacific-antarctic continental margin. *Journal of Climate*, 23(17):4508–4524.

Jacobs, S. S., Giulivi, C. F., and Mele, P. A. (2002). Freshening of the ross sea during the late 20th century. *Science*, 297(5580):386–389.

Jacobs, S. S., Jenkins, A., Giulivi, C. F., and Dutrieux, P. (2011). Stronger ocean circulation and increased melting under pine island glacier ice shelf. *Nature Geoscience*, 4(8):519–523.

Jenkins, A., Dutrieux, P., Jacobs, S. S., McPhail, S. D., Perrett, J. R., Webb, A. T., and White, D. (2010). Observations beneath pine island glacier in west antarctica and implications for its retreat. *Nature Geoscience*, 3(7):468–472.

Johnson, G. C. and Doney, S. C. (2006). Recent western south atlantic bottom water warming. *Geophysical Research Letters*, 33(14).

Johnson, G. C., Purkey, S. G., and Bullister, J. L. (2008). Warming and freshening in the abyssal southeastern indian ocean*. *Journal of Climate*, 21(20):5351–5363.

Jones, J. (2012). Climate science: Tree rings and storm tracks. *Nature Geoscience*, 5(11):764–765.

Jullion, L., Jones, S., Naveira Garabato, A., and Meredith, M. (2010). Wind-controlled export of antarctic bottom water from the weddell sea. *Geophysical Research Letters*, 37(9).

Jullion, L., Naveira Garabato, A. C., Meredith, M. P., Holland, P. R., Courtois, P., and King, B. A. (2013). Decadal freshening of the antarctic bottom water exported from the weddell sea. *Journal of Climate*, 26(20):8111–8125.

Kawase, M. (1987). Establishment of deep ocean circulation driven by deep-water production. *Journal of Physical Oceanography*, 17(12):2294–2317.

Kida, S. (2011). The impact of open oceanic processes on the antarctic bottom water outflows. *Journal of Physical Oceanography*, 41(10):1941–1957.

Kidson, J. W. (1999). Principal modes of southern hemisphere low-frequency variability obtained from ncep-ncar reanalyses. *Journal of Climate*, 12(9):2808–2830.

Kidston, J., Renwick, J., and McGregor, J. (2009). Hemispheric-scale seasonality of the southern annular mode and impacts on the climate of new zealand. *Journal of Climate*, 22(18):4759–4770.

Killworth, P. D. (1985). A two-level wind and buoyancy driven thermocline model. *Journal of physical oceanography*, 15(11):1414–1432.

Killworth, P. D., Chelton, D. B., and de Szoeke, R. A. (1997). The speed of observed and theoretical long extratropical planetary waves. *Journal of Physical Oceanography*, 27(9):1946–1966.

Klatt, O., Fahrbach, E., Hoppema, M., and Rohardt, G. (2005). The transport of the weddell gyre across the prime meridian. *Deep Sea Research Part II: Topical Studies in Oceanography*, 52(3):513–528.

Kushner, P. J., Held, I. M., and Delworth, T. L. (2001). Southern hemisphere atmospheric circulation response to global warming. *Journal of Climate*, 14(10):2238–2249.

LaCasce, J. (2000). Baroclinic rossby waves in a square basin*. *Journal of physical oceanography*, 30(12):3161–3178.

LaCasce, J. and Pedlosky, J. (2004). The instability of rossby basin modes and the oceanic eddy field*. *Journal of physical oceanography*, 34(9):2027–2041.

Large, W. and Yeager, S. (2009). The global climatology of an interannually varying air–sea flux data set. *Climate Dynamics*, 33(2-3):341–364.

Le Traon, P., Nadal, F., and Ducet, N. (1998). An improved mapping method of multisatellite altimeter data. *Journal of atmospheric and oceanic technology*, 15(2):522–534.

Lefebvre, W., Goosse, H., Timmermann, R., and Fichefet, T. (2004). Influence of the southern annular mode on the sea ice–ocean system. *Journal of Geophysical Research: Oceans (1978–2012)*, 109(C9).

Leuliette, E. W. and Miller, L. (2009). Closing the sea level rise budget with altimetry, argo, and grace. *Geophysical Research Letters*, 36(4):n/a–n/a.

Locarnini, R. A., Whitworth, T., and Nowlin, W. D. (1993). The importance of the scotia sea on the outflow of weddell sea deep water. *Journal of Marine Research*, 51(1):135–153.

Lorbacher, K., Marsland, S., Church, J., Griffies, S., and Stammer, D. (2012). Rapid barotropic sea level rise from ice sheet melting. *Journal of Geophysical Research: Oceans (1978–2012)*, 117(C6).

Lumpkin, R. and Speer, K. (2007). Global ocean meridional overturning. *Journal of Physical Oceanography*, 37(10):2550–2562.

Madec, G. (2008). Nemo ocean engine.

Maharaj, A. M., Cipollini, P., Holbrook, N. J., Killworth, P. D., and Blundell, J. R. (2007). An evaluation of the classical and extended rossby wave theories in explaining spectral estimates of the first few baroclinic modes in the south pacific ocean. *Ocean Dynamics*, 57(3):173–187.

Marshall, D. P. and Johnson, H. L. (2013). Propagation of meridional circulation anomalies along western and eastern boundaries. *Journal of Physical Oceanography*, 43(12):2699–2717.

Marshall, G. J. (2003). Trends in the southern annular mode from observations and reanalyses. *Journal of Climate*, 16(24):4134–4143.

Marshall, G. J., Stott, P. A., Turner, J., Connolley, W. M., King, J. C., and Lachlan-Cope, T. A. (2004). Causes of exceptional atmospheric circulation changes in the southern hemisphere. *Geophysical Research Letters*, 31(14).

Marshall, J., Adcroft, A., Hill, C., Perelman, L., and Heisey, C. (1997a). A finite-volume, incompressible navier stokes model for studies of the ocean on parallel computers. *JOURNAL OF GEOPHYSICAL RESEARCH-ALL SERIES-*, 102:5753–5766.

Marshall, J., Hill, C., Perelman, L., and Adcroft, A. (1997b). Hydrostatic, quasi-hydrostatic, and nonhydrostatic ocean modeling. *JOURNAL OF GEOPHYSICAL RESEARCH-ALL SERIES-*, 102:5733–5752.

Marshall, J. and Speer, K. (2012). Closure of the meridional overturning circulation through southern ocean upwelling. *Nature Geoscience*, 5(3):171–180.

Masson-Delmotte, V., Kageyama, M., Braconnot, P., Charbit, S., Krinner, G., Ritz, C., Guilyardi, E., Jouzel, J., Abe-Ouchi, A., Crucifix, M., Gladstone, R., Hewitt, C., Kitoh, A., LeGrande, A., Marti, O., Merkel, U., Motoi, T., Ohgaito, R., Otto-Bliesner, B., Peltier, W., Ross, I., Valdes, P., Vettoretti, G., Weber, S., Wolk, F., and Yu, Y. (2006). Past and future polar amplification of climate change: climate model intercomparisons and ice-core constraints. *Climate Dynamics*, 27(4):437–440.

Massonnet, F., Mathiot, P., Fichefet, T., Goosse, H., König Beatty, C., Vancoppenolle, M., and Lavergne, T. (2013). A model reconstruction of the antarctic sea ice thickness and volume changes over 1980–2008 using data assimilation. *Ocean Modelling*, 64:67–75.

McCartney, M. S. and Donohue, K. A. (2007). A deep cyclonic gyre in the australian–antarctic basin. *Progress in Oceanography*, 75(4):675–750.

Meredith, M. P., Garabato, A. C. N., Gordon, A. L., and Johnson, G. C. (2008). Evolution of the deep and bottom waters of the scotia sea, southern ocean, during 1995-2005*. *Journal of Climate*, 21(13):3327–3343.

Meredith, M. P. and Hogg, A. M. (2006). Circumpolar response of southern ocean eddy activity to a change in the southern annular mode. *Geophysical Research Letters*, 33(16).

Meredith, M. P., Locarnini, R. A., Van Scoy, K. A., Watson, A. J., Heywood, K. J., and King, B. A. (2000). On the sources of weddell gyre antarctic bottom water. *Journal of Geophysical Research: Oceans (1978–2012)*, 105(C1):1093–1104.

Meredith, M. P., Naveira Garabato, A. C., Stevens, D. P., Heywood, K. J., and Sanders, R. J. (2001). Deep and bottom waters in the eastern scotia sea: rapid changes in properties and circulation. *Journal of Physical Oceanography*, 31(8):2157–2168.

Meredith, M. P., Renfrew, I. A., Clarke, A., King, J. C., and Brandon, M. A. (2004). Impact of the 1997/98 enso on upper ocean characteristics in marguerite bay, western antarctic peninsula. *Journal of Geophysical Research: Oceans (1978–2012)*, 109(C9).

Meredith, M. P., Woodworth, P. L., Chereskin, T. K., Marshall, D. P., Allison, L. C., Bigg, G. R., Donohue, K., Heywood, K. J., Hughes, C. W., Hibbert, A., et al. (2011). Sustained monitoring of the southern ocean at drake passage: Past achievements and future priorities. *Reviews of Geophysics*, 49(4).

Munk, W. (2003). Ocean freshening, sea level rising. *Science*, 300(5628):2041–2043.

Munk, W. H. (1950). On the wind-driven ocean circulation. *Journal of meteorology*, 7(2):80–93.

Ohshima, K. I., Fukamachi, Y., Williams, G. D., Nihashi, S., Roquet, F., Kitade, Y., Tamura, T., Hirano, D., Herraiz-Borreguero, L., Field, I., et al. (2013). Antarctic bottom water production by intense sea-ice formation in the cape darnley polynya. *Nature Geoscience*, 6(3):235–240.

Olbers, D., Borowski, D., Völker, C., and WOeLFF, J.-O. (2004). The dynamical balance, transport and circulation of the antarctic circumpolar current. *Antarctic science*, 16(04):439–470.

Orsi, A., Johnson, G., and Bullister, J. (1999). Circulation, mixing, and production of antarctic bottom water. *Progress in Oceanography*, 43(1):55 – 109.

Orsi, A. H., Nowlin Jr, W. D., and Whitworth III, T. (1993). On the circulation and stratification of the weddell gyre. *Deep Sea Research Part I: Oceanographic Research Papers*, 40(1):169–203.

Ozaki, H., Obata, H., Naganobu, M., and Gamo, T. (2009). Long-term bottom water warming in the north ross sea. *Journal of Oceanography*, 65(2):235–244.

Parkinson, C. L. and Cavalieri, D. J. (2012). Antarctic sea ice variability and trends. *The Cryosphere*, 6(4):871–880.

Payne, A. J., Holland, P. R., Shepherd, A. P., Rutt, I. C., Jenkins, A., and Joughin, I. (2007). Numerical modeling of ocean-ice interactions under pine island bay's ice shelf. *Journal of Geophysical Research: Oceans (1978–2012)*, 112(C10).

Prandi, P., Ablain, M., Cazenave, A., and Picot, N. (2012). Sea level variability in the arctic ocean observed by satellite altimetry. *Ocean Science Discussions*, 9(4):2375–2401.

Pritchard, H., Ligtenberg, S., Fricker, H., Vaughan, D., Van den Broeke, M., and Padman, L. (2012). Antarctic ice-sheet loss driven by basal melting of ice shelves. *Nature*, 484(7395):502–505.

Purkey, S. G. and Johnson, G. C. (2010). Warming of global abyssal and deep southern ocean waters between the 1990s and 2000s: Contributions to global heat and sea level rise budgets*. *Journal of Climate*, 23(23):6336–6351.

Purkey, S. G. and Johnson, G. C. (2012). Global contraction of antarctic bottom water between the 1980s and 2000s*. *Journal of Climate*, 25(17):5830–5844.

Purkey, S. G. and Johnson, G. C. (2013). Antarctic bottom water warming and freshening: Contributions to sea level rise, ocean freshwater budgets, and global heat gain*. *Journal of Climate*, 26(16):6105–6122.

Rau, F., Mauz, F., de Angelis, H., Jaña, R., Neto, J. A., Skvarca, P., Vogt, S., Saurer, H., and Gossmann, H. (2004). Variations of glacier frontal positions on the northern antarctic peninsula. *Annals of Glaciology*, 39(1):525–530.

Redi, M. H. (1982). Oceanic isopycnal mixing by coordinate rotation. *Journal of Physical Oceanography*, 12(10):1154–1158.

Reynolds, R. W. and Marsico, D. C. (1993). An improved real-time global sea surface temperature analysis. *Journal of climate*, 6(1):114–119.

Ridgway, K., Dunn, J., and Wilkin, J. (2002). Ocean interpolation by four-dimensional weighted least squares-application to the waters around australasia. *Journal of Atmospheric and Oceanic Technology*, 19(9):1357–1375.

Rignot, E. (1998). Fast recession of a west antarctic glacier. *Science*, 281(5376):549–551.

Rignot, E., Jacobs, S., Mouginot, J., and Scheuchl, B. (2013). Ice-shelf melting around antarctica. *Science*, 341(6143):266–270.

Rignot, E., Velicogna, I., Van den Broeke, M., Monaghan, A., and Lenaerts, J. (2011). Acceleration of the contribution of the greenland and antarctic ice sheets to sea level rise. *Geophysical Research Letters*, 38(5).

Rintoul, S., Hughes, C., and Olbers, D. (2001). The antarctic circumpolar current system. *In: Ocean Circulation and Climate/G. Siedler, J. Church and J. Gould, eds. New York: Academic Press. p.*, pages 271–302.

Riva, R. E. M., Bamber, J. L., Lavalle, D. A., and Wouters, B. (2010). Sea-level fingerprint of continental water and ice mass change from grace. *Geophysical Research Letters*, 37(19):n/a–n/a.

Scambos, T. A., Hulbe, C., Fahnestock, M., and Bohlander, J. (2000). The link between climate warming and break-up of ice shelves in the antarctic peninsula. *Journal of Glaciology*, 46(154):516–530.

Schlitzer, R. (2000). Electronic atlas of woce hydrographic and tracer data now available. *EOS, Transactions American Geophysical Union*, 81(5):45–45.

Schmidtko, S., Heywood, K. J., Thompson, A. F., and Aoki, S. (2014). Multidecadal warming of antarctic waters. *Science*, 346(6214):1227–1231.

Schmitz, W. J. (1995). On the interbasin-scale thermohaline circulation. *Reviews of Geophysics*, 33(2):151–173.

Sen Gupta, A. and England, M. H. (2006). Coupled ocean-atmosphere-ice response to variations in the southern annular mode. *Journal of Climate*, 19(18):4457–4486.

Shepherd, A., Ivins, E. R., A, G., Barletta, V. R., Bentley, M. J., Bettadpur, S., Briggs, K. H., Bromwich, D. H., Forsberg, R., Galin, N., Horwath, M., Jacobs, S., Joughin, I., King, M. A., Lenaerts, J. T. M., Li, J., Ligtenberg, S. R. M., Luckman, A., Luthcke, S. B., McMillan, M., Meister, R., Milne, G., Mouginot, J., Muir, A., Nicolas, J. P., Paden, J., Payne, A. J., Pritchard, H., Rignot, E., Rott, H., Srensen, L. S., Scambos, T. A., Scheuchl, B., Schrama, E. J. O., Smith, B., Sundal, A. V., van Angelen, J. H., van de Berg, W. J., van den Broeke, M. R., Vaughan, D. G., Velicogna, I., Wahr, J., Whitehouse, P. L., Wingham, D. J., Yi, D., and Young, Duncan a nd Zwally, H. J. (2012). A reconciled estimate of ice-sheet mass balance. *Science*, 338(6111):1183–1189.

Shepherd, A., Wingham, D., and Rignot, E. (2004). Warm ocean is eroding west antarctic ice sheet. *Geophysical Research Letters*, 31(23):n/a–n/a.

Shepherd, A., Wingham, D., Wallis, D., Giles, K., Laxon, S., and Sundal, A. V. (2010). Recent loss of floating ice and the consequent sea level contribution. *Geophysical Research Letters*, 37(13):n/a–n/a.

Shepherd, A., Wingham, D. J., Mansley, J. A., and Corr, H. F. (2001). Inland thinning of pine island glacier, west antarctica. *Science*, 291(5505):862–864.

Siedler, G., Gould, J., and Church, J. A. (2001). *Ocean circulation and climate: observing and modelling the global ocean*, volume 103. Academic Press.

Smedsrud, L. H., Jenkins, A., Holland, D. M., and Nøst, O. A. (2006). Modeling ocean processes below fimbulisen, antarctica. *Journal of Geophysical Research: Oceans (1978–2012)*, 111(C1).

Smith, W. H. and Sandwell, D. T. (1997). Global sea floor topography from satellite altimetry and ship depth soundings. *Science*, 277(5334):1956–1962.

Sokolov, S. and Rintoul, S. R. (2002). Structure of southern ocean fronts at 140 e. *Journal of Marine Systems*, 37(1):151–184.

Sokolov, S. and Rintoul, S. R. (2007a). Multiple jets of the antarctic circumpolar current south of australia*. *Journal of Physical Oceanography*, 37(5):1394–1412.

Sokolov, S. and Rintoul, S. R. (2007b). On the relationship between fronts of the antarctic circumpolar current and surface chlorophyll concentrations in the southern ocean. *Journal of Geophysical Research: Oceans (1978–2012)*, 112(C7).

Sokolov, S. and Rintoul, S. R. (2009a). Circumpolar structure and distribution of the antarctic circumpolar current fronts: 1. mean circumpolar paths. *Journal of Geophysical Research: Oceans (1978–2012)*, 114(C11).

Sokolov, S. and Rintoul, S. R. (2009b). Circumpolar structure and distribution of the antarctic circumpolar current fronts: 1. mean circumpolar paths. *Journal of Geophysical Research: Oceans (1978–2012)*, 114(C11).

Sokolov, S. and Rintoul, S. R. (2009c). Circumpolar structure and distribution of the antarctic circumpolar current fronts: 2. variability and relationship to sea surface height. *Journal of Geophysical Research: Oceans (1978–2012)*, 114(C11).

Speer, K., Rintoul, S. R., and Sloyan, B. (2000). The diabatic deacon cell*. *Journal of physical oceanography*, 30(12):3212–3222.

Stammer, D. (2008). Response of the global ocean to greenland and antarctic ice melting. *Journal of Geophysical Research: Oceans*, 113(C6):n/a–n/a.

Stommel, H. (1948). The westward intensification of wind-driven ocean currents. *Eos, Transactions American Geophysical Union*, 29(2):202–206.

Stommel, H. (1961). Thermohaline convection with two stable regimes of flow. *Tellus A*, 13(2).

Stommel, H. and Arons, A. B. (1960). On the abyssal circulation of the world oceanii. an idealized model of the circulation pattern and amplitude in oceanic basins. *Deep Sea Research (1953)*, 6:217–233.

Straub, D. N. (1996). An inconsistency between two classical models of the ocean buoyancy driven circulation. *Tellus A*, 48(3):477–481.

Sverdrup, H. U. (1947). Wind-driven currents in a baroclinic ocean; with application to the equatorial currents of the eastern pacific. *Proceedings of the National Academy of Sciences of the United States of America*, 33(11):318.

Tamisiea, M. E. (2011). Ongoing glacial isostatic contributions to observations of sea level change. *Geophysical Journal International*, 186(3):1036–1044.

Thompson, D. W. and Solomon, S. (2002). Interpretation of recent southern hemisphere climate change. *Science*, 296(5569):895–899.

Thompson, D. W. and Wallace, J. M. (2000). Annular modes in the extratropical circulation. part i: month-to-month variability*. *Journal of Climate*, 13(5):1000–1016.

Vallis, G. K. (2006). *Atmospheric and oceanic fluid dynamics: fundamentals and large-scale circulation*. Cambridge University Press.

Vaughan, D. G., Marshall, G. J., Connolley, W. M., Parkinson, C., Mulvaney, R., Hodgson, D. A., King, J. C., Pudsey, C. J., and Turner, J. (2003). Recent rapid regional climate warming on the antarctic peninsula. *Climatic change*, 60(3):243–274.

Wang, Q., Danilov, S., Fahrbach, E., Schröter, J., and Jung, T. (2012). On the impact of wind forcing on the seasonal variability of weddell sea bottom water transport. *Geophysical Research Letters*, 39(6).

Whitworth, T., Nowlin, W., Orsi, A., Locarnini, R., and Smith, S. (1994). Weddell sea shelf water in the bransfield strait and weddell-scotia confluence. *Deep Sea Research Part I: Oceanographic Research Papers*, 41(4):629–641.

Winton, M. (1996). The role of horizontal boundaries in parameter sensitivity and decadal-scale variability of coarse-resolution ocean general circulation models. *Journal of physical oceanography*, 26(3):289–304.

Wunsch, C., Ponte, R. M., and Heimbach, P. (2007). Decadal trends in sea level patterns: 1993-2004. *Journal of Climate*, 20(24):5889–5911.

Wüst, G. (1935). Die stratosphäre des atlantischen ozeans. *Wiss. Erg. d. DAE Meteor1925–1927*, 6(2):1–288.

Yuan, X. and Martinson, D. G. (2001). The antarctic dipole and its predictability. *Geophysical Research Letters*, 28(18):3609–3612.

Zenk, W. and Morozov, E. (2007). Decadal warming of the coldest antarctic bottom water flow through the vema channel. *Geophysical Research Letters*, 34(14).

Zhang, R., Delworth, T. L., Rosati, A., Anderson, W. G., Dixon, K. W., Lee, H.-C., and Zeng, F. (2011). Sensitivity of the north atlantic ocean circulation to an abrupt change in the nordic sea overflow in a high resolution global coupled climate model. *Journal of Geophysical Research: Oceans (1978–2012)*, 116(C12).

Zwally, H., Beckley, M., Brenner, A., and Giovinetto, M. (2002). Motion of major ice-shelf fronts in antarctica from slant-range analysis of radar altimeter data, 1978-98. *Annals of Glaciology*, 34(1):255–262.